ELECTRICALLY INJECTED EXCITON-POLARITON LASERS

by

Md Zunaid Baten

A dissertation submitted in partial fulfillment
of the requirements for the degree of
Doctor of Philosophy
(Electrical Engineering)
in The University of Michigan
2016

Doctoral Committee:

Professor Pallab K. Bhattacharya, Chair
Professor L Jay Guo
Professor Jamie D. Phillips
Associate Professor Kevin P. Pipe

To my wife, Sanjina Hossain

ACKNOWLEDGMENTS

I would like to express my most sincere gratitude and appreciation to all the people who have contributed to my efforts towards this dissertation. First and foremost, I would like to thank my doctoral advisor, Prof. Pallab Bhattacharya, for his constant support, guidance and encouragement throughout the course of my PhD studies and research. His passionate pursuit of knowledge and its dissemination, his endless enthusiasm towards setting visionary goals and their timely achievement, and his inventiveness and pragmatism in overcoming challenges and difficulties are the qualities I am looking to exercise in my personal and professional life. I am particularly grateful to him for continually providing me with access to state-of-the-art experimental research facilities. I would also like to thank my doctoral committee members, Prof. Jamie Phillips, Prof. L Jay Guo, and Prof. Kevin P. Pipe for their insightful comments, valuable suggestions and enriching discussions on my dissertation.

I am thankful for the help of our current and former group members: Dr. Ayan Das, Dr. Sishir Bhowmick, Dr. Animesh Banerjee, Dr. Shafat Jahangir, Dr. Saniya Deshpande, Dr. Thomas Frost, Arnab Hazari, Aniruddha Bhattacharya and Anthony Aiello. In particular, I am grateful to my mentor in the lab, Dr. Sishir Bhowmick, who introduced me to molecular beam epitaxy, device fabrication and characterization techniques. I would like to thank both Dr. Bhowmick and Dr. Shafat Jahangir for helping me to seamlessly settle down here in Ann Arbor. I am also grateful to my good friend and former colleague, Dr. Thomas Frost, who has always been a great source of help and

support both inside and outside the labs. Even after his graduation, he has unfailingly responded to my queries regarding my research and thesis dissertation. Special appreciation goes to Arnab Hazari and Aniruddha Bhattacharya, who have been extremely supportive and co-operative colleagues throughout. Besides my group members, I would also like to thank Dr. Jimmy Chen and Dr. Alan Teran, for all the insightful and refreshing discussions we have had in our office. I also thank my fellow graduate researchers Hyunsoo Kim and Chumin Zhao for their assistance in their labs.

I would like to acknowledge the contribution of our collaborators, Prof. Alexey Kavokin and Dr. Ivan Iorsh, who have provided me with invaluable theoretical insights and suggestions. The theoretical models developed by them greatly complement the experimental studies carried out in this work. I must also express my appreciation and gratitude to all the staffs of the Lurie Nanofabrication facility, where I have met some of the most co-operative and cordial personnel in my professional career. I would like to specially thank Dennis Schweiger, Dr. Pilar Herrera-Fierro, Tom Latowski, Matthew Oonk, Greg Allion, Brian Armstrong, Steven Sostrom, Shawn Wright, Dr. Nadine Wang, Tony Sebastian, Dr. Rob Hower, Dr. Sandrine Martin, and Katharine Beach for their unfailing helpfulness regarding numerous logistics, processing and device fabrication related issues. I would also like to thank Dr. Haiping Sun and Dr. Kai Sun of the Michigan Center for Materials Characterization facility for their assistance and support with AFM, SEM, and FIB milling. I am also thankful to Steve Katnik for helping me with the Ti:Sapphire laser.

I am grateful to Lisa Vogel, Melanie Caughey, Laura Jarels, Jim Kozich, Deb Swartz, Beth Stalnaker, Anne Rhoades, Karen Liska, and Steve Pejuan for providing me

with administrative support during my graduate career. The majority of this work has been financially supported by the National Science Foundation (MRSEC program), which I gratefully acknowledge. I would also like to acknowledge King Abdullah University of Science and Technology (KAUST) for initial funding of my research, and the University of Michigan Rackham Graduate School for providing partial fellowships to support my studies.

Finally, I am grateful to my family members, near and far, who have always blessed me with goodwill. I am particularly thankful to my parents, my sister and my in-laws for their constant support and encouragement. I would also like to thank my two-year-old son, Zarif Baten, who has not only filled our life with joyful bliss, but also has added a new perspective to it. Last but not the least, I am truly grateful to my wife Sanjina Hossain, for her unconditional love and support over the last four years. Her patience, perseverance and joyfulness have constantly motivated me to move forward with my efforts, and I dedicate this work to her.

TABLE OF CONTENTS

DEDICATION ii

ACKNOWLEDGMENT iii

LIST OF FIGURES xi

LIST OF APPENDICES xix

ABSTRACT xx

CHAPTER

I. Introduction 1

1.1 Preface 1

1.2 Overview of Previous Work 3

1.3 Motivation of Present Work 5

1.4 Outline of the Dissertation 7

II. Theoretical Background 11

2.1 Introduction 11

2.2 Excitons in Semiconductors 11

2.2.1 Excitons in Bulk Semiconductors (3D Excitons) 13

2.2.2 Excitons in Quantum Wells (2D Excitons) 15

2.2.3 Excitons in Quantum Wires and Dots (1D and 0D Excitons) 16

2.2.4 Free and Bound Excitons 18

2.2.5 Bosonic Nature of Excitons 19

2.3 Semiconductor Microcavity and Cavity Photon 20

2.3.1 Distributed Bragg Reflector (DBR) 21

2.3.2 Microcavity with DBRs 23

2.3.3 Cavity Photon Characteristics....24
2.4 Light-Matter Interaction....26
2.4.1 Strong vs. Weal Coupling Regime....27
2.4.2 Exciton-Polaritons in the Strong Coupling Regime....28
2.4.2.1 Polariton Dispersion Characteristics....29
2.4.2.2 The Role of Detuning in Polariton Dispersion....31
2.4.2.3 Polariton Effective Mass....33
2.4.2.4 Impact of Homogenous and Inhomogeneous Broadening....34
2.4.3 2D, 1D and 0D Polaritons....35
2.4.4 Spin Dynamics of Polaritons....37
2.5 Polariton Lasing Phenomenon....38
2.5.1 Polariton Lifetime and Scattering Events....38
2.5.2 LP Relaxation and Bottleneck Effects....40
2.5.3 Stimulated Scattering and Dynamic Condensation....42
2.5.4 Phase Transition and Lasing Threshold....44
2.5.5 Polariton vs. Photon Lasing....46
2.6 Summary....48

III. Experimental Techniques....50

3.1 Introduction……......50
3.2 Materials Choices, Growth and Deposition Techniques....51
3.2.1 Materials Choices for the Emitter....51
3.2.2 Materials Choices for the Cavity Mirror....53
3.2.3 Materials Growth and Deposition Techniques....54
3.3 Pumping Schemes and Device Fabrication....56
3.3.1 Optical and Electrical Pumping Schemes....56
3.3.2 Fabrication of GaAs- and GaN-based Devices....58
3.3.3 Defining the Microcavity: Focused Ion Beam Etching and Electron Beam Evaporation....61
3.4 Materials Characterization....62
3.4.1 Photoluminescence Measurements....63

3.4.2 Ellipsometry and Reflectivity Measurements 64
3.4.3 Surface Morphology and Compositional Measurements 66
3.5 Device Characterization Techniques 68
3.5.1 Micro-photoluminescence Measurements 69
3.5.2 Electrical Biasing and Current Voltage Measurements 69
3.5.3 Angle-Resolved Electroluminescence and Momentum Space Mapping 70
3.5.4 Light-Current Characteristics 72
3.5.5 Spatial Coherence Measurements 73
3.5.6 Steady-State Output Polarization Measurements 74
3.5.7 Small-Signal Modulation Measurements 76
3.6 Summary 78

IV. GaAs-Based High Temperature Polariton Diode Lasers 79

4.1 Introduction 79
4.2 Enhancement of Exciton Binding Energy in a GaAs-Based System 80
4.3 Device Heterostructure 81
4.4 Material Characterization 84
4.4.1 Excitation Dependent and Time-Resolved Photoluminescence 84
4.4.2 Estimation of Exciton Binding Energy 86
4.5 Device Fabrication 89
4.6 Device Characterization 90
4.6.1 Microcavity and Diode Characteristics 90
4.6.2 Strong-Coupling Characteristics 92
4.6.3 Polariton Lasing Characteristics 94
4.6.4 Momentum Space Distribution and Spatial Coherence 97
4.7 Towards Room Temperature Operation 99
4.7.1 Device Heterostructure 99
4.7.2 Materials Characterization 101
4.7.2.1 Temperature Dependent Photoluminescence 101
4.7.2.2 Excitation Dependent Photoluminescence 104
4.7.3 Device Characteristics 106

4.8 Summary 108

V. GaN-Based Room Temperature Polariton Lasers 109

5.1 Introduction……..…..109
5.2 Background of GaN-based Polariton Lasers.....110
5.3 Device Heterostructure and Material Growth.....112
5.4 Photoluminescence Measurements 114
5.5 Device Fabrication.....117
5.6 Device Characterization.....118
5.6.1 Diode and Microcavity Characteristics.....119
5.6.2 Strong-Coupling Characteristics.....121
5.6.3 Polariton Lasing Characteristics 123
5.6.4 Momentum Space Distribution.....126
5.6.5 Spatial Coherence Measurements.....127
5.6.6 Measurement and Analysis of Stead-State Polarization 129
5.6.6.1 General Overview of the Output Polarization of a Polariton Laser.....129
5.6.6.2 Experimental Results 131
5.6.6.3 Theoretical Analysis 136
5.7 Summary……..…..137

VI. Small-signal Modulation and Role of Defects in Polariton Lasers 138

6.1 Introduction……..…..138
6.2 Small-Signal Modulation Polariton Lasers.....139
6.2.1 Measurement and Analysis of Resonant Frequency.....139
6.2.2 Differential Gain and Gain Compression 142
6.2.3 Frequency Chirping in a Polariton Laser.....145
6.2.4 Theoretical Limits of Frequency Response 146
6.3 The Role of Defects in Polariton Lasers.....148
6.3.1 Outline of the Experiment.....149
6.3.2 Estimation of Dislocation Densities.....150
6.3.3 Heterostructure and Microcavity Diode.....151

6.3.4 Strong-Coupling Characteristics 151
6.3.5 Polariton Lasing Characteristics 153
6.3.6 Measurement and Analysis of LP Occupancy 154
6.3.7 Discussion of Results 157
6.3.8 Simplified Theoretical Modeling 159
6.4 Summary 163

VII. Optical Amplification in the Strong-Coupling Regime 164

7.1 Introduction 164
7.2 Theory and Background 165
7.2.1 Theory of Bulk Polaritons 165
7.2.2 Experimental Studies on Bulk Polaritons 167
7.2.3 Bulk vs. Microcavity Polaritons 168
7.2.4 Theory of SOA in the Strong-Coupling Regime 169
7.3 Heterostructure Growth and Device Fabrication 172
7.4 Measurements and Results 173
7.4.1 Diode Characteristics and Waveguide Loss Measurements 173
7.4.2 Measurement System and Ti:Sapphire Laser Calibration 175
7.4.3 Electroluminescence Measurements 178
7.4.4 Time Integrated Intensity Measurements 180
7.5 Discussions and Conclusion 183

VIII. Summary and Suggestions for Future Work 185

8.1 Summary of Present Work 185
8.2 Suggestions for Future Work 190
8.2.1 Quantum Well-Based Room Temperature Polariton Laser Diode 190
8.2.2 Electrical Exciton-Polariton Spin Switch 192
8.2.3 Spin-Polarized Exciton-Polariton Spin Switch 194

APPENDICES 200

BIBLIOGRAPHY 210

LIST OF FIGURES

FIGURE

2.1: A schematic representation of an exciton having exciton Bohr radius of a_{BX} in a 2D crystal lattice which has a lattice constant of a ; (b) exciton dispersion relation showing the exciton binding energy, E_{BX} and the semiconductor bandgap, E_g. 12

2.2: An AFM image of InAs self-assembled quantum dots grown on InP substrate by molecular beam epitaxy for 1.55μm emission wavelength [88].. 17

2.3: Measured reflectivity spectra of 18 pairs of AlGaAs/GaAs DBR.. 21

2.4: Calculated reflectivity plotted as function of number of DBR pairs for different ratios of n_1 and n_2.....22

2.5: Measured reflectance spectra of a AlGaAs/GaAs DBR based microcavity along with calculated results obtained from propagation matrix approach.....23

2.6: Schematic representation of a planar microcavity having DBR mirrors showing the in-plane and out-of-plane wave vectors. 25

2.7: General polariton dispersion characteristics in a semiconductor microcavity. 31

2.8: Calculated polariton dispersion characteristics for two different detunings... 32

2.9: Calculated lower polariton effective masses for the two different detunings considered in Fig. 2.8... 34

2.10: A schematic representation of nanowire(s) imbedded between planar mirrors to illustrate (a) 0D, (b) 1D and (c) 2D polaritons [70].....36

2.11: Different regions of a generalized polariton dispersion, along with the carriers in band, in the context of polariton relaxation.....41

2.12: A generalized polariton phase diagram for a microcavity diode showing different regimes of operation. 45

3.1: Exciton Bohr radius, exciton binding energies and corresponding exciton dissociation temperatures of different materials plotted as a function of energy bandgap.....52

3.2: Veeco Gen 930 MBE system used for epitaxial growth in the present study [150]... 55

3.3: Conventional VCSEL structure along with the heterostructure (not drawn to scale) [81].. 58

3.4: Schematic of the edge-emitting microcavity polariton diode used in this study (not drawn to scale). 59

3.5: SEM image of a FIB etched facet of the microcavity diode.. 62

3.6: A schematic representation of the temperature and excitation dependent PL measurement system [adopted from Ref. 150]..... 63

3.7: (a) Measured refractive indices of e-beam evaporated SiO_2 and TiO_2 films using spectroscopic ellipsometry, (b) measured reflectivity of 3 pairs of e-beam evaporated SiO_2/TiO_2 DBR pairs using UV-visible spectroscopy.... 65

3.8: AFM image after etch pit dislocation treatment of a GaN-on-sapphire template.. 67

3.9: Measured etch profile during fabrication of the GaAs-based device. 68

3.10: Schematic diagram of an experimental setup for room temperature angle-resolved electroluminescence measurement.. 71

3.11: A schematic illustration of the Mach-Zender interferometer used in this study.. 74

3.12: Experimental setup of small-signal modulation response measurement.....76

4.1: (a) Bandgap energies of $Al_xGa_{1-x}As$ plotted as a function of the Al mole fraction [127], (b) exciton binding energies of $Al_xGa_{1-x}As$ based quantum well plotted as a function of quantum well width [128].....82

4.2: A schematic of the device heterostructure grown by MBE.....83

4.3: Measured excitation dependent PL spectra at T= 30 K. The inset shows a linear dependence of the integrated intensity on excitation density.....84

4.4: Measured time resolved photoluminescence from the AlGaAs/AlGaAs SQW at T=155 K along with exponential model based analysis... 86

4.5: PL emission peak energy plotted as a function of temperature (inset shows the calculated energy states of the SQW). 87

4.6: Measured values of E_{ph} , along with the values obtained for E_g, E_e, E_{hh}, and E_{BX} from our analysis.. 88

4.7: A schematic representation of the GaAs-based SQW microcavity diode 89

4.8: SEM image of the fabricated device along with the contact pads.....90

4.9: (a) Current-voltage characteristics of the microcavity diode (the inset shows the I-V characteristics in logarithmic scale), (b) measured micro-PL spectrum from the microcavity.....91

4.10: Angle resolved electroluminescence spectra measured at T=155 K.. 92

4.11: Polariton dispersion calculated using coupled harmonic oscillator model alongside the measured data.....93

4.12: Integrated EL intensity, LP emission linewidth and blue shift of LP peak emission as a function of injected current density.. 94

4.13: (a) EL spectra measured at various injection levels. Inset shows the magnified UP region; (b) LP and UP peak emission energies at higher injection levels showing the onset of the weak coupling regime.. 95

4.14: Two threshold lasing behavior with the non-linearities due to both polariton and photon lasing. Inset shows EL spectra measured above photon lasing. 96

4.15: LP ground state occupancy for different $k_{\|}$ states obtained at three injections.... 97

4.16: Interference visibility as a function of the displacement (x) between the double image of the polariton emission. Inset shows interference pattern for x = 2 μm.. 98

4.17: A schematic of the $Al_{0.41}Ga_{0.59}As/Al_{0.71}Ga_{0.29}As$ SQW p-i-n heterostructure;. 99

4.18: Analyzed electronic states of the $Al_{0.41}Ga_{0.59}As/Al_{0.71}Ga_{0.29}As$ SQW.. 100

4.19: (a) Measured temperature dependent PL spectra in the $Al_{0.41}Ga_{0.59}As/Al_{0.71}Ga_{0.29}As$ SQW, (b) multi-peak fitting based analysis.. 102

4.20: Peak emission energies of peak I and II are plotted as a function of temperature along with the analysis based on Varshni relation 103

4.21: Measured excitation dependent PL spectra at T=15 K.....104

4.22: PL peak energy values plotted as a function of the excitation power. 105

4.23: Measured excitation dependent PL spectra of the $Al_{0.41}Ga_{0.59}As/Al_{0.71}Ga_{0.29}As$ SQW at T=15 K.....106

4.24: (a) Current-voltage relations of several devices fabricated using the SQW p-i-n heterostructure, (b) measured room temperature EL spectra from the microcavity diode fabricated using the $Al_{0.41}Ga_{0.59}As/Al_{0.71}Ga_{0.29}As$ SQW.....107

5.1: (a) A schematic of the GaN-based polariton device along with the PAMBE-grown heterostructure, (b) schematic representation of the edge emission geometry.....112

5.2: X-ray diffraction rocking curves for lattice matched $In_{0.18}Al_{0.82}N$/GaN epilayers [150].....113

5.3: AFM image of the surface of lattice matched $In_{0.18}Al_{0.82}N$ on GaN-on-sapphire substrate [150].....114

5.4: Measured photoluminescence characteristics of c-plane bulk GaN on sapphire at (a) T=25 K and (b) room temperature.....115

5.5: Measured time resolved photoluminescence from bulk GaN at room temperature.....117

5.6: SEM image of a FIB etched cavity along with the p-contact pad.....118

5.7: Current-voltage characteristics of the device measured at room temperature.....119

5.8: Micro-PL of the microcavity diode measured at room temperature.. 120

5.9: (a) Five point moving average filtered angle-resolved electroluminescence measured from the microcavity diode at room temperature; (b) 2x2 coupled harmonic oscillator based analysis of the polariton dispersion along with measured data.. 122

5.10: Integrated EL intensity of the LP emission as a function of injected current density. Inset shows an EL spectra measured at an injection above the lasing threshold.....123

5.11: Two threshold lasing behavior showing the non-linearities due to polariton and photon lasing. The threshold current densities of polariton and photon lasing are indicated by arrows. 124

5.12: Measured LP emission linewidth and blueshift of LP emission peak as a function of injected current density 125

5.13: LP ground state occupancy for different $k_{||}$ states obtained from angle-resolved EL at three different injection current densities....126

5.14: (a) Interference visibility measured as a function of the injected current density for zero displacement between the double images of the LP emission. The dashed line is a guide to the eye,(b) interference visibility measured as a function of the displacement between a double image of the polariton condensate below and above the polariton lasing threshold... 128

5.15: The splitting of the ground-state degeneracy illustrated using a generalized polariton dispersion relation... 131

5.16: (a) Light-current characteristics of Device 1 and 2 at normal incidence with respect to the DBRs, (b) polar plots of the normal incidence LP electroluminescence intensities recorded as a function of angle of linear analyzer below and above threshold of Device 1 132

5.17: Measured steady-state degree of linear polarization of Device 1. The solid lines represent theoretical calculations.. 133

5.18: Measured steady-state degree of linear polarization of Device 2 as a function of injected current density. The solid lines represent theoretical calculations 134

5.19: Polarization-resolved (along 90^o angle of the linear analyzer) and unresolved light-current characteristics of (a) Device 2 and (b) Device 1. The inset shows an enlargement highlighting the different thresholds.. 135

6.1: Frequency response derived from measured time resolved EL at different DC injection levels. The solid lines represent calculated frequency responses (Inset shows the measured transient response of the polariton laser to a switching pulse at $J = 5.4J_{th}$).. 140

6.2: Measured resonance frequency as function of $n_{Lp}^{\infty 1/2}$ along with calculated results obtained from equation (2)....142

6.3: Variation of the damping factor as a function of the square of the resonance frequency. 143

6.4: Measured linewidth of LP emission peak as a function of the small signal modulating frequency, under a fixed DC bias of 1.15 J_{th}. 145

6.5: Calculated modulation frequencies for different polariton-polariton scattering rates and polariton lifetimes 146

6.6: Calculated resonance frequencies plotted as a function of the ground state LP occupancy for different values of n_T. 147

6.7: (a) Angle-resolved EL measured from the bulk-GaN, (b) corresponding polariton dispersion characteristics from 2x2 couple harmonic oscillator model.. 152

6.8: Integrated EL intensity of the LP emission, measured LP emission linewidth and blueshift of LP emission peak as a function of injected current density.. 154

6.9: LP ground state occupancy for different $k_{||}$ states obtained from angle-resolved EL at four different injections, along with Maxwell-Boltzmann distribution based analysis at $J=J_{th}$. 155

6.10: Measured polariton occupation at $J=J_{th}$ for GaN-based Device 1, GaN-based Device 2 and GaAs-based Device 1 along with the Maxwell-Boltzmann distribution based analysis. The error bars indicate experimental uncertainty, whereas the standard deviation of the temperature fits are shown in the legend 156

6.11: Arrhenius plot of the integrated photoluminescence intensity as a function of reciprocal temperature of a GaN epitaxial layer, grown on a GaN-on-sapphire template, identical to GaN-based Device 1. 158

6.12: (a) A plot of the effective LP temperature (T_{LP}) as a function of lattice temperature (T_{latt}) for the two GaN-based devices, (b) A 3D plot of effective LP temperature, lattice temperature and the 2D defect density. 162

7.1: Bulk polariton dispersion characteristics in GaN; inset shows the dispersion over a larger range of the wave vector 167

7.2: A comparison between the dispersion relation of bulk and 2D microcavity polaritons.. 169

7.3: (a) A generalized schematic of the semiconductor optical amplifier proposed by Solnyshkov et al., (b) calculated LP dispersion of a bulk-GaN waveguide.. 170

7.4: A cross-sectional schematic of the device heterostructure along with p- and n- contacts and the lateral dimensions 172

7.5: (a) Current-voltage characteristics of the bulk GaN diode; inset shows the I-V characteristics in logscale, (b) output intensity of the waveguide as a function of waveguide length.. 174

7.6: A schematic diagram of the experimental setup used in this study.....176

7.7: (a) Frequency doubled outputs of the tunable Ti:Sapphire laser for different positions of the laser's slit and prism sequence, (b) frequency doubled output of the laser, where the GaN-exciton energy is taken as the reference... 177

7.8: EL spectra measured in a direction normal to the AR-coated facet of the device.....178

7.9: Recorded EL spectra with the laser tuned to 372 nm and the device biased at different injection current densities. 179

7.10: Measured time integrated intensities I_2 and I_3 while the device's current bias is incremented approximately every 10s.....180

7.11: Measured time-integrated intensities I_1 and I_2-I_3 plotted as a function of time. 181

7.12: (a) The amplification factor plotted as a function of time corresponding to the results shown in Fig. 7.15, (b) amplification factor as a function of injection current for different values of ΔE. 182

8.1: Schematic representation of the proposed GaN/AlGaN quantum well based polariton diode laser... 191

8.2: Excitation dependent PL intensities of the InGaN/GaN multiple quantum-well heterostructure at T= 30 K.....192

8.3: Proposed electrically controllable exciton-polariton spin switching scheme 193

8.4: Principle of operation of the exciton polariton spin switch.....194

8.5: (a) Magnetization characteristics of the FeCo/MgO tunnel contact obtained by MOKE measurements, (b) peak magnetoresistance measured as function of channel length to obtain the spin injection efficiency and diffusion lengths.. 195

8.6: An image of the proposed GaAs-based edge emitting microcavity diode employing spin injectors as the n-type contact; inset shows the magnified cavity region 196

8.7: Proposed GaN-based inverted heterostructure for realizing an electrically pumped exciton-polariton spin switch. 197

8.8: (a) Output circular polarization alongside the measured magnetization of the tunnel injector contacts (the dashed line is a guide to the eye), (b) output circular polarization as a function of injection.....198

A.1: Surface- and edge-emitting geometry-based semiconductor microcavities showing the directions of excitation, light output and exciton dipole moment.....201

D.1: Theoretically calculated relation between increase of the emission linewidth and the shift of the peak emission wavelength.....209

LIST OF APPENDICES

APPENDIX

A. Exciton-Photon Coupling in Surface- and Edge-Emitting Geometries. 201

B. Theoretical Analysis of Steady-State Output Polarization. 203

C. Three-level Rate Equation based Modeling of the Polariton Laser 206

D. Change in Refractive Index and Peak Wavelength with Small Signal Biasing.....208

ABSTRACT

Exciton-polaritons or polaritons, which are part-light, part-matter hybrid quasiparticles, offer an entirely new physics for realizing semiconductor lasers. These relatively new solid-state devices, which are more commonly known as polariton lasers, can generate coherent light output at two to three thousand times lower input power than that required for an equivalent photon laser. Practical applications of polariton lasers require electrically pumped devices which can operate at high temperatures, if not at room temperature. The operation of GaAs-based electrically pumped polariton lasers, which are usually designed using the vertical cavity surface emitting geometry, has remained limited to cryogenic temperatures. Though a room temperature electrically pumped polariton laser has been recently demonstrated, several important aspects and characteristics of polariton laser diodes have hitherto remained unexplored.

In the present study, GaAs- and GaN-based electrically pumped polariton lasers have been experimentally realized based on an edge-emitting geometry where cavity feedback and current injection are orthogonal to each other. The GaAs-based device is designed with a $Al_{0.31}Ga_{0.69}As/Al_{0.41}Ga_{0.59}As$ single quantum well which emits in the visible region of the electromagnetic (EM) spectrum. The high exciton binding energy of this heterostructure enables strong coupling and polariton lasing at 155 K. The threshold for polariton lasing is observed at 90 A/cm^2, whereas conventional photon lasing is recorded in the same device at ~17 times higher pump powers. A bulk GaN-based

microcavity polariton diode laser is also experimentally realized, which operates as an ultraviolet coherent emitter at room temperature. In this device, the non-linear threshold for polariton lasing occurs at 190 A/cm^2, whereas a second non-linearity due to conventional photon lasing is observed at 46 kA/cm^2. Polariton lasing phenomena in these devices have been further confirmed with the observation of linewidth collapse and blueshift of lower polariton emission, polariton population redistribution in momentum space and spatial coherence measurements. A maximum degree of linear polarization of ~22% is also measured and theoretically analyzed in the GaN-based device.

In this work, the small signal modulation characteristics of a polariton laser is also presented for the first time. These measurements, performed on the GaN-based electrically pumped polariton laser, shows promise of the device as a low-power modulated coherent light source for medical and biomedical applications or short distance plastic fiber communication at short wavelengths (violet and ultra-violet), where a conventional laser is difficult to realize. A maximum -3 dB modulation bandwidth of 1.18 GHz is measured and the experimental results have been analyzed with a theoretical model based on the Boltzmann kinetic equations. Frequency chirping under high frequency operation has also been investigated, and gain compression in these devices has been phenomenologically defined. An area yet unexplored is the role of defects on the performance characteristics of polariton lasers. In this work, this aspect has been examined and elucidated in the context of dynamic condensation in both electric and optically pumped GaAs- and GaN-based polariton lasers. Finally, the possibility of realizing a low power optical amplifier based on strong coupling has been studied experimentally.

Chapter I
Introduction

1.1 Preface

Semiconductor lasers have revolutionized almost all areas of modern science and technology, which include high-speed telecommunication, industrial processing, scientific experiments and explorations, consumer electronics, biomedical applications and so on [1-5]. The development of semiconductor lasers dates back to the late 1950s when the fundamental quantum limit of the lasing linewidth was reported by Schawlow and Townes [6]. Ever since the early demonstrations of coherent emission using semiconductor gain media [7-12], semiconductor lasers have developed significantly, mostly because of the advancements in high quality epitaxial growth and fabrication technologies. Followed by these developments, for over half a century we have been using semiconductor lasers which operate on the principle of *light amplification by stimulated emission of radiation*. However *exciton-polaritons* or *polaritons*, which are part-light, part-matter hybrid quasiparticles, offer an entirely new physics for realizing semiconductor lasers. When an emitter in the form of bulk, quantum well, quantum wire or quantum dot is placed inside a suitably designed microcavity, the strong interaction between the confined light modes and the exciton states results in new eigenstates in the form of exciton-polaritons [13-17]. Because exciton-polaritons are half-matter, half-light

like Bosonic quasiparticles, they can be exploited to study numerous phenomena related to cavity quantum electrodynamics (QED) and many-body physics, such as Bose-Einstein condensation (BEC) [18-21], spontaneous symmetry breaking [22,23], superfluidity [24-26], Bardeen-Cooper-Schrieffer (BCS) states [27-28] and Berezinskii-Kosterlitz-Thouless (BKT) transition [29-30]. However, as far as practical applications in photonics and optoelectronics are concerned, one of the most exciting prospects of exciton-polaritons is towards the realization of an *inversionless coherent emitter*.

Imamoglu et al. first proposed the possibility of generating coherent light by spontaneous radiative recombination from a coherent exciton-polariton condensate in a semiconductor microcavity [31]. Whereas the gain mechanism in a conventional photon laser is *stimulated emission*, for a polariton device the process is *stimulated scattering*. Unlike a conventional photon laser, the separation of stimulation and emission in a polariton device leads to coherent emission without the requirement of population inversion. As a result, it is expected that the threshold energy required for coherent emission from this device would be much smaller than that of a photon laser [31-35]. This new kind of a solid-state device, which is more commonly known as a *polariton laser,* holds great promise as a low-power coherent light source for medical and biomedical applications, short distance plastic fiber communications, high-speed optical interconnects and logic circuits, and quantum information processing [36-43]. Consequently, polariton lasing has continued to be an intense topic of research in recent years. In particular, advancements in areas of materials growth, device design and device fabrication technologies have led to numerous experimental realizations of this novel light source, which even about two decades ago used to be a mere scientific curiosity.

1.2 Overview of Previous Work

In the early experimental studies on excitons in semiconductors, it was observed that under optical excitation, the excitonic transitions are significantly influenced by their apparent coupling to light. In 1957, S. I. Pekar described these changes of the excitonic spectrum with respect to an *additional wave* appearing in the semiconductor crystal [44]. The observed phenomenon was later described by J. J. Hopfield in terms of the emergence of new eigenstates in the system, resulting from linear coupling of the exciton field to the electromagnetic field [45]. These eigenstates are defined as *polaritons,* or strictly speaking *exciton-polaritons,* to distinguish them from other types of light-matter entangled coupled states such as phonon-polaritons or plasmon-polaritons. It should be noted that in our text we have interchangeably used the terms *exciton-polaritons* and *polaritons*.

The first experimental observation of polaritons was reported by Frohlic in CuCl in 1971 using two-photon absorption spectroscopy [46]. However it was not until 1977, when exciton-polaritons were first observed in a semiconductor [47]. In this study, photoluminescence obtained from high purity GaAs epitaxial layers were explained within the polariton framework. Since then, there have been numerous reports on the experimental observation of exciton-polaritons in different direct bandgap semiconductors, such as GaAs, CdS, ZnO, ZnTe, ZnSe and GaN [48]. All these experiments were performed using bulk semiconductors instead of having a quantum well (QW) active region, because light-matter coupling of two-dimensional QW exciton to the three-dimensional continuum of photons is precluded by enhanced radiative decay [49]. A major breakthrough appeared in 1992, when Weisbuch et al. reported normal-

mode splitting in a GaAs quantum well based microcavity, which consisted of GaAs/AlGaAs quantum wells imbedded between two distributed Bragg reflectors (DBRs) [13]. This work was followed by numerous observations of normal mode splitting and light matter coupling in semiconductor microcavities, mostly in GaAs-based systems because of their relatively matured growth and fabrication technologies [50-53].

Followed by the experimental development of low-dimensional systems in the form of semiconductor microcavities, Imamoglu and coauthors first theoretically proposed the idea of generating coherent emission from a degenerate condensate of exciton-polaritons and coined in the term *exciton-polariton laser* [31]. Based on this concept, the first experimental observation of polariton lasing was reported by Le Si Dang et al. at liquid He temperature in a CdTe-based microcavity [54]. Since then, dynamic condensation of polaritons and polariton lasing in different material and nanostructure systems and with different dimensionality of the polaritons have been demonstrated in a series of elegant experiments using optical excitation [18-23, 55-75]. Because of the relatively matured growth and fabrication technology of GaAs, strong-coupling and polariton lasing phenomenon have been studied extensively in GaAs-based polariton devices [13, 18, 20, 23-26, 50-53, 56-58, 63, 66]. Most of these measurements have been performed at cryogenic or low temperature, as at elevated temperatures the GaAs-based strongly coupled microcavity transitions into the weak coupling regime because of the intrinsically low exciton binding energy of the material system. To this end, wide bandgap semiconductors like GaN and ZnO gained considerable interest because of their low exciton Bohr radii and high exciton binding energies. Polariton lasing at high temperatures, if not at room temperature, has been demonstrated using

optical excitation in microcavities comprising of these material systems [21, 60, 61, 67-74]. The first observation of polariton lasing at room temperature was reported in 2007 in an optically pumped bulk-GaN based hybrid microcavity [60]. More recently, polariton lasing has been reported at 450 K using an optically pumped ZnO microwire [74].

As far as the dimensionality and nanostructures are concerned, strong-coupling and polariton lasing have been reported using bulk [60, 67, 71-73], quantum-well(s) [56-59, 61-63, 66, 75], micro- and nanowire(s) [68-70, 74] and quantum dot(s) [76, 77]. Both semiconductor and dielectric materials have been utilized to successfully realize the DBR layers of the reported polariton lasers. It has been experimentally demonstrated that the polariton lasing threshold is 1-3 orders of magnitude smaller than the photon lasing threshold measured in the same device [57, 66, 68, 70, 71].

1.3 Motivation of Present Work

As discussed in the previous section, optically pumped polariton lasers based on different materials and nanostructures have been reported to operate at temperatures ranging from cryogenic to 300 K. Practical applications of these ultra-low threshold coherent emitters require electrical injection, so that they can be conveniently integrated into optical telecommunication networks, optoelectronic integrated circuits (OEICs) or embedded systems containing optoelectronic components. Experimental realization of polariton light emitting diodes was reported in 2008 using GaAs-based microcavity diodes [78, 79]. Though clear evidences of strong-coupling were observed in these devices, any indication of polariton lasing remained non-existent. These experiments however fomented the experimental realization of the first electrically pumped polariton

lasers, which were reported simultaneously in 2013 by two groups [80, 81]. In these works, exciton-polariton laser diodes were epitaxially grown and fabricated based on a vertical cavity surface emitting structure, where InGaAs/GaAs quantum well was employed as the active region. While this is a monumental achievement towards the development of these next-generation coherent light sources, the operations of these devices are limited to cryogenic temperatures. The first electrically pumped polariton laser which can operate at room temperature was reported very recently by Bhattacharya et al. using a bulk GaN-based microcavity diode [82]. Though this is an important milestone towards the practical application of polariton lasers, several important aspects and characteristics of polariton laser diodes have hitherto remained unexplored, among which the small-signal modulation response, steady-state output polarization, and the role of defects on dynamic condensation are particularly important.

Motivated by the challenges associated with the development of electrically pumped polariton lasers, and the need for a more detailed understanding of their performance characteristics and limitations, the experimental realization and characterization of polariton laser diodes, which can operate at high temperatures, was undertaken in this work. Utilizing a single $Al_{0.31}Ga_{0.69}As/Al_{0.41}Ga_{0.59}As$ quantum well microcavity diode, a GaAs-based polariton laser has been fabricated and characterized which can operate at T=155 K. Contrary to the conventional surface emitting geometry, an edge-emitting structure has been employed in which current injection and optical feedback are orthogonal to each other. Based on the similar edge-emitting geometry, a room temperature bulk GaN-based electrically pumped polariton laser has also been designed, fabricated and characterized. Besides static characterization, we also report for

the first time small-signal modulation characteristics of an electrically pumped polariton laser. The role of defects, which are quite prevalent in GaN based material systems, has also been elucidated in the context of polariton lasing and dynamic condensation. Theoretical study shows that it is possible to amplify the guided mode in a waveguide operating in the strong-coupling regime [82]. Based on this principle, we also present a detailed experimental study of an electrically pumped semiconductor optical amplifier (SOA), which is expected to amplify the guided polariton mode in the system.

1.4 Outline of the Dissertation

This dissertation presents an experimental study on the development of high temperature electrically injected exciton-polariton lasers and devices. The thesis is organized as follows.

Chapter 2 provides a theoretical overview of the fundamental concepts related to exciton-polaritons in a semiconductor microcavity. Excitons in semiconductors having different dimensionalities, such as bulk, quantum well, quantum wire and dots, are discussed first. Next the design principle of a semiconductor microcavity employing distributed Bragg reflectors are presented and characteristics of photons in a microcavity are discussed. Then the strong-coupling regime is discussed along with theoretical formulations and its differences with the weak coupling regime are presented. Finally, the polariton lasing phenomenon is explained and its main differences with conventional photon lasing are elucidated.

In chapter 3, the experimental techniques employed in this work for material growth, device fabrication, and materials and device characterization are discussed in

detail. The materials which are commonly employed in the growth and fabrication of polariton devices are presented. The epitaxial growth and deposition techniques used in this study are also presented therein. Next the device pumping scheme, and the fabrication techniques employed to realize the scheme are discussed in detail. This is followed by a description of the materials and device characterization techniques used in this study. Relevant technical specifications of the instruments used in this study are also mentioned in this chapter.

Chapter 4 presents the experimental realization of a GaAs-based polariton diode laser which operates at T=155 K. In this chapter, we first discuss how the exciton binding energy in this system can be enhanced to facilitate high temperature operation. Next, the design and characteristics of the single $Al_{0.31}Ga_{0.69}As/Al_{0.41}Ga_{0.59}As$ quantum well used in this study are described. Then the device fabrication procedure is presented, which is followed by a detailed discussion of the results obtained from strong-coupling and polariton lasing characterization techniques. Finally, an experimental study towards the realization of a room temperature GaAs-based polariton laser is presented and the challenges and limitations involved are discussed.

Chapter 5 details the experimental realization of an electrically pumped GaN-based polariton laser which operates at room temperature. In this chapter, we first discuss in brief previous reports on GaN-based polariton lasers. Next, the device heterostructure and the excitonic transition characteristics of this system are discussed. This is followed by a description of device fabrication. Finally, the strong coupling and polariton lasing characteristics obtained from different device characterization techniques are described. The results related to strong-coupling and polariton lasing presented here are limited to

measurements performed under steady-state electrical injection. The output polarization of the device has been analyzed and explained using stochastic kinetic theory, wherein the kinetics of the system is modeled with the four coupled stochastic differential equations.

In chapter 6, an experimental study on the first small-signal modulation response of a polariton laser is presented. The device has been operated at room temperature. A maximum −3 dB modulation bandwidth of 1.18 GHz is measured in this study. The experimental results have been analyzed with a theoretical model based on the Boltzmann kinetic equations. Frequency chirping has been experimentally characterized and gain compression in a polariton laser is phenomenologically defined. In this chapter, the role of defects on the performance characteristics of these devices is also presented. Particular emphasis has been given on the lowering of the effective polariton temperature, which has been a lesser understood phenomenon. Experimental results obtained from the measurement of multiple devices are compared and analyzed in this study. Also a simplified theoretical model has been presented to phenomenologically explain the experimentally observed results.

Chapter 7 discusses the experimental study of possible amplification of guided polariton modes in an electrically pumped GaN-based device. At first, a brief theoretical overview of the concept of bulk polaritons is provided, and the theory of optical amplification in bulk GaN is discussed. Next the design, fabrication and characterization of the device are discussed. The device is expected to work as a semiconductor optical amplifier (SOA) in the strong coupling regime. Finally, based on the observed

experimental results, the challenges and difficulties associated with the experimental realization of such a device are discussed.

In chapter 8, a brief summary of the work presented in this thesis is provided. Finally, suggestions have been made for future work in regards to electrically pumped polariton lasers.

Chapter II

Theoretical Background

2.1 Introduction

Exciton-polaritons in a semiconductor microcavity offer the study of both cavity quantum electrodynamics (cavity QED) and rich many body physics. In this chapter, we briefly present a semi-classical as well as quantum description of different attributes related to strong coupling and polariton lasing phenomena in a semiconductor microcavity. The characteristics of excitons in semiconductors having different dimensionalities, and the nature of cavity photon in a microcavity are first discussed. Theoretical aspects related to the design of a semiconductor microcavity are also presented. Next, light-matter coupling in the context of exciton-polaritons are discussed and the necessary conditions for the attainment of strong coupling in a microcavity are described. The differences between the strong- and the weak-coupling regimes are also presented herein. Finally, a theoretical discussion on the polariton lasing phenomenon is presented and its differences with conventional photon lasing are elucidated.

2.2 Excitons in Semiconductors

An exciton is a charge neutral quasi-particle which arises from the Coulombic interaction of an electron and a hole. Excitons are in fact the elementary excitations in a semiconductor as the first excited state resulting from external excitation is a bound

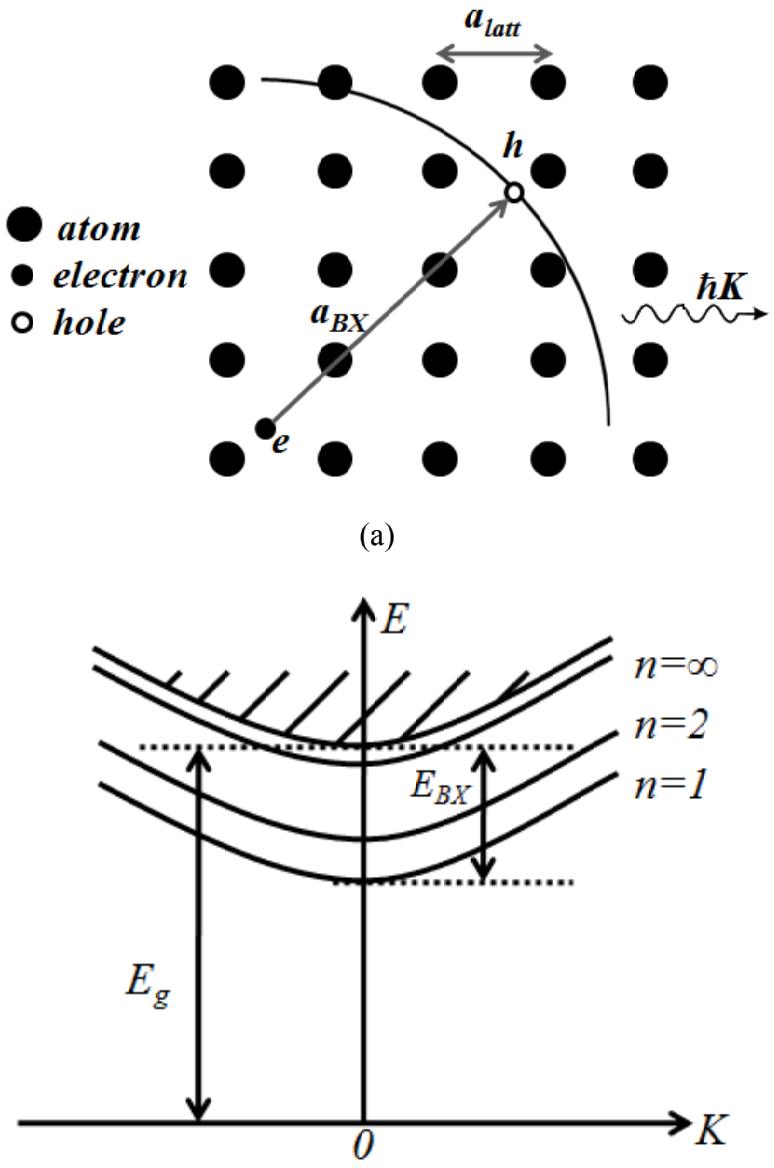

Fig. 2.1 (a) A schematic representation of an exciton having exciton Bohr radius of a_{BX} in a 2D crystal lattice which has a lattice constant of a_{latt} ; (b) exciton dispersion relation showing the exciton binding energy, E_{BX} and the semiconductor bandgap, E_g.

electron-hole pair. The associated binding energy of this pair is defined as the exciton binding energy (E_{BX}) and the spatial distance between the bound electron and the hole is known as exciton Bohr radius (a_{BX}) (Fig. 2.1(a)). Excitons are usually classified based on their spatial extent or radii in the material system. In molecular crystals, such as in

organic materials, the excitons are tightly bound and their Bohr radii are typically in the order of a single unit cell. This type of excitons are known as Frenkel excitons. On the other hand, in semiconductor based material systems, the exciton Bohr radius is much larger than the interatomic spacing because of the delocalized nature of the exciton wavefunction. This type of excitons are commonly called Wannier or Wannier-Mott excitons. The dispersion relation of a free Wannier-Mott exciton is shown in Fig. 2.1(b), where the discrete exciton states appear below the conduction band continuum [83]. The exciton binding energy and Bohr radius are strongly dependent on the dimensionality and quantum confinement of the system. In the subsequent sections, excitons in semiconductors of different dimensionalities, namely bulk, quantum well, quantum wire and quantum dots will be discussed. As the work described in this thesis is limited to semiconductor based material systems, the term 'exciton' henceforth will refer to only Wannier type excitons.

2.2.1 Excitons in Bulk Semiconductors (3D Excitons)

The Hamiltonian for excitons in a bulk semiconductor can be described by an electron term, a hole term and an electron-hole interaction term as follows [84]:

$$H_X^{bulk} = -\frac{\hbar^2\nabla_e^2}{2m_e^*} - \frac{\hbar^2\nabla_h^2}{2m_h^*} - \frac{q^2}{4\pi\varepsilon \,||\, R_e - R_h \,||} \tag{2.1}$$

Here q is the electronic charge, $\hbar$ is the Planck's constant, ε is the dielectric constant of the semiconductor, m_e (m_h) is the electron (hole) effective mass, R_e (R_h) is the spatial coordinate of the electron (hole), and ∇_e^2 (∇_h^2) is the Laplacian operator corresponding to

electron (hole) co-ordinate. By solving the Schrödinger equation, the exciton energies in a bulk semiconductor is obtained to be:

$$E_{X,n}^{bulk} = E_G + \frac{\hbar^2 K^2}{2M_X} - \frac{E_{BX}^{bulk}}{n^2} \tag{2.2}$$

Here E_G is the bandgap of the semiconductor, $E_{X,n}^{bulk}$ is the bulk exciton binding energy, $M_X = m_e + m_h$, n = 1, 2, 3... is the principal quantum number, and $K = k_e + k_h$ is the center of mass wave vector obtained from the electron and hole wave vectors k_e and k_h respectively.

As a first order approximation, the Hamiltonian of an exciton (equation 2.1) is similar to that of a Hydrogen atom if it is assumed that the proton plays the same role as the hole. Hence, by rescaling the physical quantities obtained from the solution of a Hydrogen atom problem, the bulk exciton binding energy, E_{BX}^{bulk} and bulk exciton Bohr radius, a_{BX}^{bulk} can be expressed as:

$$\begin{aligned} E_{BX}^{bulk} &= \frac{m_r^*}{n^2 \varepsilon_r^2} \times Ry \\ a_{BX}^{bulk} &= \frac{n^2 \varepsilon_r}{m_r^*} \times a_B \end{aligned} \tag{2.3}$$

In this relation $m_r^* = \left(1/m_e^* + 1/m_h^*\right)^{-1}$ is the reduced effective mass of the exciton, ε_r is the dielectric constant of the semiconductor, Ry = 13.6 eV is the Rydberg constant and a_B = 0.53 nm is the Bohr radius. According to equation 2.3, the exciton binding energy should be high in a material having small exciton Bohr radius and dielectric constant, which

corresponds to enhanced electron-hole wave function overlap and reduced dielectric screening of the Columbic interaction respectively.

2.2.2 Excitons in Quantum Wells (2D Excitons)

A quantum well consists of a narrow-bandgap semiconductor imbedded between two thicker layers of relatively wider bandgap semiconductors such that the thickness of the thin layer is comparable to the mean free path of the carriers. Unlike in a bulk, the motion of carriers in a quantum well is restricted within a plane and the allowed energy states of electrons and holes are quantized along the confinement direction, which is usually the growth direction of the semiconductor. Because of the one-dimensional confinement, excitons in a quantum well are two-dimensional (2D) in nature. Using the same notations as for the bulk case discussed previously, the Hamiltonian of a 2D exciton can be expressed as,

$$H_X^{well} = -\frac{\hbar^2 \nabla_e^2}{2m_e^*} - \frac{\hbar^2 \nabla_h^2}{2m_h^*} - \frac{q^2}{4\pi\varepsilon \| R_e - R_h \|} + U_e^{conf}(z_e) + U_h^{conf}(z_h) \qquad (2.4)$$

where $U_e^{conf}(z_e)$ and $U_h^{conf}(z_h)$ are the confinement potentials for electron and hole respectively along the growth direction *z*. By solving the Schrödinger equation for a perfect 2D system, the eigen energies of the Hamiltonian shown in equation 2.4 are derived as:

$$E_{X,n}^{well} = E_G + E_e^{conf} + E_h^{conf} + \frac{\hbar^2 K^2}{2M_X} - \frac{E_{BX}^{bulk}}{\left(n - \frac{1}{2}\right)^2} \qquad (2.5)$$

Here E_e^{conf} and E_h^{conf} are confinement energies of the electron and hole respectively and

$E_{BX,n}^{well} = E_{BX}^{bulk} \Big/ \left(n - \frac{1}{2} \right)^2$ is defined as the quantum well exciton binding energy, where n=1, 2, 3…. According to this relation, the exciton binding energy of the first excitonic state in a quantum well can be 4 times than that of the exciton in a bulk semiconductor constituting the same active region. This result is however true only for a perfectly 2D quantum well, where the electron and hole wavefunctions are bound to be delta functions along the growth direction. The finite dimensionality of practical quantum wells results in wavefunction leakage and other non-ideal effects. As a result, the binding energy of 2D excitons are observed to be about 2-3 times of their bulk counterparts [85, 86].

2.2.3 Excitons in Quantum Wires and Dots (1D and 0D Excitons)

A quantum wire is a quantum confined structure in which carrier motion is restricted in two spatial dimensions. Advancement in material growth techniques have enabled the realization of quantum wire like structures in the form of nanowires, which can be a few microns in lengths and 40 nm to 80 nm in diameters [87]. Nanowires are particularly attractive as they can be grown with a relatively low density of extended defects compared to thin film based heterostructures. Theoretically, the exciton binding energy in an ideal quantum wire diverges towards infinity. However, because of the finite diameter of a practical quantum wire, the exciton binding energy is modified by the displacement of the electron-hole pair in the cross-sectional plane. For sufficiently small displacement, the exciton binding energy of a quantum wire can be larger than the theoretical $E_{BX}^{well} = 4E_{BX}^{bulk}$ limit of a quantum well.

Quantum dots (QDs) are nanostructures in which carrier motion is restricted in all

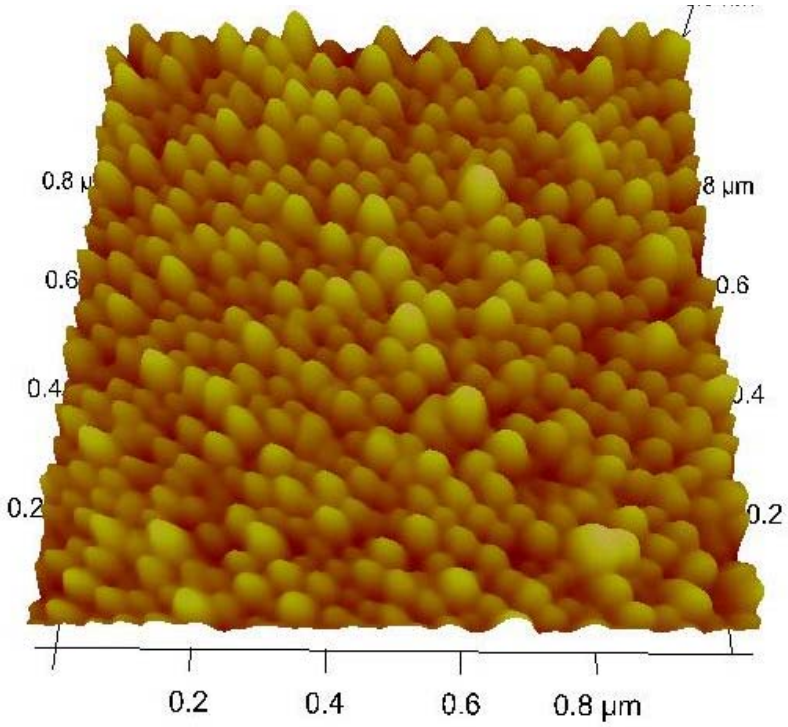

Fig. 2.2 An AFM image of InAs self-assembled quantum dots grown on InP substrate by molecular beam epitaxy for 1.55µm emission wavelength [88].

three spatial dimensions. Because of the three dimensional quantum confinement, ideal quantum dots have delta-like density of states. Though theoretically a 0D system, practical quantum dots have finite dimensions depending on the growth and/or fabrication techniques involved. Figure 2.2 shows an atomic force microscopy (AFM) image of molecular beam epitaxy (MBE) grown self-assembled quantum dots, which have average diameter of ~25 nm and height of ~5-6 nm. The 0D exciton concept inside a quantum dot is in fact valid only if the exciton Bohr radius is smaller than the quantum dot size in all three spatial dimensions. Otherwise the quantum dot exciton behaves more like a bulk exciton with the difference that the center of mass motion is quantized because of the spatial confinement. The energy of an exciton inside a quantum dot can be estimated from the relation $E_X^{dot} = E_G + E_e^{conf} + E_h^{conf} - E_{BX}^{dot}$, where E_e^{conf} and E_h^{conf} are the

electron and hole confinement energies and E_{BX}^{dot} is the QD exciton binding energy. It is noteworthy that there is no momentum term involved in the energy of QD excitons. This and the delta like density of states essentially makes excitonic transitions of a QD equivalent to the atomic transitions of a single atom [89]. For this reason QDs are considered to be highly prospective candidates for future quantum information processing and quantum computing [76, 89].

2.2.4 Free and Bound Excitons

Excitonic transitions manifest themselves as sub-bandgap, narrow spectral lines in the optical absorption spectra of semiconductors at low temperatures. The exciton energies (E_X) in these transitions are related to the incident photon energy (E_{ph}) by the relation: $E_{ph} = E_G - E_X / n^2$, where n=1, 2, 3, ... corresponds to different exciton states. The strength of these excitonic transitions is governed by the exciton oscillator strength, which is be defined in analogy with the atomic oscillator strength as follows [92]:

$$f = \frac{2m^* \omega}{\hbar} \left| \left\langle u_v \left| \vec{r} \cdot \vec{E} \right| u_c \right\rangle \right| \frac{V}{\pi a_{BX}^3} \tag{2.6}$$

Here u_c (u_v) is the electron (hole) Bloch function, ω is the frequency of the incident photon, m^* is the free electron mass, $\vec{r}$ is the relative motion co-ordinate of the exciton, $\vec{E}$ is the photon field and V is interaction volume of the system. According to equations 2.3 and 2.6, materials with high exciton binding energies should have large exciton oscillator strengths. However, in practice, homogenous and inhomogeneous broadening resulting from phonon interaction and disordered potential across the sample (arising from localized strain, defects, impurities, alloy clustering, interface roughness etc.) [90]

invariably affect the excitonic transitions and this appears as a broadening of the exciton linewidth. It is also important to note that the oscillator strength defined in equation 2.7 is for excitons which are delocalized over many lattices and are essentially *free* propagating excitons or *free excitons*. In real semiconductors however, defects and impurity centers can act as traps for excitons and form the so-called *bound-excitonic states* or simply *bound excitons*. Owing to the localization at these traps, the bound excitons do not have a kinetic energy distribution like the free excitons, and therefore they exhibit a relatively narrow linewidth in the emission spectra. In addition to this, bound excitonic luminescence is governed by the so-called *giant oscillator strength* as shown by Rashba and Gurgenishvili [91]. For these reasons, the bound exciton luminescence may appear significantly stronger than the free exciton luminescence in doped, or even nominally doped semiconductors and in semiconductors containing material defects.

2.2.5 Bosonic Nature of Excitons

Whereas fermions are characterized by the Fermi-Dirac statistics and half integer spins, bosons are governed by the Bose-Einstein statistics and integer spin quantum numbers. Because excitons have integer spin numbers resulting from the constituent fermionic particles (the electron and the hole), it is expected that excitons should exhibit bosonic characteristics. The bosonic picture of excitons is however valid only in the low density regime, where excitons behave as non-interacting particles. As the carrier density is increased, the repulsive interaction between excitons results energy renormalization and the excitonic transition shifts towards higher energy, which appear as a blueshift in the emission spectra. With further increase of the carrier density, the Coulombic interaction between the excitons' fermionic components becomes stronger, and also

progressive filling of the *phase space* takes place [92]. The latter is known as the Pauli-blocking principle, and is a direct consequence of the Pauli's exclusion principle. Quantitatively, both Coulombic interaction and phase space filling becomes non-negligible when the inter-particle distance becomes comparable to the exciton Bohr radius. As a first approximation, a critical density (n_{mott}) can be estimated as $n_{Mott} \sim 1/(\pi a_B^2)$ for 2D excitons, beyond which the exciton binding energy decreases significantly and dissociation of the exciton complex takes place [34]. This transition process is often referred to as the Mott transition and the critical density is known as Mott density. Beyond Mott transition, an excitonic system becomes uncorrelated electron-hole plasma and no longer exhibits bosonic characteristics.

2.3 Semiconductor Microcavity and Cavity Photon

A semiconductor microcavity is an optical resonator comprising of a semiconductor active region and a cavity dimension of the order of the optical wavelength. Depending on the method of light confinement, a semiconductor microcavity can be of different types, such as planar, spherical, pillar or photonic crystal microcavity. The microcavity of interest in this study is a planar semiconductor microcavity, which consists of two flat reflectors (mirrors) on the opposite sides of a semiconductor active region. These mirrors can be realized by simple cleaving, which forms mirrors at the semiconductor-air interface, or using more advanced technologies such as metallic mirrors, distributed Bragg reflectors (DBRs) etc. In this section, the design and characteristics of a DBR-based semiconductor microcavity will be presented in brief. Also the concept of cavity photon and its characteristics will be discussed.

2.3.1 Distributed Bragg Reflector (DBR)

A DBR consists of alternate layers of materials having different refractive indices where the principle of interference is employed to realize high reflectivity. It is designed based on the principle of interference in multilayer structures. It can be shown that constructive interference of light reflected at each interface of the DBR creates a stopband for photons centering around a specific wavelength. This range of wavelength or the sopband is reflected by the DBR and thus it acts as a high reflectivity mirror. If the desired center-wavelength of the stopband of a DBR is λ_B, it needs to be designed with periodic layers of two materials having thicknesses of $h_1 = \lambda_B/4n_1$ and $h_2 = \lambda_B/4n_1$, where n_1 and n_2 are their refractive indices respectively. The wavelength λ_B is known as the Bragg resonant wavelength and hence the name distributed Bragg reflector. Figure 2.3

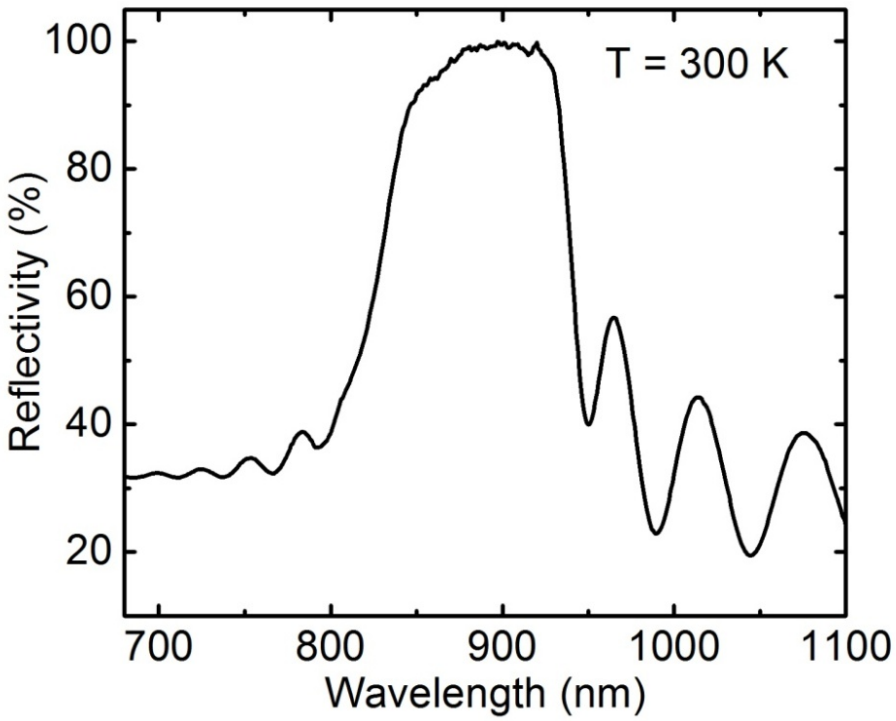

Fig. 2.3 Measured reflectivity spectra of 18 pairs of AlGaAs/GaAs DBR.

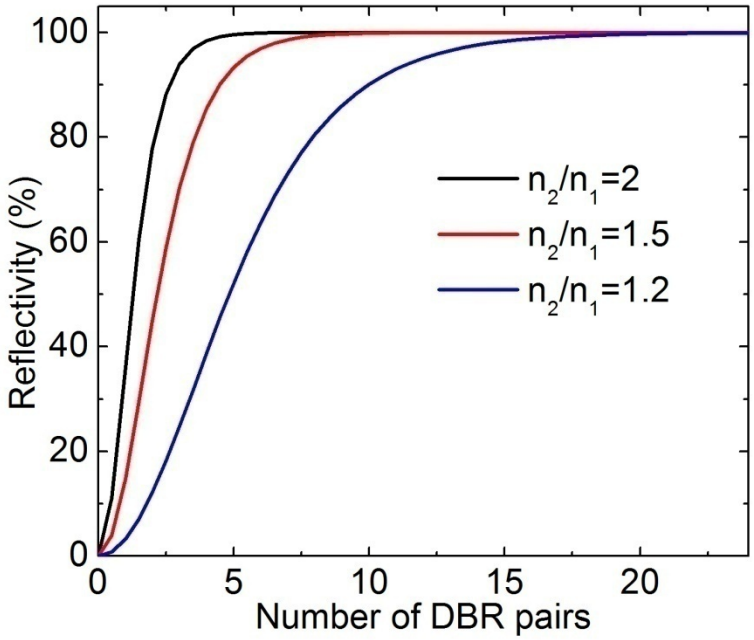

Fig. 2.4 Calculated reflectivity plotted as function of number of DBR pairs for different ratios of n_1 and n_2.

shows the measured reflectivity spectra of AlGaAs/GaAs DBRs grown by molecular beam epitaxy (MBE). The reflectivity of a DBR is dependent on the number of pairs used, and also on the refractive index contrast of the alternate layers. Using transition matrix approach, it can be shown that at Bragg resonant wavelength, the power reflectivity ($|r|^2$) of a DBR having N number of pairs is given by [93],

$$|r|^2 = \left| \frac{\left(\frac{n_2}{n_1}\right)^{2N} - 1}{\left(\frac{n_2}{n_1}\right)^{2N} + 1} \right|^2 \tag{2.7}$$

From Fig. 2.4, it is quite obvious that the DBR reflectivity can be significantly enhanced by increasing the refractive index contrast of the constituent alternate layers.

2.3.2 Microcavity with DBRs

In a planar semiconductor microcavity, an emitter having optical thickness of ~ $\lambda_c/2$ (or its integer multiple) is imbedded between two high reflectivity DBRs, which have their stop-bands centered around λ_c. For normal light incident onto such a microcavity, the transmission is found to be maximum at λ_c , which is defined as *cavity mode* of the system. Hence a semiconductor microcavity is essentially a 1-D photonic crystal where the spacer region between the two mirrors act as an impurity in the photonic bandgap. In reflectivity measurements, the cavity mode is observed as a dip in the reflectance spectra as shown in Fig. 2.5. Theoretically calculated values using propagation matrix approach are plotted along with the measured data.

An important figure of merit of a microcavity is the *cavity quality factor, Q* which is defined as the ratio of the energy stored in the cavity to the power dissipation per round

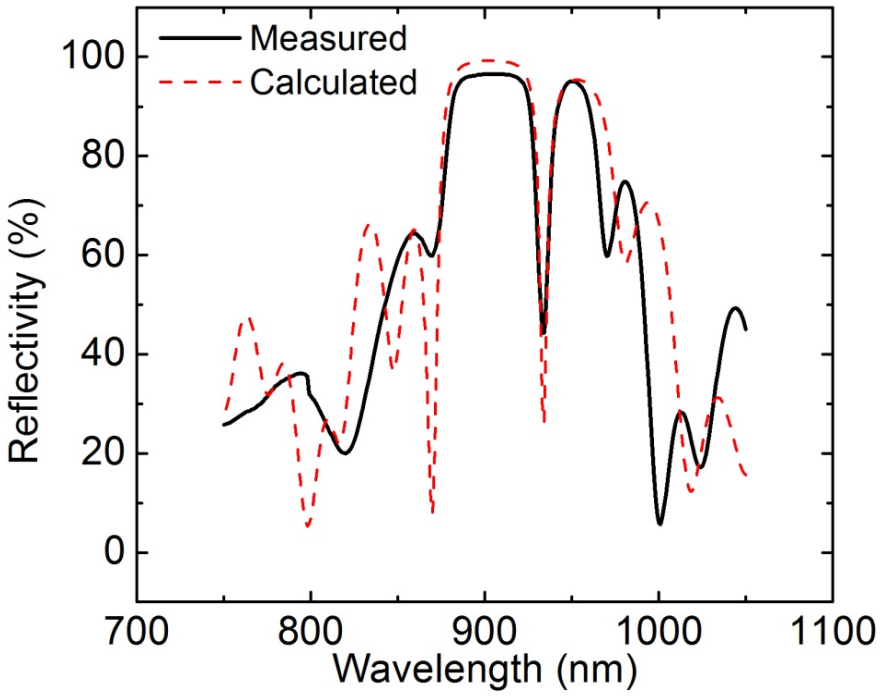

Fig. 2.5 Measured reflectance spectra of a AlGaAs/GaAs DBR based microcavity along with calculated results obtained from propagation matrix approach.

trip of a cavity photon. Quantitatively Q is defined as the ratio of the cavity mode energy (E_c) to the mode broadening (ΔE_c), i.e. $Q = E_c / \Delta E_c$. The cavity photon lifetime (τ_c), which indicates how long a photon can reside inside the microcavity before it escapes into vacuum, can be estimated from cavity Q using the relation, $\tau_c = \frac{Q}{\omega_c} = \frac{Q}{\left(E_c / \hbar\right)} = \frac{\hbar}{\Delta E_c}$

For a microcavity with mirror reflectivity values of R_1 and R_2, the cavity Q can be expressed to a first approximation as $Q \approx \frac{\pi \left(R_1 R_2\right)^{1/4}}{1-\left(R_1 R_2\right)^{1/2}}$ [92]. Thickness variation, material degradation and finite reflectivity of DBR-mirrors can reduce the cavity quality factor in an experimentally realized semiconductor microcavity.

2.3.3 Cavity Photon Characteristics

A semiconductor microcavity is essentially a light-trapping medium which allows only photons having energy equal to that of the cavity mode to out-couple with vacuum. These photons, which are usually called *cavity photons*, have substantially different characteristics from free-propagating light. For the semiconductor microcavity shown in Fig. 2.6, light is confined in the *z*-direction. In this case, the energy momentum relation of the cavity photon is given by:

$$E_{cav} = \frac{\hbar c k}{n_c} = \frac{\hbar c}{n_c}\sqrt{k_z^2 + k_{\|}^2} \tag{2.8}$$

Here c is the speed of light in vacuum, n_c is the effective refractive index of the cavity region, $\vec{k} = \vec{k_z} + \vec{k_{\|}}$ is the total wavevector of the cavity photon, and $k_{\|} = \sqrt{k_x^2 + k_y^2}$ and k_z

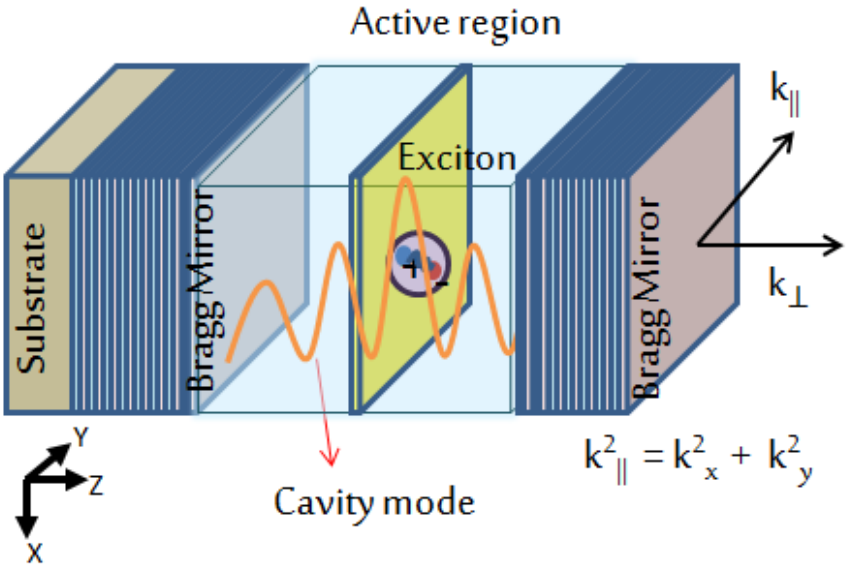

Fig. 2.6 Schematic representation of a planar microcavity having DBR mirrors showing the in-plane and out-of-plane wave vectors.

are the in-plane and out-of plane wave vectors respectively. For small in-plane wave vectors $k_{\|} \ll k_z$, and hence equation 2.9 can be approximated as:

$$E_{cav} \approx \frac{\hbar c k_z}{n_c} + k_{\|}^2 \frac{\hbar c}{n_c k_z} = E_{k_{\|}=0} + k_{\|}^2 \frac{\hbar c}{n_c k_z} \tag{2.9}$$

From phase-matching condition for cavity resonance, it can be shown that the out-of plane wavevector k_z is related to the cavity length L_c by the relation $k_z\left(2L_{cav}\right) = m\left(2\pi\right)$ where m is an integer. Therefore replacing $k_z = \frac{m\pi}{L_{cav}}$ in Eqn. 2.9, the following dispersion relation is obtained for a cavity photon:

$$E_{cav} = E_{k_{\|}=0} + \frac{\hbar^2 k_{\|}^2}{2m_c} \tag{2.10}$$

where $m_c = \hbar\pi m n_c / cL_c$ is defined as the cavity photon effective mass. For $m=1$ and $L_c = \lambda/2$, the cavity photon mass reduces to the more familiar expression of $m_c = \frac{2\hbar\pi n_c}{c\lambda}$. Whereas a free propagating photon has zero mass, the cavity photon mass is finite and non-zero. It is also important to note that because of in-plane translational invariance, the $k_{||}$ component of a cavity photon is conserved while it is outcoupled to vacuum. This property can be analytically expressed by $k_{||} = k_o \sin\theta$, where $k_o = \frac{2\pi}{\lambda}$ is the free-space wavevector and θ is the angle of detection with respect to z-axis (Fig.2.6).

2.4 Light-Matter Interaction

Light-matter interaction is an extensive area of research in quantum mechanics and cavity quantum electrodynamics. From a classical point of view, light-matter interaction is a result of resonant interaction between the oscillating electromagnetic field of light and charged particles, whereas from a quantum mechanical perspective, it is the observance of coupling of the optical field with the quantum states of the matter. Depending on the interaction strength between light and matter part of the system, light-matter interaction can be classified into weak, strong and very strong coupling regime. In this section, light-matter interaction will be discussed in the context of semiconductor microcavities, where the strong coupling regime leads to the generation of light-matter entangled eigenstates known as *exciton-polaritons* or *polaritons*. Different characteristics of polaritons are discussed here from both quantum-mechanical and semi-classical perspectives.

2.4.1 Strong vs. Weak Coupling Regime

When a semiconductor active medium is placed inside a suitably designed microcavity, the electric dipole of the exciton interacts with the electromagnetic field of light. This interaction takes place both in surface-emitting and edge-emitting structures, where the directions of excitation and optical detection are respectively parallel and perpendicular to each other (see Appendix A for details). The strength of this exciton-photon interaction ($\hbar\Omega$) is governed by the exciton optical transition matrix element (M) [92]:

$$\hbar\Omega = M = \sqrt{\frac{\pi e^2 f}{\varepsilon m^* V}\Gamma} \tag{2.11}$$

where V is the interaction volume of the system and f is the exciton oscillator strength as defined in equation 2.6. The term Γ in equation 2.11 contains the overlap integral of the electron and hole wave functions, the angular momentum conservation term governed by the selection rule, and the projection of exciton dipole moment onto the photon field. According to equations. 2.6 and 2.11, $\hbar\Omega$ should be significantly enhanced in a material system of low exciton Bohr radius and high exciton binding energy. In a high quality semiconductor microcavity, there is a periodic, reversible energy exchange between excitons and photons at a rate of $\hbar\Omega$, which can be larger than both the exciton decay rate, γ_x and cavity photon decay rate, γ_{cav}. If $\hbar\Omega >> (\gamma_{cav} - \gamma_x)/2$, there is at least one coherent energy transfer between the exciton and the photon before they decay by non-radiative recombination or out-couple with vacuum, respectively. Because of this strong dipole interaction between the photon field and the polarization field of exciton, the degeneracy between the emitter and cavity photon is lifted and new light-matter

entangled eigenstates are created in the form of exciton-polaritons or polaritons. Because these quasiparticles emerge from the strong interaction of excitons and photons, this operation regime is known as the *strong coupling regime.* The interaction strength or rate of energy transfer $\hbar\Omega$ is often referred to as the *vacuum Rabi splitting* or *normal mode splitting*, whereas the periodic energy transfer phenomenon is commonly known as *Rabi oscillation.* The Rabi oscillation period, $T_\Omega = 2\pi/\Omega$, is the timescale for one coherent energy transfer in the strong-coupling regime and is usually in the order of femtoseconds.

Whereas the strong-coupling regime is characterized by a reversible and periodic energy exchange between the emitter and cavity mode in the form of Rabi oscillation, the weak-coupling regime is governed by dissipation of uncoupled excitons and photons. This is a direct consequence of their relatively weak interaction strength compared to the respective damping factors. In the weak coupling regime, both the exciton and the cavity photon retain their uncoupled properties and no new eigen states are created in the system. However, the spontaneous emission rate of the emitter in a weakly coupled microcavity can be significantly enhanced by *Purcell effect*, in which the photon density of states is significantly increased because of resonant interaction between the emitting dipole and the cavity mode. The control of spontaneous emission rate by Purcell effect is an effective means of reducing lasing threshold of microcavity photon lasers, which invariably operate in the weak coupling regime.

2.4.2 Exciton-Polaritons in the Strong Coupling Regime

Exciton-polaritons emanate as new eigen modes of the system in the strong coupling regime, resulting from periodic and coherent energy exchange between the

cavity photon and the exciton. In this subsection, different characteristics of exciton-polaritons will be discussed from a quantum mechanical perspective. Also the impact of different parameters and non-idealities on polariton dispersion will be discussed.

2.4.2.1 Polariton Dispersion Characteristics

A exciton-polariton is essentially a linear superposition of an exciton and a photon having the same in-plane wave vector $k_{||}$. The total Hamiltonian of the exciton-polariton for a given $k_{||}$ can be expressed as [84, 93]:

$$H_{pol,k_{\|}} = H_{X,k_{\|}} + H_{\text{cav},k_{\|}k_c} + H_{\text{int},k_{\|}} = E_{X,k_{\|}}\hat{e}^{\dagger}_{k_{\|}}\hat{e}_{k_{\|}} + E_{\text{cav},k_{\|},k_c}\hat{c}^{\dagger}_{k_{\|},k_c}\hat{c}_{k_{\|},k_c} + \hbar g_{k_{\|}}(\hat{c}_{k_{\|}}\hat{e}^{\dagger}_{k_{\|}} + \hat{c}^{\dagger}_{k_{\|}}\hat{e}_{k_{\|}})$$

Here $H_{cav,k_{\|},k_c}$ is the photon Hamiltonian for in-plane wave vector $k_{||}$ and longitudinal wave vector k_c determined by cavity resonance, $E_{\text{cav},k_{\|},k_c}$ is the corresponding cavity photon energy, and $\hat{c}^{\dagger}_{k_{\|},k_c}(\hat{c}_{k_{\|},k_c})$ is the photon creation (annihilation) operator. Similarly, $\hat{e}^{\dagger}_{k_{\|}}(\hat{e}_{k_{\|}})$ and $E_{X,k_{\|}}$ are the exciton creation (annihilation) operators and exciton energy respectively corresponding to the exciton Hamiltonian ($H_{X,k_{\|}}$) for in-plane wave vector $k_{||}$. The interaction Hamiltonian term $H_{\text{int},k_{\|}}$ contains the in plane coupling strength $g_{k_{\|}}$. By neglecting the angular dependence of the coupling strength, $g_{k_{\|}}$ can be approximated to be $2g_{k_{\|}} \approx 2g_o = \hbar\Omega$. In the context of exciton-photon coupling, the Hamiltonian $H_{pol,k_{\|}}$ can be rewritten as:

$$H_{pol,k_{\|}} = E_{LP,k_{\|}}\hat{p}^{\dagger}_{LP,k_{\|}}\hat{p}_{LP,k_{\|}} + E_{UP,k_{\|}}\hat{p}^{\dagger}_{UP,k_{\|}}\hat{p}_{UP,k_{\|}} \tag{2.12}$$

where the following unitary transformation has been used:

$$\begin{aligned}\hat{p}_{LP,k} &= X_{k_\parallel}\hat{e}_{k_\parallel} + C_{k_\parallel}\hat{c}_{k_\parallel} \\ \hat{p}_{UP,k} &= -C_{k_\parallel}\hat{c}_{k_\parallel} + X_{k_\parallel}\hat{e}_{k_\parallel}\end{aligned} \tag{2.13}$$

Here $\hat{p}^{\dagger}_{LP,k_\parallel}(\hat{p}_{LP,k})$ and $\hat{p}^{\dagger}_{UP,k_\parallel}(\hat{p}_{UP,k})$ are the creation (annihilation) operators of the so called lower and upper polaritons respectively, which are the new eigen modes of the system. $X_{k_\parallel}$ and $C_{k_\parallel}$ are the Hopfield coefficients, which are defined as:

$$\begin{aligned}\left|X_{k_\parallel}\right|^2 &= \frac{1}{2}\left(1+\frac{\delta_{k_\parallel}}{\sqrt{\delta_{k_\parallel}^2+(\hbar\Omega)^2}}\right) \\ \left|C_{k_\parallel}\right|^2 &= \frac{1}{2}\left(1-\frac{\delta_{k_\parallel}}{\sqrt{\delta_{k_\parallel}^2+(\hbar\Omega)^2}}\right)\end{aligned} \tag{2.14}$$

where $\delta_{k_\parallel} = E_{cav,k_\parallel} - E_{\mathrm{X},k_\parallel}$ is known as the cavity-to-exciton detuning. The energies of the lower and upper polaritons, denoted by $E_{LP,k_\parallel}$ and $E_{UP,k_\parallel}$ respectively in equation 2.14, can be deduced by the diagonalization procedure, upon which the polariton Hamiltonian reduces to:

$$H_{pol,k_\parallel} = \begin{pmatrix} E_{cav,k_\parallel} & g_0 \\ g_0 & E_{X,,k_\parallel}\end{pmatrix} \tag{2.15}$$

By solving this eigen value problem, the lower and upper polariton energies are obtained to be:

$$\begin{aligned}E_{LP,UP,k_\parallel} &= \frac{1}{2}\{E_{X,,k_\parallel} + E_{cav,,k_\parallel} \pm \sqrt{4g_0^2+(E_{cav,k_\parallel}-E_{\mathrm{X},k_\parallel})^2}\} \\ &= \frac{1}{2}\{E_{X,k_\parallel} + E_{cav} \pm \sqrt{(\hbar\Omega)^2+\delta_{k_\parallel}^2}\}\end{aligned} \tag{2.16}$$

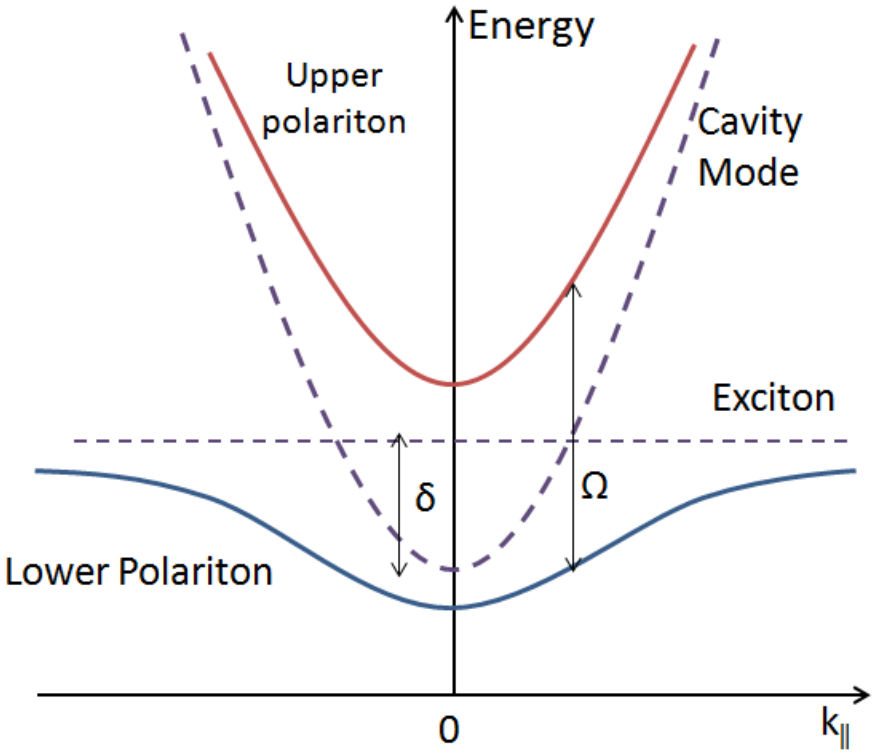

Fig. 2.7 General polariton dispersion characteristics in a semiconductor microcavity.

Figure 2.7 shows a general polariton dispersion characteristics for small in plane wave vectors $k_{||}$. It is noteworthy that equation 2.16 reduces to $E_{LP,,k_{||}} - E_{UP,k_{||}} = \hbar\Omega$ when $E_{X,k_{||}} = E_{cav,k_{||}}$. This is observed as an anti-crossing in the polariton dispersion characteristics. This anticrossing behavior at cavity-to-exciton resonance is a signature of the strong coupling regime.

2.4.2.2 The Role of Detuning in Polariton Dispersion

The excitonic and photonic nature of polaritons are strongly dependent on the cavity-to-exciton detuning at $k_{||} = 0$. It is quite obvious from equation 2.14 that the Hopfield coefficients satisfy the relation $\left|X_{k_{||}}\right|^2 + \left|C_{k_{||}}\right|^2 = 1$. From a physical perspective,

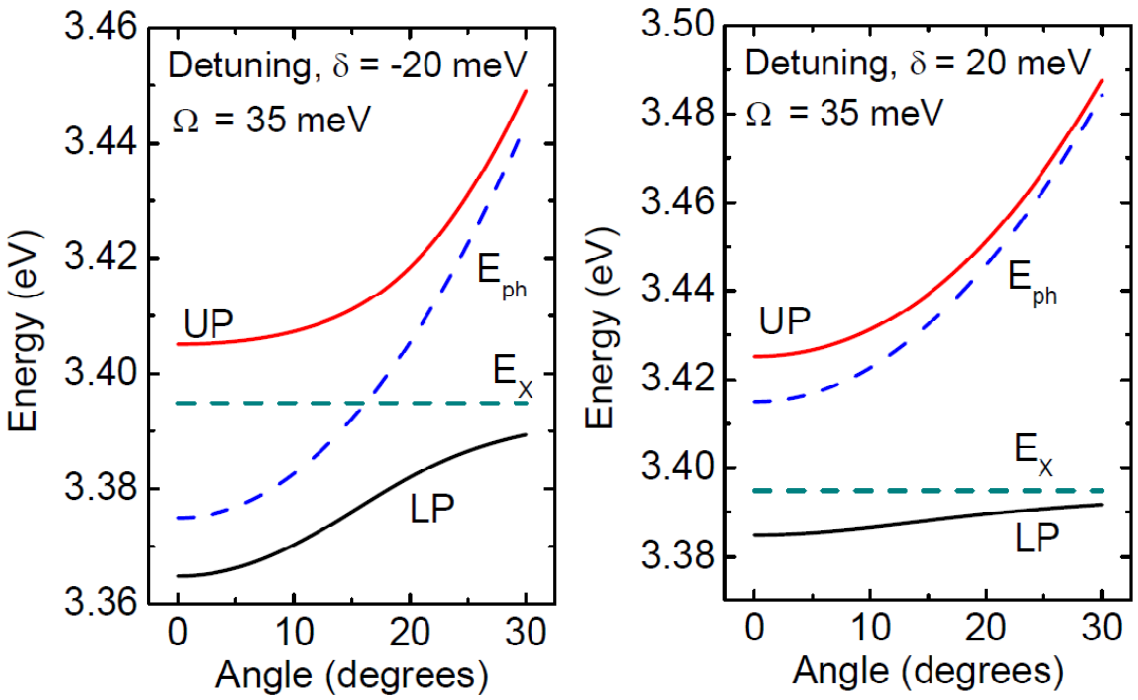

Fig. 2.8 Calculated polariton dispersion characteristics for two different detunings.

$\left|X_{k_{||}}\right|^2$ and $\left|C_{k_{||}}\right|^2$ correspond to the exciton and photon fractions in the lower polariton (LP) branch, whereas in the upper polariton (UP) branch these coefficients correspond to the photon and exciton fractions respectively. Therefore according to equation 2.16, the excitonic and photonic fractions of both the upper and lower polariton branches can be efficiently varied by changing the detuning parameter. This is further illustrated in Fig. 2.8, where polariton dispersion characteristics for two different detunings are shown corresponding to a fixed Rabi splitting and exciton energy. The bare cavity mode and exciton dispersions are also shown in the same plot using dashed lines. As can be seen in Fig. 2.8, for both the detunings, at high $k_{||}$ values, the LP branch is flat, exciton-like whereas the UP branch is parabolic, cavity photon-like in nature. However, at small in-plane momenta, which is the range of interest in our studies, the LP branch tends to be more photon-like at negative detuning, whereas it becomes more exciton-like at positive

detuning. The opposite trends are observed for the upper polaritons. Detuning also plays an important role in phase transition and dynamic condensation processes in the strong coupling regime, which will be discussed in the subsequent sections.

2.4.2.3 Polariton Effective Mass

The polariton effective mass at a particular in plane momentum $k_{||}$ can be deduced from the constituent exciton and photon masses as follows:

$$\frac{1}{m_{LP}} = \frac{\left|X_{k_{||}}\right|^2}{m_X} + \frac{\left|C_{k_{||}}\right|^2}{m_{cav}}$$
$$\frac{1}{m_{UP}} = \frac{\left|C_{k_{||}}\right|^2}{m_X} + \frac{\left|X_{k_{||}}\right|^2}{m_{cav}} \qquad (2.17)$$

Here $X_{k_{||}}$ and $C_{k_{||}}$ are the Hopfield coefficients defined in equation 2.14, m_X is the center of motions mass of the exciton and m_{cav} is the cavity photon mass. Irrespective of detuning, $\left|X_{k_{||}}\right| \approx 1$ at high in-plane wave vectors. Therefore for large values of $k_{||}$, equation 2.17 can be approximated as $m_{LP} \approx m_X / \left|X_{k_{||}}\right|^2$ and $m_{UP} \approx m_{cav} / \left|X_{k_{||}}\right|^2$, which are again indicative of the exciton and photon like nature of the lower and upper polariton respectively. However for $k_{||} \approx 0$, the polariton mass is dominated by m_{cav} as the exciton mass is about 4 orders of magnitude larger than the photon mass at the same in plane wave vector. Therefore from equation 2.17, the polariton effective masses at $k_{||} \approx 0$ can be approximated as: $m_{LP} \approx m_{cav} / \left|C_{k_{||}\approx 0}\right|^2$, $m_{UP} \approx m_{cav} / \left|X_{k_{||}\approx 0}\right|^2$, which indicates that the polaritons are more photon like at relatively small in plane wave vectors.

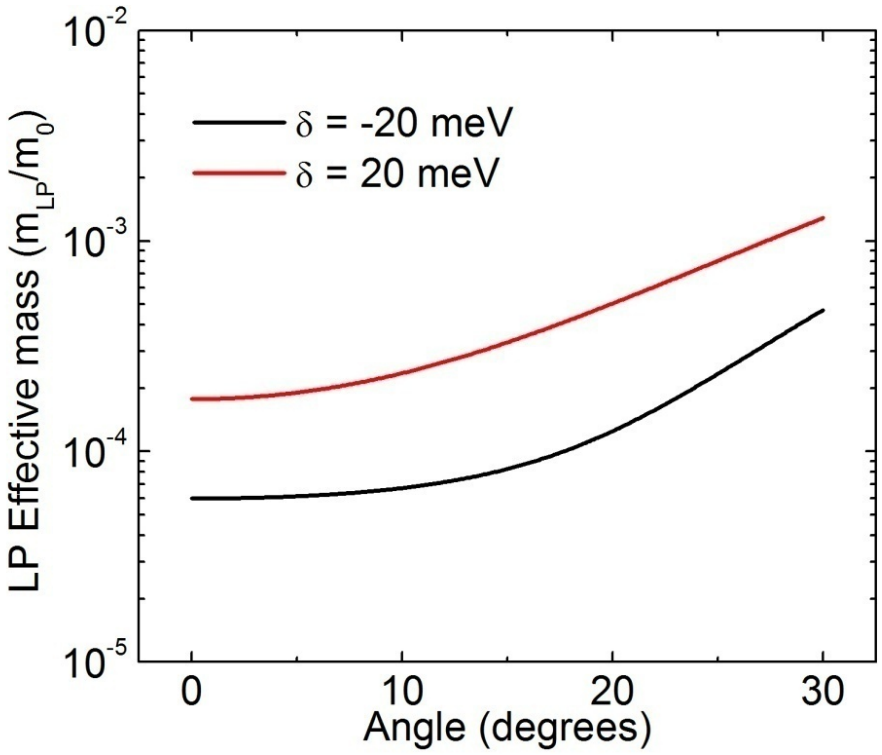

Fig. 2.9 Calculated lower polariton effective masses for the two different detunings considered in Fig. 2.8.

In Fig. 2.9, the calculated LP effective masses using equation 2.17 are plotted corresponding to the polariton dispersions shown in Fig. 2.8. It can be seen that the effective mass of the lower polariton increases as it becomes more exciton-like at high in plane wave vectors. Also the LP mass is higher for positive detuning because of the more exciton-like nature of the lower polariton, compared to the case of negative detuning.

2.4.2.4 Impact of Homogenous and Inhomogeneous Broadening

In the derivation of the polariton dispersion characteristics shown in equation 2.16, it has been assumed that the exciton and cavity photon have infinite lifetimes, i.e. their decay rates, $\gamma_X \approx 0$, $\gamma_{cav} \approx 0$. However, in a real semiconductor microcavity, both the exciton and the cavity photon have finite lifetimes because of homogenous and inhomogeneous broadening in the material system. Homogenous broadening occurs

primarily due to acoustic and optical phonon interactions, whereas inhomogeneous broadening is a consequence of non-idealities in the microcavity, such as defects, alloy disorder, monolayer fluctuation, interface roughness, impurity density variation and localized strain. To take into account the finite lifetime of excitons and cavity photons, the polariton Hamiltonian shown in Eqn. 2.16 can be modified as [84]:

$$H_{pol,k_{\|}} = \begin{pmatrix} E_{cav,k_{\|}} + i\gamma_{cav} & g_0 \\ g_0 & E_{X,k_{\|}} + i\gamma_X \end{pmatrix} \tag{2.18}$$

where the exciton and cavity photon decay rates are introduced as imaginary parts to the bare mode energies. The eigenstates of this modified Hamiltonian are:

$$\begin{aligned} E_{LP,UP,k_{\|}} &= \frac{1}{2}\{E_{X,k_{\|}} + E_{cav,k_{\|}} + i(\gamma_{cav} + \gamma_X) \pm \sqrt{4g_0^2 + [E_{cav,k_{\|}} - E_{X,k_{\|}} + i(\gamma_{cav} - \gamma_X)]^2}\} \\ &= \frac{1}{2}\{E_{X,k_{\|}} + E_{cav,k_{\|}} + i(\gamma_{cav} + \gamma_X) \pm \sqrt{4g_0^2 + [\delta_{k_{\|}} + i(\gamma_{cav} - \gamma_X)]^2}\} \end{aligned} \tag{2.19}$$

Comparing equation 2.16 with equation 2.19, the effective Rabi splitting (Ω_{eff}) in the presence of homogenous and inhomogeneous broadening can be expressed as, $\Omega_{eff} = 2\sqrt{g_o^2 - \left(\frac{\gamma_{cav} - \gamma_X}{2}\right)^2}$.

2.4.3 2D, 1D and 0D Polaritons

Depending on the dimensionality of the exciton and the cavity photon, polaritons in a semiconductor microcavity can be zero-dimensional (0D), one-dimensional (1D) or two-dimensional (2D) in nature. This is illustrated in Fig. 2.10 where different dimensionalities of polaritons are realized using nanowire active regions. In the case of a single nanowire (Fig. 2.10(a)), where the nanowire is sandwiched between planar mirrors

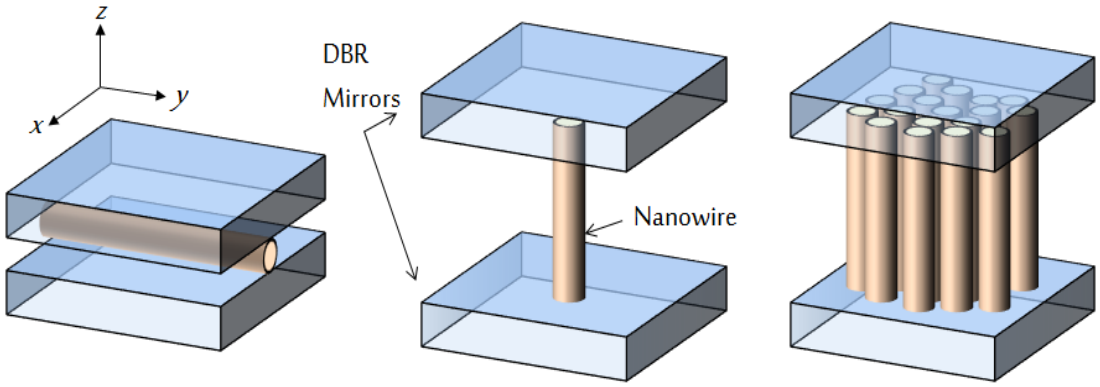

Fig. 2.10 A schematic representation of nanowire(s) imbedded between planar mirrors to illustrate (a) 0D, (b) 1D and (c) 2D polaritons [70].

both the cavity photon and the exciton are confined along the *x*- and *z*-directions and hence they are 1D in nature. Consequently, the polaritons resulting from their strong-coupling are 1D polaritons. For the case where the single nanowire is oriented along the *z*-direction (Fig. 2.10(b)), the exciton is again 1D in nature. However the cavity photon in this system becomes confined in all 3-directions, resulting in their discrete in-plane wave vectors. Therefore their coupling with excitons results 0D-polariton modes. Figure 2.10(c) shows the case where a dense array of nanowires is oriented along the *z*-direction and is embedded between two planar mirrors. In this case, because of wavefunction penetration into adjacent nanowires, the exciton becomes 3D in nature as in a bulk active region. The photon field is though confined along the *z*-direction, it gets spread over the *x*-*y* plane because of close proximity of the nanowires and assumes 2D characteristics. Hence polaritons emanating from the strong-coupling of excitons and photons in this case are 2D in nature. In the case of a quantum well (QW) active region, the cavity photon is 2D in nature and its strong coupling with 2D exciton results the formation of 2D polaritons. It should be added that besides using planar microcavities, 0D polaritons can

also be realized using photonic crystal microcavities, where the photon is confined in all three dimensions . This is similar to the case of a strongly coupled single quantum dot in a microcavity. The dimensionalities of polaritons significantly influences the scattering and dynamic condensation processes in the strong coupling regime. This will be discussed in details in section 2.4.

2.4.4 Spin Dynamics of Polaritons

The fermionic components of the exciton, namely the electron and the hole have angular momentum projections or spins projections of $J_e = \pm\frac{1}{2}$ and $J_h = \pm\frac{1}{2}$ (light holes), $\pm\frac{3}{2}$ (heavy holes) respectively on a given axis. Therefore, the total angular momentum of an exciton is J_X = ± 1 or ± 2. It is well known that the spin quantum number corresponding to a photon is ± 1. Because spin is conserved during photon absorption and creation processes, excitons having spin values of ± 2 cannot be optically excited and hence they are commonly known as 'dark excitons'. On the other hand, excitons having spin projections of ± 1 can interact with the photon field during photon absorption and creation processes and hence they are usually called 'bright excitons'. Because polaritons are essentially strongly-coupled bright-excitons and photons, they have spin projections of ± 1 on the structure axis of a semiconductor microcavity. The spin dynamics of polaritons can be exploited to study interesting physics and to realize novel spin optoelectronic devices. A detailed theory in this regard can be discussed using the pseudo-spin formalism [94, 95], which is beyond the scope of this thesis.

2.5 Polariton Lasing Phenomenon

The polariton lasing phenomenon is associated with the Bosonic nature of polaritons, which arises from the Bosonic characteristics of their constituent cavity photons and excitons. In this section, the underlying principle of polariton lasing will be discussed in the context of dynamic condensation. The differences between polariton lasing and conventional photon lasing will also be elucidated in brief.

2.5.1 Polariton Lifetime and Scattering Events

Polaritons in a semiconductor microcavity have a finite lifetime τ_c, after which they decay as photons by spontaneous radiative recombination. This lifetime can be expressed as a weighted sum of the exciton and photon lifetimes as follows:

$$\begin{aligned} \frac{1}{\tau_{LP}} &= \frac{|C|^2}{\tau_c} + \frac{|X|^2}{\tau_X} \\ \frac{1}{\tau_{UP}} &= \frac{|X|^2}{\tau_c} + \frac{|C|^2}{\tau_X} \end{aligned} \tag{2.20}$$

In real semiconductor microcavities, the exciton lifetime is in the order of nanoseconds whereas the cavity photon lifetime is in the order of picoseconds . Therefore, the upper and lower polariton lifetimes shown in equation 2.20 can be approximated as, $\tau_{LP} \approx \tau_c / |C|^2$ and $\tau_{UP} \approx \tau_c / |X|^2$ respectively. This indicates that the polariton lifetime is governed by the cavity photon lifetime, which again is dependent on the quality of DBR mirrors. Because of the constituent excitonic fraction, polaritons may undergo three different types of scatterings before they decay as photons. These are as follows.

(i) Polariton-phonon scattering: Polaritons are scattered by acoustic and optical phonons, which are quantized vibrational modes of the crystal lattice. Polaritons are expected to be more efficiently scattered by optical phonons because of their higher energy compared to that of acoustic phonons. However, whereas optical phonon energy ranges from 20 to 90 meV, the energy of an acoustic phonon is ~1meV. Hence the probability of polaritons to be scattered by optical phonon is relatively low, especially at low temperatures. The timescale of an acoustic phonon scattering process is ~10 ps [96]. It is important to note that whereas acoustic phonons are 3D in nature, microcavity polaritons can be 2D, 1D or 0D, as discussed in section 2.4.3. In the case of 1D polariton, momentum conservation in two directions (x and z in Fig. 2.10(a)) are relaxed and hence polariton-phonon scattering is significantly enhanced compared to the case of 2D polaritons. Polariton-phonon scattering is further enhanced in 0D polaritonic systems where momentum conservation is relaxed in all three directions.

(ii)Polariton-electron scattering: Polariton-electron scattering is more efficient than polariton-phonon scattering because of the small electron effective mass and strong charge-dipole interaction [32, 96]. In an optically pumped system, electron polariton scattering can be imitated by exciting a secondary quantum well adjacent to the emitter of the microcavity [97, 98] . In an electrically pumped system, it can be realized using modulation doping, which creates a 2D electron gas and increases the probability of polariton-electron scattering. The introduction of a 2D electron gas often manifests itself in the formation of a middle polariton branch, which results from the coupling of cavity photons to trions (exciton-electron complex) [81].

(iii) Polariton-polariton scattering: This is an elastic scattering mechanism which results from the dipole-dipole interaction of the excitonic components of polaritons. The timescale of these events is in the order of a few picoseconds, whereas each scattering event results an energy exchange of a few meV. In the presence of spin anisotropy, polariton-polariton scattering is found to be strongly dependent on the spin-orientation of polaritons [94, 95]. Polaritons of same spin repulse each other whereas polaritons of opposite spin experience a weak attraction. Polariton-polariton scattering is considered to be the most important scattering mechanism in the realization of polariton lasing.

2.5.2 LP Relaxation and Bottleneck Effect

Polariton lasing phenomenon is intricately related to the energy and momentum relaxation of lower polaritons (LPs) down to the ground state of the polariton dispersion. In this context, the polariton dispersion can be divided into three regions: thermalization region (I), bottleneck region (II) and polariton-trap region (III) as shown in Fig. 2.11. Upon external excitation, the electron-hole continuum leads to the formation of excitons which eventually couple with photons to form polaritons. The incoherent ensemble of excitons residing at high $k_{||}$ values of the reciprocal space is known as the *exciton reservoir*. At high in-plane momenta of the polariton dispersion, polaritons are essentially exciton-like and therefore they have relatively long lifetimes, heavy effective masses and large density of states (DOS). As a result, phonon mediated LP relaxation processes are very efficient over the thermalization region (denoted as region I in Fig. 2.11) of the dispersion. The energy difference between the bottleneck region and $k_{||}\sim 0$ state of the polariton dispersion is known as *polariton-trap depth*, which can be formulated using equation 2.19 as follows:

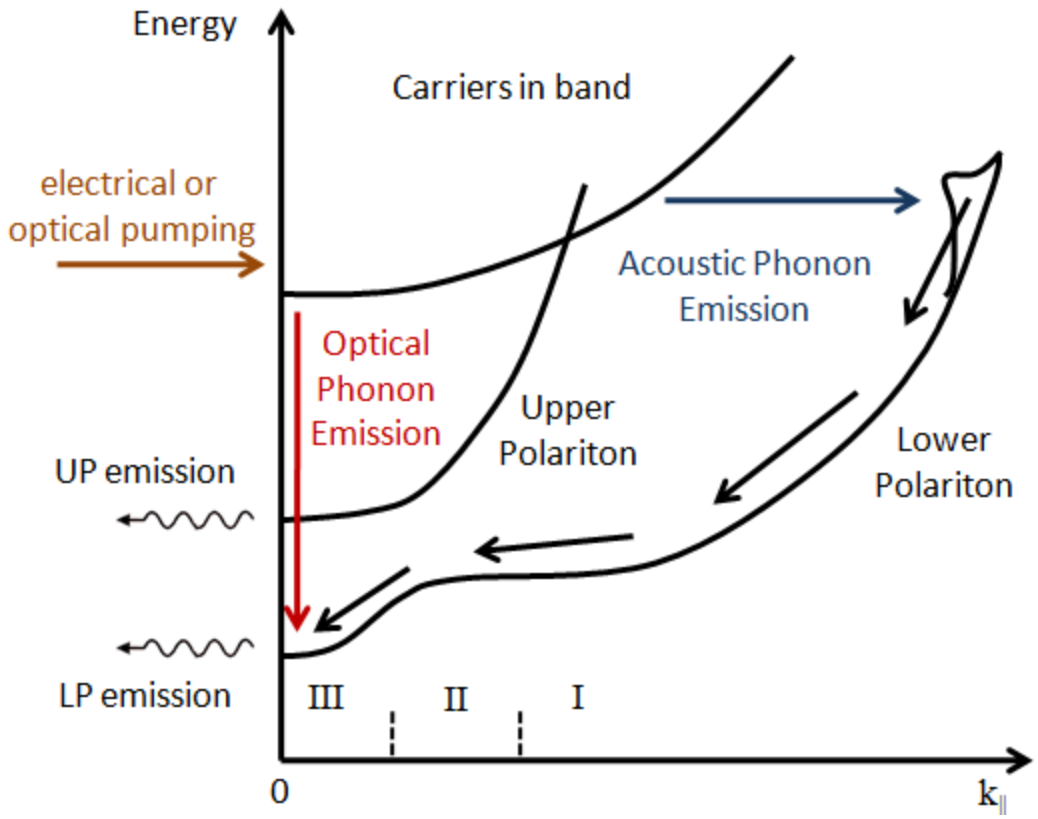

Fig. 2.11 Different regions of a generalized polariton dispersion, along with carriers in band, in the context of polariton relaxation.

$$E_{X,k_{\parallel}=0} - E_{LPk_{\parallel}} = \frac{1}{2}\{E_{X,k_{\parallel}} - E_{cav,k_{\parallel}} - i(\gamma_{cav} + \gamma_X) + \sqrt{4g_0^2 + [\delta_{k_{\parallel}} + i(\gamma_{cav} - \gamma_X)]^2}\} \qquad (2.21)$$

As can be observed in the polariton dispersion, LP relaxation from the bottleneck (region II) down to the polariton-trap (region III) requires a significant change of energy, and a simultaneous small change of momentum [99]. In the vicinity of this region, the polariton lifetime decreases by about two orders of magnitude and becomes significantly smaller than the timescales of acoustic phonon scattering, which is the dominant scattering mechanism at low temperatures. Also, the polariton effective mass decreases by about 4 orders of magnitude in this region, thereby significantly reducing the LP DOS. As a result, at low pump densities, there is also a lack of polariton-polariton scattering in this transitional region. In the presence of these effects, which are altogether known as the

bottleneck effect, it is very likely that polaritons will decay as photons before they can relax down to the bottom of the polariton trap. There are several ways of overcoming the bottleneck effect in semiconductor microcavities. These are the following.

- By increasing the pumping density, polariton-polariton scattering rate can be increased. However the system may cease to be in the strong-coupling regime if the pumping density becomes comparable to the Mott density.
- The scattering rate can be enhanced by increasing the exciton fraction near the bottleneck region. This can be attained by increasing positive detuning. However if the positive detuning is too large, the polaritons essentially become excitons.
- By increasing the temperature (T), the phonon scattering rate can be increase. However this also results homogenous broadening of the exciton linewidth. Moreover excitons tend to dissociate if the k_BT value is higher than the corresponding exciton binding energy, where k_B is the Boltzmann constant.
- By introducing excess carriers in the form of modulation doping, the polariton-electron scattering rate can be enhanced.

2.5.3 Stimulated Scattering and Dynamic Condensation

The dynamics of polariton lasing can be described using the semiclassical Maxwell-Boltzmann rate equations. In this framework, if $N_{k_\parallel}$ is defined as the LP occupation at an in plane wave vector $k_{||}$, then its rate of change is given by:

$$\frac{dN_{k_\parallel}}{dt} = P_{k_\parallel} - \frac{N_{k_\parallel}}{\tau_{LP,k_\parallel}} - \sum_{k'_\parallel} W_{k_\parallel \to k'_\parallel} N_{k_\parallel}(1+N_{k'_\parallel}) + \sum_{k'_\parallel} W_{k'_\parallel \to k_\parallel} N_{k'_\parallel} \sum (1+N_{k_\parallel}) \qquad (2.22)$$

Here $P_{k_{||}}$ is the pumping rate, $\tau_{LP,k_{||}}$ is the LP decay rate and W is the scattering rates between states $k_{||}$ and $k'_{||}$ in the momentum space. The scattering rate term W contains the contribution of different scattering events. It can be expressed using the relation: $W_{k_{||}} = W_{k_{||},pol-phon} + W_{k_{||},pol-elec} + W_{k_{||},pol-pol}$, where $W_{k_{||},pol-phon}$, $W_{k_{||},pol-elec}$ and $W_{k_{||},pol-pol}$ are the polariton-phonon, polariton-electron and polariton-polariton scattering rates respectively. When $N_{k_{||}} << 1$, LP relaxation is mostly mediated by phonon scattering processes. As the external pumping density is increased, polariton-polariton scattering becomes important. Because energy and momentum is conserved during this scattering process, it plays a substantial role in overcoming the relaxation bottleneck. During a single polariton-polariton scattering event, a LP from the bottleneck region may relax down to the polariton trap and at the same time a LP is scattered from the bottleneck region to a higher energy, exciton-like state. This process, which is also known as *pair-scattering*, is an incoherent two-body scattering process [100].

As the LP density increases, pair-scattering increases quadratically in the system and at a sufficiently high pumping density, LP relaxation to the final state i.e. to the ground state is dominated by the term $(1 + N_0)$ where N_0 is the ground state population in equation 2.22. Under this condition, the overall scattering rate increases non-linearly by what is known as the *Bosonic final state stimulation*. The enhanced scattering initiated by this Bose-Einstein statistical process is known as *stimulated scattering*. This is a phase coherent process where both polariton-polariton and polariton-phonon scattering rates are enhanced significantly [93]. Because $N_0 \geq 1$ for stimulated scattering to take place, it can be said that the system achieves *quantum degeneracy* during this process. This means a

macroscopic population of polaritons having same energy, momentum and phase builds up at the ground state. Because of the short lifetime, these polaritons though may nor attain thermal equilibrium with the lattice, they can remain at a metastable condensed state where they are in thermal equilibrium among themselves. Hence it can be said that the stimulated scattering process leads to the formation of a non-equilibrium polariton condensate. This process is often referred to as the *dynamic condensation* of polaritons. The formation of such a quasi- or non-equilibrium degenerate condensate means that upon decay by means of spontaneous radiative recombination, the exciton-polaritons will generate coherent light output and the system will act as a coherent emitter i.e. a laser. Though there is no stimulated emission of radiation, but only stimulated scattering in the process, the misnomer of 'polariton laser' is commonly used to indicate its operation as a coherent light source.

2.5.4 Phase Transition and Lasing Threshold

Depending on the pumping density and temperature of operation, a polariton diode laser can operate in the strong or weak coupling regime. This has been illustrated in Fig. 2.12 using a generalized polariton phase diagram of a microcavity diode . The horizontal dashed line in this figure indicates the upper limit of polariton density, whereas the vertical dashed line is indicative of the upper limit of temperature for the system to reside in the strong coupling regime. Excitation above or around the Mott density results screening of the excitons, thereby transitioning the system into weak coupling. Again at high temperatures, thermal broadening of excitons decreases the coupling strength and the system goes into weak coupling. In the weak coupling regime, the device operates either as a conventional light emitting diode (LED) or as a laser. The solid line of

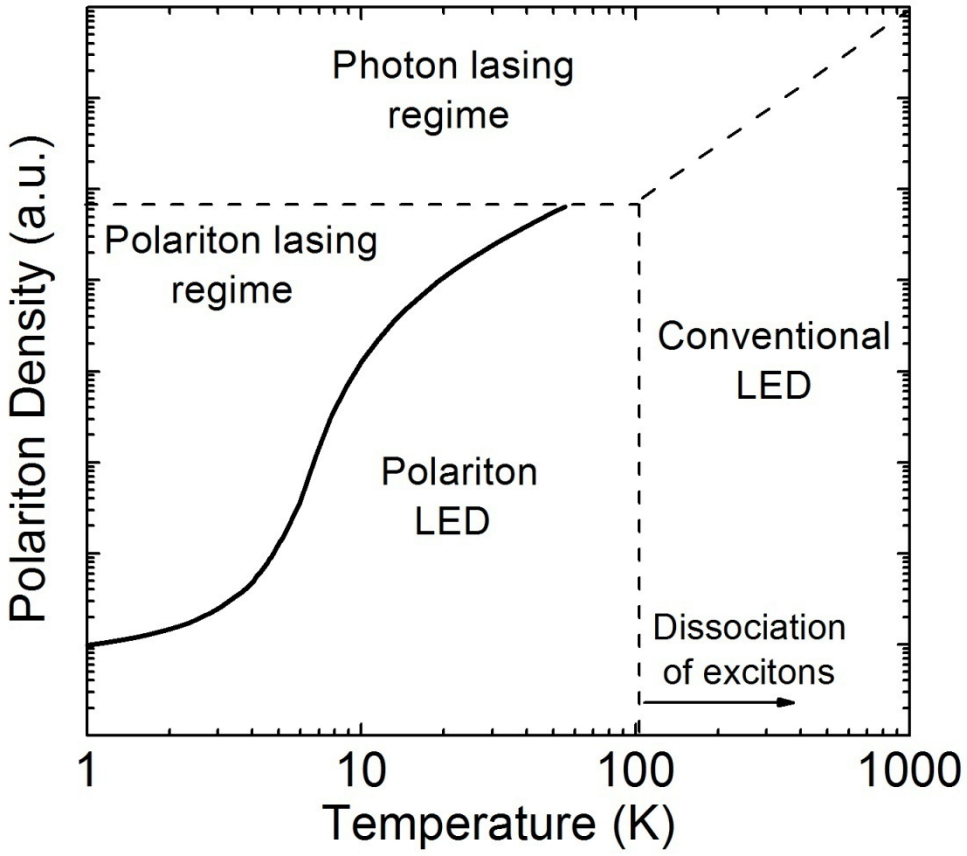

Fig. 2.12 A generalized polariton phase diagram for a microcavity diode showing its different regimes of operation.

Fig. 2.12 corresponds to the critical density and temperature of KT transition in the system [29]. A quasi- or non-equilibrium degenerate condensate of polaritons are formed only if the polariton density is above this critical density. Below this density in the strong coupling regime, the device essentially works as a polariton LED. In a 3D system, the critical density (N_c) and temperature (T_c) for a Bose-Einstein condensation (BEC)-like phase transition can expressed using the relation [49]:

$$N_{crit} = \frac{2.612}{\lambda_{dB}^3} = \frac{2.612}{\left(\frac{2\pi\hbar^2}{mkT_{crit}}\right)^{3/2}} \tag{2.23}$$

Here $\lambda_{dB} = \left(\frac{2\pi\hbar^2}{mkT_{crit}} \right)^{1/2}$ is the thermal de Brogli wavelength and m is the effective mass of the particle. In the ideal case, excess particles above the critical density acquire the lowest energy state and form a degenerate condensate. According to equation 2.23, the critical density required for dynamic condensation will be small for a system having particles of small effective mass. Because polariton effective mass is of the order of $10^{-4} m_o$ or smaller around $k_{||} \sim 0$, it is expected that the minimum density required for polaritons to form a non-equilibrium degenerate condensate will be significantly small. For e.g., at T=300 K, using $m_{LP} \approx 5 \times 10^{-5} m_o$ for a bulk GaN microcavity, λ_{dB} is obtained to be ~ 6μm. Therefore the minimum LP density required to attain polariton lasing in a bulk GaN microcavity is $\sim 1/\lambda_{dB}^2 \approx 2.7 \times 10^8 cm^{-2}$. This value is significantly smaller than the transparency density of $\sim 1.8 \times 10^{13}$ cm^{-2} in bulk-GaN, which is the minimum carrier density required to attain conventional photon lasing. Therefore, because of the small effective mass and the corresponding small density of states of polaritons, it is expected that a polariton laser will generate coherent emission at an ultra-low threshold.

2.5.5 Polariton vs. Photon Lasing

In conventional photon lasers, lasing is initiated by stimulated emission, which takes place when there is electronic inversion in the system, a condition commonly known as *population inversion.* Here amplification takes place when light generated by stimulated emission is larger than absorption in the system. On the contrary, the underlying dynamics of polariton lasing is the stimulated scattering process, which takes place when there is Bosonic final state stimulation in the ground state of the polariton

dispersion. The coherent emission in this case is generated by *spontaneous radiative recombination* of the degenerate polariton condensate. Therefore, whereas absorption has to be balanced by stimulated emission in a photon laser, in a polariton laser stimulation and emission processes are separated, thereby eliminating the requirement of population inversion. For this reason a polariton laser is often referred to as an *inversionless laser.* Besides the principle of operation, several distinct differences are observed between the output characteristics of polariton and photon lasers. These are the following.

- Because of the low effective mass and DOS of polaritons, the polariton lasing threshold can be 2-3 orders of magnitude lower than an equivalent photon laser. The photon lasing threshold has to be larger than the transparency density, which is defined as the pumping density at which the absorption and losses are equal to the gain. This density is always several orders of magnitude higher than the critical density N_{crit} , as discussed in the previous subsection.
- Collapse of the emission linewidth at the onset of lasing is observed for both polariton and photon lasers. For both the cases, there is an associated coherence time (τ_c) in the form of $\tau_c = \frac{\lambda^2}{c\Delta\lambda}$, where λ is the emission wavelength, c is the speed of light and $\Delta\lambda$ is the emission linewidth [96]. In a photon laser, the coherence time increases in proportion to the photon occupation number and the linewidth decreases accordingly to reach the Schawlow-Townes linewidth limit. However in a polariton laser, polariton-polariton scattering in the non-equilibrium degenerate condensate leads to the loss of coherence time and corresponding increase of the emission linewidth.

- Unless there is screening of the built-in electric field, as in GaN-based quantum well lasers, a red-shift of the emission peak in photon lasers may be observed because of device heating. However, in polariton lasers the emission peak blue-shifts because of energy renormalization caused by polariton-polariton scattering in the non-equilibrium polariton condensate.
- The spontaneous coupling factor β, which is a measure of the fraction of spontaneous emission coupled to the lasing mode, is usually greater than 1% in microcavity photon lasers because of Purcell effect. However in the polariton lasing regime, spontaneous emission emerges in the polariton mode which undergoes stimulated scattering and hence β is usually significantly smaller [60].
- Polariton lasers exhibit a characteristic magnetic field dependent Zeeman splitting because of the exciton-fraction of polaritons. As photon lasing is mediated by stimulated emission of uncoupled cavity photons in the weak coupling regime, such a magnetic field dependence is not observed [80].

2.6 Summary

A brief theoretical overview of microcavity exciton polaritons is presented in this chapter. The characteristics of excitons having different dimensionalities (3D, 2D, 1D and 0D) are described and it has been shown that the exciton binding energy can be significantly enhanced by increasing the quantum confinement of the active region. Also the concept of free and bound excitons has been illustrated and the Bosonic nature of excitons in the low density regime is explained. Next, we discuss the design and characteristics of semiconductor microcavities having DBRs. The relationship between

cavity photon lifetime and the quality of microcavity mirrors is also presented. This is followed by a detailed discussion of strong coupling regime in semiconductor microcavities. Using 2x2 coupled Harmonic oscillator model, the polariton dispersion characteristics has been described and the role of detuning and different non-ideal effects on the polariton dispersion have been elucidated. The idea of 1D, 2D and 0D polaritons are described assuming nanowire active region. Also the spin properties of polaritons are presented in brief. Finally, we discuss dynamic condensation and polariton lasing phenomenon and explain its main differences with conventional photon lasing. It has been shown that because of the low effective mass and density of states of the LPs, theoretically the polariton lasing threshold can be several orders of magnitude smaller than the photon lasing threshold.

Chapter III

Experimental Techniques

3.1 Introduction

Experimental realization of electrically pumped microcavity polariton lasers requires high quality epitaxially grown semiconductors and sub-micron scale device fabrication techniques. Material growth techniques having monolayer precision, such as molecular beam epitaxy (MBE) and metal-organic chemical vapor deposition (MOCVD), are employed to epitaxially grow the device heterostructure. Prior to device fabrication, the material characteristics, specially the excitonic transition characteristics are investigated by photoluminescence measurements. Also the quality of the microcavity mirrors is assessed by reflectivity, ellipsometry and micro-photoluminescence measurements. Finally, different device characterization techniques are employed to ascertain strong-coupling and polariton lasing phenomena under optical or electrical excitation. In this chapter, we first provide an overview of the materials which are commonly used to realize polariton devices. Next, we discuss the material growth and device fabrication techniques used in this study. A comparison of electrical and optical pumping schemes is also presented herein. Finally, details of the material and device

characterization techniques are described along with relevant technical specifications of the instruments used in this study.

3.2 Materials Choices, Growth and Deposition Techniques

Experimental realization of microcavity exciton-polariton lasers poses stringent requirements on the quality of active-region and cavity-mirror materials. These requirements are related to both the intrinsic properties of the material itself, and the feasibility of growth of high quality epitaxial layers. In this section, different choices of inorganic materials will be first discussed with respect to the active region and cavity mirrors of the polariton devices. Next the epitaxial growth and material deposition techniques will be briefly discussed in the context of our work.

3.2.1 Materials Choices for the Emitter

Direct-bandgap semiconductors have been the natural choice as the emitter material of semiconductor microcavities because of their significantly higher internal quantum efficiencies compared to those of indirect bandgap semiconductors. Ever since the first experimental demonstration of strong-coupling in a GaAs/AlGaAs quantum-well microcavity [13], GaAs-based heterostructures have remained to be the most commonly employed material to study dynamic condensation and polariton lasing phenomena. However these systems have the intrinsic limitations of large exciton Bohr radii and low exciton binding energies, which preclude the observation of polariton lasing at high temperatures. To this end, CdTe offers a better alternative because of its higher ionicity, smaller exciton Bohr radius and a consequently higher exciton binding energy. These also translate to about one order magnitude higher saturation density for CdTe than that

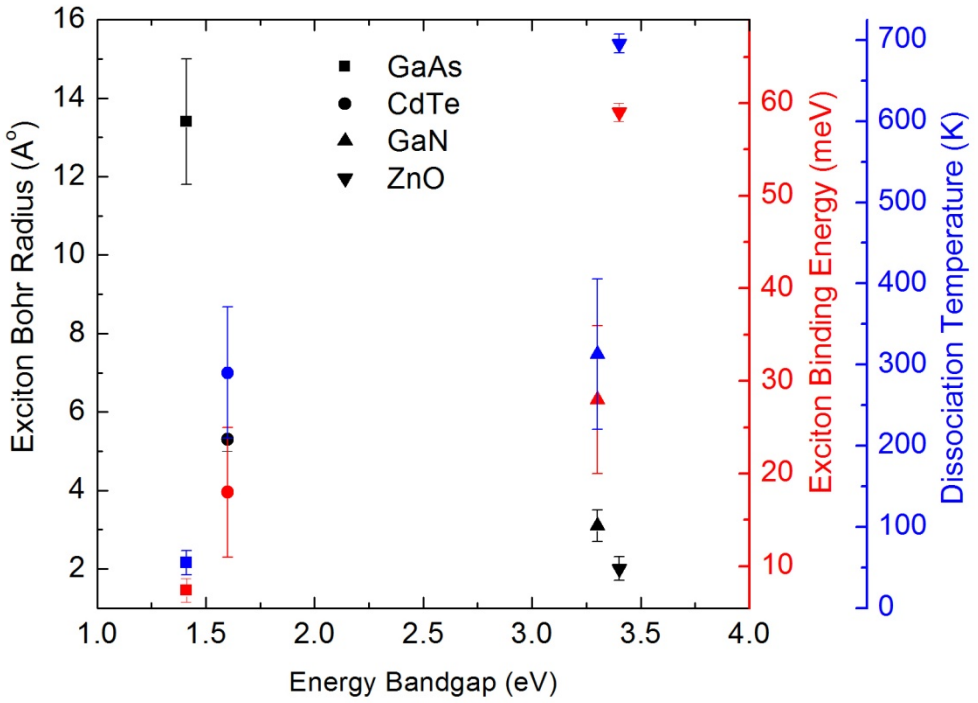

Fig. 3.1 Exciton Bohr radius, exciton binding energies and corresponding exciton dissociation temperatures of different materials plotted as a function of energy bandgap.

of GaAs, which means that polariton lasing should be observable up to higher pump densities [19, 54, 55, 59, 101]. Wide bandgap semiconductors like GaN and ZnO have also gained considerable interest in the study of exciton-polaritons because of their relatively high exciton binding energies. Whereas problems related to p-doping of GaN have been significantly overcome, reliable p-type doping of ZnO has not been achieved yet. This poses a significant challenge towards the realization ZnO-based high quality microcavity diodes [102]. Therefore among the wide bandgap semiconductors, GaN holds the most promise for the realization of electrically pumped polariton devices. Recently there has been interest in the application of two- dimensional materials like Molybdenum disulphide (MoS_2) and Molybdenum diselenide ($MoSe_2$). These materials yield direct-bandgap photoluminescence, and at the same time offer exciton binding

energies of a few 100 meV. These properties make them potential candidate for room temperature polariton lasing [103, 104]. Figure 3.1 shows a comparison of the bandgaps, exciton binding energies and corresponding exciton dissociation temperatures of some of the commonly employed materials for the study of strong-coupling and polariton lasing phenomena.

The polariton devices studied in this work have been designed, grown and fabricated using GaAs and GaN-based material systems. It will be shown that by careful bandgap engineering and heterostructure design, the exciton binding energy of a GaAs-based quantum-well can been significantly enhanced to obtain polariton lasing at high temperatures. On the other hand, by utilizing the high exciton binding energy and saturation density of GaN, room temperature polariton lasing can be obtained in a bulk-GaN microcavity double heterostructure diode. These heterostructures are discussed in detail in the corresponding chapters.

3.2.2 Materials Choices for Cavity Mirrors

Cavity mirrors of planar semiconductor microcavities are usually realized using DBRs, where materials of high refractive index contrasts are used. These materials can be either semiconductors or dielectrics, or a combination of both as in the case of a hybrid-semiconductor microcavity. In GaAs-based systems, the DBRs are usually designed with alternate layers of GaAs/AlGaAs because of their negligible lattice mismatch. However, because the maximum refractive index contrast of these pairs is ~1.2, at least 25-30 pairs of DBRs are required to form high reflectivity mirrors in this material system (Fig. 2.4). In CdTe-based microcavities, CdMnTe/CdMgTe is the commonly employed DBR

material. The lattice mismatch of these layers results cavity mirror loss, which however is compensated by the high refractive index contrast, necessitating about 17-20 DBR pairs to attain high-reflectivity mirrors [92, 101]. It is more challenging to obtain lattice-matched, semiconductor based high-reflectivity mirrors in GaN- and ZnO-based systems. For e.g., experimental realization of a high quality GaN-based microcavity requires 35 pairs of lattice-matched $In_{0.85}Al_{0.15}N/Al_{0.20}Ga_{0.80}N$ pairs. Careful stress relieving techniques have to be employed during the epitaxy of these layers to ensure crack-free growth. Nevertheless, threading dislocations are often observed in these mirrors because of the initial large number of defects in the starting substrate [102, 105]. An effective means of overcoming this problem is to employ dielectric DBRs, such as SiO_2/TiO_2, SiO_2/Si_3N_4 or SiO_2/HfO_2. The choice of these dielectric materials is very much dependent on the wavelength of operation. Because of the high refractive index contrast of these alternate layers, relatively less number of pairs are required to fabricate high reflectivity cavity mirrors. A combination of semiconductor-based bottom DBRs and dielectric-based top DBRs has also been utilized in both GaN- and ZnO-based systems to demonstrate polariton lasing at room temperature [60, 61, 67, 71]. In this work we employ all-dielectric DBRs using alternate pairs of SiO_2/TiO_2. The refractive index contrasts of these materials are ~1.8 and ~1.9, at the design wavelengths of our GaAs- and GaN-based devices respectively.

3.2.3 Materials Growth and Deposition Techniques

Experimental realization of high-quality semiconductor microcavity requires monolayer precision over the crystalline growth of semiconductor compounds and their alloys. The commonly employed epitaxial growth techniques in this regard are metal-

organic chemical vapor deposition (MOCVD) and molecular beam epitaxy (MBE). In MOCVD, crystalline growth is achieved by chemical reaction of suitable metal-organics and reactive gases in the vicinity of the growth substrate. On the other hand, MBE growth is carried out under ultra-high vacuum environment, where the source materials are heated high enough to create well collimated molecular beams towards the growth substrate. In the present study, MBE technology has been utilized for epitaxial growth of the GaAs-based structures, whereas the GaN-based heterostructures are grown by plasma-assisted MBE (PAMBE) (Fig. 3.2). The GaAs-based heterostructures are grown on (001) GaAs substrate, which has defect densities of 10^2 cm^{-2} or lower. This value can be assumed to be zero for all practical purposes and therefore negligible number of

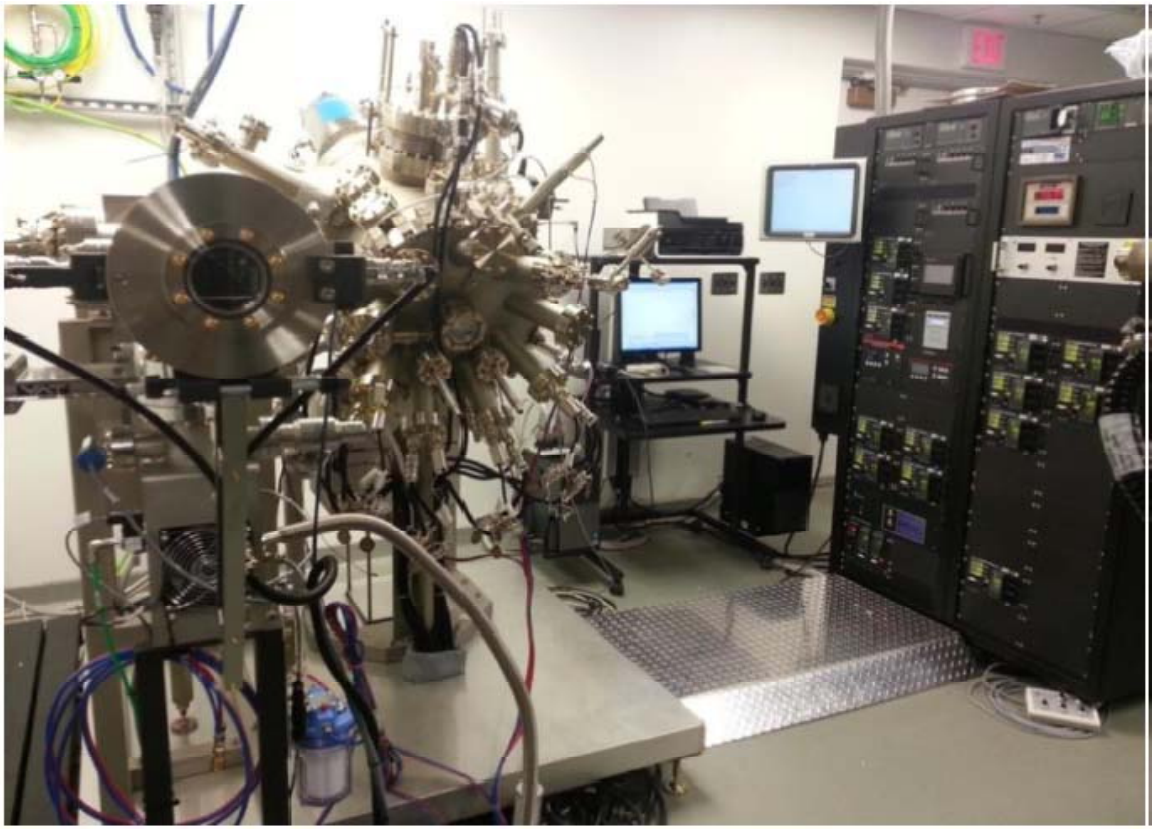

Fig. 3.2 Veeco Gen 930 MBE system used for epitaxial growth in the present study [150].

defects are expected to propagate into the active region during epitaxial growth. In GaN-based systems, however, the defect density ranges from 10^4 to $10^{10}\,cm^{-2}$, depending on whether the starting substrate is free-standing GaN, GaN-on-sapphire, silicon or SiC [106]. As a result, in spite of high-precision growth techniques, a significant number of defects are expected to propagate during epitaxial growth of high number of DBR pairs in GaN-based systems. An effective means of overcoming this problem is to utilize dielectric DBRs, which can be deposited using chemical or physical vapor deposition techniques. Plasma enhanced chemical vapor deposition (PECVD) has been reportedly employed to form SiO_2/Si_3N_4 DBR pairs in GaN-nanowire microcavities [70]. However in the present work, we utilize electron beam (e-beam) evaporation technique to form the DBRs of our microcavity diodes. This physical vapor deposition technique uses a small point source and a long throw distance, which results highly directional deposition with minimal heat transfer. Moreover, the deposition rate can be maintained at ~2 Å/s to obtain good control over the deposited dielectric layer thicknesses.

3.3 Pumping Schemes and Device Fabrication

In this section, different pumping schemes of the polariton devices are discussed. Also fabrication of the GaAs- and GaN-based devices studied in this work will be described.

3.3.1 Optical and Electrical Pumping Schemes

Optical pumping is the most commonly employed pumping scheme of polariton devices. In this technique, the active region of the semiconductor microcavity is excited through its top DBR layers with a laser of suitable wavelength and excitation density.

Optical pumping can be resonant or non-resonant in nature. In resonant pumping scheme, the device is pumped directly at the condensate energy and hence the coherence generated here may not be directly attributed to the microcavity. Non-resonant optical pumping is usually done at normal incidence at an energy above the upper DBR stop band. In this case the laser energy is at least ~100meV higher than the condensate energy and therefore coherent emission from the device can be unambiguously attributed to polariton lasing, provided that other conditions of polariton lasing are satisfied. A special case of optical pumping is the so called *magic angle* excitation scheme, in which the device is pumped at an angle such that for each excitation at wavevector k_m (which is the inflection point of the lower polariton dispersion), one lower polariton (LP) is scattered to $k=0$ and another LP is scattered to $k=2k_m$. This technique is also known as optical parametric oscillator [56, 96].

As far as practical applications are concerned, the most important pumping technique of polariton devices is however the electrical pumping scheme, in which electrons and holes are injected non-resonantly into the active region of a microcavity diode. Whereas electrically pumped photon lasers are very common nowadays, there are several technological challenges involved in the practical realization of electrically pumped polariton devices. In the vertical cavity surface emitting (VCSEL) geometry, which is the most commonly employed design for polariton devices, both the top and bottom semiconductor DBRs have to be doped for carrier injection (Fig. 3.3). This results free carrier absorption in the DBR layers [107], which invariably reduces the cavity quality factor and necessitates more number of DBR pairs to ensure sufficient optical confinement. Increasing the number of DBR pairs can significantly increase the

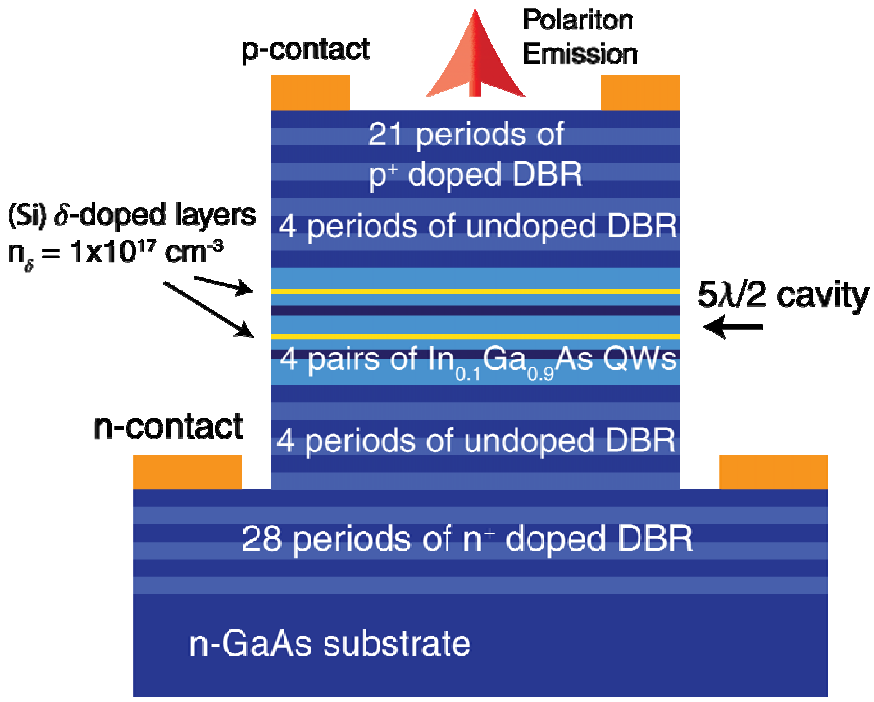

Fig. 3.3 Conventional VCSEL structure along with the heterostructure (not drawn to scale) [81].

diode series resistance, which in effect reduces the efficiency of operation under electrical injection. Moreover, dopant fluctuation, epilayer thickness variation, electrical contact degradation etc. result non-uniform carrier injection and device heating under electrical excitation. These problems are particularly severe in GaN- and ZnO-based systems, which have relatively less matured growth and fabrication technologies compared to that of GaAs [102, 105-109].

3.3.2 Fabrication of GaAs- and GaN-based Devices

In order to overcome the limitations of the conventional surface emitting geometry, a novel edge-emitting design has been employed in this work for electrical injection of the microcavity polariton devices. As shown in Fig. 3.4, in this geometry, the directions of optical feedback and carrier injection are orthogonal to each other. Because

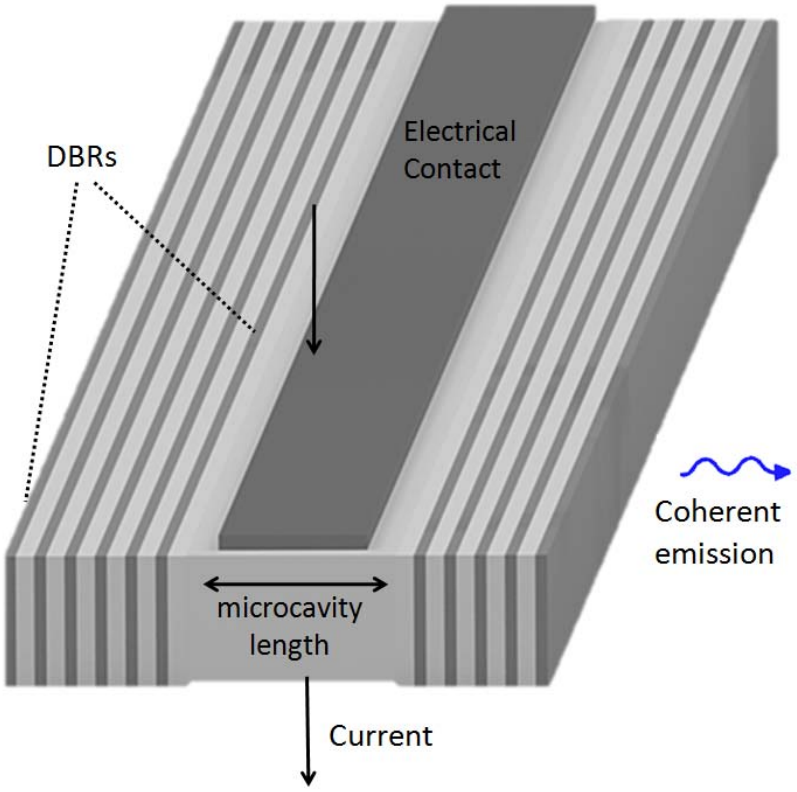

Fig. 3.4 Schematic of the edge-emitting microcavity polariton diode used in this study (not drawn to scale)

the carriers injected into this device do not have to transport through the DBR layers, the series resistance of the diode should remain significantly small. Also optical absorption at the electrical contacts is non-existent in the direction of light detection, which is not the case in a VCSEL. Moreover, because the mirrors here are not a part of the diode, the device heterostructure remains free of cracks or propagating defects which may otherwise arise from the growth of large number of DBR pairs above the emitter region. This facilitates the growth of high quality epitaxial layers, which is essential for uniform current injection into the active region of the device. In what follows, we discuss the general processing and fabrication steps of the GaAs- and GaN-based devices used in this study.

a. Fabrication of GaAs-based devices: The process is initiated by alignment mark and p-contact patterning onto the MBE grown heterostructure by UV projection lithography, which has a resolution of 0.75 μm. Prior to metal deposition, the native oxide is removed from the exposed surface by buffer hydrofluoric acid (BHF) solution. Using e-beam evaporation, Pd/Zn/Pd/Au is deposited as the p-contact metal, which is subsequently rapid thermal annealed in an inert N_2-atmosphere for 1 min at a temperature of 410º C. Next a 1 μm x 20 μm microcavity mesa is defined by reactive ion etching using a high density plasma etch tool. Here Ar/BCl_3 are used as the etchant gases to obtain an etch rate of ~ 8.5 nm/s. Then Ni/Ge/Au/Ti/Au is selectively deposited onto the n^+-doped region to form the n-contacts, after the removal of native oxide. The n-contact metal is annealed in N_2- environment for 1 min at a temperature of 360º C. To facilitate electrical probing of the device, 700 nm SiO_2 contact pad is deposited by plasma enhanced chemical vapor deposition at a heated substrate temperature of 200 ^oC. Finally Ti/Au interconnect for both n- and p-metal contacts are deposited on the contact pads.

b. Fabrication of GaN-based devices: Prior to the fabrication of the GaN-based devices, the PAMBE grown heterostructure is cleaned with acetone, IPA and HCl:DI water solution to remove organic or metallic droplets. Fabrication is initiated by selective deposition of Ni/Au p-contact, followed by rapid thermal annealing at 550^o C in an air ambient for two minutes. Next a 1 μm x 40 μm cavity region is defined by UV projection lithography, which is subsequently etched down to the n-contact region using high density plasma etching. Ar/Cl_2 reactant gases are used to obtain a etch rate of ~ 4 nm/s,. The etch step is followed by plasma enhanced chemical vapor deposition of 1 μm SiO_2 using SiH_4/N_2O gases, at a heated substrate temperature of 380 ^oC. The oxide is next

patterned and etched using $SF_6/C_4F_8/Ar$ gases to form the contact pads. Finally Ti/Au is deposited onto the n-doped substrate and onto the contact pads to realize the n-contacts and interconnects respectively.

3.3.3 Defining the Microcavity: Focused Ion Beam Etching and Electron Beam Evaporation

The semiconductor microcavities in this work are defined by focused ion beam (FIB) milling, followed by the deposition of dielectric DBRs using e-beam evaporation technique. FIB milling is a maskless, resistless, direct-write fabrication technology which can be employed to realize local modification of a sample or surface, or to create sub-micron scale features. This high precision technique has been successfully applied in the fabrication of microelectronic and optoelectronic devices, fault analysis of integrated circuits, sample preparation for transmission electron microscopy (TEM) and micromachining [110, 111]. In our context, it is particularly important as this technique has been reportedly very effective in forming high quality laser facets of GaAs- and GaN-based photon lasers [111-115]. The FIB milling performed in this work has been carried out using a FIB/SEM Dualbeam system, where commercial Gallium is used as the liquid metal ion source. A drawback of FIB is its long processing time and low throughput. To overcome this limitation, an initial etching is carried out using inductively coupled plasma (ICP) enhanced reactive etching, as discussed in the previous section. Next FIB etching is performed at relatively high injections, which span over the range of 50 pA to 1nA. To avoid re-deposition of the etched materials, FIB milling of the microcavities is conducted using multiple serpentine scans. A final FIB etching is carried out at a very low injection of below 30 pA to ensure optically flat surfaces along the lengths of the

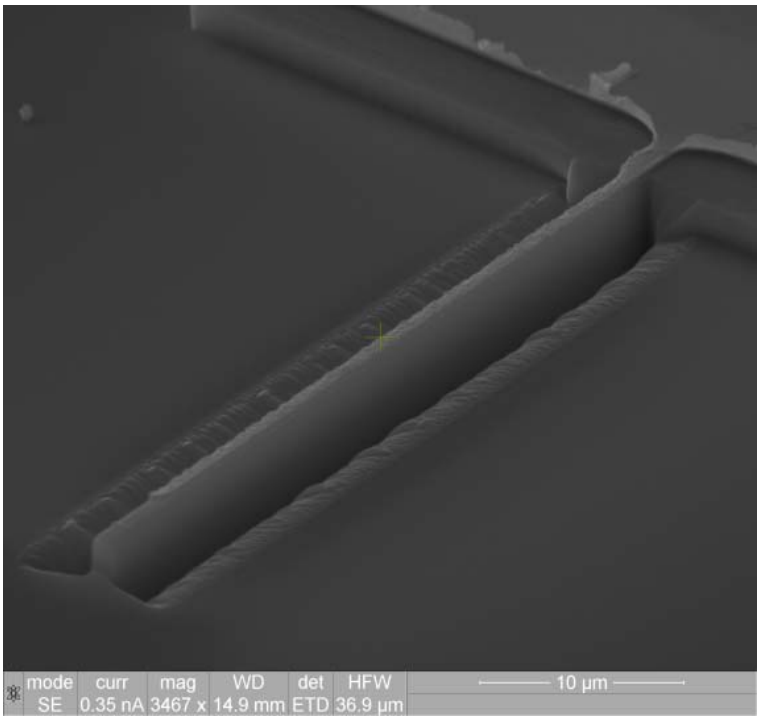

Fig. 3.5 SEM image of a FIB etched facet of the microcavity diode.

cavities. Studies show that the surface roughness of FIB etched GaN can be in the same order as that of as-grown GaN. Furthermore, surface-damages caused by FIB or ICP are reportedly recovered by rapid thermal annealing. Figure 3.5 shows the scanning electron microscope (SEM) image of a FIB etched cavity facet. Alternate 5-7 pairs of SiO_2/TiO_2 layers are deposited onto the opposite sides of the FIB etched cavity facets using e-beam evaporation technique, which has already been discussed in the previous subsection.

3.4 Materials Characterization

Prior to fabrication of the device, the MBE grown heterostructure and starting substrate are characterized by photoluminescence, surface morphology and compositional measurements. The DBR materials are characterized using reflectivity and ellipsometric measurements. These material characterization techniques are discussed in this section.

3.4.1 Photoluminescence Measurements

Both temperature dependent and time resolved photoluminescence (PL) measurements have been performed in this work to characterize the semiconductor active regions. Temperature dependent measurements have been performed by mounting the sample inside a liquid-Helium (He) cooled closed-cycle cryostat and exciting it with a continuous wave (cw) 325 nm He-Cd laser. The excitation density onto the sample is varied using a neutral density filter to conduct excitation dependent PL measurements at any fixed temperature. The temperature of the sample can be varied and stabilized over the range of 10 K - 300 K using a temperature controller having autotuning capability. Photoluminescence from the sample is focused into a triple-grating, 0.75 m focal length

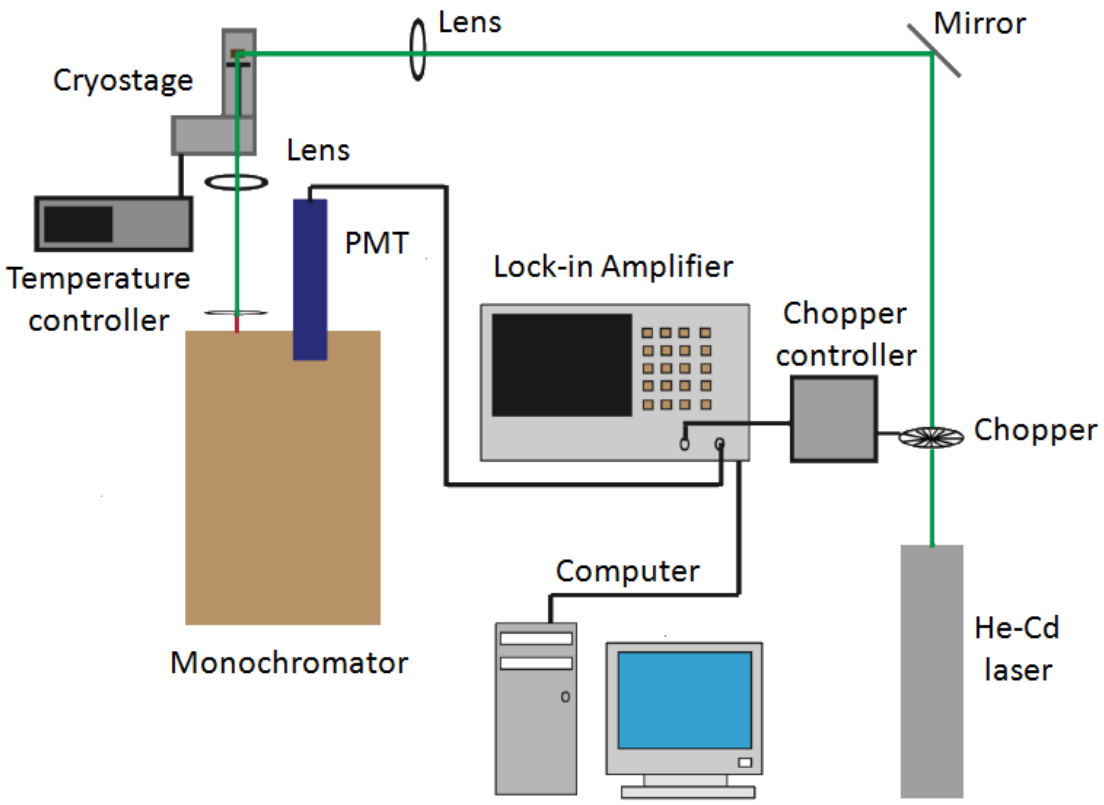

Fig. 3.6 A schematic representation of the temperature and excitation dependent PL measurement system [adapted from Ref. 150].

monochromator, which has a maximum grating of 1200 g/mm to obtain spectral resolution of 0.023 nm at 435.8 nm. The signal is detected using a photomultiplier (PMT) tube and a phase-sensitive lock-in amplifier. A schematic of the temperature and excitation dependent PL measurement system is shown in Fig 3.6.

Time resolved photoluminescence or TRPL measurements have been performed by mounting the sample inside a liquid-He cooled , closed-cycle cryostat and exciting it with a frequency tripled mode-locked, tunable Ti:Sapphire laser (λ=267nm). The laser emission has a pulse width of 130 fs and a repetition rate of 80 MHz, which makes it suitable for studying transients having timescales of a few picoseconds to several nanoseconds. The sample emission is focused at the imaging plane of a triple grating monochromator, which has a spectral resolution of 0.03 nm and a focal length of 0.75 m. A single photon avalanche photodiode detector, which is integrated with a universal time interval and frequency counter, is coupled to one of the output slits of the monochromator to collect the transient information. The timing resolution of the single photon counter used in this study is 40 fs, whereas the universal time counter can measure time intervals with 25 ps rms resolution. The other output slit of the monochromator is coupled to a high gain PMT, which can be used to measure the emission spectra. This allows spectral detection and filtering of the transition of interest.

3.4.2 Ellipsometry and Reflectivity Measurements

Prior to deposition onto the device facets, thickness, reflectivity and stopband of the dielectric DBRs are measured and calibrated using ultraviolet (UV)-visible spectroscopy and spectroscopic ellipsometry. Ellipsometry has been performed using a

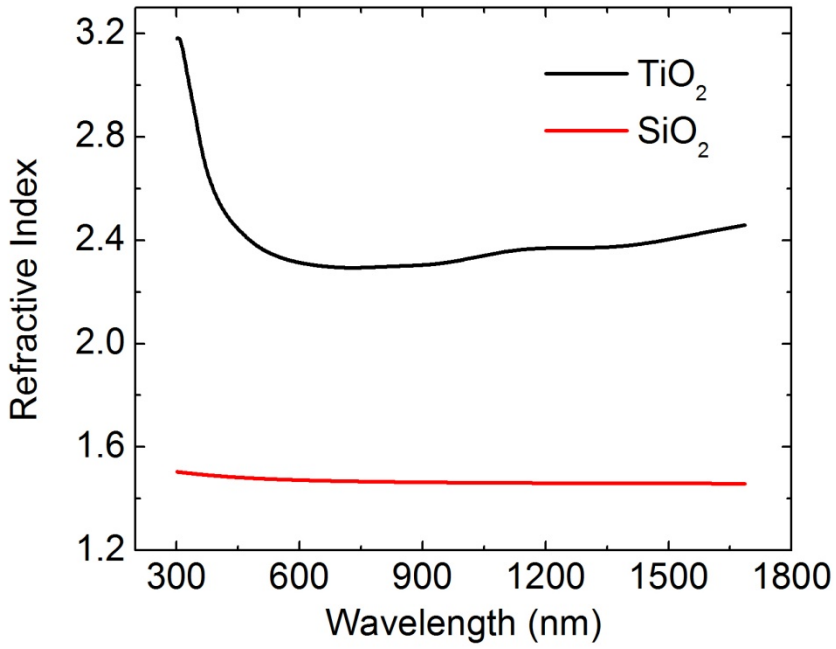

(a)

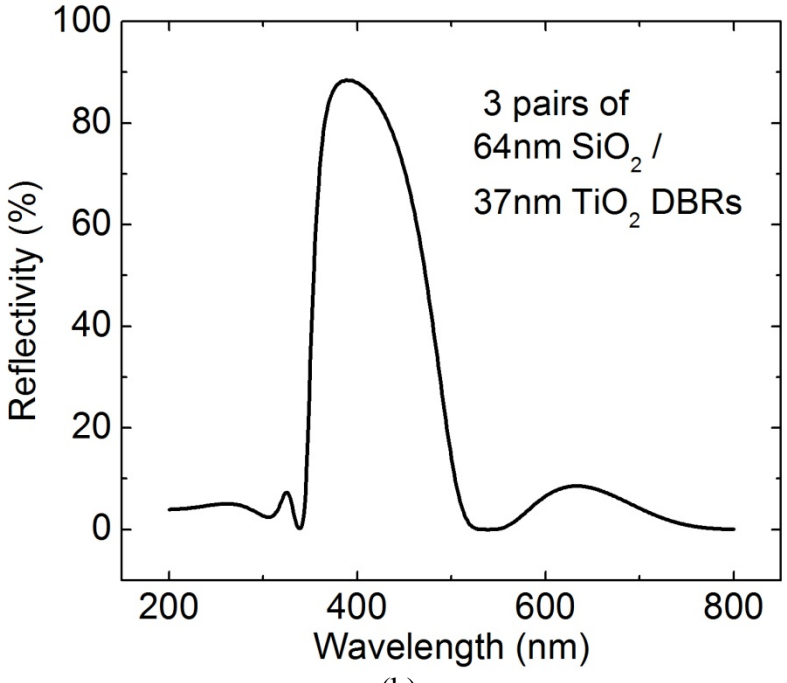

(b)

Fig. 3.7 (a) Measured refractive indices of e-beam evaporated SiO_2 and TiO_2 films using spectroscopic ellipsometry, (b) measured reflectivity of 3 pairs of e-beam evaporated SiO_2/TiO_2 DBR pairs using UV-visible spectroscopy.

variable angle spectroscopic ellipsometer, which is equipped with a high speed CCD detector that collects reflected signal over a spectral range of 193-1683 nm simultaneously. The tool has the capability of extracting sample thicknesses ranging from 1 nm to several micrometers. Hence it can been successfully utilized to measure and calibrate the desired SiO_2/TiO_2 layer thicknesses, which is within a range of 40 nm - 60 nm in our study. During fabrication of the microcavity diode, ellipsometry has been performed to measure the thickness of the SiO_2 contact pad, which is formed using PECVD. The plasma etch rate of SiO_2 is also calibrated using spectroscopic ellipsometry.

Besides thickness measurements, the ellipsometer has also been utilized to measure refractive indices of the dielectric and semiconductor materials used in this study. Figure 3.7(a) shows the measured refractive indices for e-beam evaporated SiO_2 and TiO_2. The ellipsometer used in our study allows reflection intensity measurements over an angular range of 0^o - 45^o. In order to measure normal incidence reflectivity, UV-visible spectroscopy has been performed in our study. Figure 3.7(b) shows the measured reflectivity using UV-vis spectroscopy for 3 pairs of SiO_2/TiO_2 deposited onto a calibration sample.

3.4.3 Surface Morphology and Compositional Measurements

In order to optimize the MBE growth conditions, MBE grown epitaxial layers and heterostructures have been studied with x-ray diffraction (XRD) and atomic force microscopy (AFM) measurements. XRD has been used to extract compositional information and to estimate lattice mismatch between the epilayers. This has been particularly useful in optimizing the growth condition of lattice matched $In_{0.18}Al_{0.82}N$

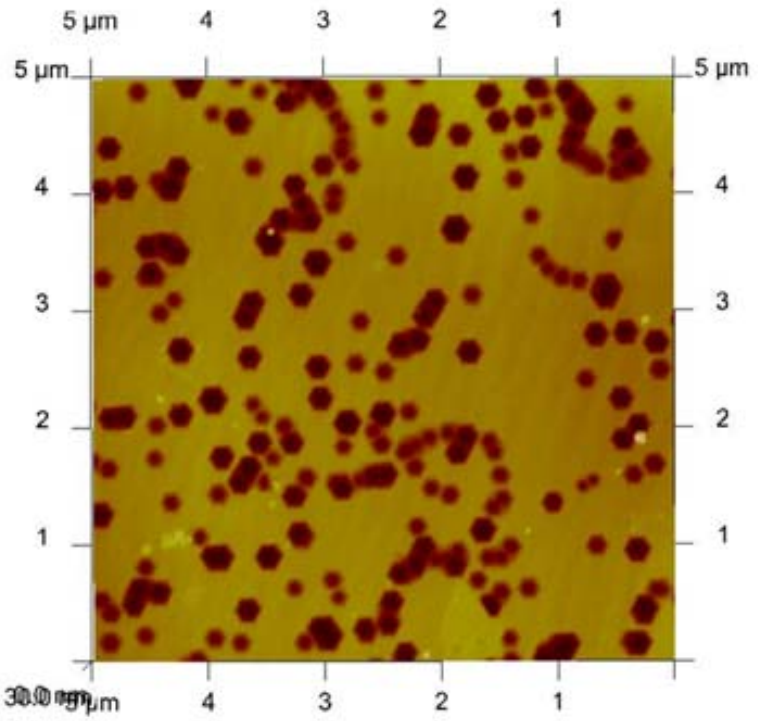

Fig. 3.8 AFM image of a GaN-on-sapphire surface after etch pit dislocation treatment.

layer on GaN-on-sapphire substrate. Details of this study is discussed in chapter 5. AFM, on the other hand, has been utilized to estimate surface roughness and crystal defect densities of different epitaxial layers so that the substrate temperature and source fluxes can be calibrated accordingly during MBE growth. An important experiment carried out using AFM is the etch pit dislocation (EPD) measurement, which is a means of estimating the number of defects in the starting GaN on sapphire template [116-117]. In this experiment, the templates are selectively etched with a eutectic mixture of molten bases. AFM measurements are subsequently performed on the etched samples. Figure 3.8 shows an AFM image of a GaN surface after etch pit dislocation treatment. These experiments are discussed in detail in chapter 7. Surface roughness of the dielectric DBRs is also estimated using AFM. From AFM imaging of 6 pairs of SiO_2/TiO_2 stacks, an average rms surface roughness of 2.2 nm is measured, which leads to a reduction in the

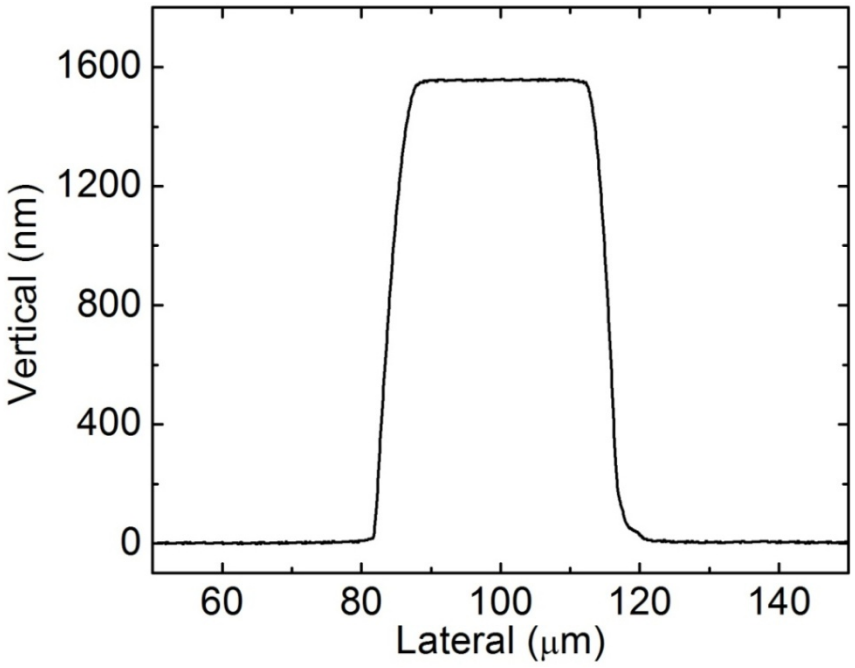

Fig. 3.9 Measured etch profile during fabrication of the GaAs-based device.

reflectivity of R/R_0 by about ~0.6% [82]. Surface roughness of the FIB etched cavities is observed by scanning electron microscopy (SEM), using dualbeam capabilities of the SEM/FIB tool. Stylus profilometer, which is also a surface profiling equipment, has been used during fabrication of the microcavity diode. This tool has the capability of measuring step heights ranging from 500 Å to 150 μm. Fig. 3.9 shows the measured profile of a inductively coupled plasma etched GaAs calibration sample, from which an etch rate of ~ 8.5 nm/s is estimated.

3.5 Device Characterization Techniques

The polariton diode lasers in this study have been characterized both at room and low temperature. The GaAs-based polariton laser is characterized at T=155 K, whereas measurements on the GaN-based devices have been made at room temperature. In this section, we discuss the device characterization techniques used in this study. Except for

microphotoluminescence measurement, all other measurements have been performed under electrical biasing of the fabricated microcavity diode.

3.5.1 Micro-photoluminescence Measurements

Microphotoluminescence (micro-PL) measurements have been performed to estimate the cavity quality factor of the microcavity diode. These measurements have been performed using a frequency tripled Ti:Sapphire laser, a triple-grating monochromator having spectral resolution of 0.03 nm, a high-gain photomultiplier tube, focusing optics and optical fibers. Two techniques have been employed to measure the micro-PL. In both of these techniques, the microcavity is excited non-resonantly with λ=266 nm, which is the frequency tripled output of the tunable Ti:Sapphire laser. In one setup, the same objective lens is used to focus the laser beam onto one facet of the microcavity diode and to collect the photoluminescence signal, and then convey it to the monochromator using achromatic doublet lenses. The sample is positioned using a piezoelectric stage having a precision of ± 0.05 μm and the laser beam is focused with a spot size of ~20-50 μm. In the other setup, the laser beam is focused on one facet of the device along the axis of cavity resonance and the photoluminescence is collected from the other cavity-facet using an UV multi- or single-mode optical fiber. The optical fiber is coupled to the monochromator, which spectrally resolves and conveys the signal to the photomultiplier tube.

3.5.2 Electrical Biasing and Current-Voltage Measurements

All the devices studied in this work have been pumped electrically at room or low temperature. The current-voltage (I-V) characteristics of the fabricated devices are

initially measured using a semiconductor characterization system, which has a voltage range of ±210 V and a current range of ±100 mA. During electroluminescence measurements, the device is biased in the constant current mode using a dual-channel source meter which is capable of applying continuous wave (cw) current over a range of 100 nA to 10 A with a minimum resolution of 2 pA. It is well known that under cw operation, the active device temperature can well exceed 100^{o}C because of heat generated in the non-radiative recombination centers [118]. Such high temperatures are detrimental to the diode performance, and more importantly to the sustainability of strong-coupling in the microcavity diode. Hence for room temperature measurements at high injection current densities, the device is biased with a low noise AC/DC current source, which has been employed to generate 10 kHz rectangular current pulses with a duty cycle of 5%. At higher biases, especially in the photon lasing regime, the device is mounted and cooled using a temperature-controlled Peltier cooler. For electrical probing at room temperature, gold plated tungsten probes mounted onto x-y-z micrometer stages have been used. For low temperature measurements, the device is mounted onto a metal chip carrier and the device contact pads are wire-bonded with Au. The device is mounted inside a continuous flow liquid-He cooled cryostat, which has external connections for applying electrical bias.

3.5.3 Angle-Resolved Electroluminescence and Momentum Space Mapping

Angle-resolved electroluminescence has been measured under cw electrical bias at room and low temperatures. The direction normal to the DBR mirrors is considered to be 0^{o} and the detection angle is varied in a plane perpendicular to the growth axis. The device is mounted such that its emission spot can be taken as the pivot-point for angular

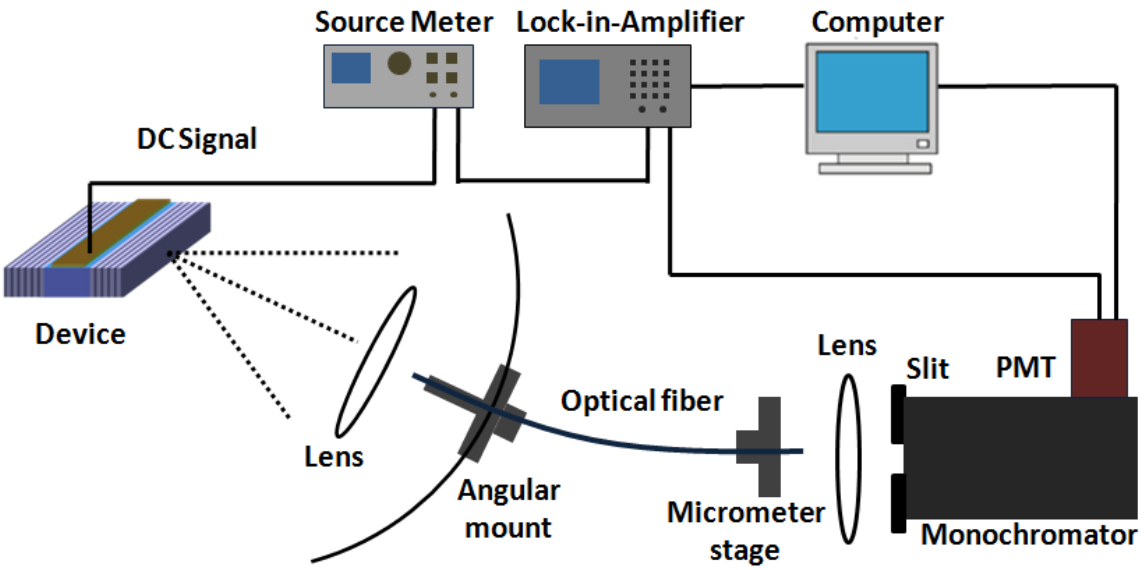

Fig. 3.10 Schematic diagram of an experimental setup for room temperature angle-resolved electroluminescence measurement.

detection of device electroluminescence (Fig. 3.10). Light is collected using a lens-coupled optical fiber, which is mounted on a digital read-out angular mount having a precision of 0.1°. The detection angle is varied in the $k_{||}$ plane for electroluminescence measurements up to a maximum of 30°. The electroluminescence collected with the fiber is transmitted to a 0.75 m Czerny-Turner imaging monochromator, which has a spectral resolution of 0.023 nm at 435.8 nm and maximum grating number of 1200 g/mm. The light is subsequently detected with a photomultiplier tube, which is coupled to one of the exit slits of the monochromator. Micrometer stages are used both at the receiving and detection ends to optimize optical alignment of the measurement setup.

The polariton occupation in k-space at different injection levels was measured by angle-resolved electroluminescence. Below threshold, the number of polaritons per *k*-state is estimated from the LP electroluminescence integrated intensity by taking into account the radiative lifetime. At and above threshold, the occupation is calculated from

the output power measured with a power meter. The polariton occupation number per $k_{||}$ state is calculated using the formula, $I_{LP} = \frac{\eta N_{LP}(k_{||}) |C(k_{||})|^2 M}{\tau_C}$, where η is the collection efficiency, $\tau_C / |C(k_{||})|^2$ is the radiative lifetime of LPs, M is the number of transverse states included in the detection cone, and $|C(k_{||})|^2$ is the photon fraction at a wave vector $k_{||}$. The number of states within the detection cone is given by $M = D^2 / 16(k_o \Delta\theta)^2$, where D is the diameter of the emission spot, $k_o = 2\pi / \lambda$ and $\Delta\theta$ is the detection half angle [57, 119].

3.5.4 Light-Current Characteristics

The light-current (L-I) characteristics of the device were determined by recording the electroluminescence (EL) in the direction normal to the DBR mirrors (zero angle), as a function of continuous wave injection current. Two methods have been used to record the L-I characteristics and both of them yielded identical results. In the first technique, EL spectra are recorded using a combination of optical fiber, collection optics, high resolution monochromator and photomultiplier tube. The electroluminescence, collected using a multimode optical fiber mounted onto a x-y-z micrometer stage, is transmitted to a 0.75 m monochromator which has a minimum spectral resolution of 0.03 nm. Light is detected using the high gain PMT, which is out-coupled to one of the exit slits of the monochromator. Finally EL spectra is recorded with optimum spatial resolution, signal integration time and detector sensitivity. Upon analysis, integrated intensity of the polariton emission is plotted as a function of forward bias current to obtain the L-I characteristics. The spectral characteristics obtained in this measurement also yields the

emission linewidth and peak energy positions

In the second technique employed for L-I characterization, the output power is directly measured with a power meter of suitable sensitivity. In cases where the signal intensity is below the sensitivity of the power-meter, device luminescence is detected using the PMT, following calibration with the power-meter. Unlike the first measurement technique, this technique does not yield spectral information. However because of the short response time of the power-meter/PMT, this method is particularly useful for measuring the L-I characteristics in the photon lasing regime, where the injection current densities can cause irreversible damage to the electrical contacts if the device is pumped for too long.

3.5.5 Spatial Coherence Measurements

The far-field interference pattern of the polariton condensate is measured using a slightly misaligned Mach-Zehnder interferometer to ascertain spatial coherence of the output LP electroluminescence. A schematic of this measurement setup is shown in Fig 3.11. A beam splitter is utilized to split the output luminescence from the device. This generates two identical copies of the LP emission, which are next transmitted through two perfectly balanced arms of the interferometer. The two copies of the emission intensity profile are then made to interfere with each other in the far-field by overlapping them spatially. This has been accomplished by translational movement of one of the reflecting mirrors (Mirror 2), which is mounted diagonally on a piezo-stage. The piezo-stage can be controlled using a closed-loop feedback system, which provides a minimum spatial resolution of 20 nm. The system creates a double image of the condensate at the image plane, where a pinhole is placed for spatial filtering of the dark and bright fringes.

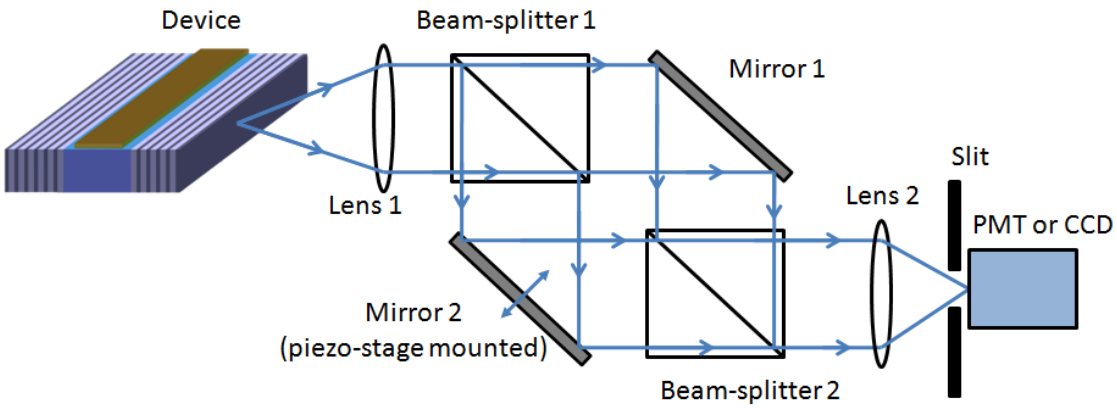

Fig. 3.11 A schematic illustration of the Mach-Zender interferometer used in this study.

The intensities of the dark and bright fringes have been measured using a PMT, following spectral-filtering with an imaging monochromator. Finally the visibility of the interference patterns is calculated using the relation $V = (I_{max} - I_{min})/(I_{max} + I_{min})$ where I_{max} and I_{min} are intensities of the bright and dark fringes respectively.

For room temperature measurements, the visibilities at several injections are calculated from the recorded LP emission intensities without actually imaging the interference pattern. This is done because the output luminescence at the far-field image plane is below the sensitivity of the CCD camera at our disposal. However at low temperature, the signal intensity is strong enough at an injection above the polariton lasing threshold so that an interference pattern can be detected by the CCD camera, which is positioned at the image plane of the interferometer [120].

3.5.6 Steady-State Output Polarization Measurements

Steady-state linear polarization of the output of the polariton lasers has been measured under cw electrical bias at room temperature.. The output electroluminescence

is collected in the normal direction ($k_{||}$~0) using a UV multimode optical fiber and transmitted through a Glan-Thompson linear analyzer, whose orientation is referenced to the structural growth axis of the microcavity diode. The polarization-resolved luminescence is then spectrally dispersed by a 0.75 m Czerny-Turner imaging monochromator (with a spectral resolution of 0.023 nm at 435.8 nm) and detected by a photomultiplier tube. At a particular current bias, measurement of the electroluminescence for different angular orientations of the linear analyzer gives the degree of linear polarization, which is defined as $\left(I_{\max}-I_{\min}\right)/(I_{\max}+I_{\min})$. Here $I_{\max}$ and $I_{\min}$ are the maximum and minimum polarization resolved intensities respectively. This measurement, when performed as a function of injection current density, renders information about the steady-state buildup of linear polarization in the polariton device [121].

The same experimental setup has been employed to measure the linear polarization-resolved output light-current (L-I) characteristics. In this measurement, the L-I characteristics of the device has been measured in the normal direction ($k_{||}$~ *0*) to the DBR mirrors under cw electrical injection, with the linear analyzer oriented along $\theta = 0^{o}$, 45^{o} and 90^{o} with respect to the crystallographic growth axis. Under the same measurement conditions and identical optical alignments, the unresolved light-current characteristics are measured without employing any polarization-splitting optics. A comparison of the results of these two measurements gives information about the nature of the polarization resolved L-I characteristics of the polariton laser diode.

3.5.7 Small-signal Modulation Measurements

Small-signal modulation measurements have been performed only at room temperature because reliable transmission of high-frequency electric pulses to the device is limited by electrical wirings of the cryostat. Experimental setup of the small-signal modulation measurement consists of the following: GSG probe, bias tee, optical fiber, single photon detector, single photon counter, AC pulse generator, DC source meter, triple grating monochromator, Peltier cooler and temperature controller (Fig. 3.12). For this measurement, the contact pads of the devices are carefully designed with 50 μm spacing so that they can be conveniently probed with the 100 μm pitch Beryllium Copper tip GSG probe. The highest frequency that can be transmitted through this probes is 40 GHz. To avoid possible device heating, the device is mounted and cooled on a

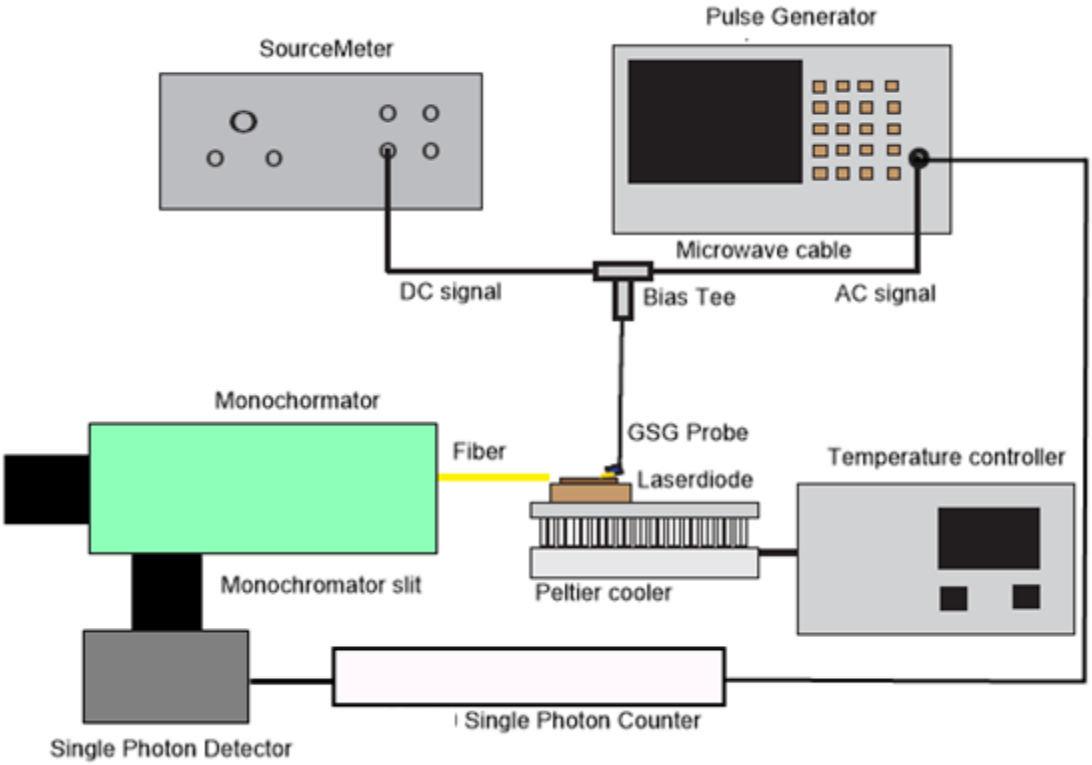

Figure 3.12 Experimental setup of small-signal modulation response measurement.

temperature controllable Peltier cooler. The high frequency pulses in this experiment has been generated in the form of a square wave using a low jitter pulse-pattern generator, where the output signal frequency can be varied from 15 MHz - 3.35 GHz. The maximum rise and fall times of the square-wave pulses is ~120 ps. The timing resolution of the single photon detector is 40 ps and time intervals can be measured with 25 ps rms resolution using the frequency counter. These specifications are essential for detection of the fast dynamics of a polariton device under high frequency electrical injection [122].

The small-signal modulation response of the device is measured by superimposing a small-signal periodic switching pulse (1-3 mV) on different DC bias voltages set above the polariton lasing threshold. The output electroluminescence, collected normal to the cavity mirrors using an UV optical-fiber, is transmitted to a monochromator having a minimum spectral resolution of 0.03 nm. The transient information is subsequently collected using the combination of high-speed single photon detector and frequency counter. The modulation response is derived by the fast Fourier transform (FFT) of the measured transient response. The RC effect of the microcavity diode has been taken into account in the modulation response by measuring the diode series resistance and contact pad capacitance using a semiconductor characterization system. In order to measure the chirp of the polariton laser, an UV photomultiplier tube is connected at one of the exit slits of the monochromator. In this experiment, chirp of the polariton laser has been recorded as an average broadening of the coherent emission spectra under small signal (2 mV) pulsed bias condition above threshold (1.15 J_{th}) for different modulation frequencies.

3.6 Summary

In this chapter, we provide a description of the experimental techniques employed in this work. First, we provide a comparison of the commonly used materials in semiconductor microcavities and discuss the advantages of using all-dielectric DBRs. The epitaxial growth and deposition techniques used in this study are discussed. Next we describe the challenges associated with electrical pumping and describe how these limitations are overcome in an edge-emitting geometry. As described herein, conventional processing and fabrication techniques have been utilized to realize the proposed polariton device geometry. Different materials characterization techniques, which include photoluminescence, reflectivity, ellipsometric measurements, SEM, AFM and surface profilometry, are also discussed in the context our study. Finally, we present the device characterization techniques used in our study. Measurements performed both at room temperature and low temperature have been described. Except for micro-PL measurement, all other measurements performed on the devices are done under cw or pulsed electrical excitation. The measurements performed to ascertain strong-coupling and polariton lasing of the fabricated devices have been described in detail. Also the experimental setups and specifications of steady-state output polarization and high frequency small-signal modulation response measurements have been elucidated.

Chapter IV

GaAs-based High Temperature Polariton Diode Lasers

4.1 Introduction

In spite of the highly matured epitaxial growth and device fabrication technologies of GaAs-based material systems, experimental demonstration of GaAs-based polariton diode laser has hitherto remained limited to cryogenic temperatures [80, 81]. At or near room temperature, only strong coupling has been observed in GaAs-based electrically pumped polariton devices [78, 79, 123-125]. This limitation has been mainly attributed to the intrinsically low exciton binding energy of this material system. Furthermore, the reported devices are grown and fabricated based on the conventional vertical cavity surface emitting geometry, where doping of the DBR layers results cavity mirror loss in the form of free carrier or interband absorption [102, 107]. This, in effect, reduces the polariton lifetime and creates a polariton relaxation bottleneck, thereby further prohibiting the emergence of polariton lasing phenomenon. In this chapter, we present the experimental realization of a GaAs-based polariton laser which can operate at T=155 K under electrical excitaion. It will be shown that high exciton binding energies can be attained using a $Al_{0.31}Ga_{0.69}As/Al_{0.41}Ga_{0.59}As$ single quantum well, which facilitates the observation of strong coupling and polariton lasing at high temperatures.

Also contrary to the surface emitting geometry, an edge emitting geometry has been employed to realize the device. Finally, an experimental study aimed towards the realization of a room temperature GaAs-based polariton laser is presented and the potential challenges have been elucidated on the basis of the observed results.

4.2 Enhancement of Exciton Binding Energy in a GaAs-based System

Bulk GaAs has a low exciton binding energy of ~4 meV because of its intrinsically large exciton Bohr radius (~11.4 nm) and dielectric constant (ε_r = 13.1). However, experiments show that the exciton binding energy in $Al_xGa_{1-x}As$ alloys increases steadily from ~ 4 meV in GaAs (x=0) to ~10 meV in $Al_{0.25}Ga_{0.75}As$ because of the reduced exciton Bohr radius and lower dielectric screening [86, 126]. There is a sharp increase of the binding energy for x>0.25, similar to the ionization energy behavior of deep donors in this alloy system, which is a result of multivalley effects in the vicinity of the direct-to-indirect bandgap transition regime [86, 127]. Furthermore, as discussed in section 2.1, the exciton binding energy in a planar GaAs/AlGaAs quantum well can be ~4 times than in bulk GaAs [85, 128]. Therefore, to take advantages of the high Al mole fraction as well as of the 2D confinement in a quantum well, we have designed the GaAs-based polariton device with an $Al_{0.31}Ga_{0.69}As/Al_{0.41}Ga_{0.59}As$ quantum well as the emitter. The exciton Bohr radius and binding energy of this system can be theoretically approximated by solving the Schrödinger equation for a 2D Hydrogen atom, which to a first approximation, is similar to a QW-exciton problem. In regards to the binding energy of the lowest exciton state, the following relations are derived from the solution of Schrödinger equation for relative motion [129]:

$$a_{BX}^{bulk} = \frac{4\pi\hbar^2}{e^2}\frac{\varepsilon}{Zm^*}$$
$$E_{1s} = -\frac{Ze^2}{2\pi\varepsilon}\frac{1}{a_{BX}^{bulk}} \qquad 4.1$$

Here $Z = 1$ (because it is a Hydrogen atom problem), $m^* = \left(1/m_h^* + 1/m_e^*\right)^{-1}$ is the reduced effective mass, ε is the dielectric constant and a_{BX}^{bulk} is the 3D exciton Bohr radius of the QW material, which in this study is $Al_{0.31}Ga_{0.69}As$. By estimating these material parameters using the virtual crystal approximation [130], we obtain $a_{BX}^{bulk} \sim 7.73$ nm for bulk $Al_{0.31}Ga_{0.69}As$. In an ideal quantum well, the 2D exciton Bohr radius (a_{BX}^{bulk}) reduces to $a_{BX}^{well} \approx a_{BX}^{bulk}/4 = 1.93$ nm and the corresponding exciton binding energy becomes E_{1s} ~31 meV. Using the same formulation, we observe that this value of E_{1s} is significantly larger than those of ideal GaAs/AlGaAs (E_{1s}~20 meV with a_{BX}^{well} ~2.85 nm) and InGaAs/GaAs (E_{1s}~13 meV with a_{BX}^{well} ~4.5 nm) quantum wells, which are the commonly employed active regions in GaAs-based polariton devices [13, 18, 20, 23-26, 51-53, 56-58, 66, 76].

4.3 Device Heterostructure

As can be observed from the bandgap energies plotted as a function of the Al mole fraction (Fig. 4.1(a)), $Al_xGa_{1-x}As$ is an indirect bandgap semiconductor for x > 0.41. Because free excitonic transitions are very susceptible to multivalley scattering and phonon scattering effects in indirect bandgap semiconductors, the quantum well is designed with $Al_{0.31}Ga_{0.69}As/Al_{0.41}Ga_{0.59}As$, where both the barrier and the active regions are direct bandgap semiconductors. The conduction and valence band offsets of this

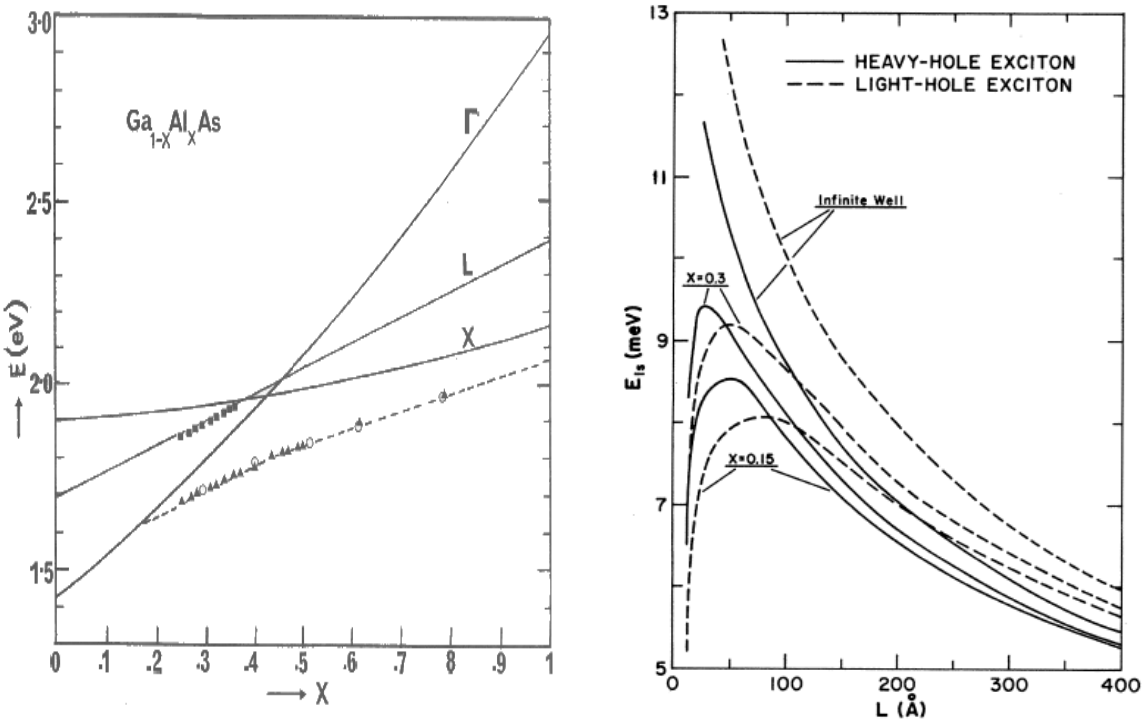

(a) (b)

Fig. 4.1 (a) Bandgap energies of $Al_xGa_{1-x}As$ plotted as a function of the Al mole fraction [127], (b) calculated exciton binding energies of $Al_xGa_{1-x}As$ based quantum well plotted as a function of quantum well width [128].

system are 0.072 and 0.048 eV (at T= 155 K), respectively, assuming $\Delta E_c = 0.6\Delta E_g$. A single quantum well (SQW) is used to minimize inhomogeneous broadening of the emission linewidth due to interface roughness scattering [131, 132]. As discussed in the previous section, a quantum well (QW) comprising of this material system should exhibit a high exciton binding energy of ~31 meV. Unfortunately, such a high value of the exciton binding energy for this material system can be obtained only in a perfectly two-dimensional QW, where there is perfect overlap between the delta-like electron and hole wavefunctions along the growth axis. Nevertheless, theoretically it can be shown that the electron-hole wavefunction overlap, and consequently the exciton binding energy in a SQW can be increased by reducing the quantum well width, such that the wavefunctions

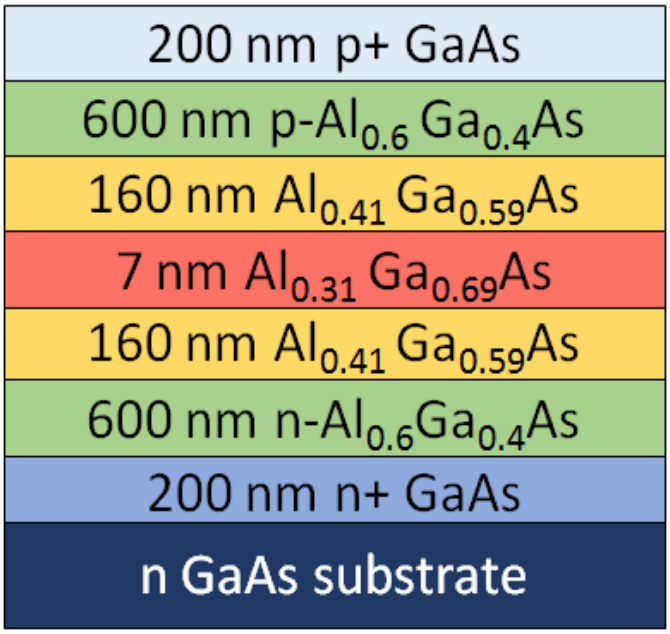

Fig. 4.2 A schematic of the device heterostructure grown by MBE.

are mostly confined within the well. Based on the theoretically calculated data shown in Fig. 4.1(b), a quantum well width of 7 nm is chosen in our design, because a smaller well width may lead to wave function leakage and a consequent reduction of the exciton binding energy. Figure 4.2 shows a schematic of the p-i-n microcavity diode heterostructure, which has been grown by molecular beam epitaxy on (001) GaAs substrate. The 160 nm $Al_{0.41}Ga_{0.59}As$ layers, along with a 7 nm $Al_{0.31}Ga_{0.69}As$ SQW in the center, serves as the waveguide of the device. The waveguide region is surrounded by 600 nm p- and n- doped $Al_{0.6}Ga_{0.4}As$ layers, which provide optical confinement. Transfer matrix method based analysis shows a modal confinement of 2.5% for a single waveguide mode, the antinode of which coincides with the SQW. An effective refractive index of ~3.46 is obtained from this analysis. The heavily doped p- and n-type GaAs layers are grown to facilitate low resistance ohmic contacts of the device.

4.4 Materials Characterization

4.4.1 Excitation Dependent and Time Resolved Photoluminescence

Excitation dependent and time-resolved photoluminescence measurements have been performed by exciting the active region of the SQW sample with an UV laser. To avoid absorption of the exciting laser in the top contact and cladding layers, the MBE grown full heterostructure is initially etched down to the top barrier layer by ICP reactive ion etching in a BCl_3:Cl_2:Ar environment. The prepared sample is next mounted inside a closed cycle liquid-He cooled cryostat, where it is excited using a cw 325 nm He-Cd laser. The excitation density is varied using a neutral density filter and the incident power is measured and calibrated using an optical power-meter. Figure 4.3 shows PL emission

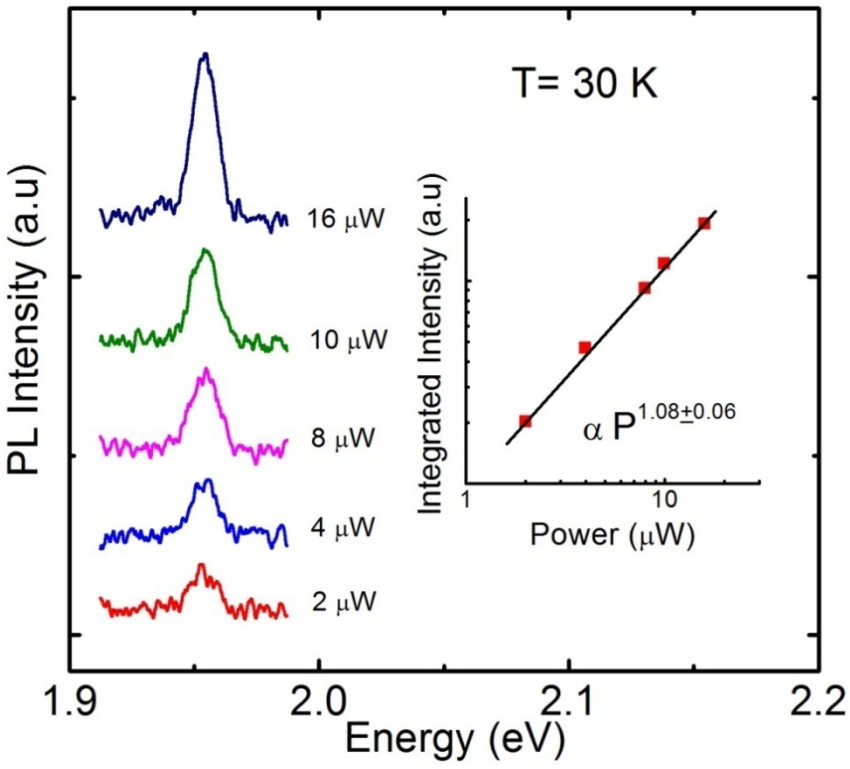

Fig. 4.3 Measured excitation dependent PL spectra at T= 30 K. The inset shows a linear dependence of the integrated intensity on excitation density.

spectra from the $Al_{0.31}G_{0.69}As/Al_{0.41}Ga_{0.59}As$ SQW measured at 30 K under different excitation densities. The measured linewidth of the exciton transition at 30K is 7.8 meV (2.531 nm). The PL emission is also measured at 155 K, which is the measurement temperature of the polariton device. The homogeneously broadened linewidth at 155 K is ~8.5±0.3 meV. As shown in the inset of Fig. 4.3, a linear dependence of the integrated intensity on excitation is obtained from our analysis of the measured spectra. Also the peak energy position remains invariant with excitation, which indicates the absence of band filling of defect bound states. This confirm the free excitonic behavior of the luminescence and indicates that the excitons in the system are less likely to be bound by defects or disorders.

To obtain the lifetime of the excitonic transition, TRPL measurements have been performed at 155 K using a frequency tripled Ti:Sapphire laser which has a repetition rate of 80MHz and pulse width of ~60-130 fs. The sample is mounted inside a liquid-He cooled cryostat and the photoluminescence (PL) is detected using the combination of a single-photon detector and a frequency counter. Figure 4.4 shows the measured PL transient from the $Al_{0.31}Ga_{0.69}As/Al_{0.41}Ga_{0.59}As$ single quantum well at T=155 K. Upon analysis of the measured data with a stretched exponential model $I = I_o \exp\left[-\left(\frac{t}{\tau}\right)^{\beta}\right]$, we obtain τ = 468 ps with $\beta \approx 1$. The near unity value of β indicates the absence of carrier depopulation due to screening of piezoelectric field or a degree of compositional fluctuation, both of which lead to a change in the carrier lifetime. These effects are quite prevalent in InGaN quantum wells, where the value of β ranges from 0.5-0.7 [133, 134].

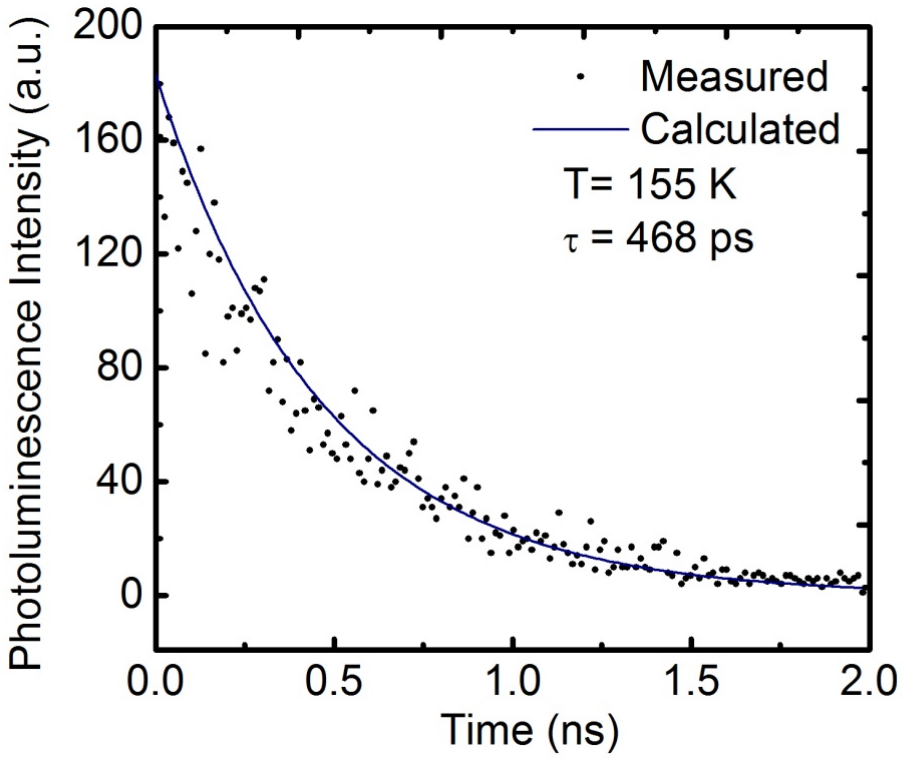

Fig. 4.4 Measured time resolved photoluminescence from the AlGaAs/AlGaAs SQW at T=155 K along with exponential model based analysis.

4.4.2 Estimation of Exciton Binding Energy

The exciton binding energy E_{BX} in the $Al_{0.31}G_{0.69}As/Al_{0.41}Ga_{0.59}As$ SQW is estimated from temperature dependent photoluminescence measurements performed over a temperature range of 30 K - 200 K. The temperature of the sample, which is mounted inside a continuous flow liquid-He cryostat, is varied and stabilized using an autotuning temperature controller. The sample is optically pumped at a fixed excitation density of the cw 325 nm He-Cd laser. The PL emission from the sample is focused onto a monochromator, where it is spectrally resolved and detected using a high gain PMT and lock-in-amplifier. Figure 4.5 shows the measured PL peak emission energy as a function of temperature. The measured values are in good agreement with the empirical Varshni

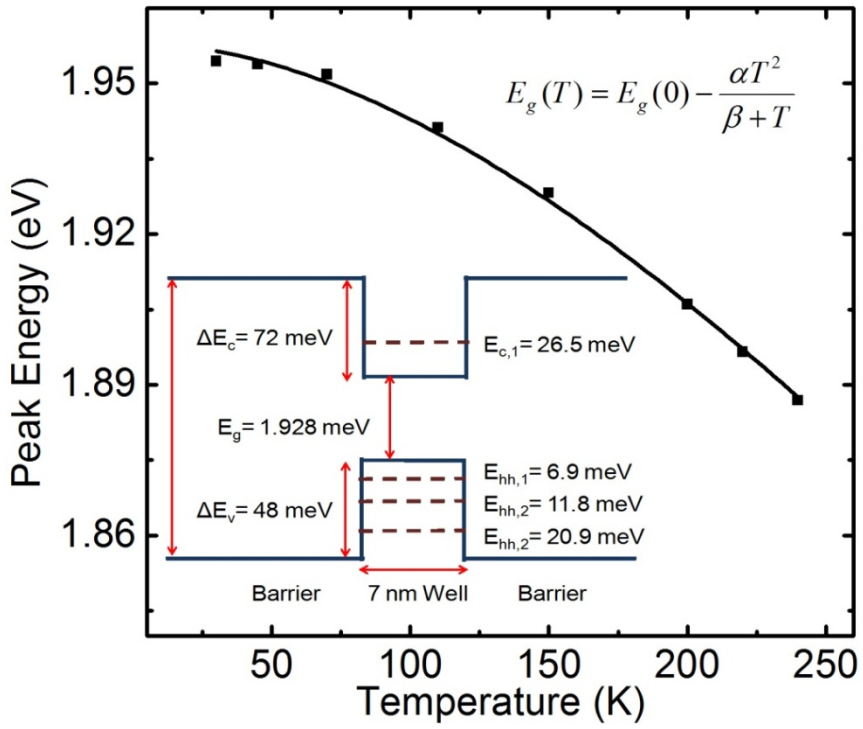

Fig. 4.5 PL emission peak energy plotted as a function of temperature (inset shows the calculated energy states of the SQW).

relation, which is $E_g(T) = E_g(0) - \frac{\alpha T^2}{\beta + T}$. Here $E_g(0)$ is the bandgap at temperature T=0 K, α and β are empirical parameters [130]. As obtained from the solution of time independent Schrödinger equation for a SQW (shown as an inset of Fig. 4.5), the PL peak energy corresponds to the energy difference between the e_1-hh_1 states. To estimate the exciton binding energy, the measured temperature dependent PL results are analyzed over the temperature range of 140-170 K using the relation: $E_{ph} = E_g + E_e + E_{hh} - E_{BX}$, where E_{ph} is the peak energy of the PL spectra, E_g is the bandgap of the $Al_{0.31}Ga_{0.69}As$ well, and E_e and E_{hh} are the confinement energies of the bound states of the electron and heavy hole, respectively. The temperature dependence of the bandgap is estimated by Varshni relation and the material parameters are calculated using the virtual crystal approximation [130]. The bound state energies E_e and E_{hh}, are calculated by solving the Schrödinger

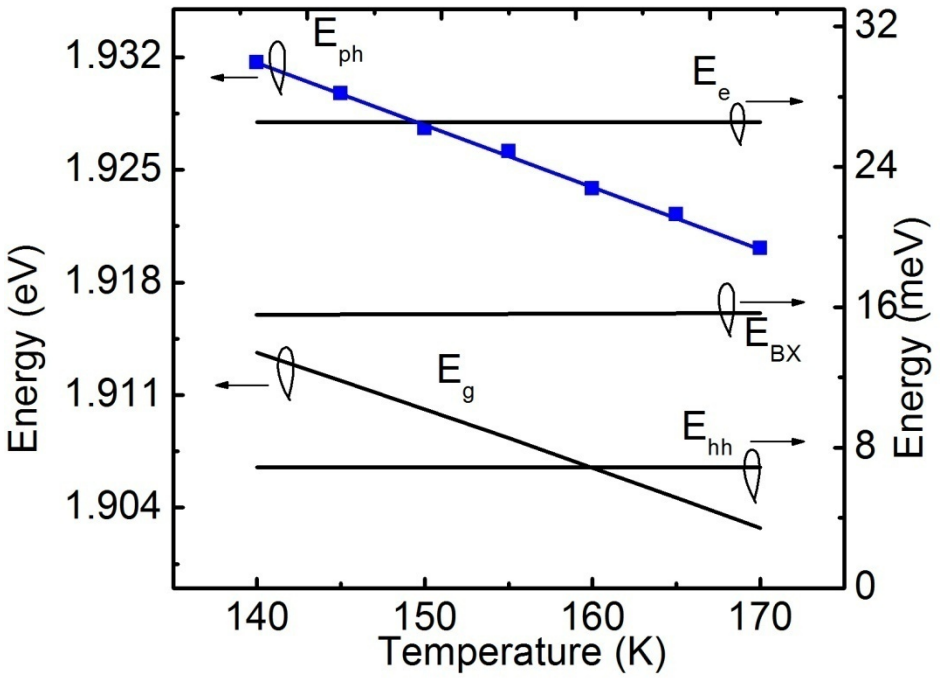

Fig. 4.6 Measured values of E_{ph} , along with the values obtained for E_g, E_e, E_{hh}, and E_{BX} from our analysis.

equation using these material parameters. Uncertainties in the quantum well thickness and compositions affect the calculation of the bound state energies, and also of the bandgap of the $Al_{0.31}Ga_{0.69}As$ well material. The quantum well thickness is limited by the accuracy of the MBE growth (0.5 monolayer), whereas the compositions of the well and barrier materials are confirmed by high resolution X-ray diffraction analysis. The effect of uncertainties in quantum well and barrier composition and well thickness is taken into account in our analysis. It has been assumed that E_{BX} does not vary over the considered temperature range. Figure 4.6 shows the measured values of E_{ph} , along with the values obtained for E_g, E_e, E_{hh}, and E_{BX} from our analysis. At T=155 K, the values of E_e, E_{hh}, and E_{BX} are estimated to be 26.5±0.13 meV, 6.9±0.07 meV, and 15.8±1.8 meV, respectively. From $E_{BX} = k_B T$, we obtain T=180 K, which indicates that the binding energy is sufficiently high for the excitons to remain stable well above the cryogenic temperature.

4.5 Device Fabrication

A detailed outline of the processing and fabrication steps of the edge-emitting polariton devices has already been given in chapter 3. Nevertheless, we discuss the fabrication of the GaAs-based device here for completeness. The fabrication is initiated by selective deposition and annealing of Pd/Zn/Pd/Au (10nm/20nm/20nm/ 300nm) p-contact metal, definition of the 1 μm x 20 μm microcavity region by reactive ion etching down to the n^+ GaAs layer and selective deposition and annealing of Ni/Ge/Au/Ti/Au (25nm/325nm/65nm/20nm/300nm) n-contact on this layer. This is followed by deposition of 700 nm SiO_2 contact pads and subsequent deposition of Ti/Au interconnect metal for both p- and n- contacts. The contact pads are designed to be large enough to facilitate Au-Au wire bonding with the chip carrier. The final dimensions of the 929 nm (5λ) x 20 μm cavity are defined by focused ion beam (FIB) etching. Five and six pairs of SiO_2/TiO_2 DBR mirrors, as schematically shown in Fig.4.7, are deposited on the two sides of the FIB etched facets by e-beam evaporation to complete the 5λ bulk resonant cavity. A SEM

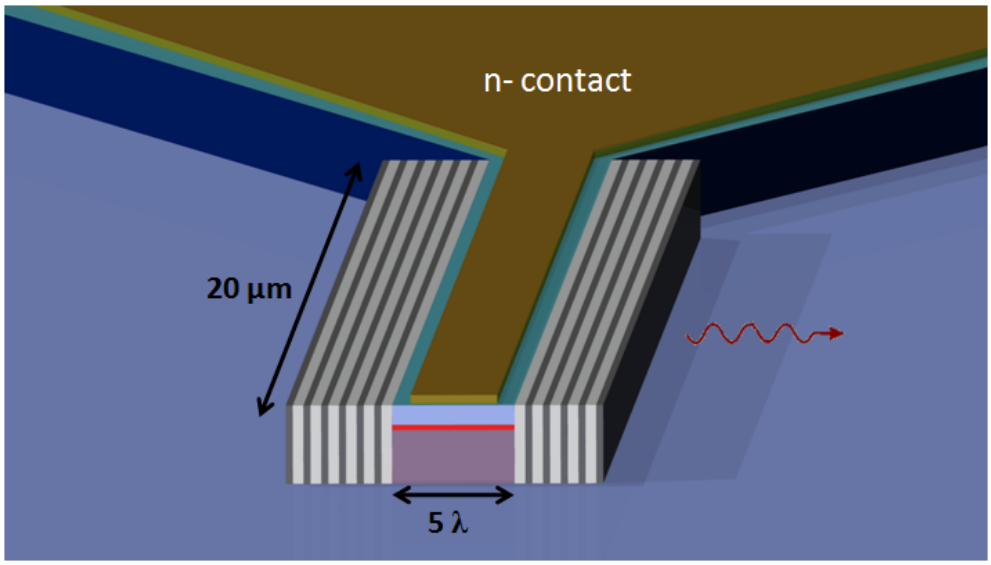

Fig. 4.7 A schematic representation of the GaAs-based SQW microcavity diode.

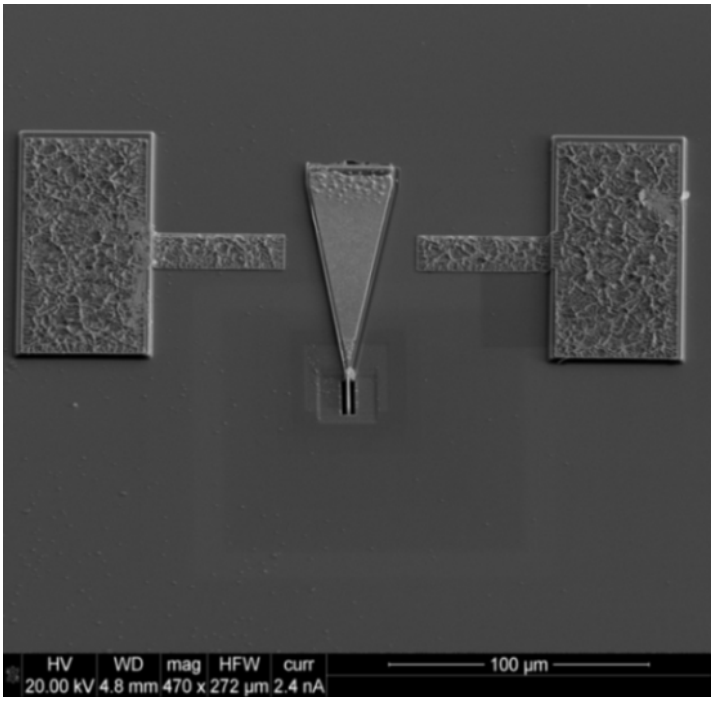

Fig. 4.8 SEM image of the fabricated device along with the contact pads.

image of the completed device, along with the contact pads, is shown in Fig. 4.8.

4.6 Device Characterization

4.6.1 Microcavity and Diode Characteristics

The diode current voltage (I-V) characteristics, measured using a semiconductor characterization system, is shown in linear and logarithmic scales in Fig. 4.9(a). A low reverse leakage current of 5.23 x 10^{-10} A and a diode series resistance of 8.92 Ω is observed in the I-V characteristics. The quality factor (Q) of the microcavity is derived by micro-photoluminescence measurements at room temperature. In this measurement, the microcavity is excited non-resonantly with a frequency tripled (λ=266 nm) Ti:Sapphire laser. The same objective lens is used to focus the laser beam onto one facet

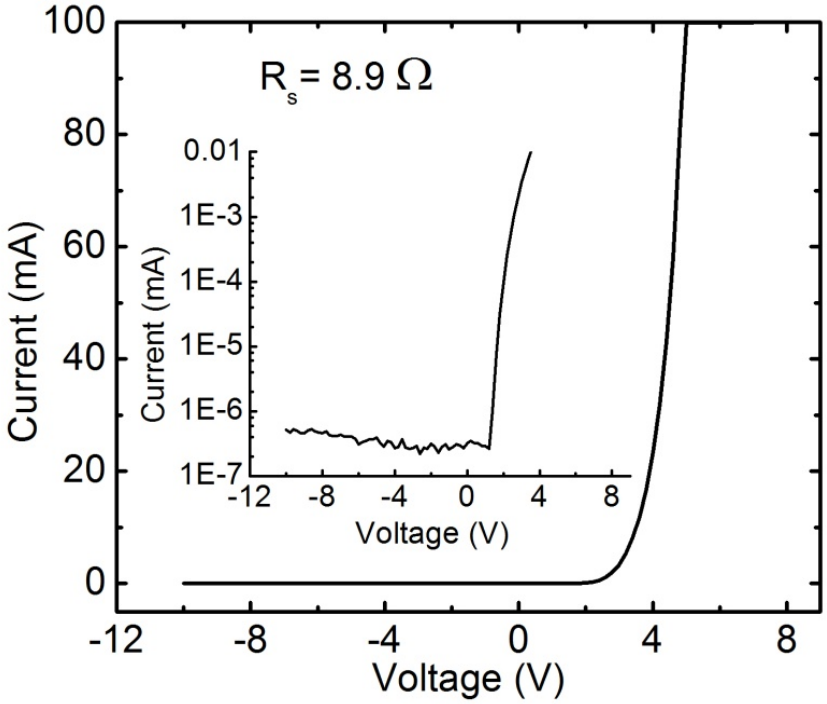

(a)

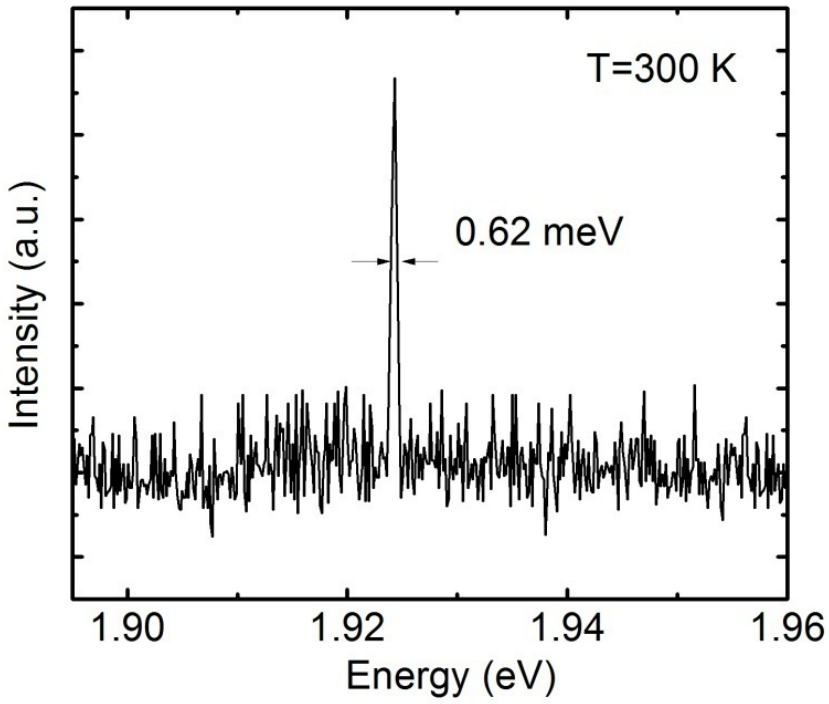

(b)

Fig. 4.9 (a) Current-voltage characteristics of the microcavity diode (the inset shows the I-V characteristics in logarithmic scale), (b) measured micro-PL spectrum from the microcavity.

of the microcavity diode and to collect the photoluminescence signal and then convey it to the monochromator using achromatic doublet lenses. As shown in Fig. 4.9(b), the cavity mode linewidth at $E_c = 1.9161$ eV (647.03 nm) is $\gamma_c = 0.62$ meV (0.2094 nm). This corresponds to a cavity quality factor of ~3091 and a corresponding cavity mode lifetime of τ_c=1.06 ps. Polarization selection rules indicate that quantum well excitons couple to TE-polarized cavity photons [135].

4.6.2 Strong-Coupling Characteristics

The polariton dispersion characteristics are determined from angle-resolved electroluminescence (EL) spectra measured under low forward bias current density at 155 K. The detection angles in this measurement are varied in a plane perpendicular to the growth axis. Figure 4.10 shows EL spectra recorded up to a maximum detection angle

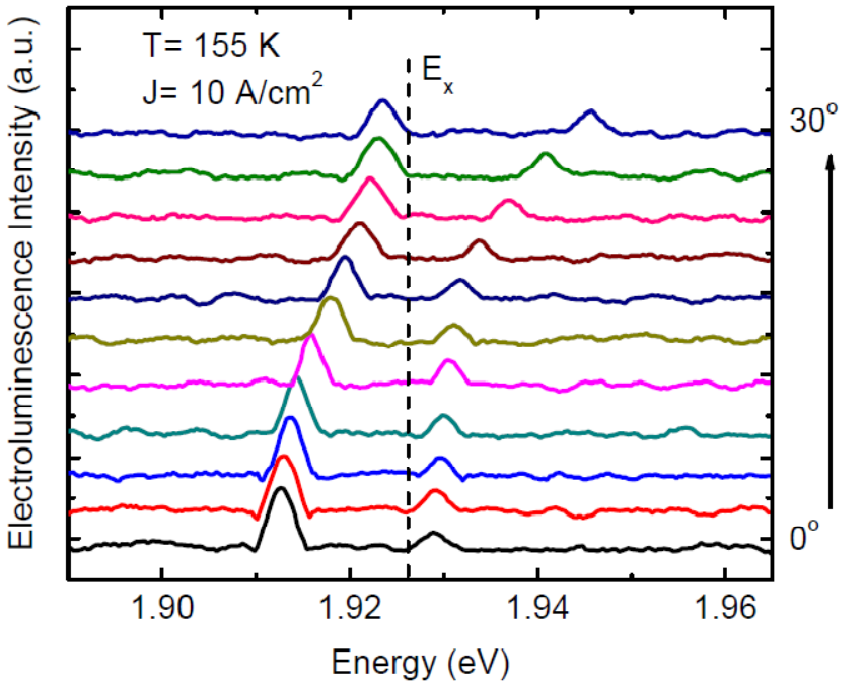

Fig. 4.10 Angle resolved electroluminescence spectra measured at T=155 K.

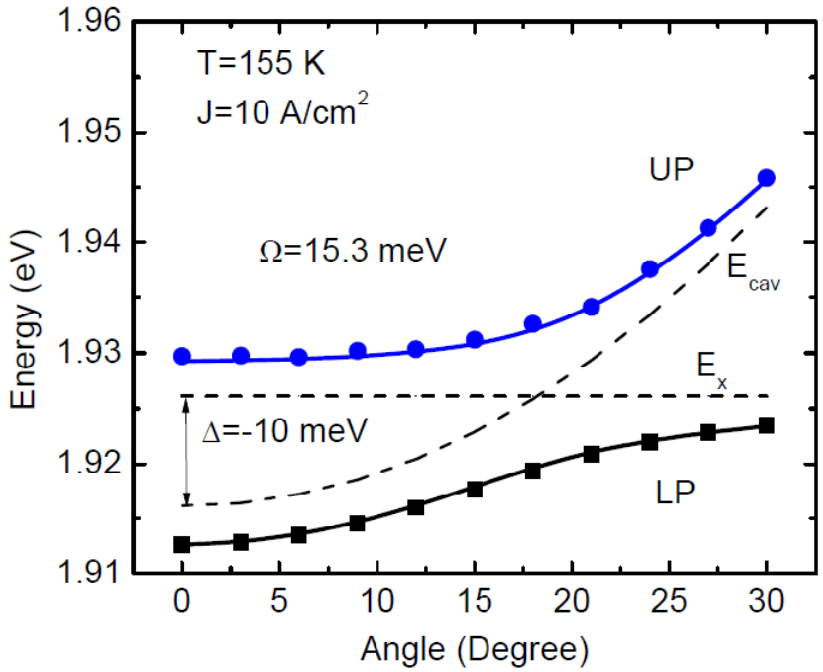

Fig. 4.11 Polariton dispersion calculated using coupled harmonic oscillator model alongside the measured data.

of 30^o , where the direction normal to the DBRs is considered to be 0^o. The peak below the exciton resonance energy and asymptotically approaching this energy at higher angles is identified as the lower polariton (LP) transition. The weaker peak above the exciton resonance is identified as the upper polariton (UP) transition. Using the one-to-one correspondence between the angle of the out-coupled photon and the in-plane wave number of the polaritons, we obtain the polariton dispersion relations shown in Fig. 4.11 together with the measured exciton and cavity photon energies. This data is analyzed with a 2x2 coupled harmonic oscillator model, using an exciton linewidth γ_x= 8.3 meV and γ_c= 0.62 meV. A cavity-to-exciton detuning δ = -10meV and Rabi splitting Ω_{VRS} = 15.3 meV are derived from the analysis. The depth of the energy trap formed by the LP branch in momentum space is ~13.6 meV, which is larger than the k_BT value at 155 K.

4.6.3 Polariton Lasing Characteristics

Electroluminescence from the device is measured in the normal direction (normal to the DBR mirror) as a function of cw forward bias. A distinct nonlinear threshold is observed in the light-output at a current density of 90 A/cm^2, as shown in Fig. 4.12. The subtreshold slope in the measured emission characteristics is 0.97 whereas above the nonlinear threshold, the slope is 3.2. The nonlinear threshold is accompanied by a steep reduction of linewidth of the LP emission, also depicted in Fig. 4.12. The LP coherence time of ~4.9 ps, corresponding to the minimum linewidth of 0.85 meV (0.2841 nm) is larger than the LP radiative lifetime, $\tau_{LP} = \tau_C / \left|C_{k_{\|}=0}\right|^2$ =1.3696 ps. Beyond 100 A/cm^2, the emission linewidth increases again. The blueshift of the LP emission peak at the onset of

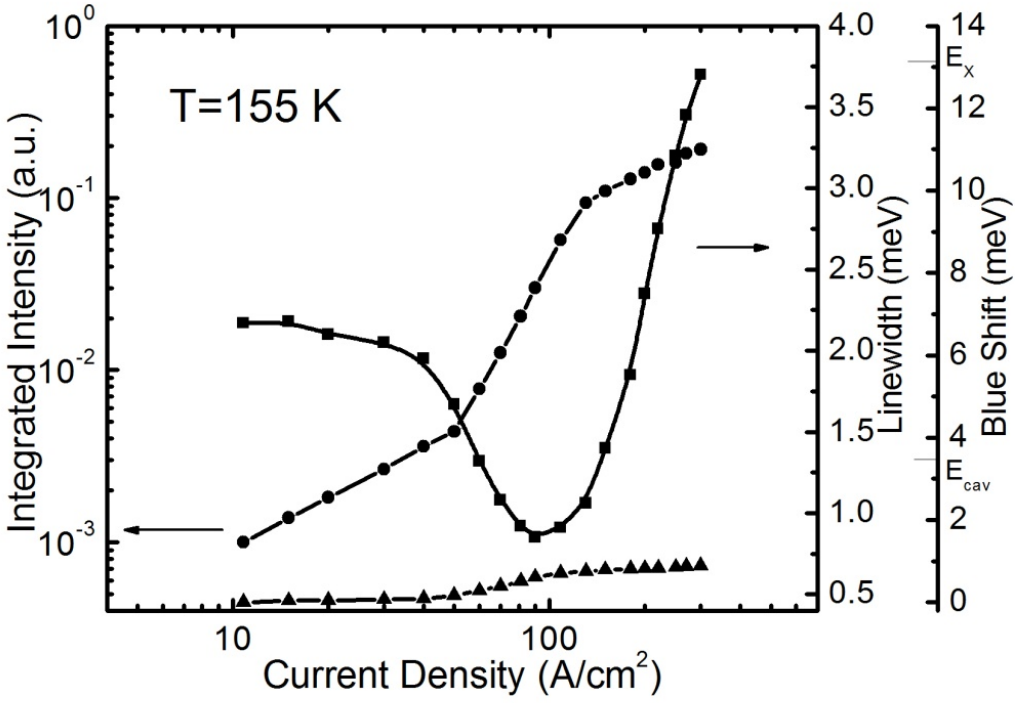

Fig. 4.12 Integrated EL intensity, LP emission linewidth and blue shift of LP peak emission as a function of injected current density.

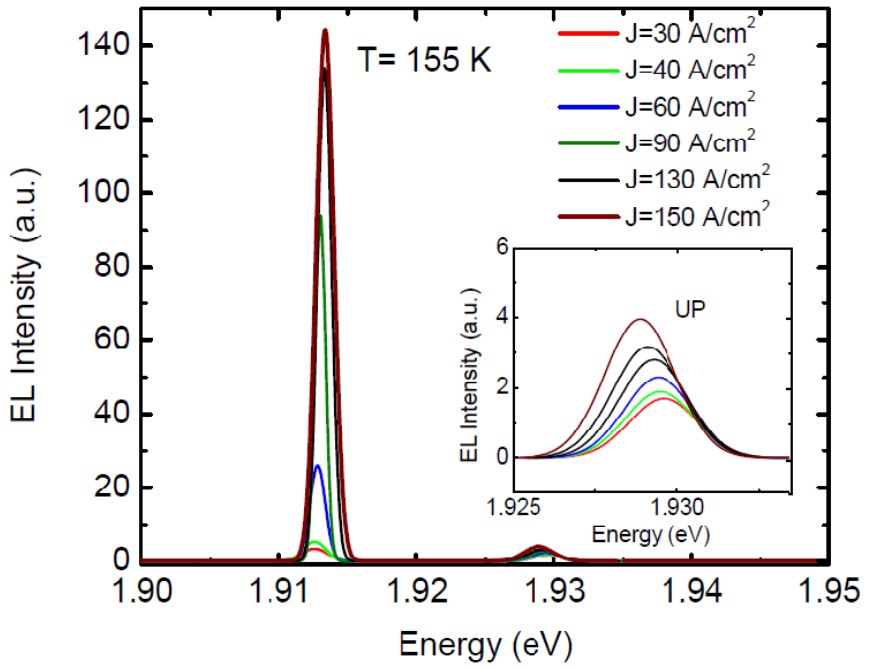

(a)

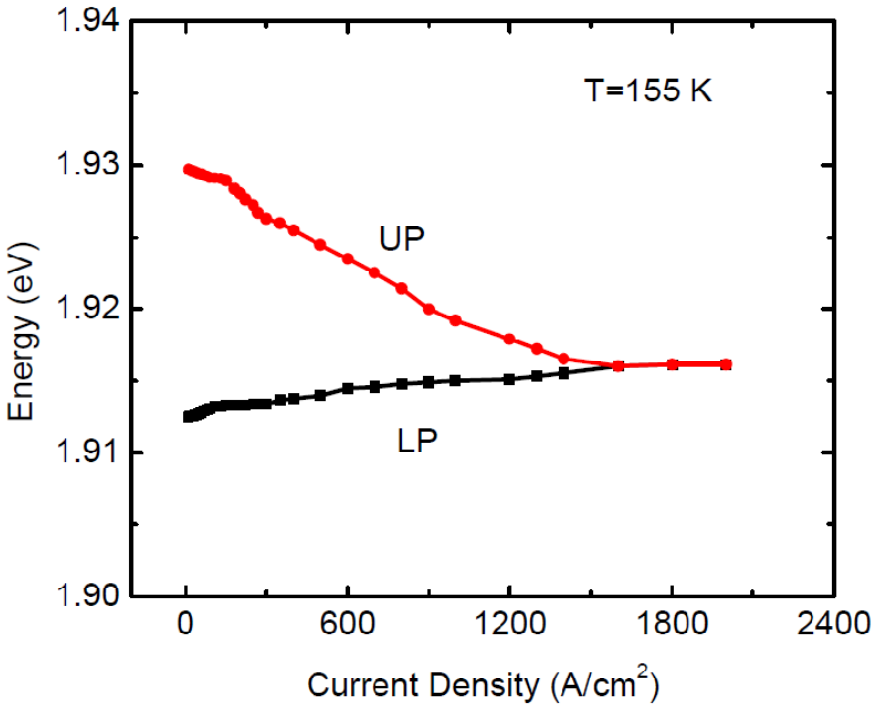

Fig. 4.13 (a) EL spectra measured at various injection levels. Inset shows the magnified UP region; (b) LP and UP peak emission energies at higher injection levels showing the onset of the weak coupling regime.

polariton lasing is a signature of the enhanced polariton-polariton scattering.. The measured blueshift for LP emission is ~0.89 meV (Fig. 4.12). The polariton spectral characteristics are shown in Fig. 4.13(a), where both the LP and UP transitions are visible at all injections. With further increase of injection current and using a pulsed mode bias beyond 500 A/cm^2 , the data shown in Fig. 4.13(b) and 4.14 are recorded. Under these conditions, the coupling strength between the excitons and photons decreases because of reduced exciton oscillator strength resulting from phase-space filling [96]. As a results, the two polariton peaks gradually merge into a single transition, signaling the onset of the weak coupling regime. Furthermore, a second threshold is observed at ~32 kA/cm^2 (Fig. 4.14), which is ascribed to photon lasing mediated by population inversion and stimulated emission. The linewidth of the emission for photon lasing is ~2.4 meV (0.80 nm).

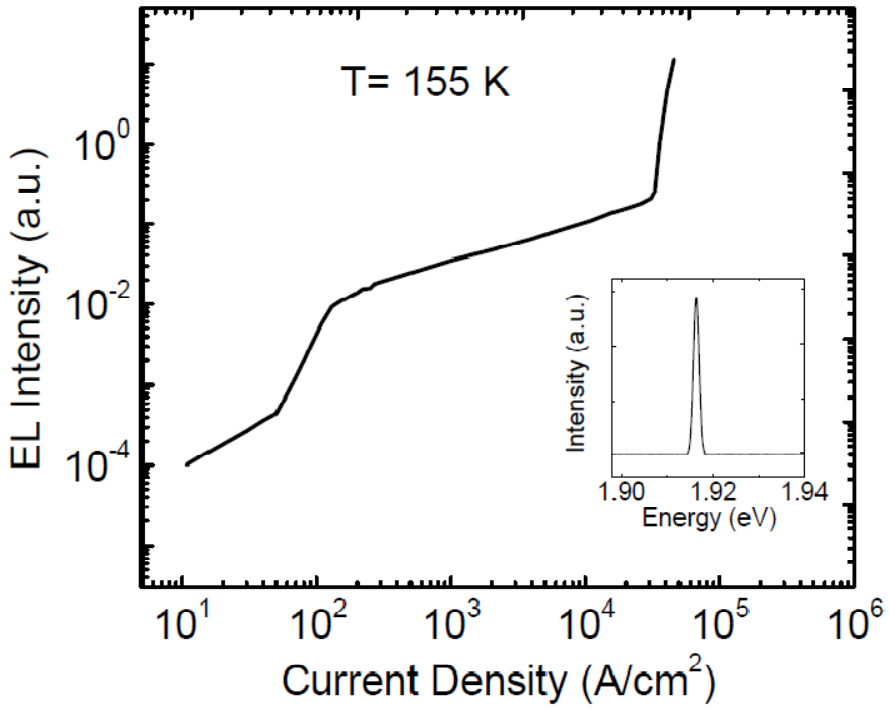

Fig. 4.14 Two threshold lasing behavior with the non-linearities due to both polariton and photon lasing. Inset shows EL spectra measured above photon lasing.

and the peak emission energy coincides with the cavity mode, as shown in the inset to Fig. 4.14. The LP density is related to the injection current density by the relation $n_{LP} = J\tau / q$ where τ is the total exciton lifetime. Using this relation, the polariton density at the non-linear threshold is ~2.63 x 10^{11} cm^{-2}. The polariton density at which this system transitions to the weak coupling regime, is derived from the data of Fig. 4.13(b) to be 4.5 x 10^{12} cm^{-2}, which is ~17 times larger than the threshold density.

4.6.4 Momentum Space Distribution and Spatial Coherence

To ascertain that the observed first non-linear threshold in the emission characteristics is due to dynamic Bose condensation, we measured the LP population distribution in k-space at different injection levels by angle-resolved EL. The occupations in k-space, derived from the measured emission intensities at 155 K, are plotted in Fig. 4.15. The occupation is characterized by a non-thermal random distribution below

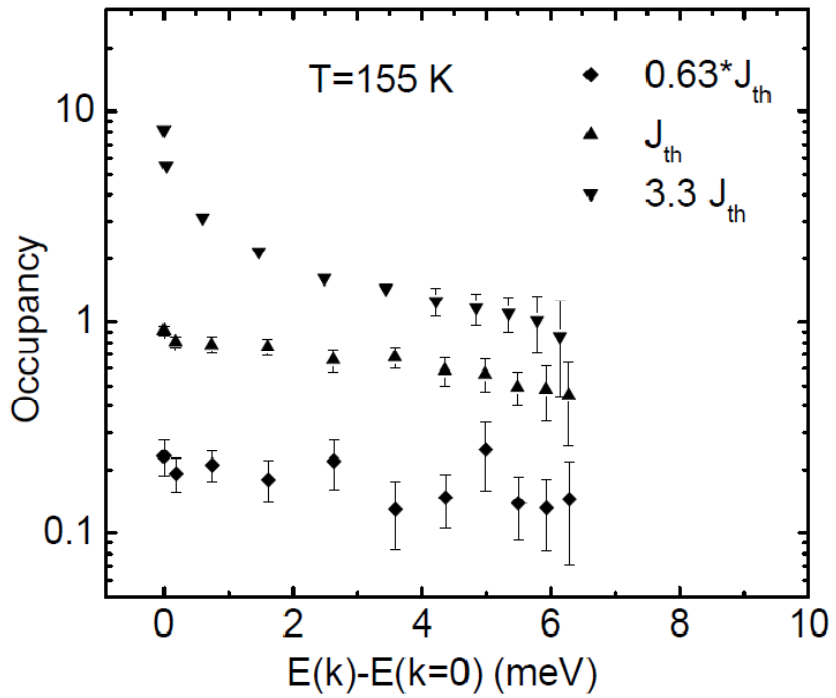

Fig. 4.15 LP ground state occupancy for different $k_{||}$ states obtained at three injections.

threshold and a Boltzman-like distribution at threshold. A bimodal distribution and strong peaking of the occupation at and near $k_{||} = 0$ is observed for injection above threshold. There is no signature of an energy relaxation bottleneck at any injection level. At $J = J_{th}$, the occupancy is analyzed with the Boltzmann thermal distribution, which is $N = N_0 \exp\left(-\left(E(k_{||}) - E(0)\right)/k_B T_{LP}\right)$. Here $E(k_{||})$ is the LP energy at $k_{||}$, N_0 is the occupancy at $k_{||} = 0$ and T_{LP} is the LP temperature. According to our analysis, the LP temperature at threshold is T_{LP}=190 K.

The spatial coherence properties of the polariton emission have been measured with a Mach-Zehnder interferometer. The visibility of the observed fringes is plotted in Fig. 4.16 as a function of displacement (x) between the two identical images of polariton emission. A value of 47% is obtained for J= 1.8 J_{th}, whereas below threshold (at J=0.8 J_{th})

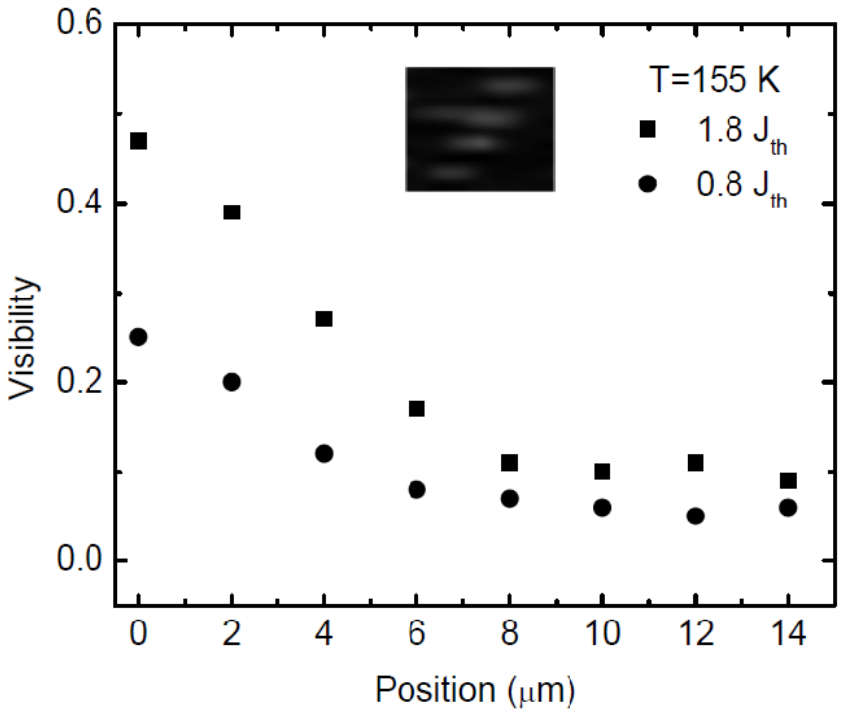

Fig. 4.16 Interference visibility as a function of the displacement (x) between the double image of the polariton emission. Inset shows interference pattern for x = 2 μm;

the visibility decreases to 25%. The full width at half maximum (FWHM) of the distribution above threshold gives an estimate of the spatial coherence length or size of the condensate, which is found to be ~3.8 μm.

4.7 Towards Room Temperature Operation

As has been discussed in the previous section, the exciton binding energy in a GaAs-based system can be significantly enhanced by increasing the Al-mole fraction in the quantum well. To this end, an experimental study has been performed to explore the possibility of realizing a GaAs-based room temperature polariton laser diode using a $Al_{0.41}Ga_{0.59}As/Al_{0.71}Ga_{0.29}As$ single quantum well.

4.7.1 Device Heterostructure

A schematic of the device heterostructure used in this study is shown in Fig. 4.17. The heterostructure, which is grown by MBE on (001) GaAs substrate, consists of a single $Al_{0.41}Ga_{0.59}As/ Al_{0.71}Ga_{0.29}As$, quantum well. According to Fig. 4.1(a), the well

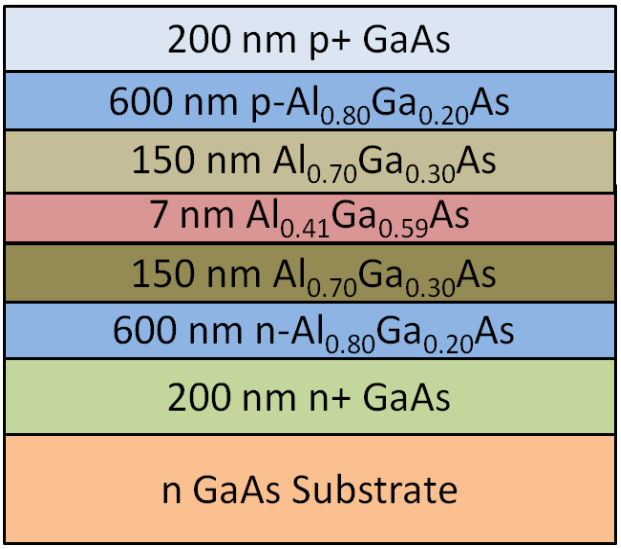

Figure 4.17 A schematic of the $Al_{0.41}Ga_{0.59}As/Al_{0.71}Ga_{0.29}As$ SQW p-i-n heterostructure;

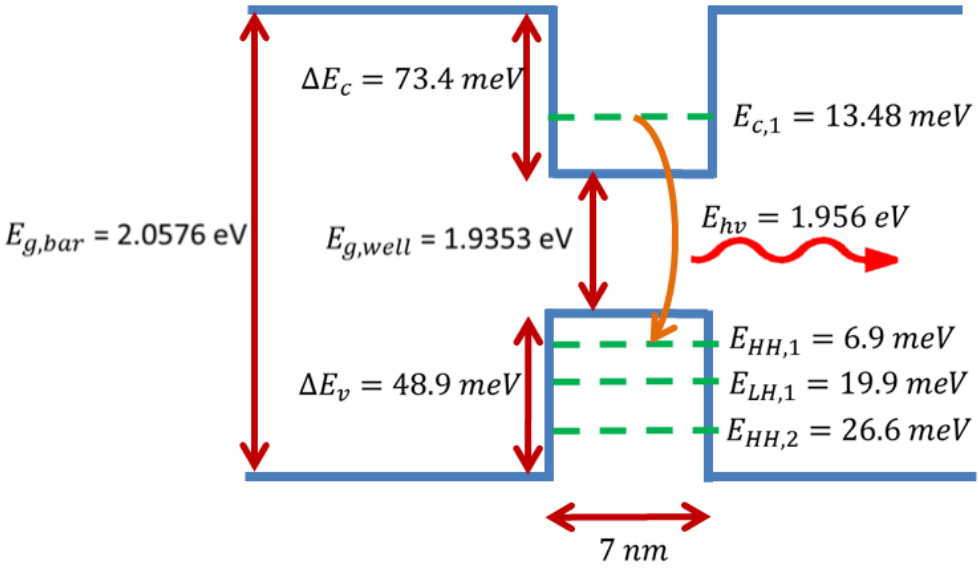

Figure 4.18 Analyzed electronic states of the $Al_{0.41}Ga_{0.59}As/Al_{0.71}Ga_{0.29}As$ SQW.

region of this heterostructure is a direct bandgap material, whereas the barrier is an indirect bandgap semiconductor. The conduction and valence band offsets here are ~0.072 eV and~0.048 eV respectively, assuming $\Delta E_c = 0.6\Delta E_g$. To maximize the exciton binding energy, the quantum well width of the active region is designed to be 7 nm. In order to minimize inhomogeneous broadening, only a single quantum well (SQW) has been employed in the heterostructure. The 160 nm $Al_{0.41}Ga_{0.59}As$ layer, along with the $Al_{0.31}Ga_{0.69}As$ single quantum well (SQW) in the center, serves as the waveguide of the device. The waveguide region is surrounded by 600 nm p- and n-doped $Al_{0.6}Ga_{0.4}As$ layers, which provide optical confinement. An effective refractive index of ~3.3 is obtained from transfer matrix method based analysis. The heavily doped p- and n-type GaAs layers are grown to facilitate low resistance ohmic contacts of the device. Figure 4.18 shows the analyzed electronic states of the designed heterostructure. $E_{c,1}$-$E_{hh,1}$ is expected to be the dominant excitonic transition in the SQW because of its larger oscillator strength. According to [136], the electron and hole effective masses

corresponding to these states are $0.1m_0$ and $0.592m_0$ respectively. These values correspond to a 3D exciton Bohr radius of 7.23 nm. Therefore, according to Eqn. 4.1, the exciton binding energy of an ideal $Al_{0.41}Ga_{0.59}As$/ $Al_{0.71}Ga_{0.29}As$ SQW is E_{1s} ~34 meV. Such a high exciton binding energy should facilitate the experimental observation of strong coupling and polariton lasing at or near room temperature.

4.7.2 Materials Characterization

Photoluminescence studies have been performed to study excitonic transition characteristics of the SQW. Because the exciting laser is significantly absorbed by the top cladding and contact layers, the MBE grown full heterostructure is initially carefully etched down to the top $Al_{0.71}Ga_{0.29}As$ barrier layer by ICP reactive ion etching in a BCl_3:Cl_2:Ar environment. Temperature and excitation dependent PL measurements have been subsequently performed to estimate the nature of the excitonic transitions.

4.7.2.1 Temperature Dependent Photoluminescence

Temperature dependent measurements have been performed by exciting the sample with a 405nm solid state laser. The sample is mounted inside a closed-loop Helium cryostat and the temperature is varied from 10 K to 110 K using a temperature controller having auto tuning capability. As can be observed in the measured temperature dependent PL spectra (Fig. 4.19(a)), two distinct emission peaks are observed at all temperatures. At T = 10K, the emission linewidth of the lower energy peak (peak I) is ~25 meV and the higher energy peak (peak II) is ~17 meV , as derived by multi-peak fitting based analysis (Fig. 4.19(b)). The energy difference between the two peaks is ~40 meV, which is smaller than the bandgap energy difference of ~120 meV between the

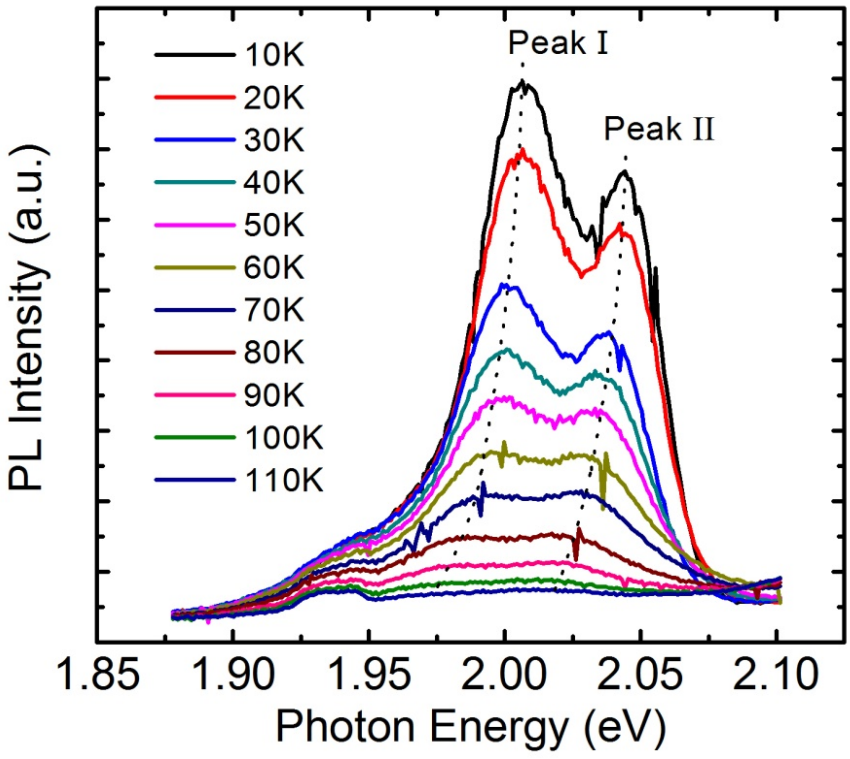

(a)

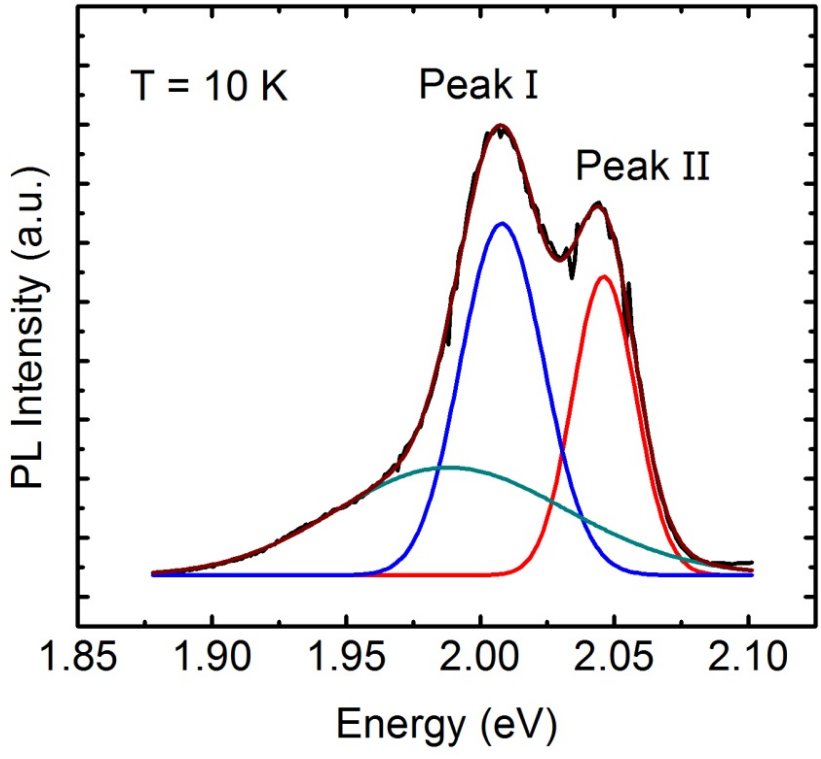

(b)

Fig. 4.19 (a) Measured temperature dependent PL spectra in the $Al_{0.41}Ga_{0.59}As/Al_{0.71}Ga_{0.29}As$ SQW, (b) multi-peak fitting based analysis.

well and barrier materials. The observed broad and weak emission between 2 eV - 2.02 eV may be attributed to surface states. According to Fig. 4.19(b), all the transitions in the measured PL spectra show a Gaussian lineshape instead of a Lorentzian, which is indicative of the presence of inhomogeneous broadening of the excitonic resonances. In Fig. 4.20, the emission energies of peak I and II are plotted as a function of temperature along with the analysis based on Varshni relation. As expected, both the peaks red-shift with increasing temperature because of lowering of the bandgap energy. However instead of a monotonic decrease, a slight S-shaped behavior is observed in the temperature dependence of the PL emission peaks. This S-shaped behavior is commonly attributed to the redistribution of carriers within the ensemble of localized states which may arise because of compositional inhomogenity in a material system having high Al mole-

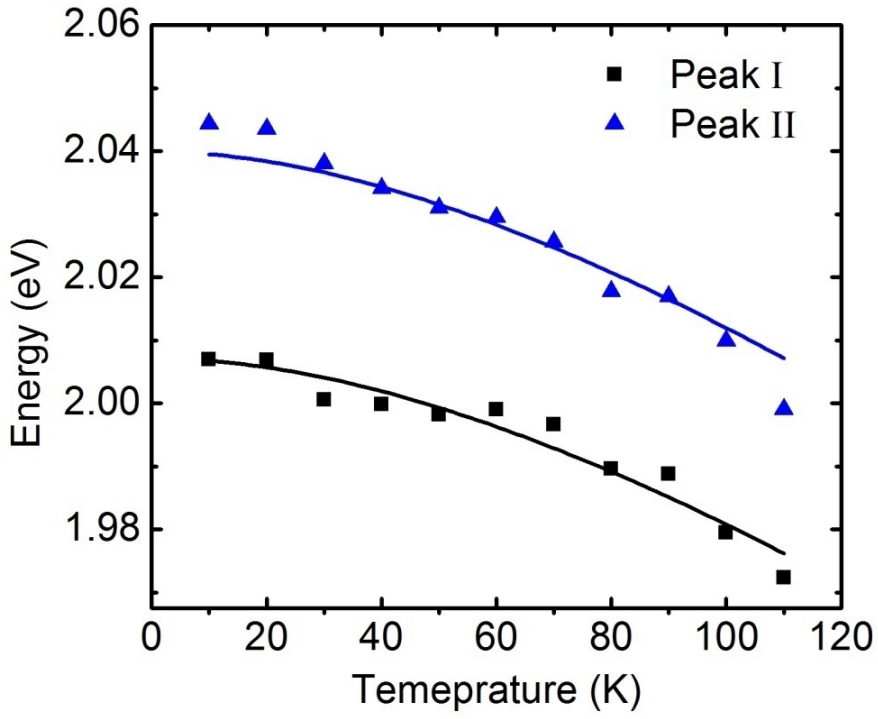

Fig. 4.20 Peak emission energies of peak I and II are plotted as a function of temperature along with the analysis based on Varshni relation.

fraction [137]. Radiative recombination, thermal escape and re-capture of the excitons in these localized states may have resulted such a non-monotonic decrease of the emission peak energy as the temperature is increased.

4.7.2.2 Excitation Dependent Photoluminescence

Excitation dependent photoluminescence measurements have been performed at T = 15 K by exciting the prepared sample with a 405 nm solid-state laser. The excitation density has been varied from 0.7 to 7 mW using a neutral density filter. The measured excitation dependent PL spectra are shown in Fig. 4.21, where two distinct peaks are observed at all excitation densities. It is also noteworthy that both the peaks blueshift as the excitation density is increased. This is further illustrated Fig. 4.22, where a maximum

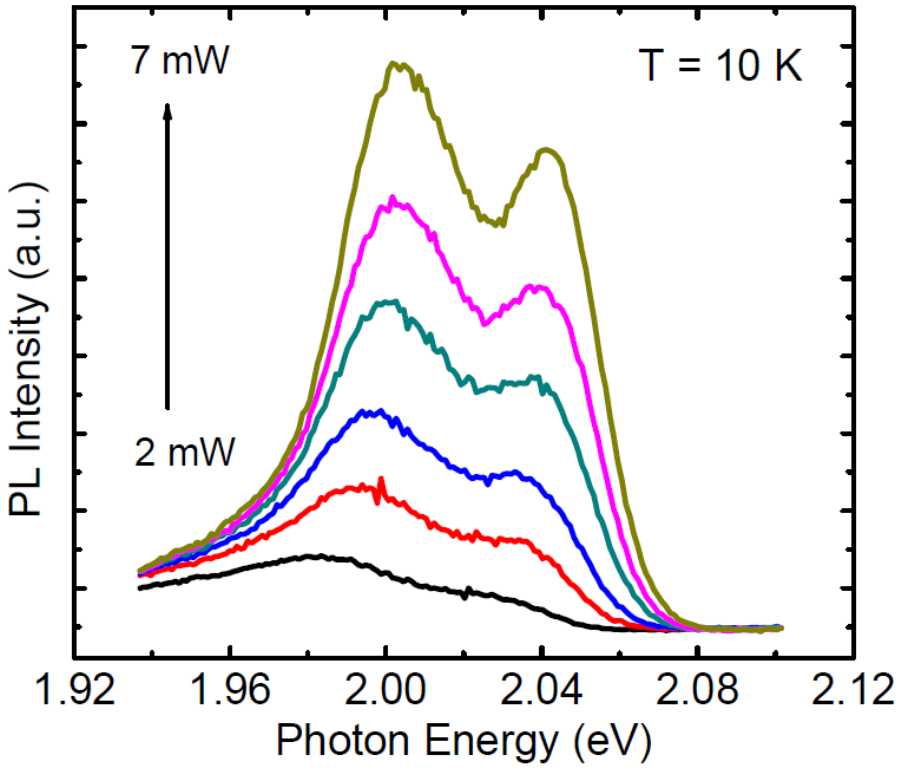

Figure 4.21 Measured excitation dependent PL spectra at T=15 K.

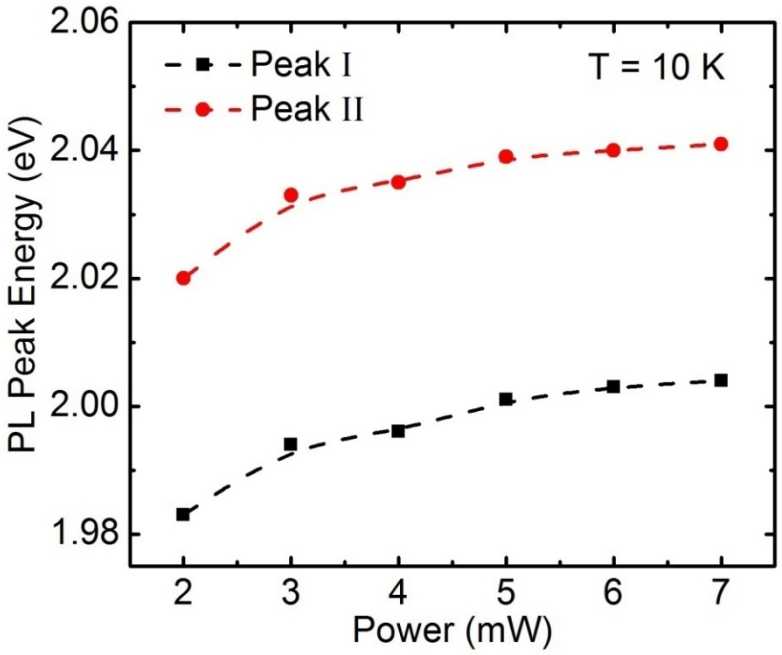

Fig. 4.22 PL peak energy values plotted as a function of the excitation power.

blueshift of ~20 meV is measured for both the peaks. Such a shift of the peak emission energy may be related to the filling of higher energy bound excitonic states of the SQW. It is noteworthy that the free exciton energy is usually observed to remain invariant with excitation if the pumping density is kept below the saturation density. In Fig. 4.23, the integrated PL intensities corresponding to both the peaks are plotted as a function of the optical excitation density. A linear dependence on the excitation is observed for both the peaks using the relation $I \propto P^n$, where I is the integrated intensity and P is the pumping density. Though such a dependence is usually associated with free excitons, it has been reported that depending on the excitation density, $n \geq 1$can be observed for donor and acceptor bound excitonic transitions as well [138]. The dominance of bound excitonic transitions over free excitons may preclude the observation of strong-coupling in a semiconductor microcavity.

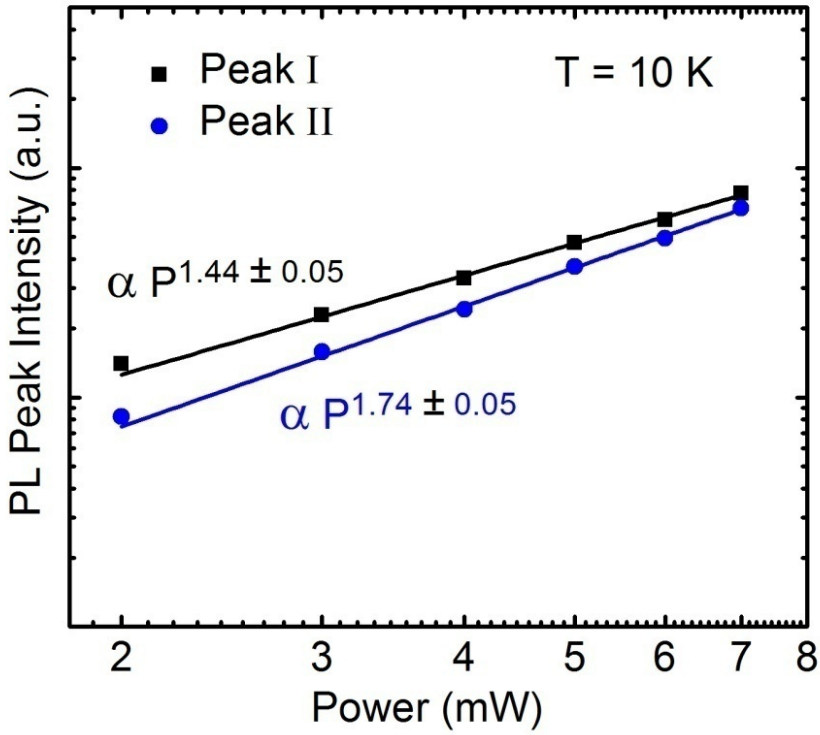

Fig. 4.23 Measured excitation dependent PL spectra of the $Al_{0.41}Ga_{0.59}As/Al_{0.71}Ga_{0.29}As$ SQW at T=15 K

4.7.3 Device Characterization

In order to study the electrical and electroluminescence characteristics of the SQW heterostructure, a microcavity diode has been fabricated based on the same edge-emitting geometry discussed in section 4. All measurements on this device have been performed under cw electrical excitation at room temperature. From the measured current-voltage characteristics (Fig. 4.24), the series resistance of the microcavity diode is ~8.9 ohms and the device turn on voltage is ~3.5V. Figure 4.19 shows the measured EL spectra, which were recorded for emission normal to the DBR mirrors. In contrast to the measured low temperature PL, only a single peak is observed at all injections in the measured EL spectra. This indicates thermal dissociation of the bound exciton at room temperature. The peak emission energy of the measured EL is ~620 nm, which is in good

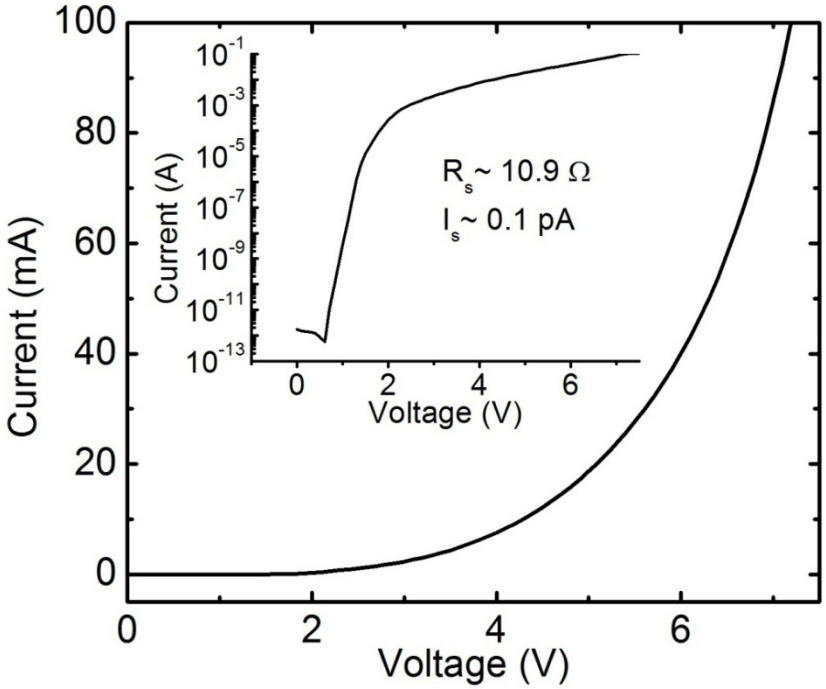

(a)

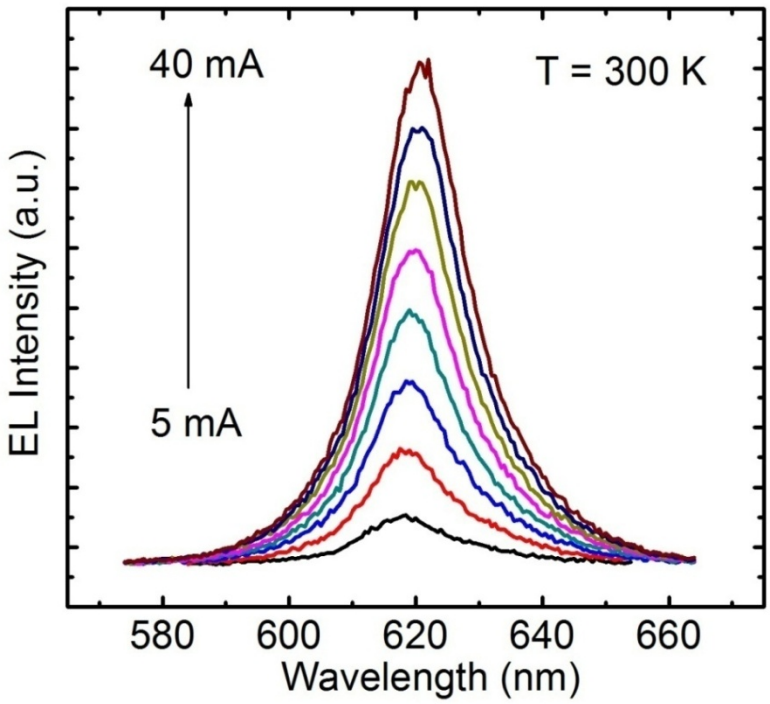

(b)

Fig. 4.24 (a) Current-voltage relations of several devices fabricated using the SQW p-i-n heterostructure,(b) measured room temperature EL spectra from the microcavity diode fabricated using the $Al_{0.41}Ga_{0.59}As/Al_{0.71}Ga_{0.29}As$ SQW.

agreement with the results obtained from our analysis shown in Fig. 4.24(b). The minimum measured linewidth of the EL emission is ~27 meV. It is possible that multivalley scattering effects in the vicinity of the direct-to-indirect bandgap transition of the quantum-well material system results in inhomogeneous broadening of the free excitonic transition. Furthermore, the dominance of bound excitonic transitions, as observed from low temperature PL measurements, is not favorable to exciton-photon coupling in a semiconductor microcavity. These factors may have precluded the observation of strong coupling and polariton lasing in this material system.

4.8 Summary

In conclusion, we present results on strong coupling and polariton lasing from a $Al_{0.31}G_{0.69}As/Al_{0.41}Ga_{0.59}As$ SQW microcavity diode. The exciton binding energy of this GaAs-based system has been enhanced significantly by reducing the quantum well width and by increasing the Al composition in the active region. Instead of the conventional surface emitting geometry, the device is realized with an edge-emitting structure, which enables the fabrication of a low resistance microcavity diode. Strong coupling and polariton lasing characteristics with a non-linear threshold of 90 A/cm^2 have been recorded at 155 K, with no observation of any polariton relaxation bottleneck. Photon lasing is also observed in the same device at higher injected current densities. In order to realize a GaAs-based room temperature polariton device, we have also presented our study of a $Al_{0.41}Ga_{0.59}As/Al_{0.71}Ga_{0.29}As$ SQW p-i-n microcavity heterostructure and diode. Localized defects, disorders, alloy broadening and/or multi-valley scattering effects may have degraded the free excitonic transition characteristics in this system to impede the observation of strong-coupling.

Chapter V

GaN-based Room Temperature Polariton Diode Lasers

5.1 Introduction

In spite of the relatively matured growth and fabrication technologies, room temperature operation of GaAs-based polariton laser diodes have remained elusive, mainly because of the low exciton binding energy of this material system. In this regard, wide bandgap materials like GaN and ZnO are potential candidates for high temperature operation because of their high exciton binding energies and oscillator strengths [139, 140]. As far as electrical pumping is concerned, GaN holds more promise than ZnO because of recent advancements in epitaxial growth, p-doping and fabrication of this material system. Moreover, because of emission in the UV regime of the electromagnetic spectrum, realization of a GaN-based polariton laser diode may usher towards the commercial development of an ultra-low threshold coherent light source which can have applications in biochemical analysis, photo-alignment of nematic liquid crystals, eye surgery, and other industrial applications [141-146]. In this chapter, we describe our study towards the experimental realization of a bulk GaN-based polariton laser diode which can operate at room temperature and detailed characterization of this device, including the output polarization. Whereas current planar GaN-based UV lasers have

threshold currents ~10 kA/cm^2 or higher [147], the polariton lasers realized in this work have threshold current densities in the range of 125 A/cm^2 to 375 A/cm^2. Photon lasing has been observed in the same devices having threshold current densities more than two orders of magnitude higher than those of the equivalent polariton lasers.

5.2 Background of GaN-based Polariton Lasers

GaN-based room-temperature optically excited polariton lasers have been designed with all-semiconductor or hybrid dielectric-semiconductor microcavities having bulk, quantum well, or nanowire active regions. Experimental realization of the first room-temperature GaN-based polariton laser was reported using a bulk active region, where SiN/SiO_2 and AlInN/AlGaN were used as the bottom and top DBRs respectively [60]. Enhanced strong-coupling with a large Rabi splitting of 56 meV has been demonstrated using a GaN/AlGaN multiple quantum well polariton laser [61]. Ultra-low threshold polariton lasing and Bose-Einstein condensation have been demonstrated using a single GaN-based nanowire embedded into all-dielectric microcavities [21, 68]. Optically pumped polariton laser has also been reported using a GaN nanowire array clad by Si_3N_4/SiO_2 DBRs [70]. In regards to electrical injection, it has been theoretically shown that bulk GaN-based microcavity diode offers the simplest solution towards realizing an electrically driven polariton laser [147]. A threshold current density of 50 A/cm^2 is estimated for this device and it has been predicted that this value can be further reduced by employing a multiple quantum-well based active region, which should offer better carrier confinement and higher exciton binding energy than the bulk. An InGaN/GaN multiple quantum well based electrically driven polariton laser has been theoretically predicted and analyzed by Iorsh et al. [148], where a threshold current

density of 6 A/cm^2 is calculated. More recently, a bulk GaN-based electrically pumped polariton laser has been demonstrated to operate at room temperature with a non-linear threshold of 169 A/cm^2 [82]. The reported device exhibits unambiguous evidence of strong-coupling and polariton lasing when operated under cw electrical bias. However, a detailed study of the small-signal modulation response and steady steady-state output polarization of GaN-based polariton laser diodes is yet to be reported.

The proposed GaN-based room temperature polariton laser diodes in [147, 148] are based on the vertical cavity surface emitting geometry, which poses several difficulties as far as experimental realization is concerned. The growth of high-quality GaN-based DBRs has been observed to be difficult, particularly because of large dislocation densities in the starting substrate, lattice mismatch between alternate pairs of DBRs and also the large number of pairs required to realize high-reflectivity mirrors. In general, nitride-based DBRs are realized using Al(Ga)N/(Al)GaN, AlInN/GaN and AlN/GaN. Among these material systems, AlN/GaN has the highest refractive index contrast and hence it requires the least number of DBR pairs. However, the hole thermal activation energy in Mg-doped Al(Ga)N increases significantly as the Al content is increased. This in effect reduces the p-region electrical conductivity and increases the device series resistance [148]. The heat-induced effects resulting from high series resistance are particularly detrimental to GaN-based VCSELs because of high thermal resistance of this material system. In regards to MQW based VCSELs, the built in polarization of GaN-based systems results quantum confined stark effect (QCSE) induced carrier leakage, which can significantly increase the threshold current density in a laser diode [149]. In order to overcome these difficulties of the GaN-based surface emitting

structure, an edge-emitting structure has been employed in this work where bulk-GaN is used as the active region and SiO_2/TiO_2 pairs are used to form the DBRs. The device, which is schematically shown in Fig. 3.4, can also be viewed as an *in-plane* vertical cavity surface emitting laser (VCSEL) or a very short-cavity Fabry-Pérot laser. Optical feedback and current injection are orthogonal to each other in this geometry, which eliminates many of the difficulties associated with a conventional VCSEL structure.

5.3 Device Heterostructure and Material Growth

The device heterostructure used in this study is schematically shown in Fig. 5.1. The active region of the microcavity diode consists of 300 nm undoped GaN, 300 nm

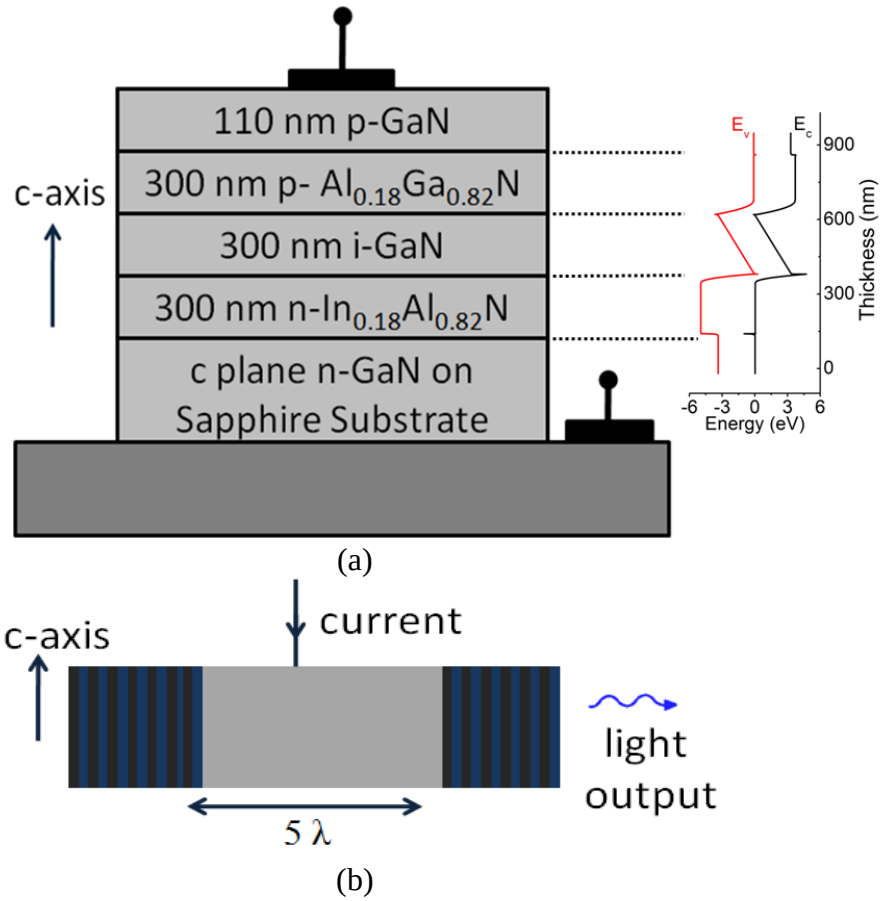

Fig. 5.1 (a) A schematic of the GaN-based polariton device along with the band diagram of the heterostructure (b) schematic representation of the edge emission geometry.

p (Mg) doped $Al_{0.10}Ga_{0.90}N$ and 110 nm p (Mg) doped GaN. The 300 nm n (Si) doped $In_{0.18}Al_{0.82}N$ layer is lattice matched to GaN and allows the growth of high quality epitaxial layers. Moreover, $In_{0.18}Al_{0.82}N$ has a high refractive index contrast with GaN, which enhances optical confinement. Also the large conduction band offset between $In_{0.18}Al_{0.82}N$/GaN lowers substrate leakage in the n-doped region. In the p-doped region, the $Al_{0.10}Ga_{0.90}N$ acts as an electron blocking layer because of its higher bandgap and also provides photon confinement because of its lower refractive index than GaN. Therefore, the $In_{0.18}Al_{0.82}N$ and $Al_{0.10}Ga_{0.90}N$ layers of this heterostructure form the lower and upper cladding respectively for bulk-GaN waveguide layer. The energy-band diagram, which is shown as an inset in Fig. 5.1(a), is obtained by self-consistently solving coupled Schrödinger-Poisson equations at zero applied bias, considering a conduction band offset of $\Delta E_c = 0.6\Delta E_g$, and Ga-polar c-plane (0001) GaN growth substrate [150].

Epitaxial growth of the heterostructure in this study is performed by plasma-assisted molecular beam epitaxy on c-plane GaN-on-sapphire substrate. In order to grow

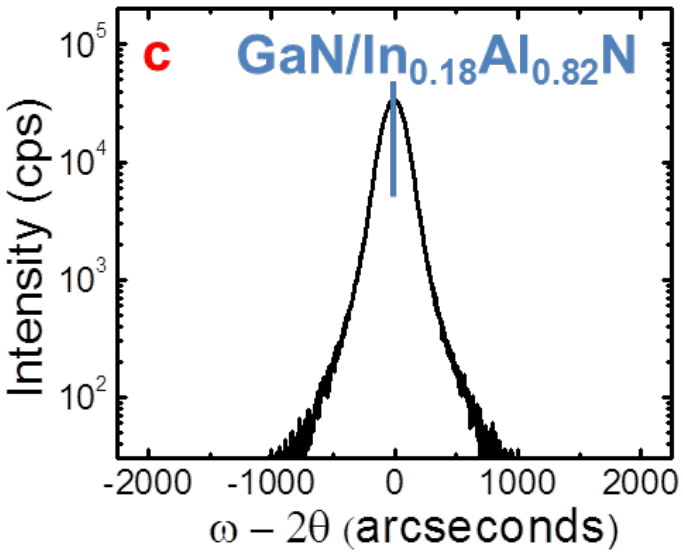

Fig. 5.2 XRD rocking curves for lattice matched $In_{0.18}Al_{0.82}N$/GaN epilayers [150].

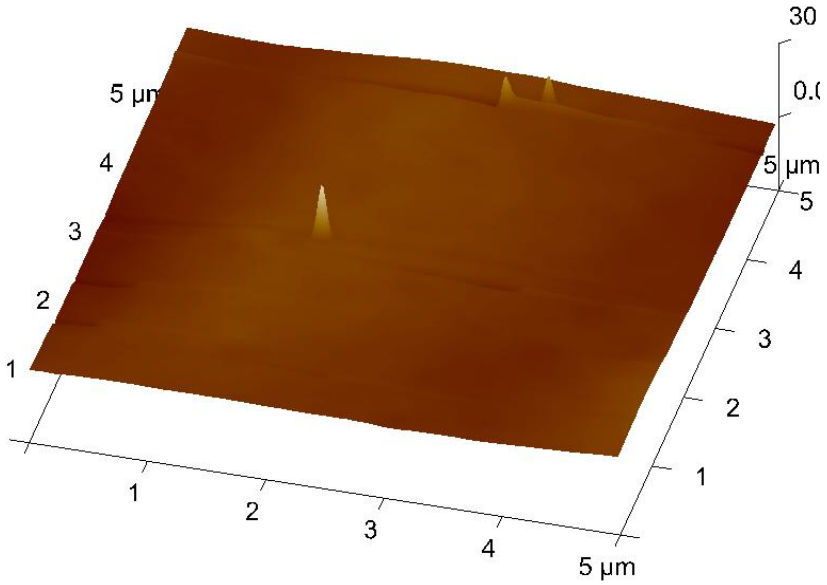

Fig. 5.3 AFM image of the surface of lattice matched $In_{0.18}Al_{0.82}N$ on GaN-on-sapphire substrate [150].

high quality epitaxial layers, the substrate temperature, the In and Al fluxes and the III/V ratios have been varied and optimized. The growth of lattice matched $In_{0.18}Al_{0.82}N$ layer is confirmed by x-ray diffraction measurements (Fig. 5.2). The smooth surface morphology of lattice matched $In_{0.18}Al_{0.82}N$ layer, as observed by AFM measurements (Fig. 5.3), facilitates the growth of low defect density, high quality GaN active region of the microcavity diode. As will be shown in the next chapter, the defect density in the active region is estimated to be of the same order as that of the starting substrate.

5.4 Photoluminescence Measurements

The excitonic transitions of the active region have been studied by photoluminescence measurements of c-plane GaN-on-sapphire using a 325 nm He-Cd laser at room and low temperatures. To ensure that the detection geometry of the sample is same as that of the microcavity diode, detection of the photoluminescence is done

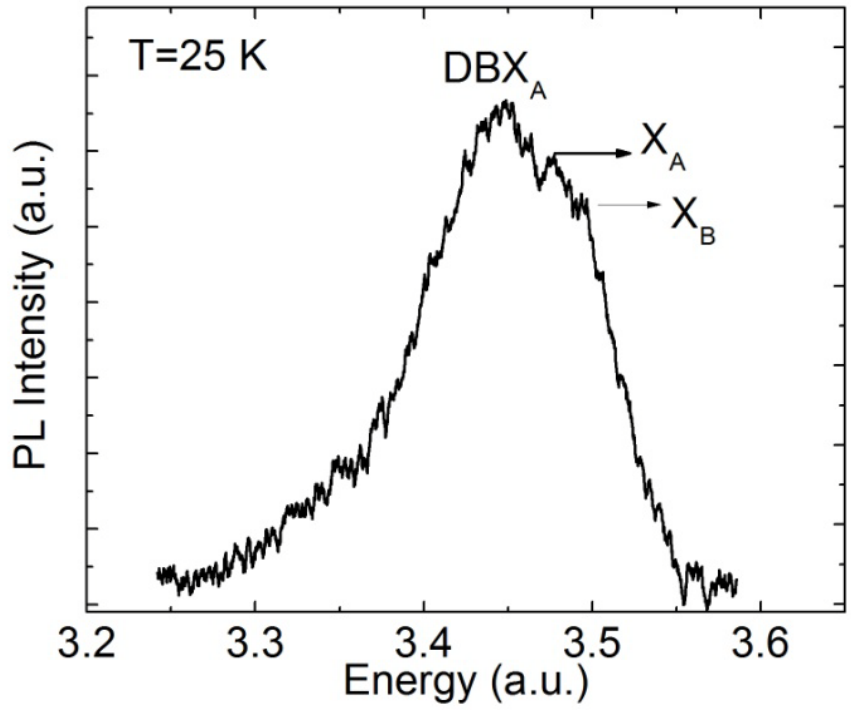

(a)

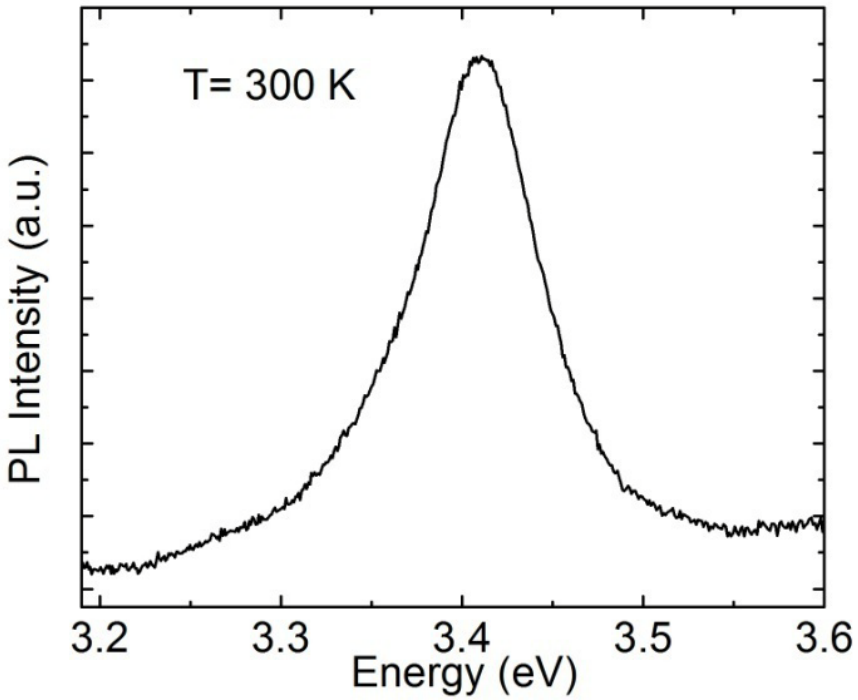

(b)

Fig. 5.4 Measured photoluminescence of c-plane bulk GaN on sapphire at (a) T=25 K and (b) room temperature

perpendicular to the c-axis. The PL spectra are recorded using a monochromator having spectral resolution of 0.03 nm and a high sensitivity photomultiplier tube. As shown in Fig. 5.4(a), low temperature PL spectra shows the free excitonic transitions X_A and X_B at 3.475 and 3.491 eV respectively. The X_A exciton transition is found to be dominant witha linewidth of 7.8 meV at T=25 K. Whereas X_B transition has been observed to be strong in some photoluminescence studies of bulk GaN, in our case the X_A transition is dominant, probably because the polarization is fixed by crystal defects [151, 152]. The donor bound exciton DBX_A is observed at 3.448 eV, whereas the weaker emission within a lower energy range of 3.36-3.43 eV may be attributed to the surface states [82]. At room temperature, the different exciton peaks merge to show a broad emission having a peak at ~3.418 eV (Fig. 5.4(b)).

In order to estimate the temporal dynamics of the free excitonic transition, time resolved photoluminescence measurements have been performed at room temperature using a frequency tripled Ti:Sapphire laser which has a repetition rate of 80 MHz and a

pulse width of 130 ps. The sample emission was spectrally filtered using a monochromator at the GaN excitonic peak and detected using a single photon avalanche photodiode with a response time of 40 ps. A measured PL transient is shown in Fig. 5.5. Analysis using the stretched exponential model, $I = I_o \exp\left[-\left(\frac{t}{\tau}\right)^{\beta}\right]$ shows a mono-exponential decay with a lifetime of $\tau = 710$ ps and $\beta = 1$. This indicates the absence of carrier depopulation due to carrier screening of the piezoelectric field or a degree of compositional fluctuations, both of which are expected to be absent in bulk GaN,

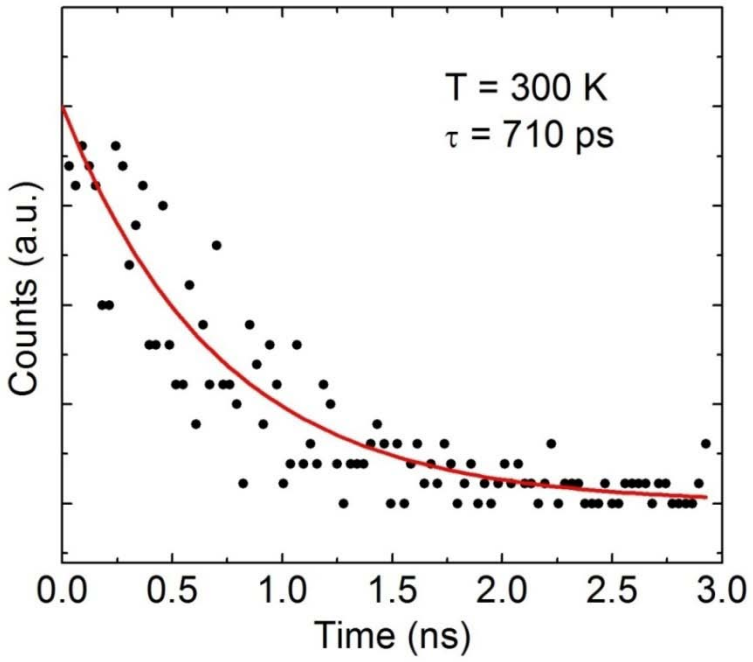

Fig. 5.5 Measured time resolved photoluminescence from bulk GaN at room temperature.

contrary to the case of single or multiple InGaN/GaN QW-based active region [133].

5.5 Device Fabrication

Device fabrication of the bulk-GaN microcavity diode is initiated by selective deposition of the Ni-Au (5nm/200 nm) p-contact by electron beam evaporation followed by rapid thermal annealing of the contact at 550^{o} C in air for two minutes. Next, a 1 μm x 40 μm density plasma under a Cl_2:Ar environment. The etch rate is calibrated to be ~4.5nm/s. The etching is followed by selective deposition of Ti/Au (10nm/200nm) by electron beam evaporation onto the n-doped substrate to form the n-contact. Prior to both p- and n-contact deposition, the native oxide is removed by a HCl:H_2O solution. To form the 690 nm (5λ) x 40 μm cavity, focused ion beam (FIB) etching is done on the previously defined 1 μm x 40 μm region. To ensure optically flat surfaces along the length of the cavity, a final FIB etching is conducted at very low injection. A scanning

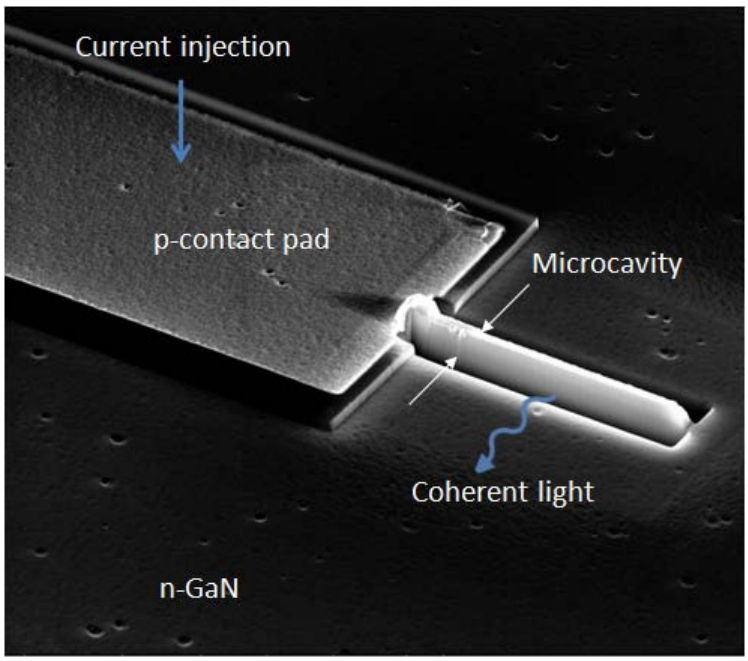

Fig. 5.6 SEM image of a FIB etched cavity along with the p-contact pad.

electron microscope (SEM) image of a 690 nm x 20 μm FIB etched cavity, along with the p-contact pad, is shown in Fig. 5.7. Finally, using electron beam evaporation, five and six pairs of SiO_2/TiO_2 distributed Bragg reflector (DBR) mirrors are deposited on opposite sides of the FIB etched facet. An average rms roughness of 2.2 nm is obtained from atomic force microscopy measurements of the dielectric stack. This leads to a reduction in the reflectivity by 0.4%.

5.6 Device Characterization

Several bulk GaN-based polariton laser diodes have been experimentally characterized in this study. All the measurements have been performed at room temperature. Also other than micro-photoluminescence measurements, all the measurements have been performed under electrical biasing. The results obtained from these measurements are discussed herein.

5.6.1 Diode and Microcavity Characteristics

The current voltage characteristics of the device at room temperature is shown in Fig. 5.7. The diode is characterized by a turn-on voltage of 4.5V and a series resistance of 27ohms. The leakage current of the diode is less than 2×10^{-8} A and the shunt resistance is ~5.5 MΩ. The carrier recombination rate across the diode is analyzed by self-consistently solving the Poisson equation and the electron and hole continuity equations. At an injection level of ~200 A/cm^2, (around the polariton lasing threshold), the electron-hole recombination takes place predominantly in the unintentionally doped GaN region and to a smaller extent in the p-GaN region [82].

To measure the quality factor of the microcavity, micro-PL measurement has been performed on the fabricated microcavity diode after DBR deposition. The microcavity

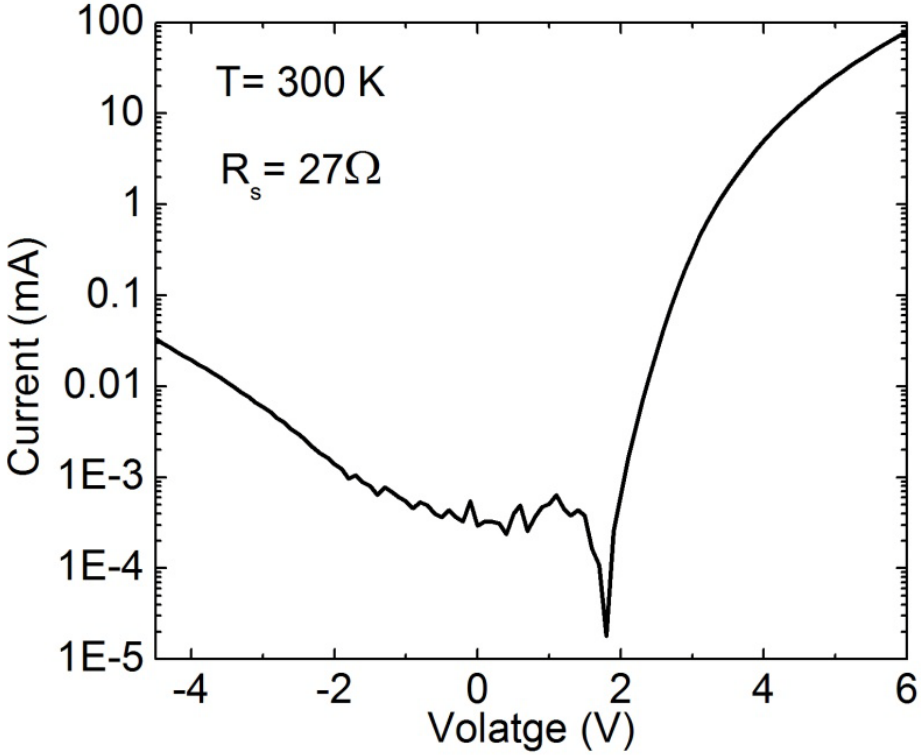

Fig. 5.7 Current-voltage characteristics of the device measured at room temperature.

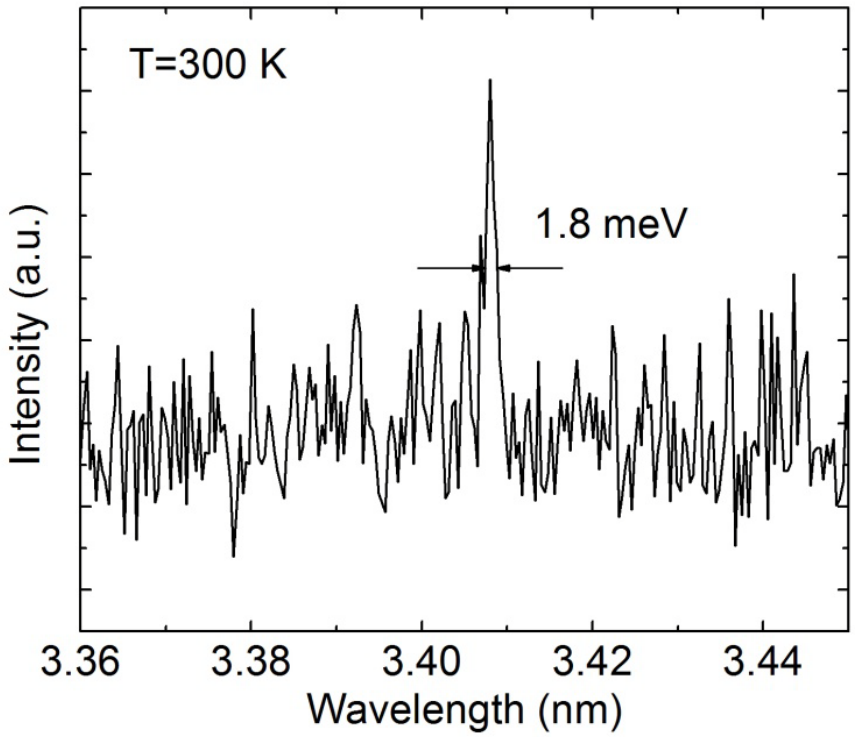

Fig. 5.8 Micro-PL of the microcavity diode measured at room temperature.

diode is optically excited non-resonantly with a frequency-tripled Ti-sapphire laser (λ=267 nm), focused to a spot size of ~50 μm in diameter on one facet of the device, along the axis of cavity resonance. The photoluminescence is collected from the other facet of the device and transmitted by an UV multimode optical fiber to a monochromator having a spectral resolution of 0.03 nm. Figure 5.8 shows the measured cavity resonance, which has a full-width-half-maximum of 1.8 meV and a peak energy of 3.408 eV. This corresponds to a cavity quality factor of ~1893 and a cavity photon lifetime of 0.366 ps. Such a high value of Q is considered to be necessary to achieve low injection polariton lasing and short-cavity photon lasing in this material system [153].

5.6.2 Strong Coupling Characteristics

To ascertain strong coupling in the bulk GaN-based microcavity diode, angle-resolved electroluminescence measurements have been performed under cw electrical injection below the polariton lasing threshold. In this measurement, the normal direction is considered to be perpendicular to the DBR mirrors and the measurements are done in the c-plane. As shown in the measured angle-resolved EL spectra (Fig. 5.9(a)), distinct lower polariton (LP) peaks are observed below the exciton energy (E_X = 3.408 eV) at all angles. At higher angles, the LP peaks tend to approach the exciton energy asymptotically. It is noteworthy that the upper polariton transitions are generally not observed in the polariton dispersion of microcavities with large bandgap bulk semiconductors, such as GaN and ZnO since these transition energies lie within or are very close to the conduction band continuum of states. As a result the transitions are broadened and not observed clearly [60, 67, 69, 154-156]. The polariton dispersion characteristics corresponding to the measured angle-resolved EL has been analyzed using the 2x2 coupled harmonic oscillator model considering strong coupling of the cavity photon to the X_A exciton. The dispersion characteristics is shown in Fig. 5.9(b), alongside the measured LP emission peak energies. The cavity-to-exciton detuning δ and the interaction potential or Rabi splitting, Ω are determined to be -7 meV, and ~32 meV, respectively. This splitting value is close to those reported for bulk GaN microcavities [151, 154-156]. From the dispersion, the spontaneous radiative recombination lifetime of the lower polaritons in is estimated to be $\tau_{LP} = \tau_c / |C|^2$ = 0.602 ps at $k_{||} = 0$.

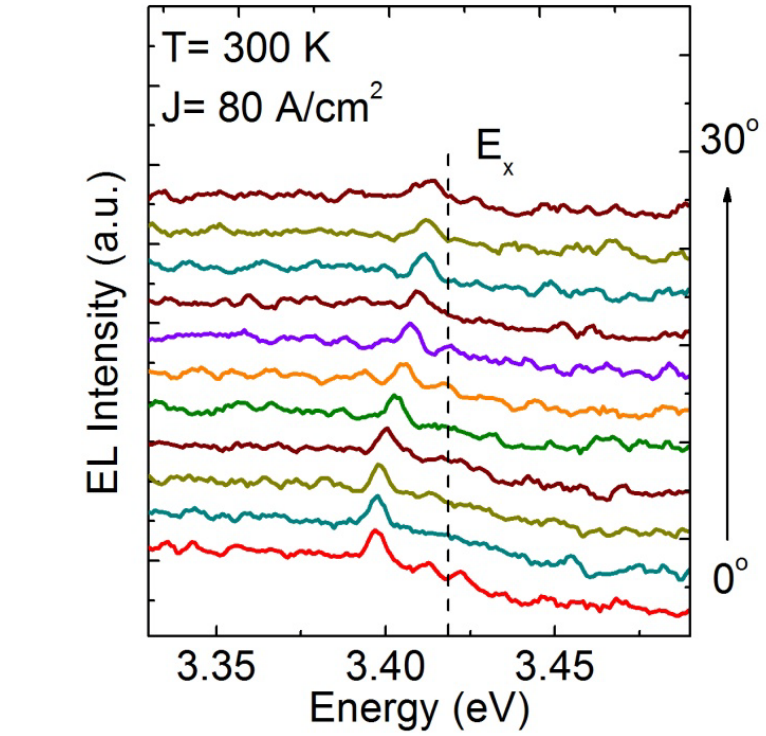

(a)

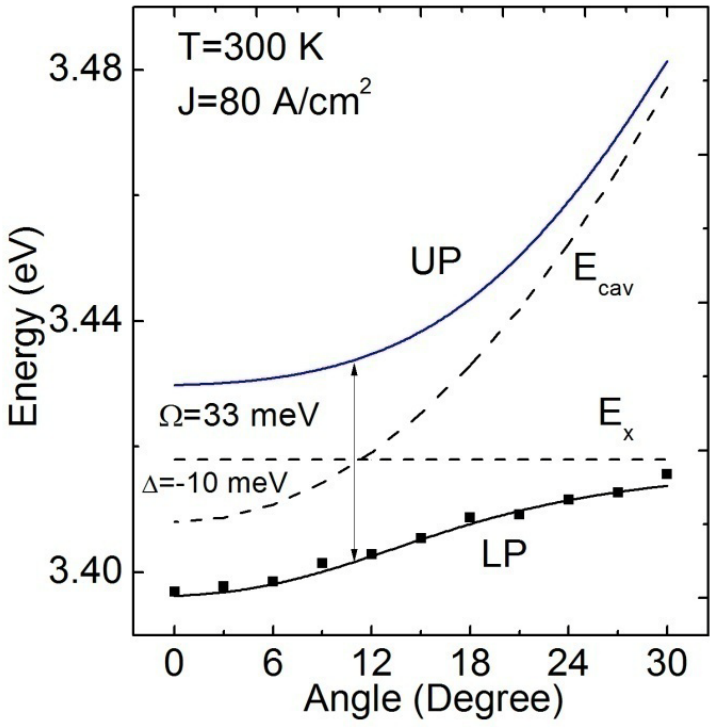

(b)

Fig. 5.9 (a) Five point moving average filtered angle-resolved electroluminescence measured from the microcavity diode at room temperature; (b) 2x2 coupled harmonic oscillator based analysis of the polariton dispersion along with measured data.

5.6.3 Polariton Lasing Characteristics

To investigate the nonlinear output characteristics of the GaN microcavity diode, the electroluminescence from the device is measured in the normal direction as a function of cw forward bias. The variation of integrated intensity with current is depicted in Fig. 5.10. The inset to this figure shows the output spectrum for 220 A/cm^2 forward current density. A distinct nonlinear threshold is observed in the characteristics at 190 A/cm^2 . However, it should be noted that the actual current through the microcavity region is much smaller. It may be noted from Fig. 5.10 that the slope of the light-current characteristics is sub-linear (~0.8) in the pre-threshold regime. We believe this behavior is due to non-radiative recombination and carrier leakage from the active recombination

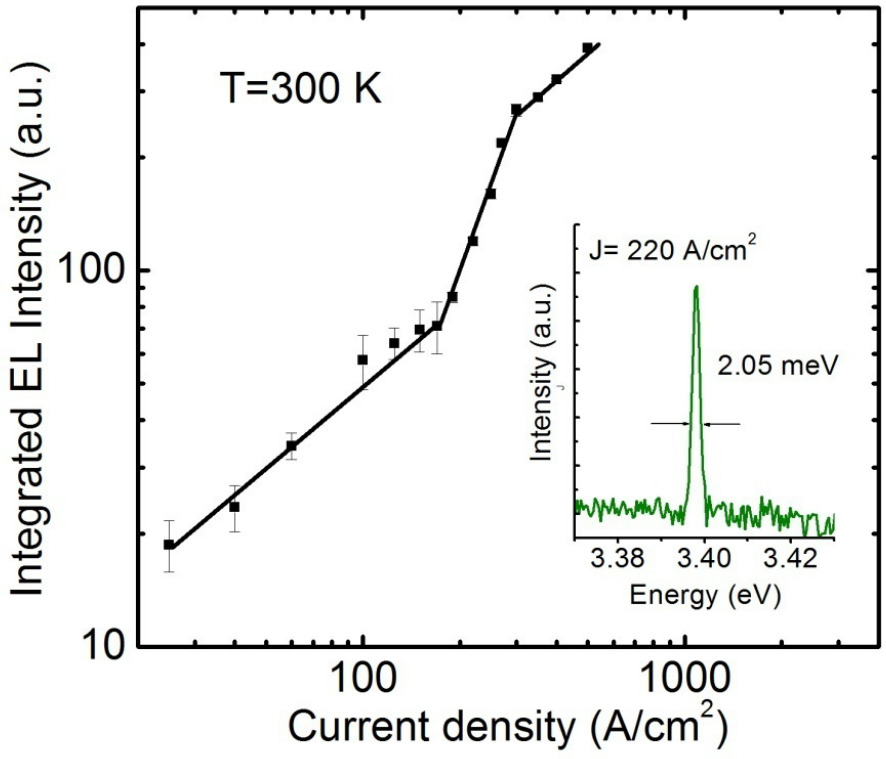

Fig. 5.10 Integrated EL intensity of the LP emission as a function of injected current density. Inset shows an EL spectra measured at an injection above the lasing threshold.

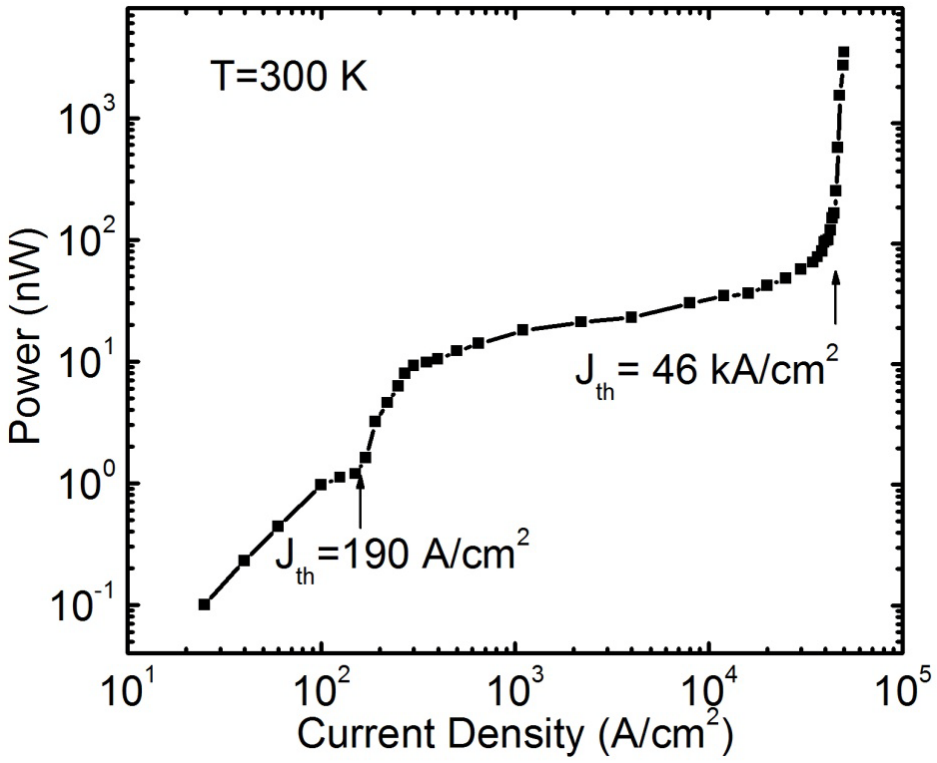

Fig. 5.11 Two threshold lasing behavior showing the non-linearities due to polariton and photon lasing. The threshold current densities of polariton and photon lasing are indicated by arrows.

region. The LP density at threshold is calculated to be $2.28\times10^{16}\,\mathrm{cm}^{-3}$ using the relation $n_{LP}^{th} = J_{th}\tau / qd$ where the exciton lifetime of $\tau = 0.57$ ns, as obtained from TRPL measurements [82]. This threshold density is significantly smaller than the transparency density ($\sim 3\times10^{18}$ cm^{-3}) [157] and the Mott density ($1-2\times10^{19}\,\mathrm{cm}^{-3}$) [60] reported for GaN. The injection current was further increased, using pulsed mode bias beyond 1.5 kA/cm^2, and a second non-linear threshold is observed at 46 kA/cm^2 (Fig. 5.11). This non-linearity, which is accompanied by a three-orders-of-magnitude increase in the output power compared to that in the polariton lasing regime, is due to conventional photon lasing.

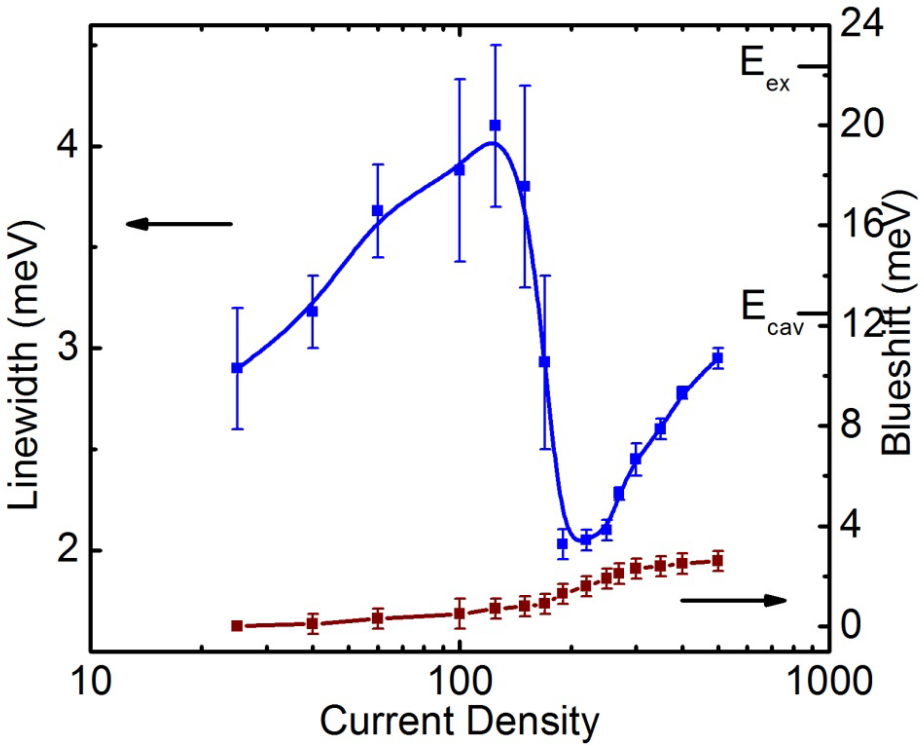

Fig. 5.12 Measured LP emission linewidth and blueshift of LP emission peak as a function of injected current density.

The measured variation of the linewidth of the LP emission with injection is plotted in Fig. 5.12. The minimum linewidth of 1.95 meV corresponds to a LP coherence time of 2.12 ps. Beyond the minimum, the linewidth increases again due to exciton-exciton interactions. Also plotted in Fig. 5.12 is the measured blueshift of the LP emission peak, caused by polariton-polariton and polariton-exciton interactions [30]. From the measured blueshift δE of 1.9±0.28 meV around the non-linear threshold, the polariton density can be estimated using $\delta E \cong 3.3\pi E_x^B a_B^3 N_{3D}$ [158]. Here E_x^B and a_B are the exciton binding energy and Bohr radius, respectively. Using values of E_x^B = (28±8) meV [159, 160] and a_B = (3.5±0.1) nm, a value of N_{3D} = (1.53±1.13) x 10^{17} cm^{-3} is derived, which is slightly larger than the value derived from the measured current

density. A larger value results because the formula for the blueshift quoted above takes only phase space filling into account, while the measured blueshift can include both saturation of the oscillator strength and phase space filling. These values are again smaller than the Mott density and the transparency density, confirming that the observed non-linearity is indeed due to polariton lasing.

5.6.4 Momentum Space Distribution

The polariton occupation in momentum space at different injection levels has been measured by angle-resolved electroluminescence. The occupation is calculated from the output power measured with an optical power-meter. The polariton occupation number per $k_{||}$ state is calculated using the relation described in section 3.5 and is plotted in Fig. 5.13 for three different injection levels. From a non-thermal distribution below

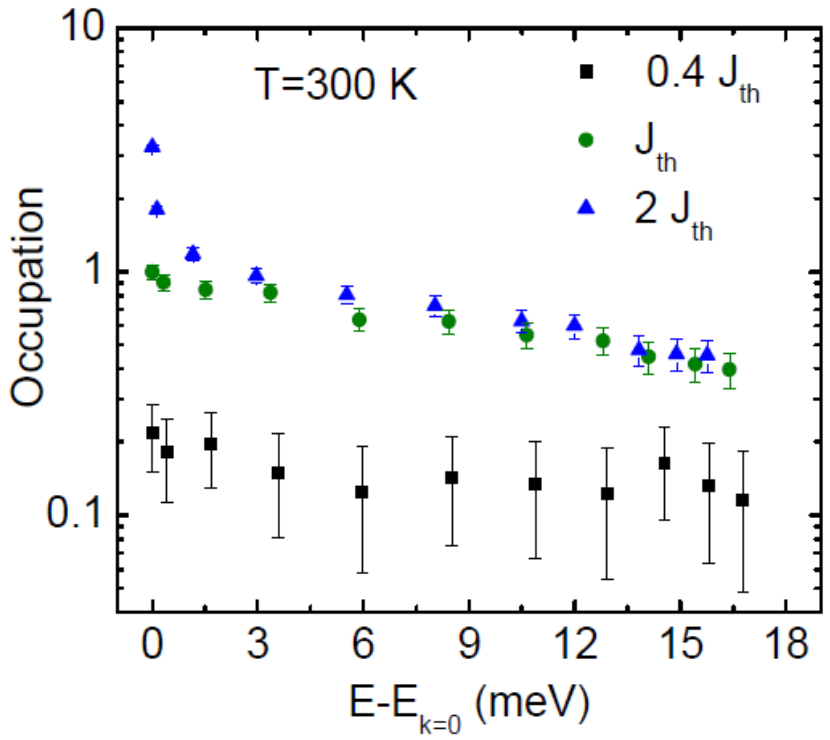

Fig. 5.13 LP ground state occupancy for different $k_{||}$ states at three different injections.

threshold, a Boltzmann-like distribution emerges just below and at threshold. A bimodal distribution and strong peaking of the occupation at and near $k_{||}=0$ is observed for injection above threshold. There is no evidence of a relaxation bottleneck at any injection. Such a complete suppression of the relaxation bottleneck is attributed to the efficient polariton-acoustic phonon scattering mechanism at room temperature [155]. To estimate the effective polariton temperature (T_{LP}), the polariton occupation at $J=J_{th}$ is analyzed with Maxwell-Boltzmann distribution: $N = N_0 \exp\left(-\frac{E(k_{||}) - E(0)}{k_B T_{LP}}\right)$, where $E(k_{||})$ is the LP energy at $k_{||}$ and N_0 is the occupancy at $k_{||} = 0$. A T_{LP} value of 230 K is obtained from this analysis.

5.6.5 Spatial Coherence Measurements

It is known that polariton lasing generally originates from a non-equilibrium Bose-Einstein condensate (BEC) obtained by a dynamical balance between injection and polariton (photon) loss. One of the characteristics of this condensate, similar to that of an equilibrium BEC, is long-range spatial coherence. In this work, we have measured the spatial coherence properties of the polariton emission of one of the devices with a slightly misaligned Mach-Zehnder interferometer [81]. The experimental setup for this measurement is discussed in detail in section 3.5. The visibility of the fringes is measured as a function of displacement between two identical images of polariton emission for injection levels below and above the lasing threshold. The measured visibility is plotted as a function of the injection current in Fig. 5.14(a). A peak visibility of ~ 38 % is recorded above threshold at an injected current density of $J = 1.3\ J_{th}$. While the peak visibility should ideally approach unity at zero displacement between two identical

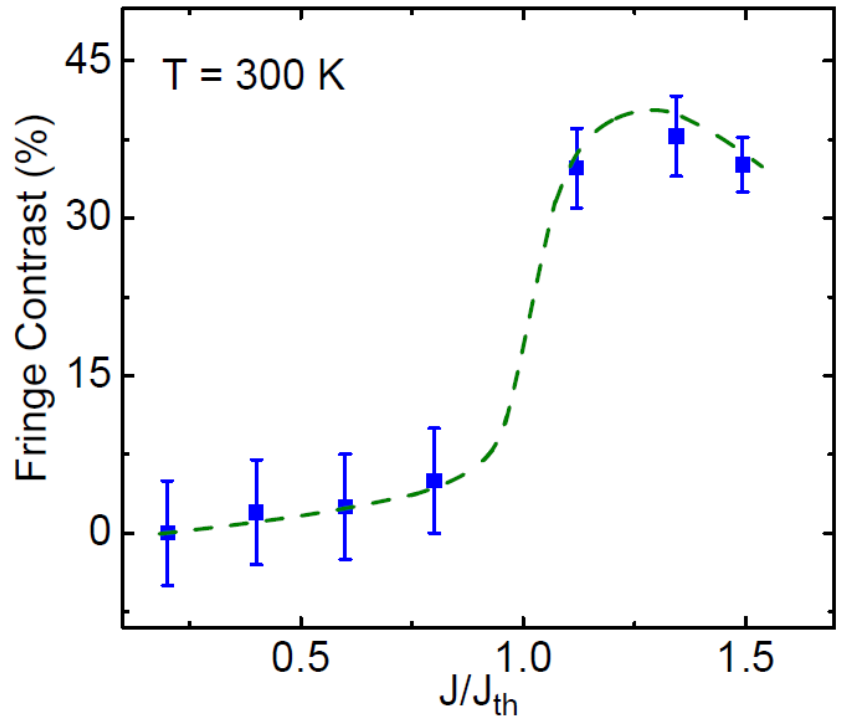

(a)

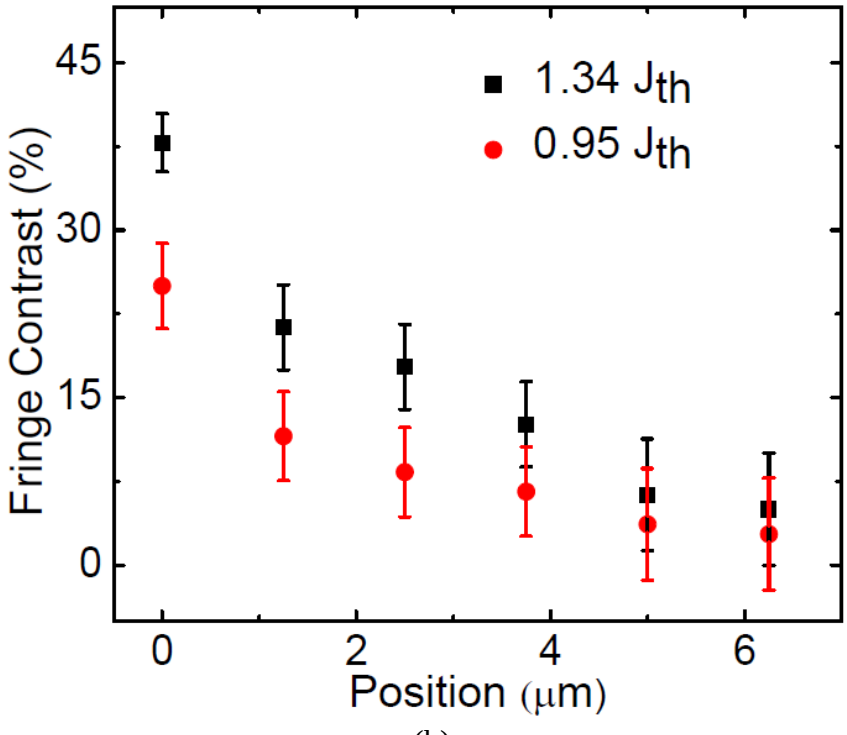

(b)

Fig. 5.14 (a) Interference visibility measured as a function of the injected current density for zero displacement between the double images of the LP emission. The dashed line is a guide to the eye,(b) interference visibility measured as a function of the displacement between a double image of the polariton condensate below and above the polariton lasing threshold.

images of the polariton condensate, such high values have not been experimentally reported. This is probably due to quantum fluctuations in the condensate and the fact that the condensate fraction of the polariton gas should be less than 50%,which has been theoretically predicted [161]. The visibility of the fringes is plotted in Fig. 5.14(b) as a function of displacement between two identical images of the LP emission for injection levels below and above the polariton lasing threshold. The full-width at half maximum (FWHM) of the distribution above threshold is ~4 μm, which is the approximate size of the relevant condensate.

5.6.6 Measurement and Analysis of Steady-State Output Polarization

5.6.6.1 General Overview of the Output Polarization of a Polariton Laser

An important characteristic of the output of a polariton laser is its polarization [19-20, 22, 162-170]. The build-up of polarization in a polariton laser is commonly attributed to *spontaneous symmetry breaking*, which is a direct consequence of the Bosonic characteristics of polaritons. Though polariton lasing does not necessarily imply Bose-Einstein condensation, it is well established that a non- or quasi-equilibrium macroscopic coherent condensate is formed at the non-linear threshold of a polariton laser. This macroscopic condensate is usually described using a wavefunction $\Psi\left(\vec{r}\right)$, which has a random phase prior to spontaneous symmetry breaking. However, at the *polariton lasing threshold*, because of small deterministic perturbative term(s) in the system Hamiltonian, the condensate attain a specific phase, which remains the same throughout the condensate. Under this condition, output polarization is imparted by

$\Psi_{\uparrow}\left(\vec{r}\right)$ and $\Psi_{\downarrow}\left(\vec{r}\right)$, which are respectively the spin-up and spin-down components of the condensate wavefunction.

It is important to note that below the *non-linear threshold*, $\left|\Psi\right| = 0$ and hence the optical output is essentially unpolarized [19-20, 22, 61, 81, 167, 169, 170]. As the non-linear threshold is reached, because of spontaneous symmetry breaking in the degenerate condensate, there is spontaneous build-up of linear polarization in the emission spectra [22, 163-165, 168, 169]. In the absence of reduced symmetry or material disorders, this polarization is random in nature. However, in practical semiconductor microcavities, it is usually *pinned* along a preferential orientation, because of disorders in the active region material or reduced symmetry of the quantum confined structure, such as a quantum-well, wire or dot. Disorders or reduced dimensionalities of the material system also breaks the ground state degeneracy into two closely spaced states, as shown in Fig. 5.15. Above threshold, the condensate occupies the lowest of these two states and the linear polarization of the emission corresponds to this state. The buildup of linear polarization is usually followed by its decrease at higher injections beyond the polariton lasing threshold. This phenomenon is commonly described as the *depinning effect*, which is attributed to repulsive polariton-polariton interaction and self-induced Larmor precession of the Stokes vector of the polariton condensate.

In all the reported experiments [19-20, 22, 57, 61, 166, 168, 169], except one with a GaAs-based microcavity at 30 K [81], the device has been excited with linearly or circularly polarized light. We report here the first experimental study of the output polarization characteristics of a GaN-based electrically pumped microcavity polariton

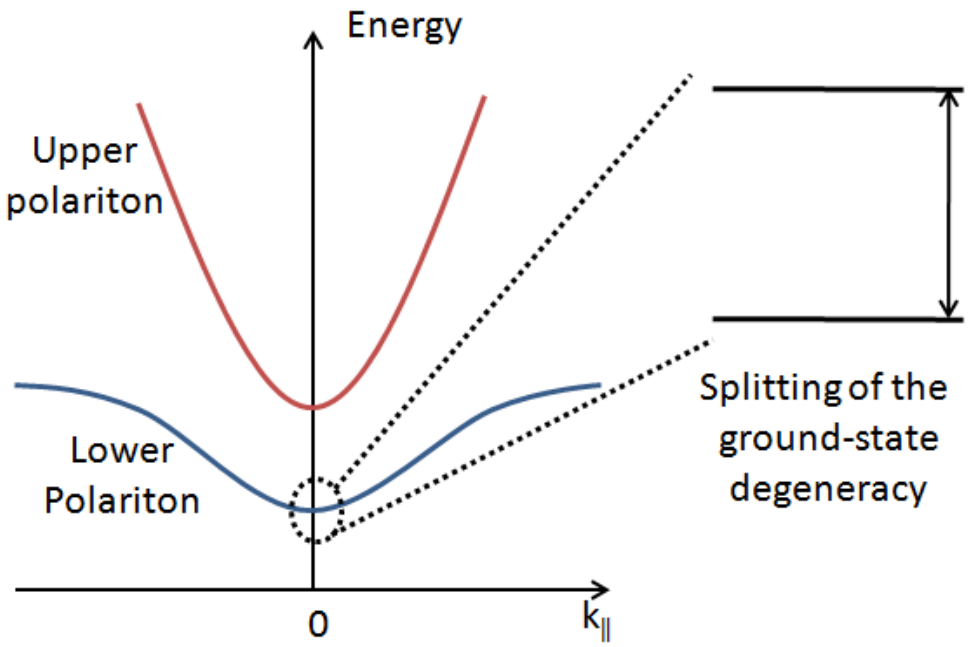

Fig. 5.15 The splitting of the ground-state degeneracy illustrated using a generalized polariton dispersion relation.

laser. Details of the experimental setup are discussed in section of chapter . Measurement results and theoretical analysis follows in the subsequent sections.

5.6.6.2 Experimental Results

The degree of linear polarization of the polariton emission in the normal direction ($k_{\|}$~0) as a function of injection current has been measured in two devices, which are denoted as Device 1 and Device 2 henceforth. The light current characteristics of the two devices are shown in Fig. 5.16(a). Here Device 1 exhibits a higher non-linear slope (~13.4) than that of Device 2 (~6.1). In Fig. 5.16(b), the electroluminescence intensity of Device 1 is plotted as a function of the angle of the linear analyzer. Below the non-linear threshold, the emission is depolarized. Above threshold, a maximum linear polarization of ~ 22 % is recorded for an injection level of 275 A/cm^2. The linear polarization is found

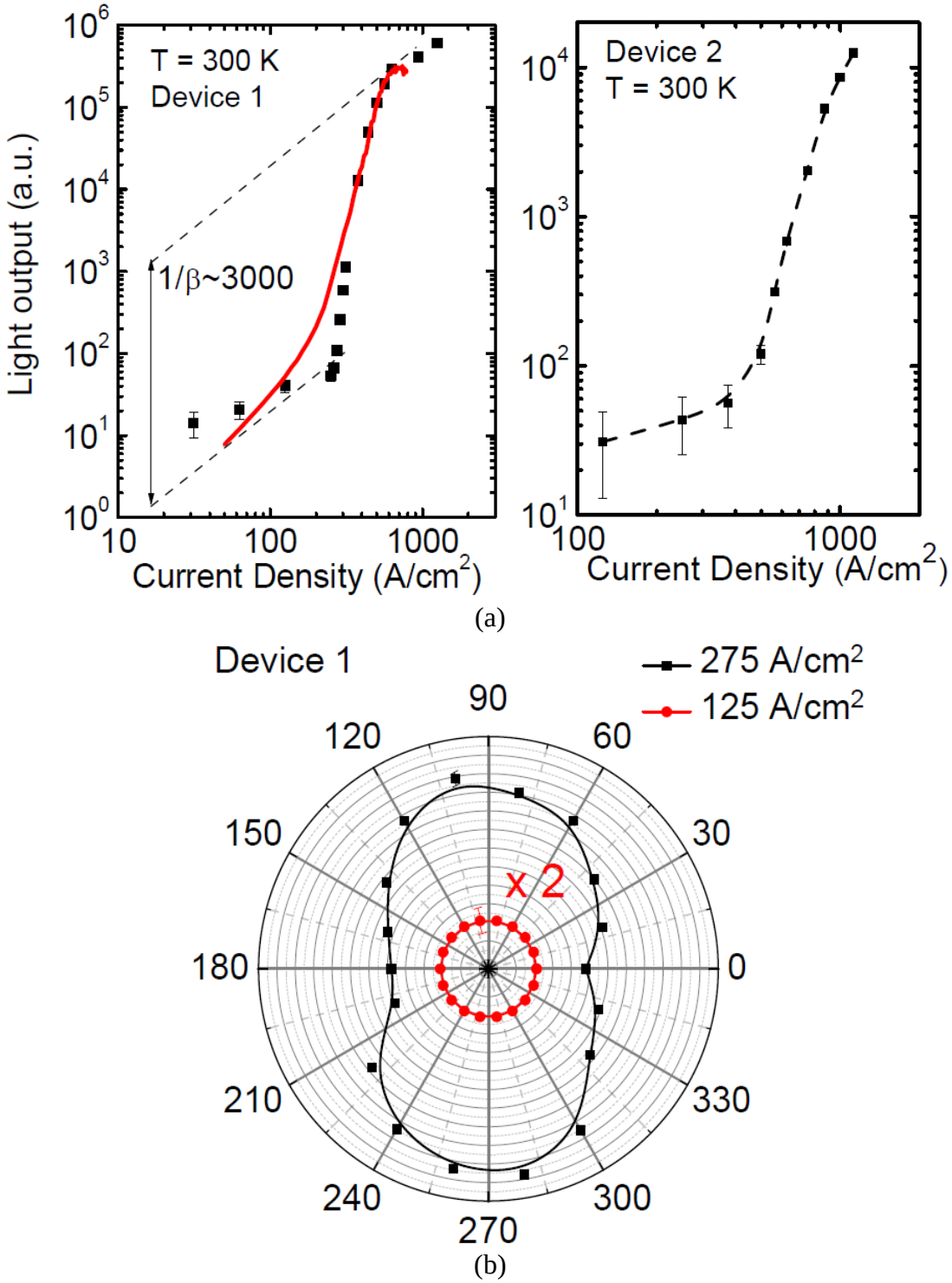

Fig. 5.16 (a) Light-current characteristics of Device 1 and 2 at normal incidence with respect to the DBRs, (b) polar plots of the normal incidence LP electroluminescence intensities recorded as a function of angle of linear analyzer below and above threshold of Device 1

to be preferentially oriented along the $[1\bar{1}00]$ crystallographic axis in all the devices.

Figures 5.17 and 5.18 depict the measured steady state linear polarization of the output LP electroluminescence as a function of the injection current for the two devices. The output is essentially unpolarized below the threshold value, the degree of linear polarization being below the detection limit. At threshold, there is a sharp increase in linear polarization due to stimulated LP scattering from the unpolarized reservoir to the polarized seed condensate in the presence of a small linear polarization splitting [171]. This is followed by a peaking and a steady decrease at higher injection, which is the depinning effect also observed by Levrat *et al.* [169]. The depinning effect is a result of strong polariton-polariton repulsive interactions and self-induced Larmor precession of the Stokes vector of the condensate [168, 169]. The measured thresholds for linear

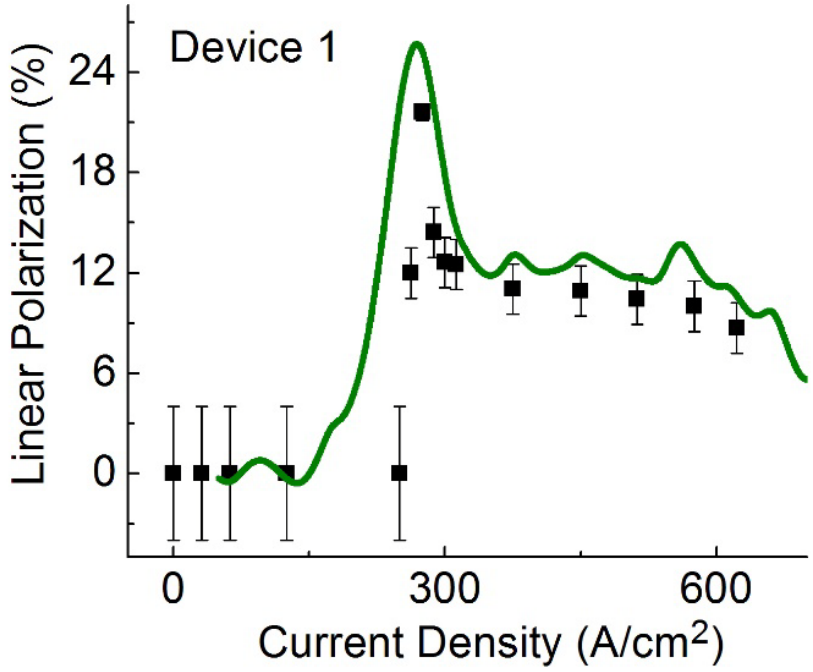

Fig. 5.17 Measured steady-state degree of linear polarization of Device 1. The solid lines represent theoretical calculations.

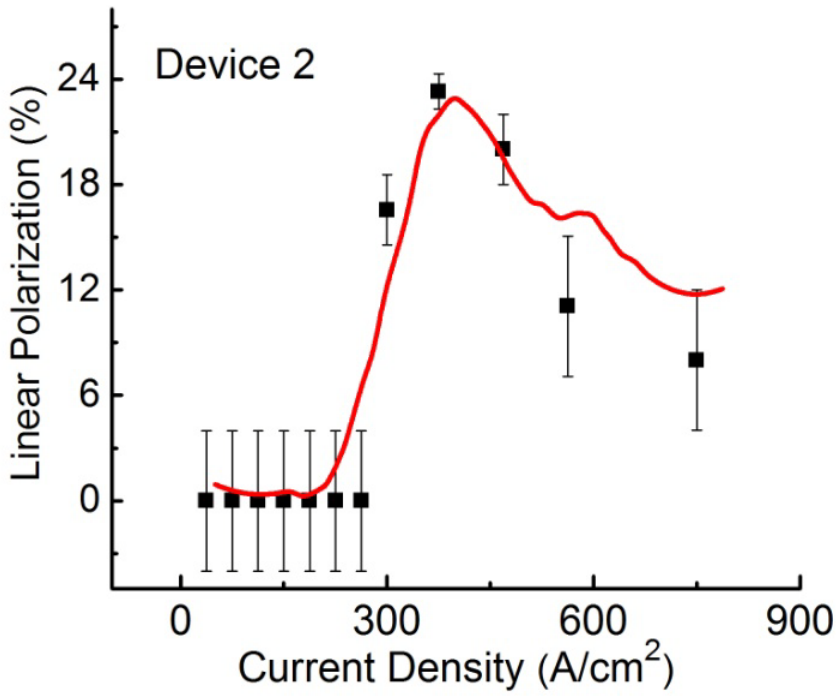

Fig. 5.18 Measured steady-state degree of linear polarization of Device 2 as a function of injected current density. The solid lines represent theoretical calculations.

polarization agree with the non-linear threshold in the light-current characteristics within the experimental accuracy.

Polarization-resolved light-current characteristics are also measured and are plotted alongside the polarization integrated characteristics for two devices in Fig. 5.19. The data of Device 2 in indicate that the value of the threshold current density remains unchanged for the two cases within the experimental accuracy (Fig. 5.19(a)). In contrast, the similar data for Device 1 shown in Fig. 5.19(b) indicate a reduction of the threshold current density of the polarization-resolved output by ~70 A/cm^2 compared to that of the polarization unresolved output as one can clearly see in the inset. This effect was only observed in one device, nonetheless during repeated measurements. The lower threshold of a specific linear polarization resolved electroluminescence probably results from a spatially inhomogeneous polarization splitting in the GaN microcavity, similar to

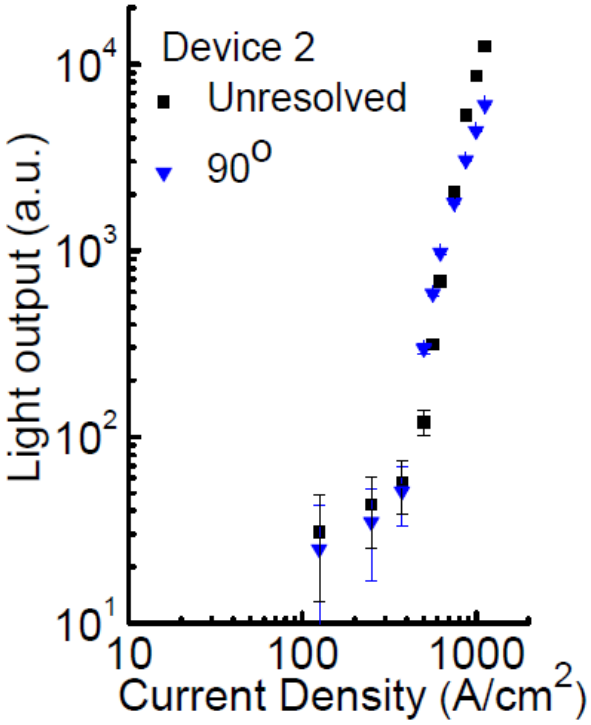

(a)

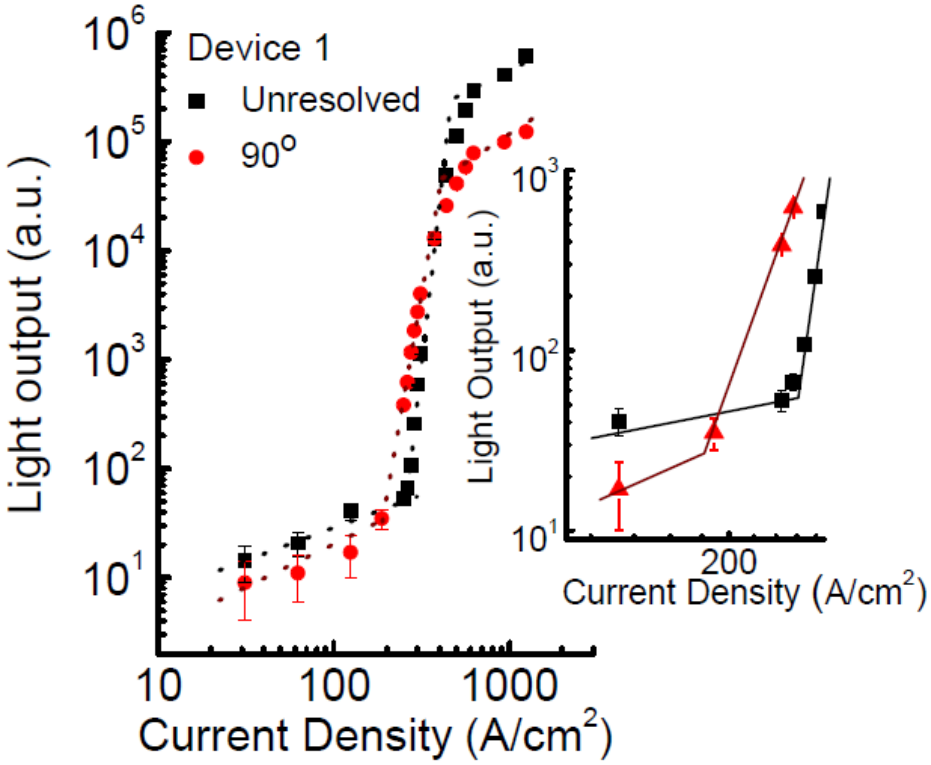

(b)

Fig. 5.19 Polarization-resolved (along 90° angle of the linear analyzer) and unresolved light-current characteristics of (a) Device 2 and (b) Device 1. The inset shows an enlargement highlighting the different thresholds.

what has been observed before in a CdTe microcavity [171,172]. Some parts of the sample may be characterized by a large splitting of the linearly polarized modes and a specific linear polarization build-up occurs with a lower threshold. In other domains the polarization splitting is negligibly small, resulting in emission which will be unpolarized in the steady state. The lowering of threshold observed here is less than the expected factor of 2 due to deviations in the microcavity characteristics from an ideal case. Nonetheless, this is the manifestation of inhomogenity, probably arising from defects, in the linear polarization resolved electroluminescence of a polariton laser.

5.6.6.3 Theoretical Analysis

The experimental results are analyzed with the stochastic kinetic theory [168, 169] wherein the kinetics of the system is modeled with the four coupled stochastic differential equations (see Appendix B for details). Figure 5.16(a) shows the calculated dependence of the condensate occupation number $n(t)$ on the injected current density alongside the measured data for Device 1. Figures 5.17 and 5.18 show the calculated dependence of the linear polarization degree of the polariton laser emission on the pump current to be compared to the measured data of Device 1 and 2. We observe that the calculated linear polarization shows a good agreement with the measured data, in general. One can see that the difference in current density dependence of the linear polarization between Devices 1 and 2 is chiefly due to the different spin relaxation and polariton radiative decay rates. The spin relaxation rate and the polariton radiative decay rate is ~ 30% faster and ~ 30% slower respectively, in Device 2 as compared to Device 1. We ascribe these differences to the different magnitudes of photonic disorder in the two devices. The value of the peak polarization degree of ~ 22 % is governed by the ratio of

the polarization relaxation rate γ and the polariton radiative decay rate Γ_c. The lower is this ratio, the shorter time the polariton condensate possesses for relaxation to the lowest energy polarization state. We observe that this ratio and thus the degree of peak polarization is lower than that reported by Levrat *et al.* [169]. The rate of the decrease of the linear polarization beyond the peak depends on the ratio of the nonlinear coefficient α_1 and the linear polarization splitting Ω (Appendix B).

5.7 Summary

In conclusion, we demonstrate polariton lasing from a bulk GaN microcavity diode at room temperature under steady-state conditions. The nonlinear threshold is observed at 190 A/cm^2, which is more than two orders of magnitude smaller than the photon lasing threshold in the same device. The nonlinearity in the output characteristics is accompanied by linewidth narrowing and a small blueshift of the emission peak. The measured population redistribution in momentum space and spatial coherence as a function of injection current confirm polariton condensation. The output polarization below and above threshold has also been characterized. The experimental results have been theoretically analyzed by modeling the kinetics of the system with a system of coupled stochastic differential equations. A maximum degree of linear polarization of ~ 22% is observed in our measurements. It is envisaged that an array of the devices presented here will constitute a coherent linearly polarized ultraviolet light source with acceptable power and ultra-low threshold.

Chapter VI

Small-signal Modulation and Role of Defects in Polariton Lasers

6.1 Introduction

The characterization of optically or electrically pumped polariton lasers made with a variety of material systems has enabled a detailed study of the underlying physical processes such as polariton scattering and Bose-Einstein condensation [18-21], spontaneous symmetry breaking [22, 23] and superfluidity [24-26] in the condensate. However, all the results hitherto reported have been obtained under steady state conditions with continuous wave electrical biasing or optical excitation. The small-signal modulation bandwidth of a conventional semiconductor laser is intrinsically limited by gain compression and related hot carrier effects [173]. Since polariton lasers operate at much lower injection levels, it is expected that the intrinsic modulation bandwidth would not be similarly affected [148]. Other related effects such as chirp and self-pulsation should be small or non-existent. Dynamic characterization would also elucidate the similarities, or lack thereof, in terms of key lasing parameters such as differential gain and damping factor and the physical processes underlying them in a polariton laser. In this chapter, the small signal modulation characteristics of a GaN-based electrically pumped polariton laser operating at room temperature is discussed. Besides dynamic

characteristics, an area which has remained rather unexplored is the role of defects on the performance characteristics of polariton lasers. In this chapter, this attribute has been examined and elucidated in the context of dynamic condensation in both electric and optically pumped polariton lasers.

6.2 Small-Signal Modulation of Polariton Lasers

In this section we discuss the small signal modulation characteristics of a GaN-based electrically pumped polariton laser operating at room temperature. The experimental results have been analyzed with a theoretical model based on the Boltzmann kinetic equations and the agreement is very good. We have also investigated frequency chirping during such modulation. Gain compression phenomenon in a polariton laser is interpreted and a value is obtained for the gain compression factor. The details of material growth, device fabrication, strong-coupling and steady-state polariton lasing characteristics of the device under discussion have already been discussed in detail the previous chapter.

6.2.1 Measurement and Analysis of Resonance Frequency

Frequency response of the polariton laser diode is estimated by time resolved electroluminescence measurements at different DC injection levels using the experimental setup described in section 3.5.7. The modulation response at various injection levels is shown in Fig. 6.1, where the inset shows the measured transient response of the polariton laser to a high speed switching pulse. A -3dB modulation bandwidth of 1.18 GHz was measured at an injection current density of 5.4 J_{th} and the resonance frequency, f_r, at this injection level is 0.9 GHz. The solid curves in Fig. 6.1

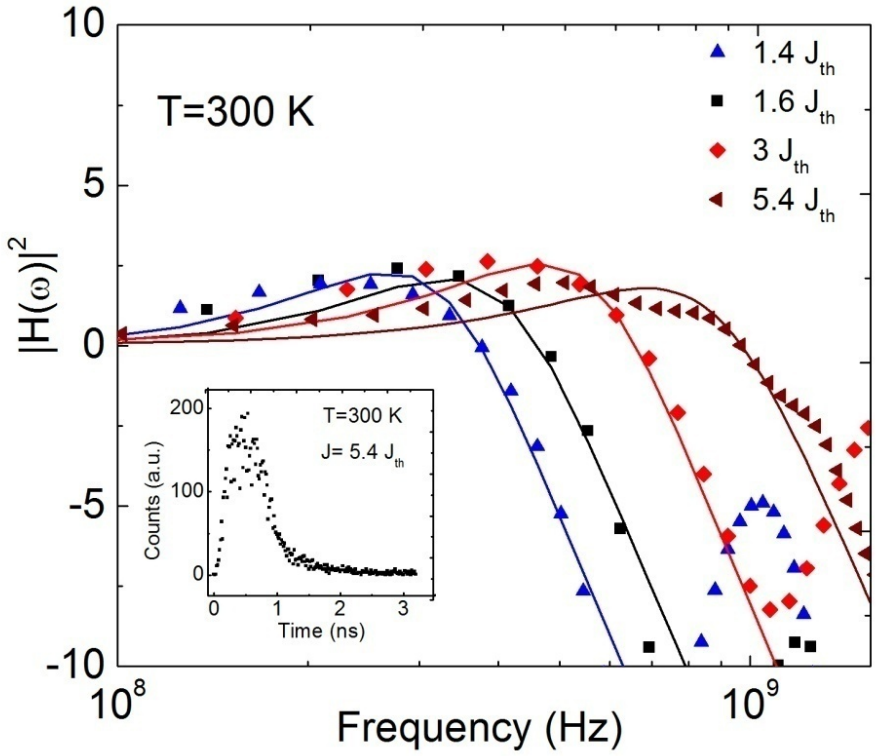

Fig. 6.1 Frequency response derived from measured time resolved EL at different DC injection levels. The solid lines represent calculated frequency responses (Inset shows the measured transient response of the polariton laser to a switching pulse at J = 5.4J_{th}).

represent the modulation response calculated in accordance with the transfer function, $|M(f)|^2 \propto \frac{1}{\left(f^2 - f_r^2\right)^2 + \left(\frac{\gamma_d}{2\pi}\right)^2 f^2}$, where γ_d is defined as the damping factor. The modulation response was derived by the fast Fourier transform (FFT) of the measured transient response. The RC effect of the microcavity diode is also taken into account in the modulation response.

Emission is stimulated in a conventional photon laser, whereas in the polariton laser polariton-polariton scattering is stimulated once the occupation is unity. The separation of stimulation and emission in a polariton laser leads to coherent emission without the requirement for population inversion. Iorsh et al. [148] have theoretically

investigated the small-signal modulation behavior of III-nitride electrically pumped polariton lasers. According to their theory, the resonance frequency of the modulation response, $\omega_R(\text{pol})$, in the framework of the Boltzmann kinetic model is given by:

$$\omega_R^2(\text{pol}) \cong 2\sqrt{\frac{b}{\tau_{LP}^{3}}}\left(n_{LP}^{\infty} - n_T\right) \tag{6.1}$$

where n_{LP}^{∞} is the steady-state polariton density at $k_{\parallel} \sim 0$, b is the polariton-polariton scattering rate beyond threshold and τ_{LP} is the LP radiative lifetime. In equation 6.1, we have added the term n_T as compared to the expression in [148]. This term accounts for the fraction of the polariton states which have been trapped in localized states and dislocations and do not contribute to the laser kinetics. Of course, the right hand-side of equation 6.1 should always be positive within the limits of validity of this model, i.e., conditions above threshold. Equation 6.1 is similar in nature to that for a photon laser, where $\omega_R^2 \cong \dfrac{v_g \dfrac{dg}{dn} N_p}{\tau_{ph}}$. Here v_g, dg/dn, N_p and τ_{ph} are the photon group velocity, differential gain, photon density in the cavity and cavity photon lifetime, respectively. The exciton-exciton scattering rate is extracted from the simple three level rate equations of the polariton laser (see Appendix B for details). The value of *b* is obtained by setting the threshold current density to the experimentally observed value of 190 A/cm^2. This gives us $b = 0.7\times10^{-12}\,\text{ps}^{-1}$, which is very close to the value obtained from coupled semiclassical Boltzmann equation based analysis [148]. Figure 6.2 shows a plot of the measured resonance frequency plotted as a function of $n_{LP}^{\infty 1/2}$. Here the solid line

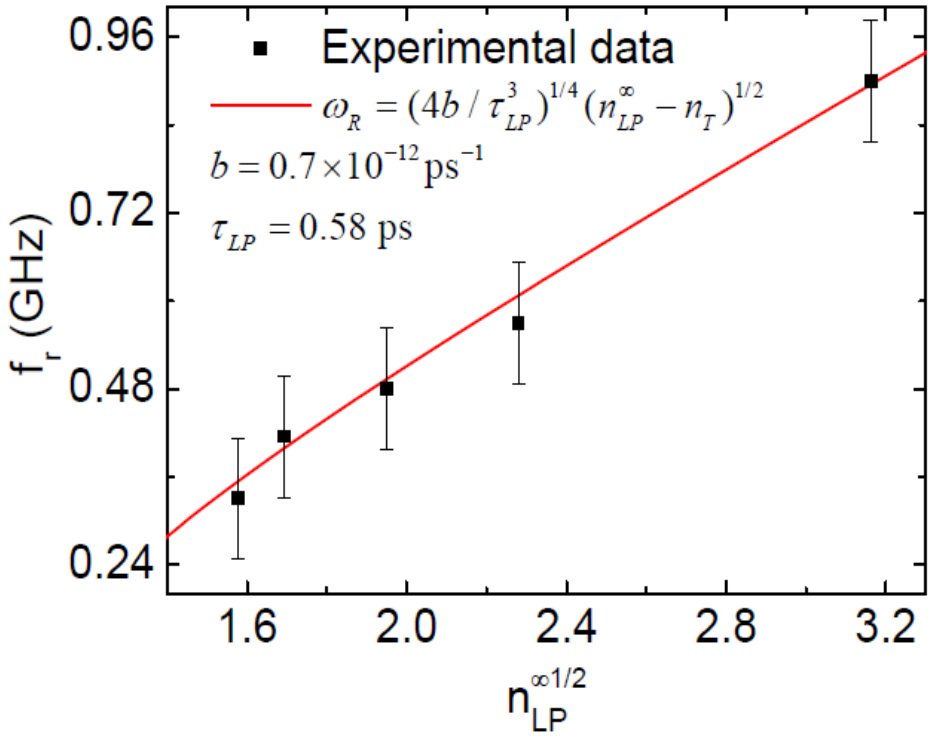

Fig. 6.2 Measured resonance frequency as function of $n_{Lp}^{\infty 1/2}$ along with calculated results obtained from equation (2).

represents analysis of the data in accordance with equation 6.1. In this analysis, a value of $n_T = 1.1$ is obtained from the fitting of the experimental data to equation 6.1.

6.2.2 Differential Gain and Gain Compression

Gain and differential gain are related to stimulated emission in a photon laser. Polariton lasing arises from stimulated polariton scattering with excitons, free carriers or phonons. This results in gain, which may be described by the negative imaginary part of the refractive index. Gergel' et al. have described gain induced by exciton Bose condensation and have derived the complex dielectric function explicitly [174]. Phenomenologically, therefore, a differential gain in a polariton laser may be expressed using the following relation:

$$\frac{dg}{dn}(\text{pol}) = \frac{2}{v_g}\sqrt{\frac{b}{\tau_{LP}}} \qquad [\text{cm}^{-1}] \tag{6.2}$$

The important aspect of this equation is that the differential gain is large for a large scattering rate *b* and small τ_{LP} , i.e. a large coupling strength and a negative detuning. It may be noted that the small-signal modulation response depicted in Fig. 6.1 is damped. The damping factor γ_d can be derived from analysis of the modulation response. For large resonance frequency, the damping factor in a polariton laser is given by $\gamma_d(\text{pol}) \cong \omega_R^2 \tau_{LP}$ [148]. In a well-designed photon laser damping is generally a result of gain compression due to the accumulation of hot carriers in the active region and subsequent spectral and

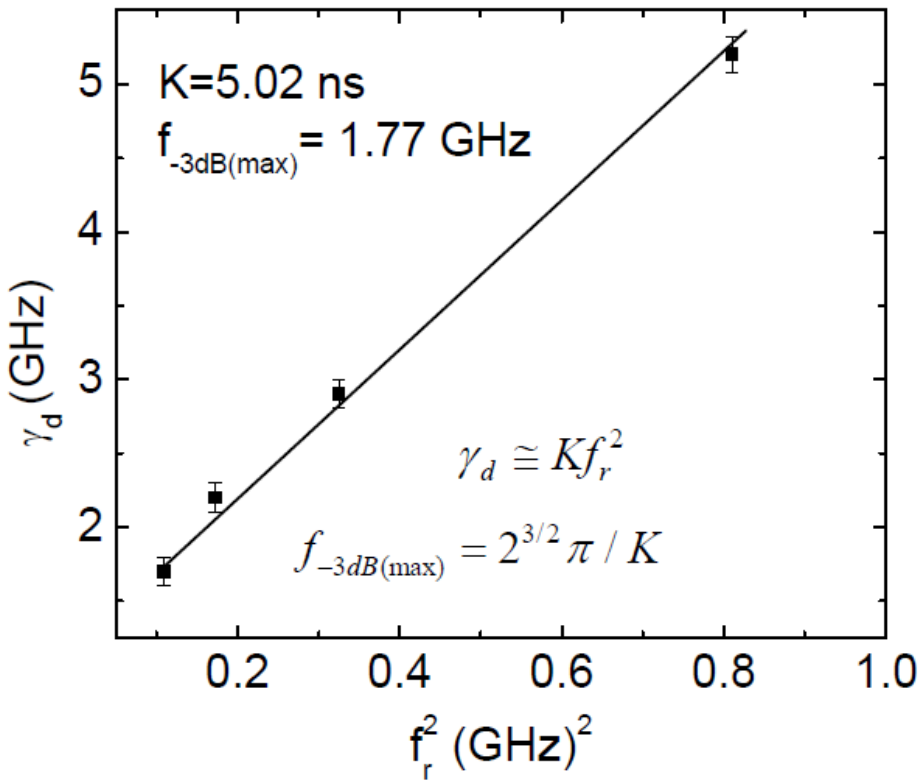

Fig. 6.3 Variation of the damping factor as a function of the square of the resonance frequency.

spatial hole burning. In a polariton laser, such damping can be caused by saturation of the oscillator strength by phase space filling [175] at high injection levels and the decrease of the Rabi oscillation frequency and the resultant exciton-photon coupling. Hence the damping factor can be expressed as,

$$\gamma_d(\text{pol}) = Kf_r^2 \tag{6.3}$$

where $K = 4\pi^2\tau_{LP}$. Including gain compression, the *K*-factor of a polariton laser may phenomenologically be expressed as,

$$K = 4\pi^2\left[\frac{\varepsilon_{LP}}{2\sqrt{b/\tau_{LP}}} + \tau_{LP}\right] \quad [\text{s}] \tag{6.4}$$

where the gain compression factor ε_{LP} is dimensionless. The damping factor γ_d is plotted against the square of the resonance frequency in Fig. 6.3. From the slope of this plot, a value of *K*=0.52 ns is derived. The intrinsic -3 dB modulation bandwidth of the polariton laser, given by $f_{-3dB} = 2^{3/2}\pi/K$, is determined to be 1.77 GHz. The differential gain is calculated to be $1.89\times10^{-4}\,\text{cm}^{-1}$ from equation 6.2 using the values of *b* and τ_{LP}. Finally, the gain compression factor is derived from equation 6.4 to be $\varepsilon_{LP} = 2.78\times10^{-4}$. In comparison, the differential gain and gain compression factor of GaN-based red-emitting InGaN/GaN quantum dot lasers are reported to be $5.3\times10^{-17}\,\text{cm}^2$ and $2.87\times10^{-17}\,\text{cm}^3$, respectively [176]. The *K*-factor reported for a similar green emitting quantum dot laser is 1.24 ns and the corresponding gain compression factor and differential gain are $1.22\times10^{-17}\,\text{cm}^3$ and $3\times10^{-17}\,\text{cm}^3$ respectively [177].

6.2.3 Frequency Chirping in a Polariton Laser

Frequency chirping in a semiconductor photon laser is generally a result of periodic modulation of the refractive index of the gain medium due to injection of carriers. Chirp is small in lasers having a large differential gain, such as quantum dot lasers [178], in which the carrier injection levels are small. In experiments, chirp manifests itself in the broadening of the emission spectra, from which a shift of the peak emission wavelength can be estimated as a function of modulation frequency. In this study, chirp of the polariton laser has been recorded as an average broadening of the coherent emission spectra under small signal (2 mV) pulsed bias condition above threshold (1.15 J_{th}) for different modulation frequencies. With an injection carrier density of ~10^{15} cm^{-3} in the polariton laser the estimated shift of the emission peak, $\Delta\lambda$~0.056 Å

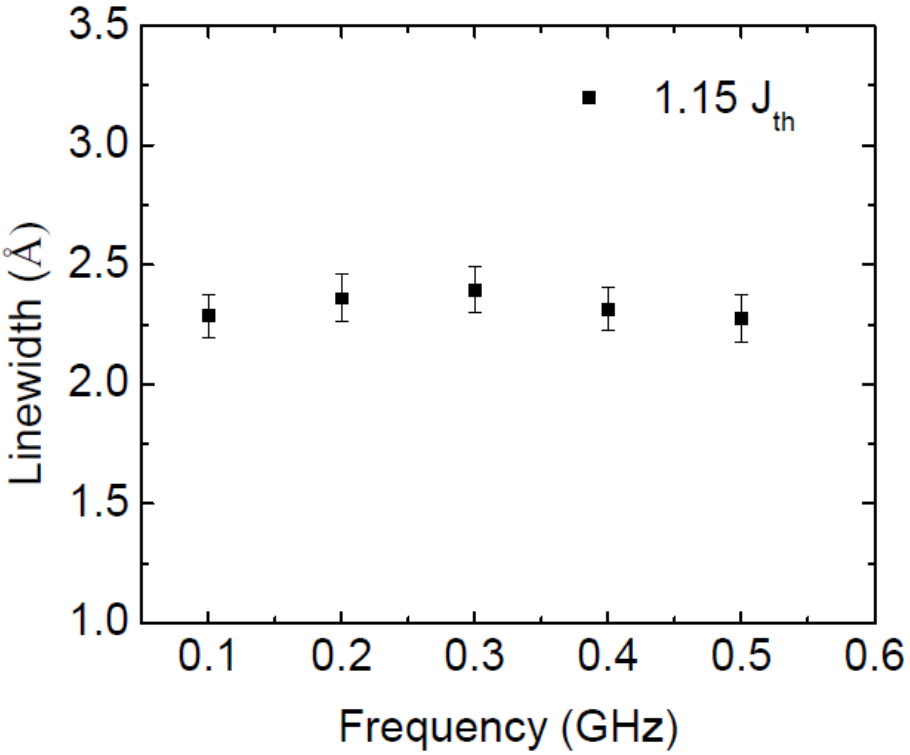

Fig. 6.4 Measured linewidth of LP emission peak as a function of the small signal modulating frequency, under a fixed DC bias of 1.15 J_{th},

(see Appendix C for details). The data shown in Fig. 6.4 indicate that the expected near-zero chirp is within the measurement error limits. Therefore because of the relatively small injection current density, frequency chirping is expected to be negligible in polariton lasers. This is advantageous for possible modulated polariton laser applications.

6.2.4 Theoretical Limits of Frequency Response

In the theoretical work of Iorsh et al. [148], a -3dB modulation bandwidth of ~19 GHz has been predicted for an electrically driven InGaN quantum well based polariton laser diode. In our work, we have instead employed a bulk GaN active region in order to overcome several challenges related to material growth and electronic properties. The highest -3dB modulation bandwidth measured in our device is ~1.2 GHz, whereas an

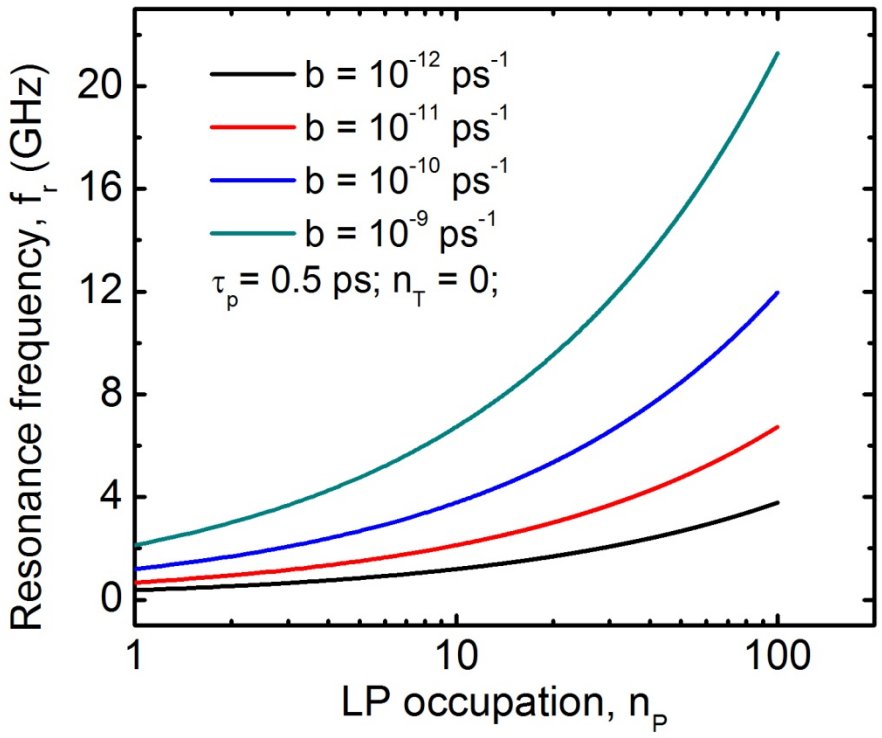

Fig. 6.5 Calculated modulation frequencies for different polariton-polariton scattering rates and polariton lifetimes

intrinsic modulation bandwidth of ~1.8 GHz is phenomenologically predicted. It is expected that higher values of these parameters can be obtained by using a quantum well based active region.

In Fig. 6.5, resonance frequencies of the bulk-GaN polariton device is calculated using equation 6.1 for different polariton-polariton scattering rates. As can be seen, the resonance frequencies can be significantly increased by increasing the scattering rate. This can be attained by adjusting the cavity to exciton detuning of the microcavity, as discussed in [148]. Also according to equation 6.1, defects and dislocations in the active region of the polariton laser are important limiting factors of ω_R as they reduce the number of polaritons which can contribute to the lasing phenomenon. This is particularly important for materials having high dislocation densities, such as GaN. As shown in

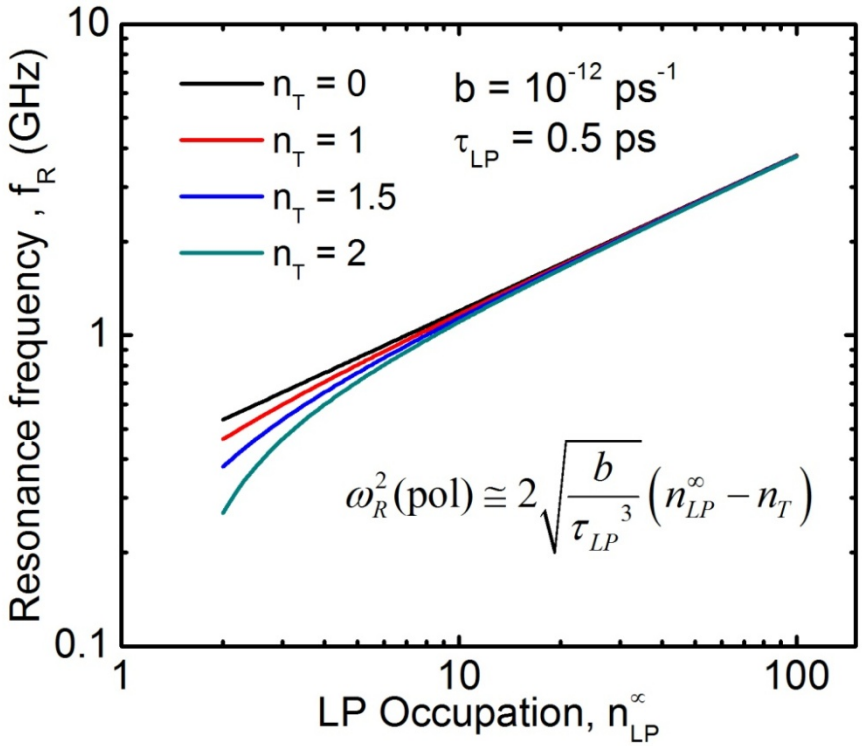

Fig. 6.6 Calculated resonance frequencies plotted as a function of the ground state LP occupancy for different values of n_T.

Fig. 6.6, the resonance frequency value increases significantly with the decrease of n_T. particularly in the low density regime. In addition to high frequency response, other performance characteristics of polariton lasers are significantly influence by the number of dislocations and defects in the active region of the device. This is discussed in detail in the next section.

6.3 The Role of Defects in Polariton Lasers

In a semiconductor microcavity polariton laser, a macroscopic and coherent state of exciton-polaritons is generated by a dynamic condensation process, which involves polariton-phonon, polariton-carrier and polariton-polariton scattering, and finally stimulated polariton-polariton scattering. While the polariton lifetime has to be comparable to the scattering-mediated relaxation time of the polaritons for polariton lasing to occur, the system is in a metastable condensed state in which the polaritons are only in equilibrium among themselves and not with the lattice, which is at the ambient or measurement temperature [29, 179]. Thus the polariton temperature in the condensate at $k_{||}$~0 in the lower polariton dispersion, T_{LP}, is generally larger than T_{latt}, the lattice temperature. This has been consistently the case for GaAs-based devices and GaN nanowire polariton lasers embedded in a dielectric microcavity [18, 20, 21, 57, 81, 120]. For a near-equilibrium Bose-Einstein condensate, which can be achieved by incorporating a potential trap in the microcavity [20, 21], a value of T_{LP} very close to T_{latt} can be attained. However, as shown in section 5.6.4, the calculated T_{LP} is significantly smaller than 300 K in our room temperature GaN-based polariton diode lasers. In this section, we elucidate the role of defects in lowering the effective polariton temperature in electrically and optically pumped polariton lasers. At first an outline of the experiment is

presented. Next, the observed results are discussed in detail. Finally, a simplified theoretical model is presented to explain the observed phenomenon.

6.3.1 Outline of the Experiment

On a closer examination of the characteristics of the materials with which the polariton lasers are fabricated, it becomes apparent that there is a significant difference in the defect (dislocation) density in the active region, which originates from the dislocations present in the starting substrate material. In the case of GaAs, the defect density is $\leq 10^2$ cm^{-2} and is considered to be zero for all practical purposes. However, in the case of GaN, the defect density in the active region ranges from 10^4-10^{10} cm^{-2}, depending on whether it is epitaxially grown on GaN substrates, GaN-on-sapphire templates, silicon substrates, or SiC substrates. In the special case of GaN nanowires grown on silicon, the defect density is known to be very small ($\sim 10^2$ -10^4 cm^{-2}) because of the large surface-to-volume ratio of the nanowires [87, 180, 181].

In the present study, we have investigated the relation between the defect density in the active region and the value of T_{LP} as determined from analysis of measured polariton occupation in momentum space. We have analyzed results obtained from five different polariton lasers, three GaN-based and two GaAs-based. The GaN-based devices are operated at room temperature, while the GaAs-based devices show polariton lasing at lower temperatures. The GaAs-based device operated at T=155 K (denoted as GaAs Device 1) has been discussed in detail in chapter 4, whereas the device operated at cryogenic temperature (denoted as GaAs Device 2) was reported by our group in [81]. One of the GaN-based devices, which was reported by our group in [21], consists of a

single GaN nanowire embedded in a dielectric microcavity and is optically pumped. The two other GaN-based devices have bulk GaN in the active region and are electrically excited. One of these devices has already been discussed in detail in chapter 5 and it is denoted as GaN Device 2 henceforth. The other bulk GaN polariton diode laser, which is denoted here as GaN Device 1, is discussed in detail in the subsequent sections.

6.3.2 Estimation of Dislocation Densities

The defect density in the substrate and active region of the GaN-based devices were determined from etch pit dislocation measurements [116, 117]. The sample is selectively etched with a eutectic mixture of molten bases (NaOH, KOH and MgO) at 450^0C under 50 mTorr ambient pressure for 15 minutes. Atomic force microscopy (AFM) measurements are subsequently performed on the etched samples to determine the dislocation density. GaN-based devices 1 and 2 were grown and fabricated on GaN-on-sapphire templates obtained from different sources. The dislocation densities corresponding to substrates of these two devices are obtained to be 6.4 x 10^8 cm^{-2} and 7.2 x 10^8 cm^{-2} respectively. The defect density in the active region of GaN device 1 was also measured, and a value of 6.1 x 10^8 cm^{-2} is obtained, which confirms that the defect density in the active region is almost identical to that in the starting substrate. The defect density in the single GaN nanowire was estimated from transmission electron microscopy (TEM) measurements [87, 181] and is very small (~10^2 -10^4 cm^{-2}) because of radial strain relaxation and large surface-to-volume ratios. For the GaAs-based devices, the defect density is very small (less than 10^2 cm^{-2}) because of the nearly lattice matched epitaxial growth and hence has been considered to be zero in this study. The dislocation densities of all the devices examined in this study are listed in Table 1. In what follows, the

microcavity, strong-coupling and polariton lasing characteristics of GaN Device 1 are described in detail.

6.3.3 Heterostructure and Microcavity Diode

The edge-emitting electrically pumped GaN-based Device 1 was epitaxially grown, fabricated and characterized in the present study. As can be seen, the heterostructure of this device is identical to that of GaN Device 2. However it is important to note that the starting GaN-on-sapphire substrates of the two devices are different. Device fabrication is initiated by selective deposition of Ni-Au p-contact, followed by rapid thermal annealing at 550^{o} C in an air ambient for two minutes. Next a 5 μm x 40 μm cavity region is defined by standard UV lithography and high density plasma etching, down to the substrate through the $In_{0.18}Al_{0.82}N$ layer. This is followed by plasma enhanced chemical vapor deposition of 1 μm SiO_2 contact pads and subsequent deposition of Ti/Au interconnect metal for both p- and n-contacts using electron beam evaporation technique. The final dimensions of the cavity, 690 nm (5λ) length x 40 μm width are patterned by focused ion beam (FIB) etching. Six and seven pairs of SiO_2/TiO_2 distributed Bragg reflector (DBR) mirrors are deposited on opposite sides of the FIB etched cavity by electron beam evaporation. The current voltage characteristics of the device shows a turn-on voltage of 4.6 V and a series resistance of 35 ohms.

6.3.4 Strong-Coupling Characteristics

Angle-resolved electroluminescence (EL) of the polariton laser diode is measured at room temperature using a digital-readout angular mount which has an angular

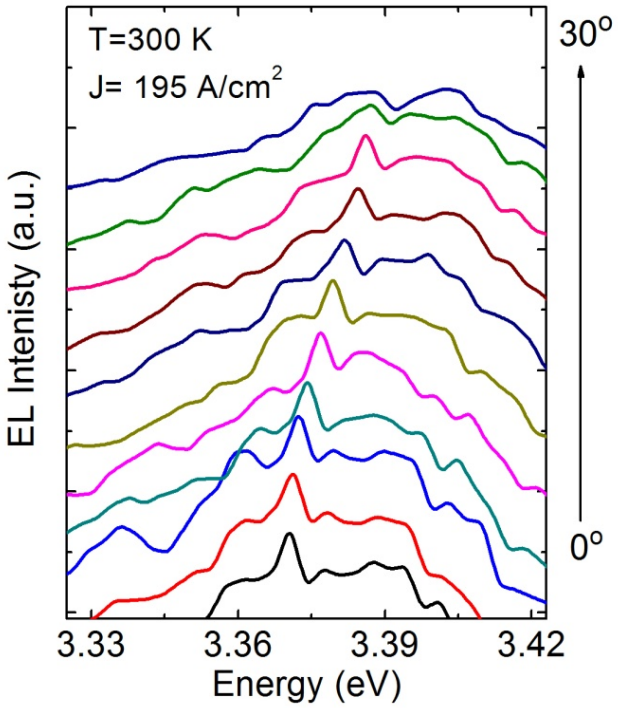

(a)

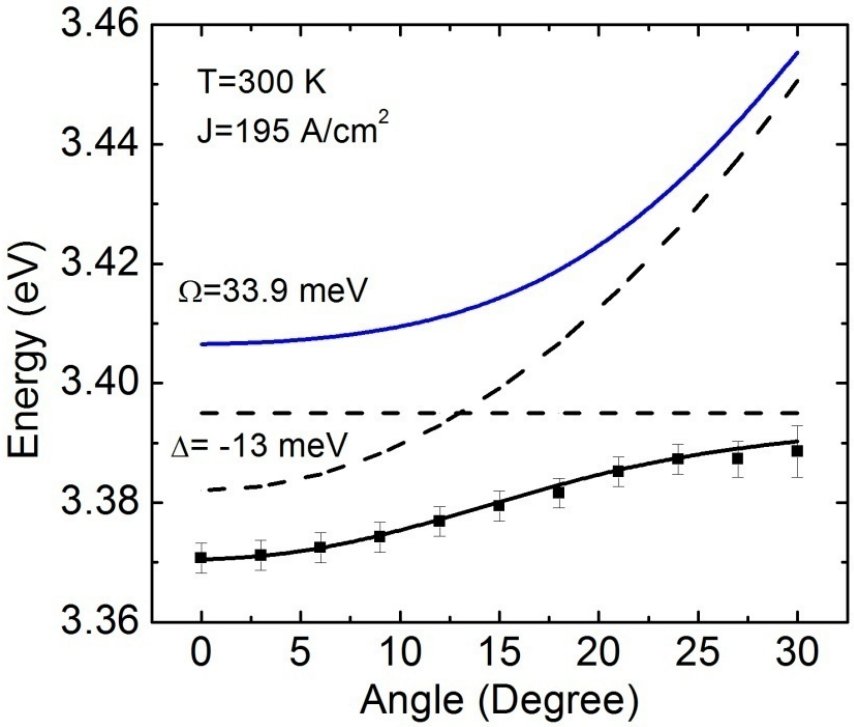

(b)

Fig. 6.7 (a) Angle-resolved EL measured from the bulk-GaN, (b) corresponding polariton dispersion characteristics from 2x2 couple harmonic oscillator model.

precision of 0.1°. Distinct lower polariton (LP) peaks are observed below the exciton energy (E_X = 3.395 eV) at all angles and the LP peaks tend to approach the exciton energy at higher angles (Fig. 6.7(a)). The corresponding polariton dispersion characteristics, which is calculated using 2x2 coupled harmonic oscillator model, is shown in Fig. 6.7(b). The cavity-to-exciton detuning δ and the Rabi splitting Ω are determined to be -13 meV and 33.9 meV, respectively. The strong-coupling regime of the other devices have been discussed in chapter 4 and 5 and are reported in [21, 81].

6.3.5 Polariton Lasing Characteristics

The electroluminescence output of the device was measured as a function of continuous wave (CW) diode injection current in the direction normal to the distributed Bragg reflector (DBR) mirrors of the microcavity (zero angle). Two methods were used to record the light-current (L-I) characteristics. In the first, the integrated intensity of the polariton emission was plotted as function of forward bias current. In the second, the output power was directly measured with a power-meter. Both techniques yielded identical trends in the output characteristics. The variation of the integrated electroluminescence intensity with injection current density at room temperature is depicted in Fig. 6.8. A non-linear threshold is observed at a current density J_{th}=205 A/cm^2 which is similar to the value observed previously in chapter 5. The corresponding LP density at threshold is 3.03x10^{16} cm^{-3}, calculated with an exciton lifetime of 0.71 ns. The non-linear region of the electroluminescence is characterized by a slope of ~3.3. The onset of threshold and non-linearity is accompanied by a sharp reduction of emission linewidth and a small blue-shift of the polariton emission (3.5 meV). The minimum

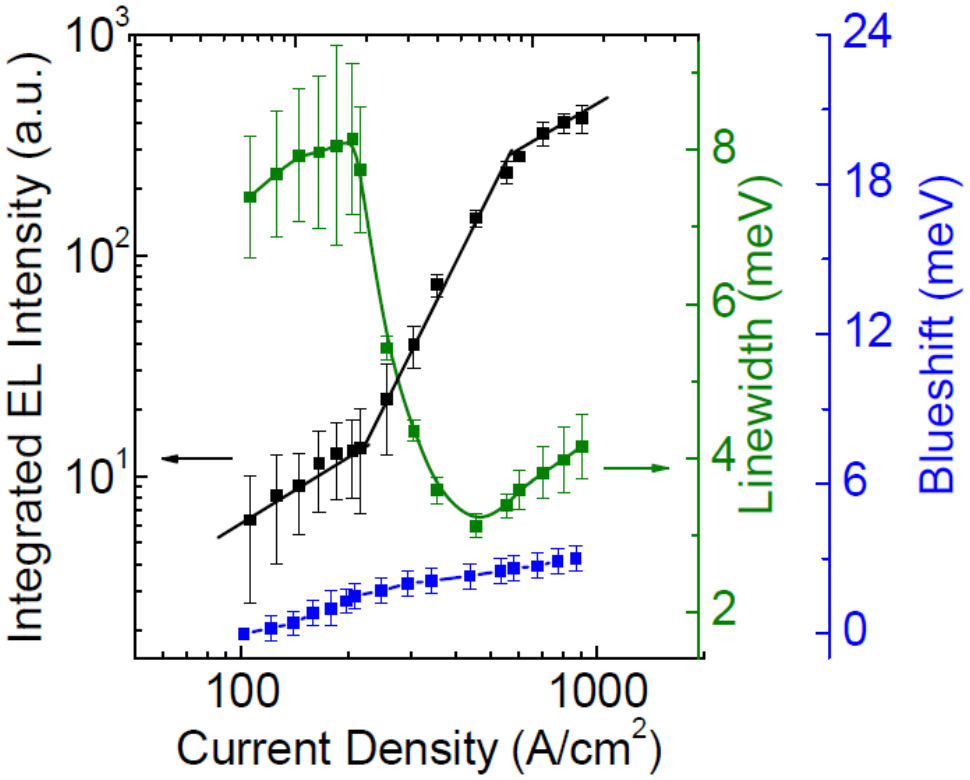

Fig. 6.8 Integrated EL intensity of the LP emission, measured LP emission linewidth and blueshift of LP emission peak as a function of injected current density.

recorded linewidth is 2.96 meV, which corresponds to a LP coherence time of 1.4ps. The LP radiative lifetime is calculated using the relation $\tau_c = \tau_{LP} / |C_{k=0}|^2$, where the cavity photon lifetime τ_c is estimated by microphotoluminescence measurements performed onto the microcavity. From the obtained quality factor of ~2090 and a cavity photon lifetime of ~0.408 ps, the LP lifetime is obtained to be $\tau_{LP} = 0.596$ ps.

6.3.6 Measurement and Analysis of LP Occupancy

The polariton occupation in momentum space at different injection levels has been measured by angle-resolved electroluminescence. Below threshold, the number of polaritons per $k_{||}$-state is estimated from the LP electroluminescence integrated intensity

by taking into account the radiative lifetime. At and above threshold, the occupation is calculated from the output power measured with a power meter. Next the polariton occupation number per $k_{||}$ state is calculated using the relation, $I_{LP} = \frac{\eta n_{LP}^{\infty}(k_{||}) |C(k_{||})|^2 \, Mhc}{\tau_C \lambda}$, the different terms of which are defined in section 3.5.3. The polariton distribution in momentum space as a function of injection is shown in Fig. 6.9. A random and non-thermal LP occupation below threshold transforms to a peaked occupancy at $k_{||}$~0 above threshold. Also, there is no evidence of a polariton relaxation bottleneck at any injection. The measured polariton occupation at threshold is analyzed by the Maxwell-Boltzmann distribution $N = N_0 \exp\left(-\left(E(k_{||}) - E(0)\right) / k_B T_{LP}\right)$. The

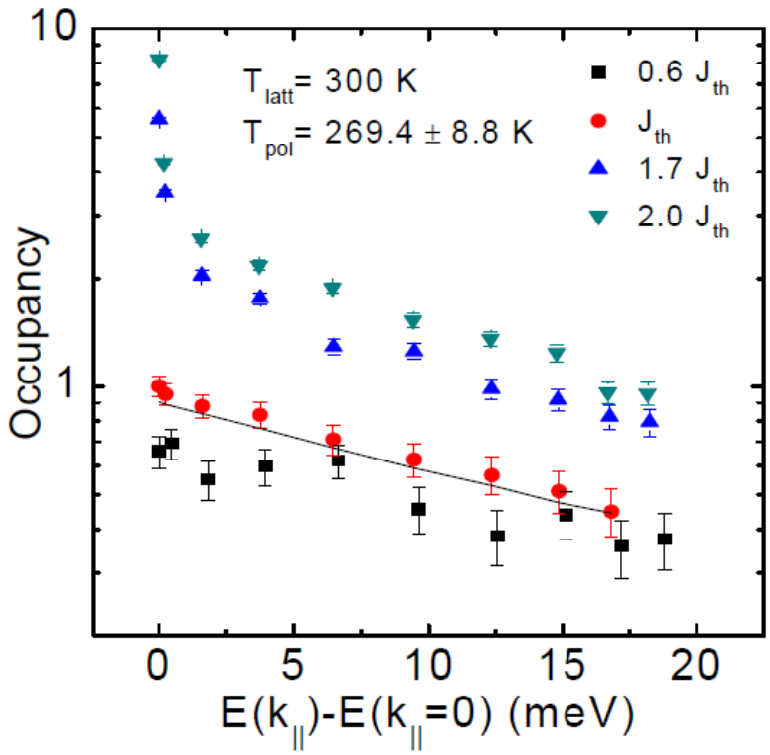

Fig. 6.9 LP ground state occupancy for different $k_{||}$ states obtained from angle-resolved EL at four different injections, along with Maxwell-Boltzmann distribution based analysis at $J=J_{th}$.

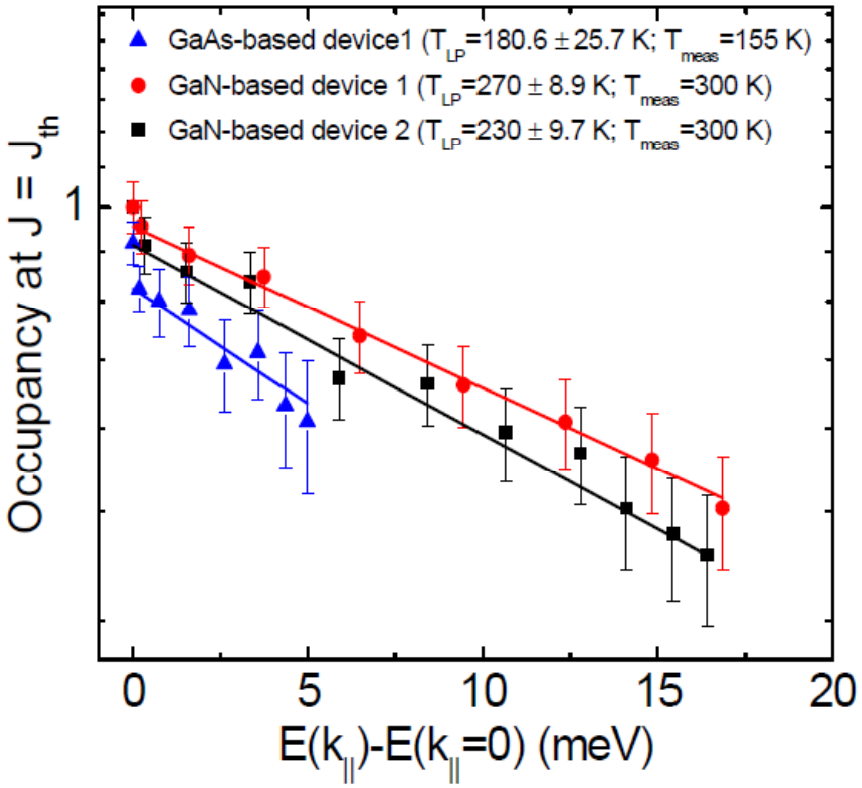

Fig. 6.10 Measured polariton occupation at $J=J_{th}$ for GaN-based Device 1, GaN-based Device 2 and GaAs-based Device 1 along with the Maxwell-Boltzmann distribution based analysis. The error bars indicate experimental uncertainty, whereas the standard deviation of the temperature fits are shown in the legend.

analysis, along with the measured data, for GaN Device 1 and GaN Device 2 are illustrated in Fig. 6.10. According to our analysis, the effective lower polariton temperature i.e. T_{LP} of GaN Device 1 and GaN Device 2 are 270±8.9 K and 230±9.7 K respectively. It is to be noted again that the measurements for these two devices were done at 300 K. The standard deviation here is derived from analysis of the occupation data, whereas the error bars in Fig. 6.10 indicate the uncertainty in experimental data. Also shown for comparison in Fig. 6.10 is the measured LP occupation data for GaAs Device 1 at 155 K. From analysis of this data with the Maxwell-Boltzmann distribution, a value of T_{LP}=190±30.5 K is derived. The values of T_{LP} and the measurement temperature

Table 6.1 Dislocation density, T_{LP} and τ_{LP} values in polariton lasers

Device	Dislocation density, n_{2d} (cm^{-2})	Measurement (lattice) temperature (K)	Polariton lifetime, τ_{LP} (ps)	LP temperature from analysis of occupation data, (K)
GaN Device 1	$6.44\pm0.34 \times 10^8$	300	0.60	270±8.9
GaN Device 2	$7.22\pm0.34 \times 10^8$	300	0.58	230±9.7
GaN Nanowire Device [a]	$\sim 10^2 - 10^3$	300	0.55	357
GaAs Device 1	~ 0	155	1.4	190±30.9
GaAs Device 2 [b]	~ 0	30	4.2	57

a) Ref. [21]; b) Ref. [81]

(T_{meas}) of these three devices are listed in Table 1. The values of T_{meas} and T_{LP} for the GaN nanowire and a surface-emitting InGaAs/GaAs quantum well polariton laser are also listed in the Table. Also the LP lifetimes of the considered devices are shown herein.

6.3.7 Discussion of Results

Dislocations and defects manifest themselves in a manner similar to impurity levels in a semiconductor, in that they create defect-bound excitons. The optical binding energy of impurity-bound excitons in GaN is ~5-7 meV [182, 183]. To estimate the binding energy, temperature dependent photoluminescence (PL) measurements are performed on GaN epitaxial layer, grown on a GaN-on-sapphire template identical to GaN Device 1. As shown in Fig. 6.11, the integrated PL intensities obtained from the temperature dependent measurements are analyzed with the Arrhenius formula:

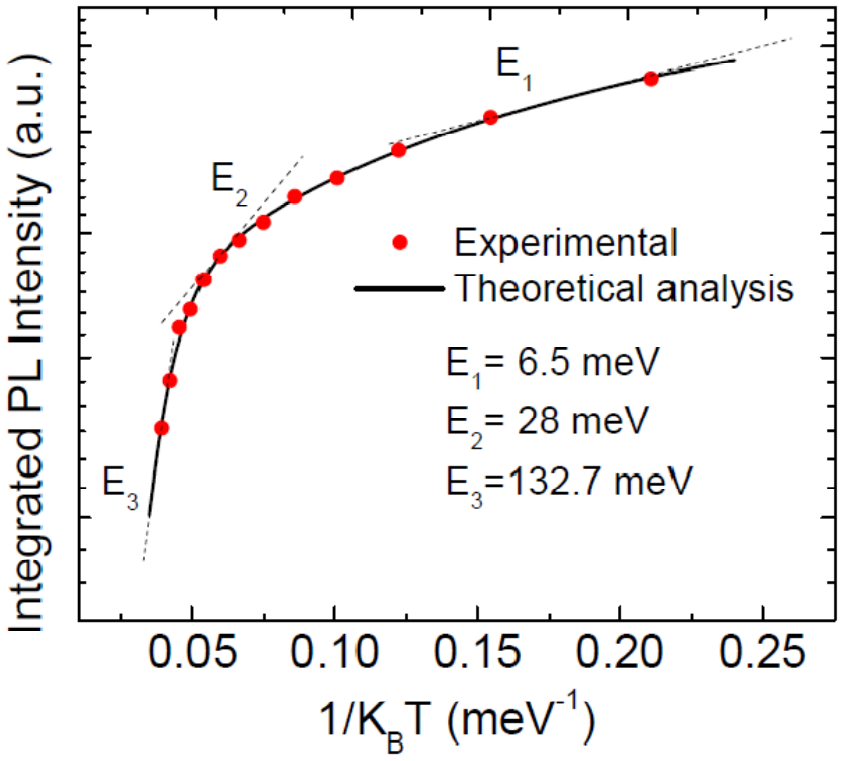

Fig. 6.11 Arrhenius plot of the integrated photoluminescence intensity as a function of reciprocal temperature of a GaN epitaxial layer, grown on a GaN-on-sapphire template, identical to GaN-based Device 1.

$I/I_o = 1\Big/\left[1 + A\exp\left(\frac{-E_1}{kT}\right) + B\exp\left(\frac{-E_2}{kT}\right) + C\exp\left(\frac{-E_3}{kT}\right)\right]$, where three non-radiative recombination channels having activation energies of E_1, E_2 and E_3 are considered. As discussed in Ref. 184, E_1 can be attributed to the binding energy of the excitons to defects and is found to be $\Delta = E_1 = 6.5$meV from our analysis. The formation of defect bound excitons will probably lower the polariton density and a fraction of the condensate. The thermal activation energy E_2 is related to the free exciton luminescence quenching and is of the same order of the X_A exciton binding energy [184]. The quenching of the luminescence represents the deactivation of the free exciton. The third channel having an activation energy of E_3 may be related to some deep level trap, which are quite prevalent in GaN-based material systems [184, 185]. It is difficult to comment on the exact nature

of the deep level without doing measurements such as deep level transient spectroscopy. Studies show that a deep level with a relatively low activation energy is more likely to be related to linear line defects due to dangling bonds along dislocation cores [185].

The observed lower polariton temperature in the devices with large defect densities can depend on the injection technique and polariton decay rates. With reference to the data listed in Table 1 and the description of the devices, it seems that the lowering of T_{LP} is independent of the pumping scheme. The polariton lifetime is determined by the cavity detuning and cavity quality factor. In examining the polariton lifetimes, which will affect the kinetics for the different devices, it is apparent that there is no correlation between τ_{LP} and the observation of T_{LP} smaller than T_{latt}. The observed lowering of T_{LP} in all probability originates from non-equilibrium effects originating from thermodynamic and kinetic factors and how the defects alter the coupling of excitons to cavity photons. A full Boltzmann equation solution of the problem, including the emission-capture processes at the defects, is required and this is beyond the scope of this thesis. Instead, a simplified theoretical model based on the assumption of thermal equilibrium is presented here which can phenomenologically describe the observed lowering of the polariton temperature.

6.3.8 Simplified Theoretical Modeling

In this simplified model [186], a bulk (three dimensional) semiconductor having a defect density n_T has been assumed. It is also assumed that the polariton gas may be described by the Bose-Einstein statistics. The chemical potential in this case would be pinned to the energy of the polariton condensate which is assumed to be independent on

the concentration of traps. We are interested in the high-energy tail of the polariton distribution that can be conveniently approximated by the Boltzmann exponential tail. We realize that the thermal equilibrium approximation is never perfectly valid, strictly speaking, but it is convenient as it allows introducing the effective polariton temperature T_{LP} and it is usually rather accurate in polariton lasers (see e.g. Refs. 18-20). The concentration of trapped exciton-polaritons n_T can be linked to the effective polariton temperature T_{LP} using the Boltzmann statistics as,

$$n = n_T + \frac{1}{2}\left(\frac{m}{\pi\hbar^2}\right)^{3/2}\left(k_B T_{LP}\right)^{3/2} \tag{6.5}$$

where k_B is the Boltzmann constant. Excitons can be trapped to shallow defects in a disordered semiconductor at low temperatures which is the most likely mechanism of polariton trapping in our system. n_T is linked to the defects concentration via the thermal activation law:

$$n_T \cong n_D\left(1 - e^{-\Delta/k_B T_{LP}}\right) \tag{6.6}$$

Here T_{latt} is the lattice temperature. Note, that the exciton trapping probability depends on the lattice temperature (not on T_{LP}) because the activation of trapped quasiparticles goes through their interaction with acoustic phonons. Equations 6.5 and 6.6 link the effective temperature of polaritons to the lattice temperature and concentration of polaritons. The next step is to exclude the concentration of polaritons. In order to do so, we assume that if there are no defects, the effective polariton temperature is equal to the lattice temperature. This assumption can only be correct in the case of full thermalization of the polariton gas,

that may or may not occur in the polariton lasing regime. We consider it as a useful limiting case that allows us to estimate the effective temperature lowering due to the trapping of a part of polaritons in defects. Within this approximation,

$$n = \frac{1}{2}\left(\frac{m}{\pi\hbar^2}\right)^{3/2}\left(k_B T_{latt}\right)^{3/2} \tag{6.7}$$

For the case of one-dimensional defects such as dislocations, the volume defect density n_D can be expressed via the two-dimensional defect density n_{2d} as $n_D \approx (n_{2d})^{3/2}$. Finally, the effective temperature T_{LP} can be expressed through the lattice temperature T_{latt} using Eqs. 6.5-6.7 as:

$$k_B T_{Lp} = k_B T_{latt}\left[1 - 2\left(\frac{\pi\hbar^2 n_{2D}}{m k_B T_{latt}}\right)^{3/2}\left(1 - \exp\left(-\frac{\Delta}{k_B T_{latt}}\right)\right)\right]^{2/3} \tag{6.8}$$

Remarkably, Eq. (4) predicts $T_{LP} \le T_{latt}$, while of course for a kinetically driven condensation process, T_{LP} will be larger than T_{latt}. The fact that $T_{LP} \le T_{latt}$ as predicted by Eq. 6.8, is indeed observed in the two bulk GaN-based polariton lasers, whereas $T_{LP} > T_{latt}$ is observed for the GaN nanowire laser and the two GaAs-based lasers listed in Table 1. Figure 6.12(a) shows a plot of the effective temperature T_{LP} versus T_{latt} for the two GaN devices, where the effective mass has been extracted from the angle dependent electroluminescence data and the value of Δ=6.5 meV is assumed. It can be seen that for the constant lattice temperature of 300K, the effective polariton temperature is lower, as derived from analysis of the occupation data of Fig.6.10. Thus it is essential to take into

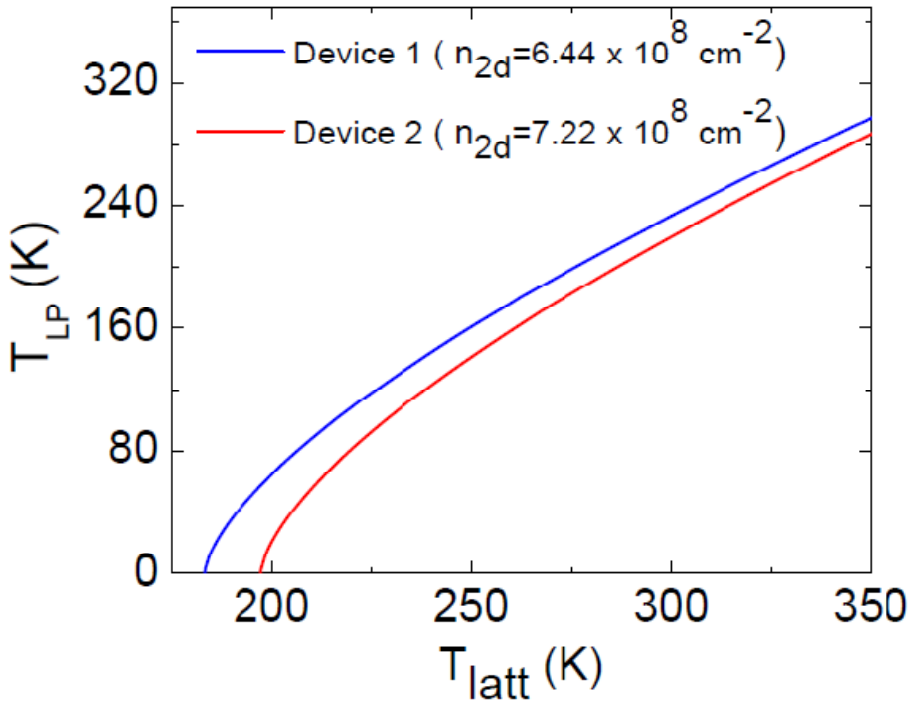

(a)

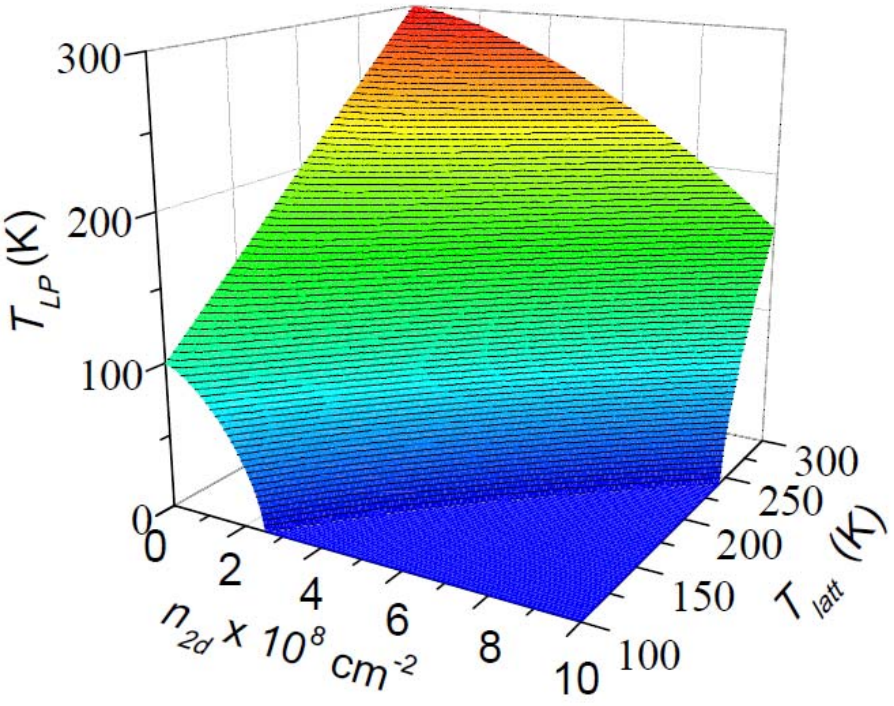

(b)

Fig. 6.12 (a) A plot of the effective LP temperature (T_{LP}) as a function of lattice temperature (T_{latt}) for the two GaN-based devices, (b) A 3D plot of effective LP temperature, lattice temperature and the 2D defect density.

account the presence of impurities and defects in the active region of the polariton laser to accurately characterize the polariton condensate. Figure 6.12(b) shows a three-dimensional plot with n_{2d}, T_{LP} and T_{latt} as variables. It is seen that the lowering of T_{LP} is maximum at low lattice temperatures and high defect densities.

6.4 Summary

In conclusion, we have investigated the small-signal electrical modulation characteristics of a polariton laser at room temperature. The variation of the resonance frequency, derived from the measured modulation response, with polariton occupation in the ground state has been analyzed with a rate equation model from which the polariton-polariton scattering rate is derived. The linewidth of coherent emission beyond threshold exhibits negligible broadening with high frequency modulation, which indicates that chirp is negligible. Differential gain and gain compression in a polariton laser are also phenomenologically defined, calculated and interpreted in terms of lasing parameters. We also discuss the role of defects in optically and electrically pumped polariton lasers. Though the study focuses mostly on dynamic condensation and effective temperature of the lower polariton condensate, it is believed that the presence of defects will affect other characteristics of polariton lasers as well, for e.g. the small signal modulation response, as has been observed in our study. Higher resonance frequencies and modulation bandwidths should be attained in polariton devices made with defect-free material.

Chapter VII

Optical Amplification in the Strong-Coupling Regime

7.1 Introduction

Optical amplifiers are deemed to be one of the most important components in modern optical communication networks [187-191]. As data transmitted over optical fibers are susceptible to signal attenuation and dispersion, it is imperative to have regenerators or optical amplifiers in the communication link for reliable transfer of information. The process of regeneration involves photo-detection, electrical signal amplification and retransmission. On the other hand, optical amplification offers a simplified means of in-line transmission of the optical signal without any optoelectronic conversion. Optical amplifiers are generally categorized as optical fiber amplifiers (OFAs) and semiconductor optical amplifiers (SOAs) [190]. While OFAs, such as Erbium doped fiber amplifiers (EDFAs), have dominated optical communication networks, recent development in semiconductor materials growth and device fabrication technologies have generated renewed interests in SOAs for short- and long-haul optical communications. Besides their realization as basic signal amplifiers, they can also be employed as optical switch, modulator, wavelength converter or other functional elements in optical communication networks and processing systems [187-191].

Conventional SOAs, which are designed and implemented based on the principle of stimulated emission in the gain medium, invariably operate in the weak-coupling regime [190, 191]. However, a recent theoretical study by Solnyshkov et al. shows that optical amplification in a semiconductor gain medium can be realized by means of stimulated scattering as well, provided the device is operating in the strong-coupling regime [192]. In this chapter we report our experimental studies towards the possible realization of a bulk GaN-based SOA, which is expected to operate in the strong-coupling regime. Though this material system does not allow amplification in the telecommunication wavelength (1.3 or 1.5 μm), it holds promise for short-range amplifications in areas related to biomedical and sensors, optoelectronic integrated circuits (OEICs) and all-optical computing and quantum information processing systems.

7.2 Theory and Background

Experimental realization of a SOA based on guided polaritons in a bulk-GaN waveguide is intricately related to the theory and concept of bulk polaritons. In this section, the theory of bulk polaritons and its major differences with microcavity polaritons is presented. Next, the underlying theory behind optical amplification in the strong-coupling regime is elucidated based on the framework presented in [192].

7.2.1 Theory of Bulk Polaritons

The concept of bulk polaritons was first proposed in the early works of Huang, Pekar and Hopfield in the 1950s [44, 45, 193]. Huang first observed that the nature of light can depart from that of an electromagnetic wave and assume a more mechanical nature because of interaction between the photon field and ionic-polarizability of the

solid. Later Hopfield defined this entity as a *polariton* and suggested that in an infinite crystal (which can be a bulk semiconductor), the exciton is strongly coupled to a single photon mode because of momentum selection rules arising from translational invariance of the system [45]. This coupled mode, which is defined as a polariton, is in fact the true propagating mode in the system. In this picture, the one-to-one coupling between excitons and photons having same momenta results in the emergence of two normal modes, which are the so called upper and lower polaritons. In analogy with two linearly coupled harmonic oscillators, the bulk polariton dispersion characteristics can be expressed using the following relation:

$$E_{LP,UP} = \left(\frac{E_X + E}{2}\right) \mp \sqrt{\left(\frac{E_X - E}{2}\right)^2 + \left(\hbar\Omega\right)^2} \qquad (7.1)$$

Here E_x and E are the energies of the coupled exciton and photon and $\hbar\Omega$ is the coupling strength, as described in our discussion of microcavity polaritons. Based on this equation, the UP and LP dispersion characteristics of bulk polaritons in a GaN-based system is shown in Fig. 7.1. A distinct anticrossing exists between the two polariton modes, in the vicinity of which the polaritons are a mixture of the constituent exciton and photon modes. However, far from this anticrossing or the bottleneck region, the lower and upper polaritons posses characteristics similar to those of uncoupled excitons (at high values of k) and photons (at small values of k). Because of the absence of a $k=0$ state in this dispersion relation, bulk polaritons tend to accumulate more near the bottleneck region [96] and light is emitted at the corresponding energy and momentum upon their spontaneous radiative recombination. For this reason, due consideration of polaritonic

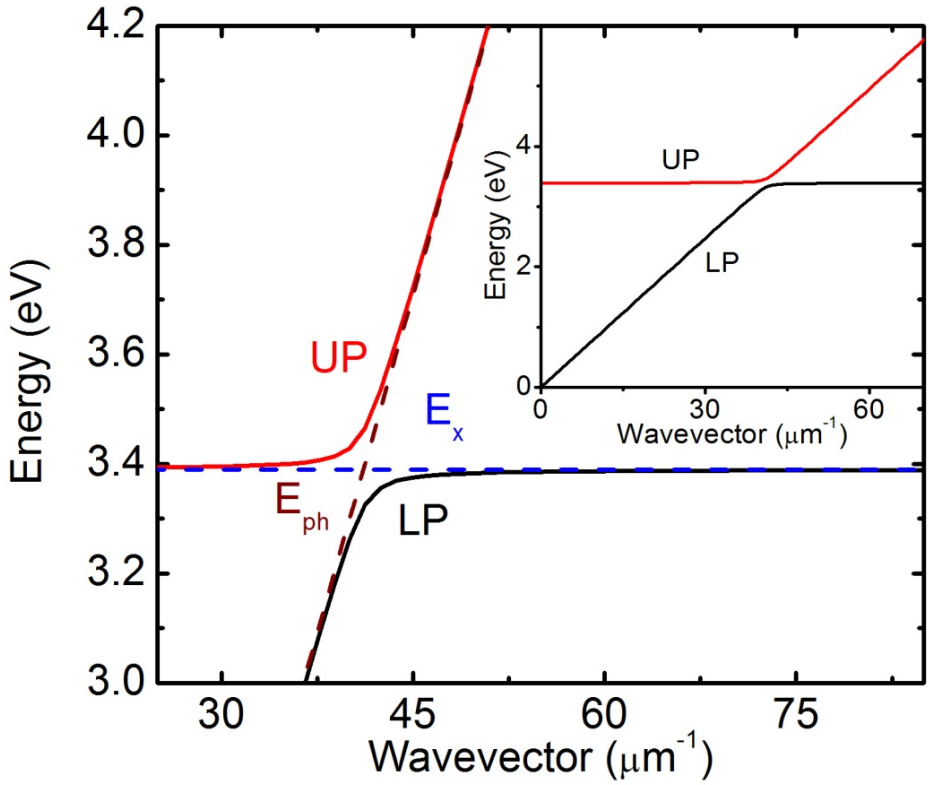

Fig. 7.1 Bulk polariton dispersion characteristics in GaN; inset shows the dispersion over a larger range of the wave vector

effects is necessary in the theoretical analysis of photoluminescence measurements performed on bulk semiconductors.

7.2.2 Experimental Studies on Bulk Polaritons

Experimental investigation of bulk polaritons has remained limited to the case of optically excited systems. Ever since the proposition by Hopfield, numerous experiments have been performed to study bulk polaritons in direct bandgap semiconductors and halides. The first experimental observation of bulk polaritons was reported by Frohlic et al. [46] in CuCl. Weisbuch et al. reported the first experimental study of bulk polaritons in semiconductors, employing high purity GaAs epitaxial layers [47]. Since then bulk polaritonic effects have been observed and studied using resonant and non-resonant PL

spectroscopy in GaAs, CdS, ZnO, ZnTe and ZnSe material systems [48, 194-196]. In bulk GaN semiconductor, which is the material used in this study, polaritonic effects have been studied by photoluminescence and photoreflectance measurements at low temperatures. However, because bulk polaritons are stationary states which transform into photons only at the crystal surface, their experimental detection and theoretical interpretation is found to be rather complicated compared to the case of microcavity polaritons. In what follows, we describe the basic differences between bulk and microcavity polaritons.

7.2.3 Bulk vs. Microcavity Polaritons

A generalized dispersion characteristics of the bulk polaritons, along with that of a 2D microcavity polariton, is shown in Fig. 7.2. An important difference between bulk and microcavity polariton is that whereas microcavity polaritons have reduced dimensionalities of wavevector $k_{||}$, bulk polaritons have the same 3D wavevectors as their strongly coupled excitons and photons. Similar to the case of microcavity polaritons, the LP and UP branches of bulk polaritons are exciton- and photon-like respectively at high $k_{||}$. However, whereas microcavity polaritons have well defined minima at $k_{||}\sim 0$, the $k=0$ state of the bulk polariton is non-existent because a photon with $k=0$ does not exist in the strict sense. This means that a dynamic condensation process is prohibited in the bulk polariton picture, contrary to the case of microcavity polariton. Also, whereas both the UP and LP branches of the microcavity polaritons reside within the light cone (which is defined by the dispersion of the free-space photon), the LP branch of the bulk polariton lies outside. Consequently bulk polaritons from the LP branch are not out-coupled to free space and hence are not detectable in experiments. Moreover, because of their 3D wave-

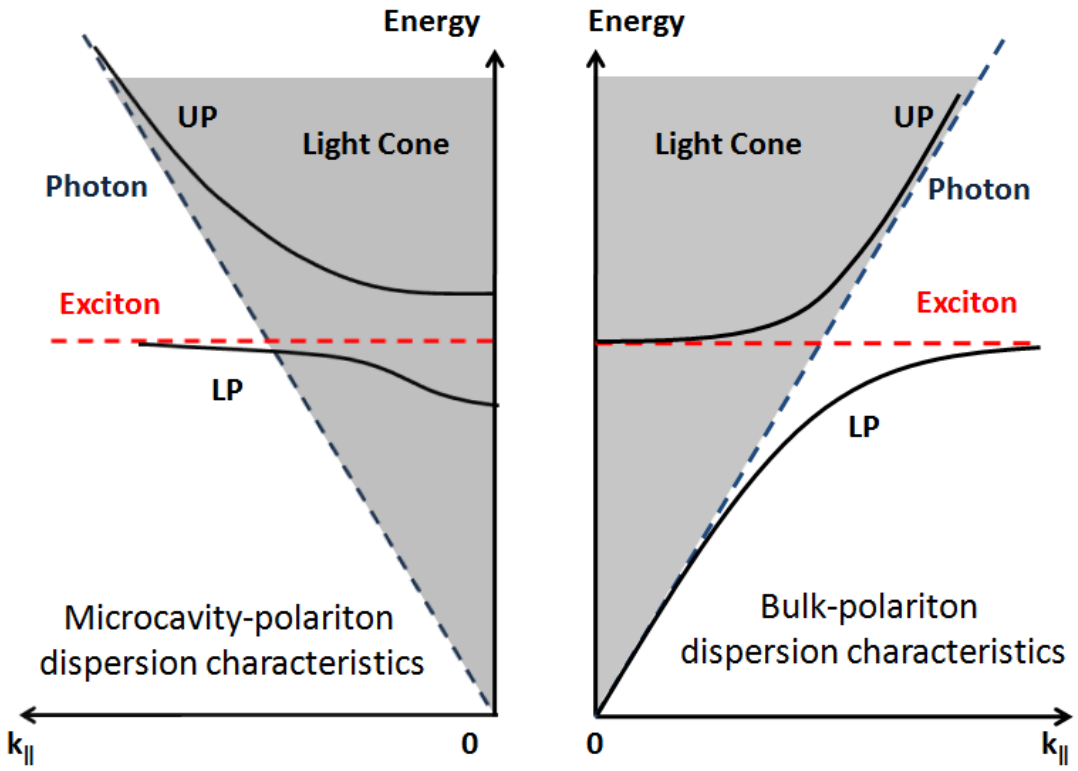

Fig. 7.2 A comparison between the dispersion relation of bulk and 2D microcavity polaritons.

vectors, bulk-polaritons have large phase and kinetic energy and hence they are very susceptible to dephasing channels in the crystal, such as defects, impurities or photonic disorder. Bulk polariton based systems also offer less flexibility than microcavity-based environments because in the bulk polariton case, design parameters like dimensionality of the emitter, number of quantum wells, cavity length etc. are non-existent. For these reasons, experimental detection and characterization of bulk polaritons are more difficult than their microcavity-polariton counterparts.

7.2.4 Theory of SOA in the Strong-Coupling Regime

While conventional SOAs work on the principle of stimulated emission, a novel scheme of optical amplification has been proposed by Solnyshkov et al. [192] based on stimulated scattering of guided polariton modes. The suggested gain medium in this

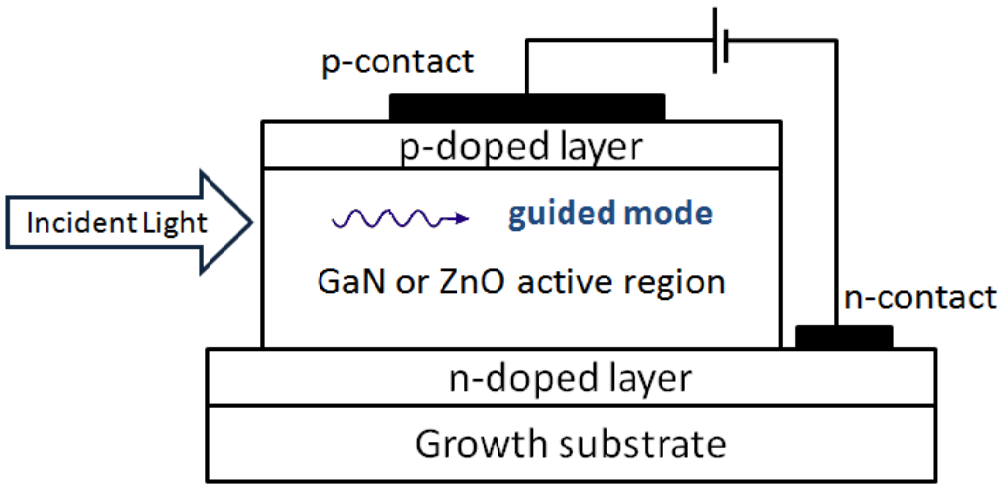

(a)

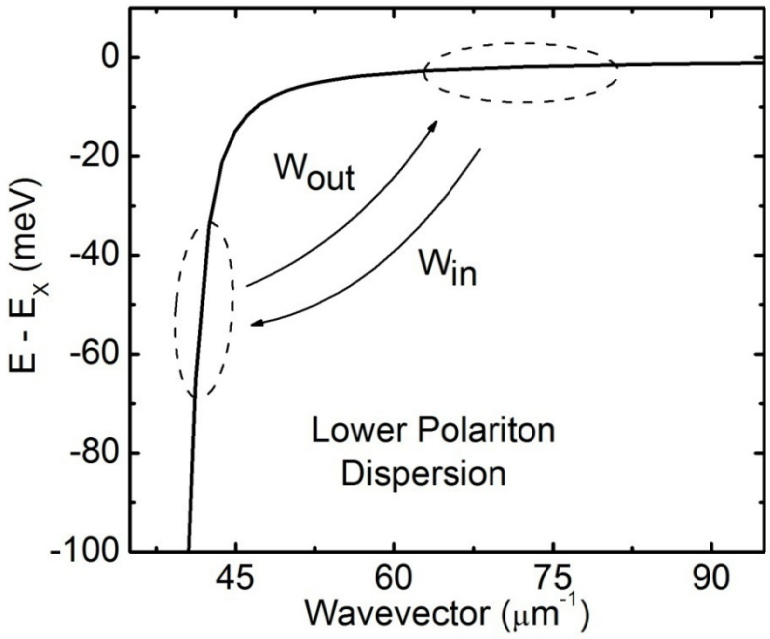

(b)

Fig. 7.3 (a) A generalized schematic of the semiconductor optical amplifier proposed by Solnyshkov et al., (b) calculated LP dispersion of a bulk-GaN waveguide.

scheme is bulk GaN or ZnO, which are wide bandgap semiconductors with high exciton binding energies and oscillator strengths. It is expected that strong-coupling, and thereby optical amplification can be achieved in these systems at room temperature under electrical or optical excitation. A schematic of the proposed electrically pumped device

comprising of bulk GaN or ZnO as the waveguide and gain region is shown in Fig. 7.3(a). Assuming single mode propagation, the polariton dispersion for this waveguide can be obtained by combining the eigen-value equation of a symmetric dielectric slab waveguide and the bulk polariton dispersion relation (Eqn. 7.1). Figure 7.3(b) shows the lower polariton dispersion for a bulk-GaN waveguide. Electrical or optical excitation of this device creates an exciton reservoir, which enables relaxation of exciton-polaritons from the reservoir down to the guided mode region, i.e. towards smaller wavevector of the polariton dispersion (Fig. 7.3(b)). The efficiency of this process is strongly dependent on $\Delta E = E - E_X$, which is the energy difference between the guided mode and the exciton state. Using semi-classical Boltzmann equation based analysis it can be shown that for an optimal value of ΔE, the exciton reservoir results stimulated scattering to the guided polariton mode and amplifies the propagating signal, provided that losses are overcome in the medium. Whereas in a conventional SOA an electron and a hole recombine to create a photon, in the strongly-coupled SOA, two excitons in the reservoir scatter with each other for one of them to relax down to the guided exciton-polariton mode and amplify the propagating signal. These scattering rates are in the order of ps^{-1}, which is fast enough to amplify the signal in spite of the high propagation velocity (~ 10^7 m/s) of the guided mode.

According to the theoretical calculations reported by Solnyshkov et al. [192], the guided polariton mode should be ~35 meV below the exciton energy in a bulk GaN waveguide for signal amplification to occur. Besides ΔE, the incident signal intensity is also important in this theoretical framework. The signal intensity should be sufficiently low as otherwise the exciton reservoir gets depleted at high signal intensities. Depending

on the guided signal intensity, a maximum amplification factor of ~9dB has been predicted at room temperature in a bulk GaN waveguide.

7.3 Heterostructure Growth and Device Fabrication

The device heterostructure used in this study is grown by plasma-assisted molecular beam epitaxy (PAMBE) on c-plane GaN-on-sapphire substrate. The PAMBE grown heterostructure (Fig. 7.4) is identical to that of the GaN-based polariton laser diode discussed in Chapter 5.. The 300 nm intrinsic bulk-GaN active region, which is embedded between AlGaN and InAlN cladding layers, acts as the waveguide in this device. Device fabrication has been carried out by standard UV-lithography, reactive ion etching, plasma enhanced chemical vapor deposition and electron beam evaporation techniques. The length (L) and width (W) of the device are defined along x- and y-axis (Fig. 7.4) respectively. Devices having lengths of 500 µm and 80 µm were fabricated for

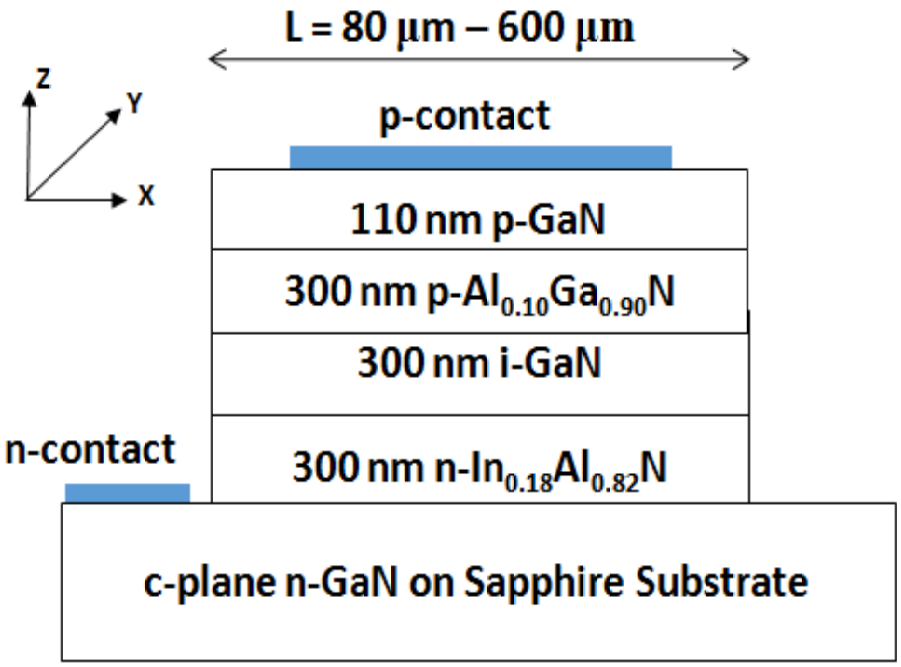

Fig. 7.4 A cross-sectional schematic of the device heterostructure along with p- and n-contacts and the lateral dimensions.

electrical measurements in this study. Four other devices having L = 600, 700, 800 and 900 μm were fabricated to measure the waveguide loss. The widths of all the devices are kept fixed at W=50 um. To facilitate probing of the devices with smaller dimensions, metal interconnects have been formed onto SiO_2 contact pads. The p- and n-contacts of the devices are realized with Ni/Au (5nm/200nm) and Ti/Au (20nm/200nm) ohmic contacts respectively. After initial pattering and reactive ion etching, both the facets of the device are etched down by focused ion beam milling (FIB) to define the length. A subsequent FIB milling has been performed at low injection to form optically smooth surfaces. Finally, using e-beam evaporation technique, SiO_2 is deposited onto both the FIB etched facets to form antireflection coatings. The optimal thickness of the deposited SiO_2 is calibrated using spectroscopic ellipsometry prior to deposition onto the facets.

7.4 Measurements and Results

The material characteristics of the bulk-GaN active region were studied by temperature dependent and time-resolved photoluminescence measurements and have already been described in chapter 6. Waveguide loss, electroluminescence and time-integrated intensity measurements have been performed on the fabricated devices to study possible optical amplification effects. These measurements and the obtained results are discussed as follows.

7.4.1 Diode Characteristics and Waveguide Loss Measurements

The diode current-voltage (I-V) characteristics, measured at room temperature, (Fig. 7.5(a)) shows a turn-on voltage of ~3 V and a minimum reverse leakage current of ~ 1nA. The series resistance is estimated to be ~114 ohms at a forward bias of 4 volts. In order to characterize the waveguide, the propagation loss, which includes the scattering

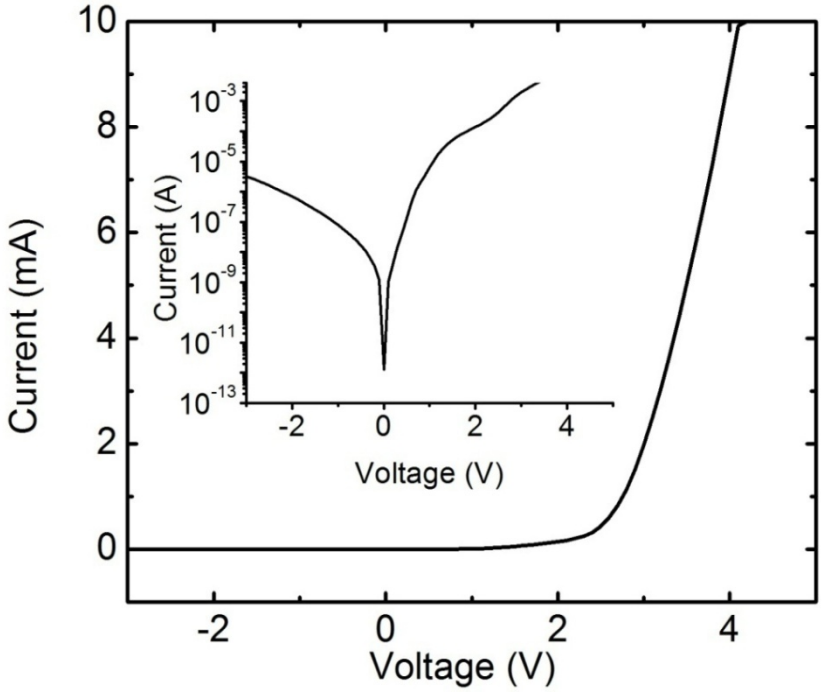

(a)

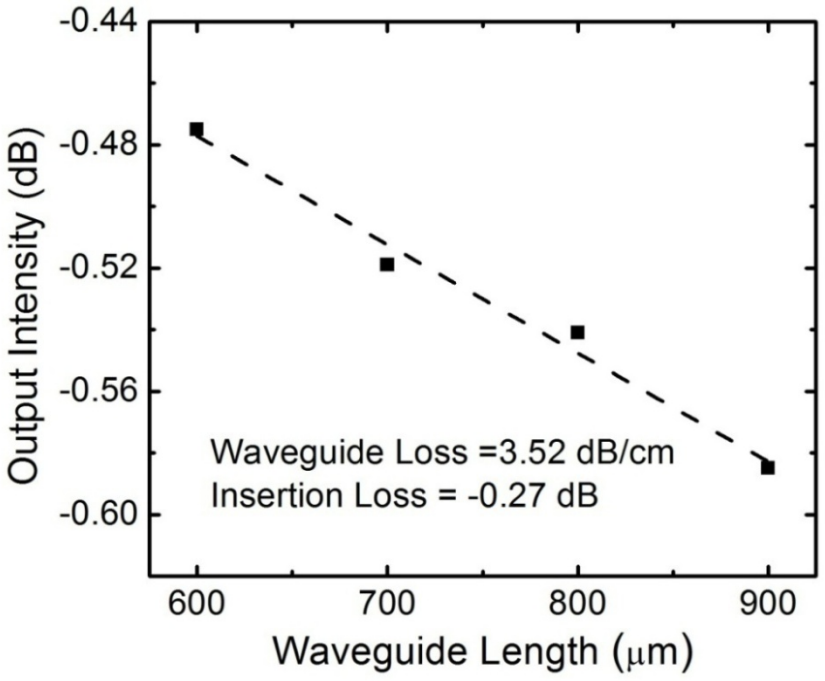

(b)

Fig. 7.5 (a) Current-voltage characteristics of the bulk GaN diode; inset shows the I-V characteristics in logscale, (b) output intensity of the waveguide as a function of waveguide length.

loss and substrate leakage, is obtained from transmission measurements on devices having different lengths. In this measurement, the waveguides are end-fired with a 540 nm He:Ne laser focused to a 10 μm^2 spot and the output intensity is measured with a charged coupled device (CCD) detector. The measured output intensity as a function of guide length is plotted in Fig. 7.5(b), from which a loss of $\gamma = 3.52$ dB/cm is derived. The insertion loss is estimated to be -0.27 dB/cm.

7.4.2 Measurement System and Ti:Sapphire Laser Calibration

The experimental arrangement for the measurements performed in this study is schematically shown in Fig. 7.6. The light intended to be amplified by the device is generated using a tunable, frequency doubled Ti:Sapphire laser. The resonator cavity of this laser contains a birefringent Ti:Sapphire rod, along with adjustable optical components. Electronic driver circuits and chiller mediated temperature controller have been utilized to minimize timing jitter and to stabilize the laser output. Nevertheless, to take into account any temporal fluctuation, the frequency doubled output of the laser is transmitted through a beam splitter into a multi-mode fiber and monitored using a UV-spectrometer. The other output from the beam splitter is collected using a single mode fiber and incident on one facet of the device, as shown in the schematic diagram of Fig. 7.6. The power of the incident light is adjusted using a neutral density filter to ensure that the signal intensity is low enough for the device to amplify. At the detection end, light is collected from the other facet of the device using a multi-mode fiber, which is coupled to a photomultiplier tube (PMT) and a triple grating monochromator having a minimum spectral resolution of 0.023 nm. The device is electrically biased with a continuous wave DC signal at room temperature. The measurement setup has been calibrated to take into

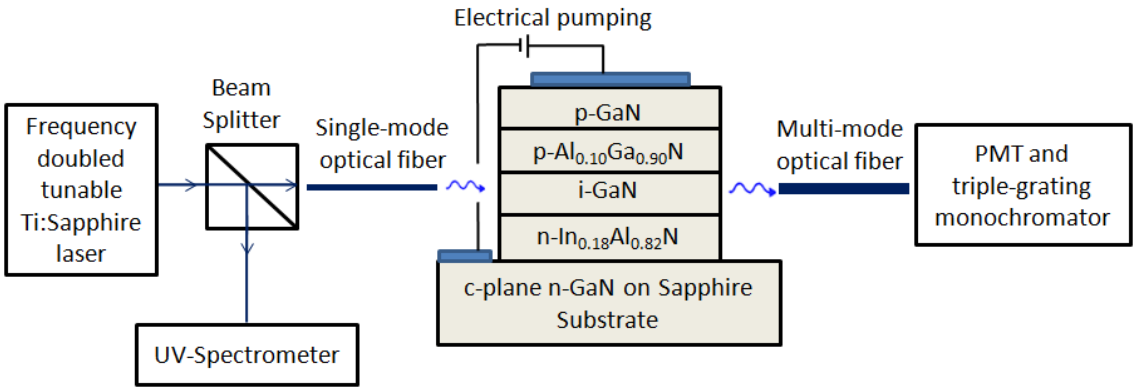

Fig. 7.6 A schematic diagram of the experimental setup used in this study.

account fiber losses and fiber-coupling losses.

The photon energy incident onto the waveguide is varied by tuning the slits and prism sequence of the Ti: Sapphire laser. Fig. 7.7(a) shows frequency doubled outputs of the Ti:Sapphire laser obtained under different positions of the slit and prism sequence. The energy reference of Fig. 7.7(b) is the GaN exciton energy of 3.418 eV, as obtained from room temperature photoluminescence measurements (Fig. 7.7(b)). The laser wavelength has been varied to obtain the optimal exciton to photon energy difference $\Delta E = E - E_X$, as reported in [192]. The linewidth of the incident laser beam is ~0.865 nm (7.81 meV) and the lineshape is near Gaussian. Two techniques have been employed to study possible amplification effects. In the first, electroluminescence spectra, along with the laser beam being incident onto the device, is recorded using the PMT and the monochromator over a range of injection current densities and incident photon energies. In the second technique, output light from the device facet is spectrally filtered using the monochromator and time integrated luminescence is recorded using the PMT. The current densities and photon energies have been varied in this scheme as well to obtain the necessary scattering rate required for amplification of the guided polariton mode.

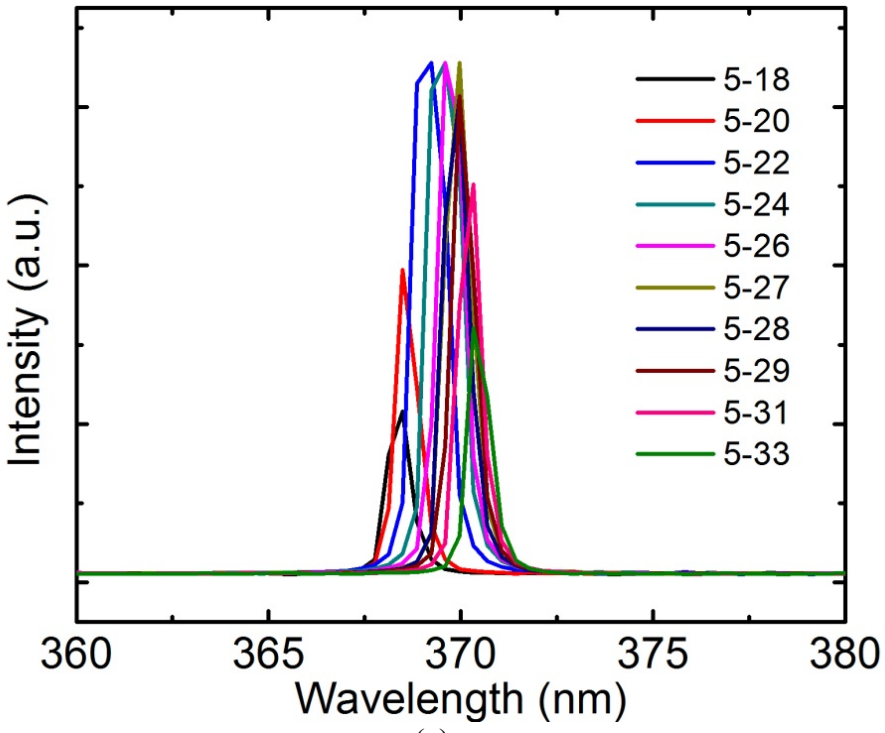

(a)

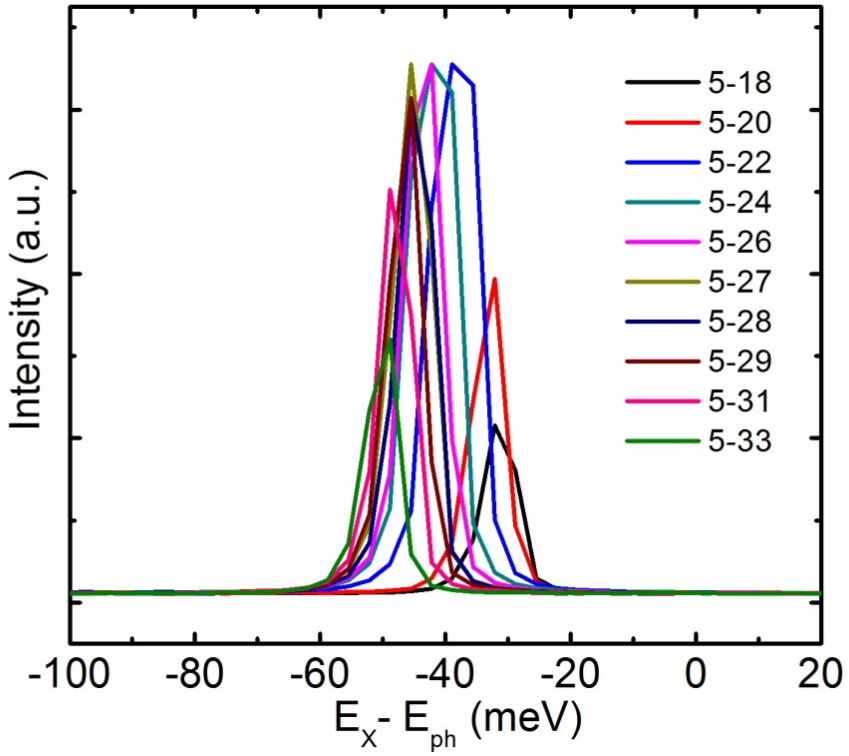

(b)

Fig. 7.7 (a) Frequency doubled outputs of the tunable Ti:Sapphire laser for different positions of the laser's slit and prism sequence, (b) frequency doubled output of the laser, where the GaN-exciton energy is taken as the reference.

7.4.3 Electroluminescence Measurements

Electroluminescence (EL) spectra measured from the device under different cw electrical injections are shown in Fig. 7.8. The output light is collected normal to the AR-coated facet using a multimode optical fiber and recorded using a PMT coupled to the monochromator. The maximum current bias applied to the 400 x 50 μm^2 device is 30 mA, whereas for the 80 x 50 μm^2 device it is 6 mA. These values of the current bias correspond to a current density of 150 A/cm^2 and a carrier density of ~1.8 x 10^{16} cm^{-2}. Hence the injected carrier density is lower than the threshold carrier densities obtained for a electrically pumped GaN-based polariton laser having identical active region. This is one of the necessary conditions for optical amplification effect in this device [192], similar to the case of conventional SOAs, which are operated below the photon lasing threshold.

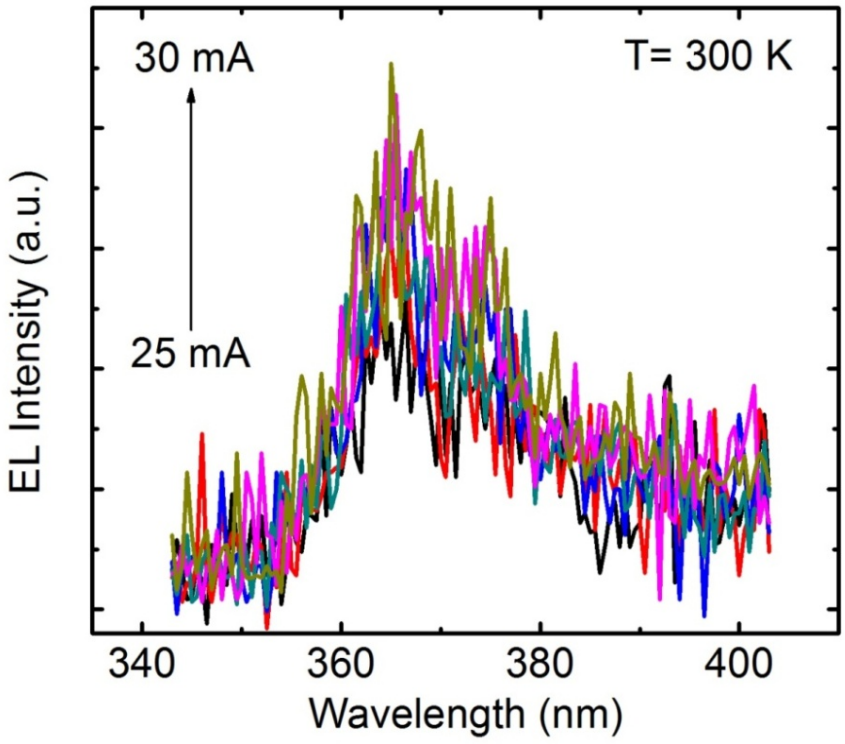

Fig. 7.8 EL spectra measured in a direction normal to the AR-coated facet of the device.

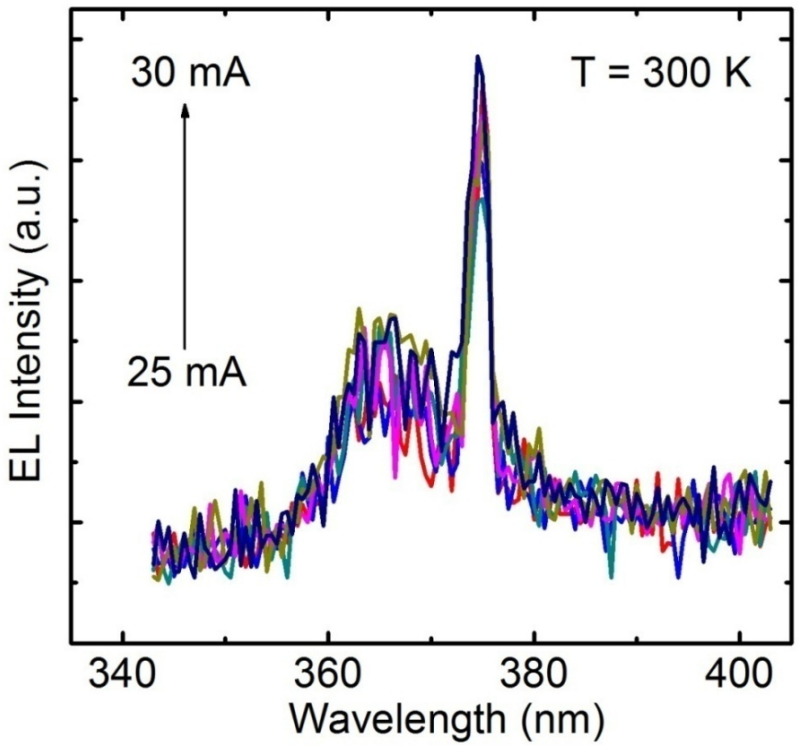

Figure 7.9 Recorded EL spectra with the laser tuned to 372 nm and the device biased at different injection current densities.

Next, using identical optical alignment and detection settings, the Ti:Sapphire laser output is made incident normal to one facet of the amplifier device using a single mode UV optical fiber and light output from the other facet of the amplifier is recorded. By tuning the Ti: Sapphire laser, the incident photon energy is varied to obtain the optimal ΔE values for possible amplification effect. The recorded EL spectra with the laser tuned to 372 nm and the device biased at different injection current densities are shown in Fig. 7.9. As can be seen, both the GaN and the laser peak can be resolved in the EL spectra. The previously recorded EL spectra with the laser beam off (Fig. 7.8) serves as the baseline to analyze possible amplification effects. However no amplification of the incident light is observed upon comparison between the two sets of EL spectra.

7.4.4 Time-Integrated Intensity Measurements

In this scheme, the luminescence is spectrally filtered using a monochromator with a minimum spectral resolution of 0.03 nm, and then recorded using a high gain PMT with an integration time of 300 ms. At first, the laser beam is incident onto one facet of the device and the luminescence intensity I_1 is recorded from the other facet without any applied electrical bias. Next, using identical measurement setup, luminescence intensity I_2 from the output facet is recorded under different forward bias currents. In this measurement, the current bias is gradually increased from 2 mA to 6 mA and each current bias is maintained for ~10s, which is significantly larger than the PMT's signal integration time of 300 ms. Hence, an amplification effect should appear as an increase of the output luminescence at some current bias of the device. However, it is important to

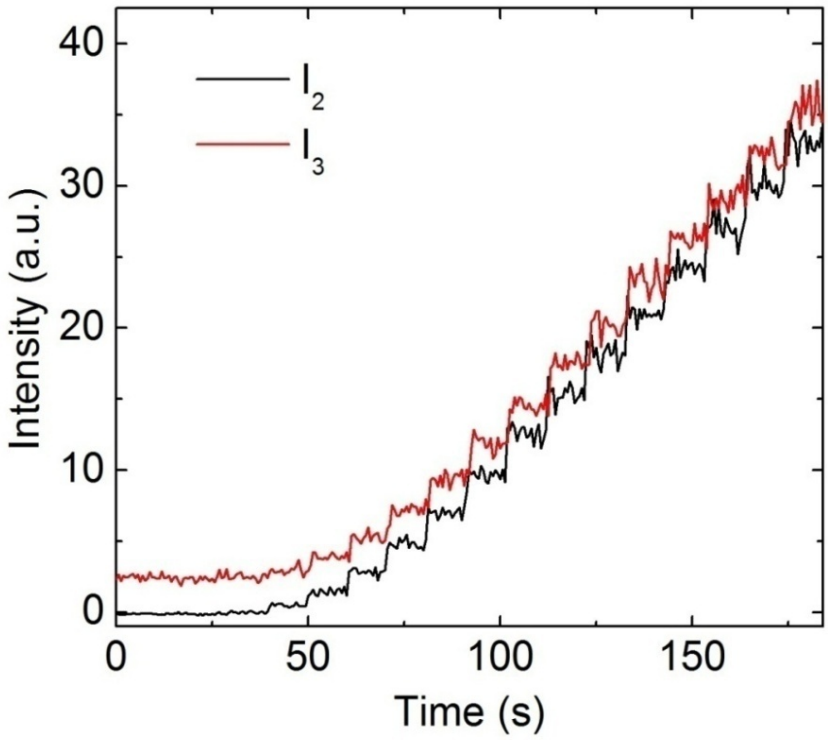

Fig. 7.10 Measured time-integrated intensities I_2 and I_3 while the device's current bias is incremented approximately every 10s

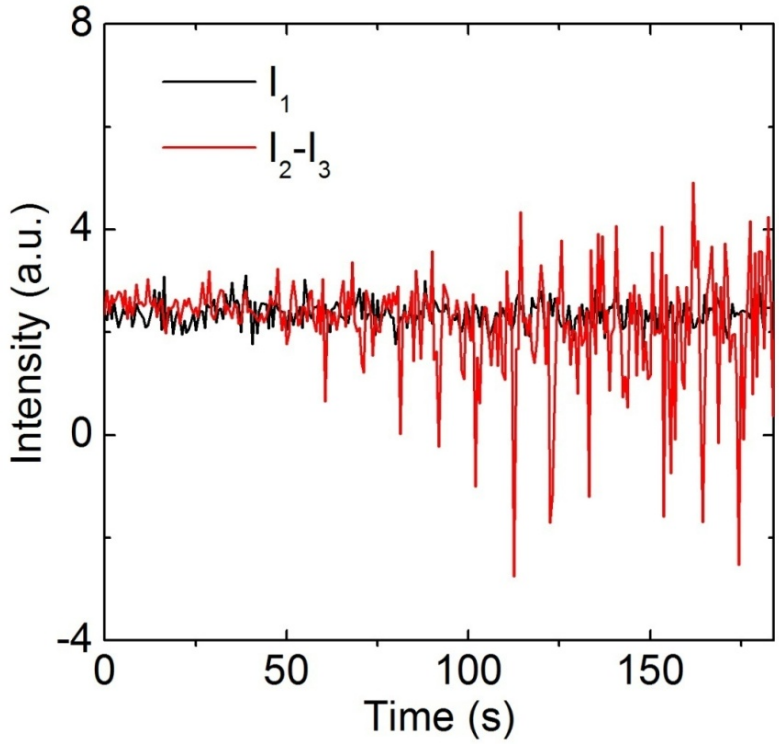

Fig. 7.11 Measured time-integrated intensities I_1 and I_2-I_3 plotted as a function of time

note that because of the close proximity between E_X and E_{ph}, the recorded intensity I_2 comprises of both the EL emission and the guided photon counts. Hence for comparison, under same optical alignment and forward bias currents, device EL intensity I_3 is recorded without any laser beam being incident onto the facet.

Figures 7.10 and 7.11 show the measured intensities I_1, I_2 and I_3 for an incident beam, λ=367 nm, which corresponds to $\Delta E = -40$ meV. It can be shown that I_2-I_3 , which is plotted in Fig. 7.11, takes into account the waveguide loss, fiber losses and the fiber coupling losses. Therefore, an approximate estimate of signal amplification can be obtained from the ratio (I_2-I_3)/I_1, which we define here as amplification factor. As shown in Fig. 7.12(a), at all injection levels, $(I_3 - I_2)/I_1 \approx 1$, within the thermal noise of the PMT sensitivity. This corresponds to an amplification 0 dB. In our measurement, the

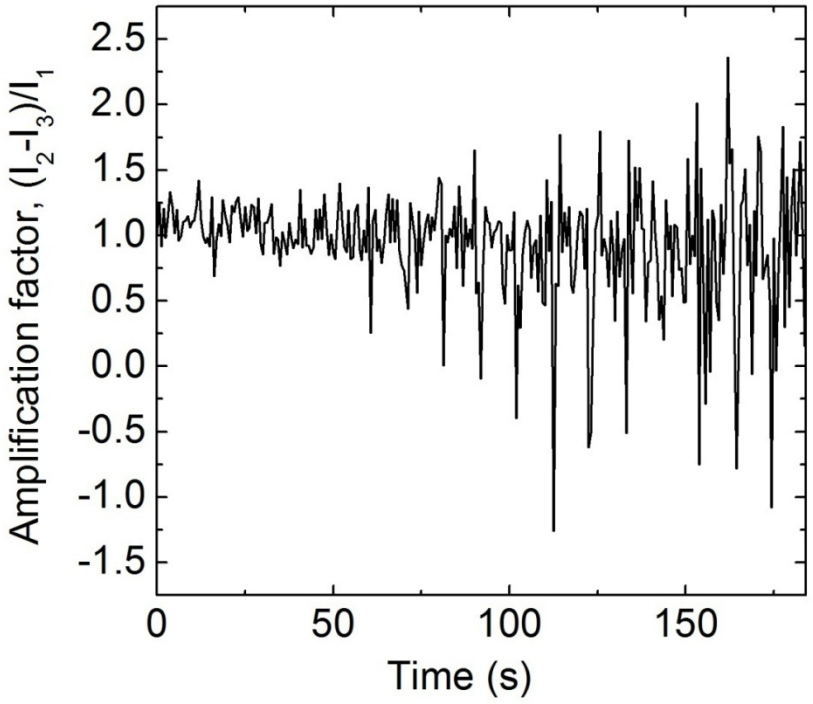

(a)

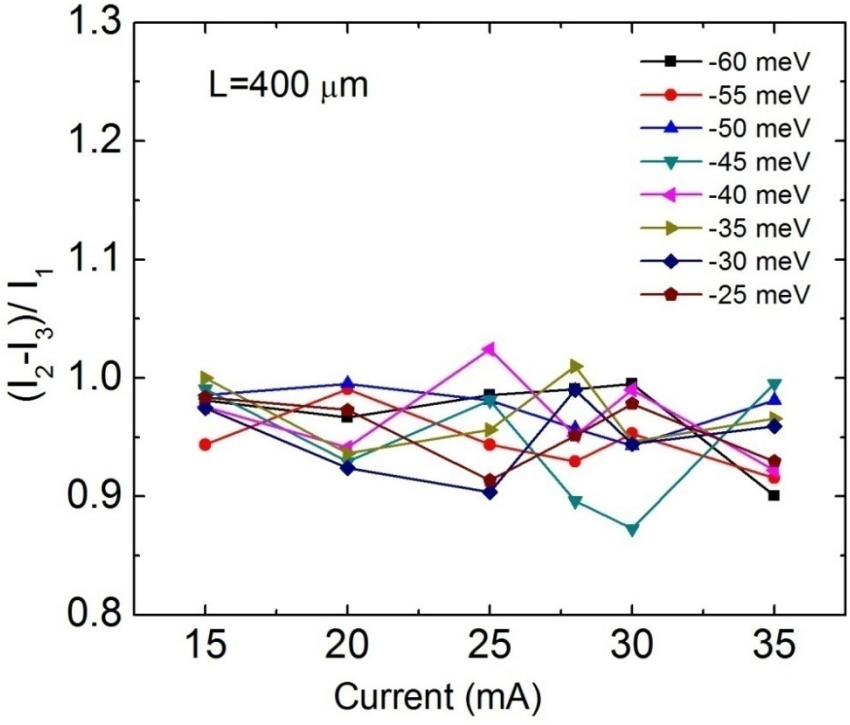

(b)

Fig. 7.12 (a) The amplification factor plotted as a function of time corresponding to the results shown in Fig. 7.15, (b) amplification factor as a function of injection current for different values of ΔE

incident laser peak emission energy has been varied between 365 and 372 nm, which corresponds to ΔE values of 0 and -100 meV respectively. The amplification factor is plotted as a function of the incident peak emission energy in Fig. 7.12(b) for different applied current biases. It is obvious that the amplification ratio is ~1 or slightly less over the entire range.

7.5 Discussions and Conclusion

Based on the experimental results of the present study, we cannot confirm the observation of optical amplification of the guided polariton mode in our bulk GaN-based device. Several challenges and limitations can be associated with this observation. As discussed earlier, optical amplification in the current scheme is closely related to the bulk polariton modes, which have been observed in GaN only at low temperatures, in high quality MBE or HVPE grown epitaxial layers. Because of the nature of the bulk-polariton dispersion characteristics (Fig. 7.1), it is expected that only excitons with large wave vectors may scatter to the guided polariton mode to fulfill momentum conservation requirement. This indicates that the scattering rate may be insufficient for signal amplification to take place. It is also noteworthy that the dispersion characteristics of the polariton in this scheme is strongly non-linear at the exciton-to-waveguide mode anticrossing. This may cause the guided polariton mode to get distorted while propagating through the waveguide. Consequently, instead of an amplified signal, a spread in time low amplitude signal may be observed at the output. Time evolution of the propagating mode can provide further insight in this regard. The defects and dislocations appearing in the active region of the material system may also preclude the presence of

strong coupling, and thereby annul possible amplification effects. This problem is particularly severe for GaN-based systems which have dislocation densities of 10^6-10^8 in the starting substrate. In a separate experiment discussed in the previous chapter we have shown that excitons bound to defects do not contribute to the strong-coupling phenomenon. Finally, while GaN has high exciton binding energy and oscillator strength, the values of these parameters are still smaller than those of ZnO, which is one of the proposed material systems in the theoretical study [192]. Hence it remains to be seen whether the optical amplification effect can be observed in a bulk ZnO based system under electrical or optical excitation.

Chapter VIII

Summary and Suggestions for Future Works

8.1 Summary of Present Work

The work presented in this thesis concentrated on the development and understanding of electrically injected exciton polariton lasers. To this end, we have designed, epitaxially grown, fabricated and characterized GaAs- and GaN-based polariton lasers which can operate at high temperature and room temperature respectively. Besides steady state characterization, small-signal modulation response of polariton laser diodes have been studied experimentally in this work. We have also elucidated the role of defects on the performance characteristics of polariton lasers, particularly its influence on lowering the effective polariton temperature in the non-equilibrium polariton condensate. Finally design, growth, fabrication and characterization of a bulk GaN based semiconductor optical amplifier has been conducted and the challenges associated with its realization are discussed from an experimental perspective. In what follows, the discourse appearing in different chapters are presented in brief.

A theoretical overview of exciton-polaritons in semiconductor microcavities is presented in Chapter I. It is shown that the exciton binding energy can be significantly

enhanced by reducing the dimensionality of excitons in semiconductors. The cavity photon characteristics on the other hand is strongly dependent on the quality of the microcavity mirrors. It has been theoretically shown that high quality mirrors can be realized using DBRs, where the principle of interference is employed. Next the strong-coupling phenomenon is explained in the context of exciton-polaritons in a semiconductor microcavity. The polariton dispersion characteristics have been derived and explained using the 2x2 coupled harmonic oscillator model. Also the nature of 2D, 1D and 0D polaritons are discussed. Finally, the underlying principles of polariton lasing is discussed. It is shown that in a polariton laser, the separation of stimulation and absorption eliminates the requirement of population inversion for light amplification. Moreover, the low polariton effective mass significantly reduces the critical density for dynamic condensation. Altogether, it should operate as an *ultra-low threshold, inversionless* coherent emitter.

The theoretical framework provided in chapter 2 is followed by the experimental techniques used in this work. Different semiconductors and dielectric materials with respect to the experimental realization of polariton lasers are discussed. Wide bandgap semiconductors are deemed to be more suitable for realizing high temperature polariton lasers because of their high exciton binding energies. However, there are several challenges associated with the growth and fabrication of conventional surface emitting microcavity diodes using these materials. To this end, we have presented a novel edge emitting geometry, where the cavity is defined by focused ion beam milling and e-beam evaporation technique. The material and device characterization techniques used in this work are also discussed. These techniques are necessary to ascertain, as well as to

characterize, the strong-coupling and polariton lasing phenomena in the final fabricated devices.

Based on the edge emitting geometry discussed in chapter 2, we present in chapter 3 the experimental realization of a GaAs-based high temperature polariton diode laser which operates at 155 K. Here we first discuss how the exciton binding energy can be increased in a SQW GaAs-based system by increasing the Al composition and reducing the well width. The excitonic transition characteristics of the MBE grown heterostructure shows an exciton binding energy of 15.8 meV, as obtained from temperature dependent PL measurements. The strong-coupling regime of the fabricated low series-resistance microcavity diode is characterized by a Rabi splitting of 15 meV, whereas the polariton lasing is characterized by a threshold current density of 90 A/cm^2. Photon lasing is observed from the same device at ~17 times higher injection density. Momentum space distribution and spatial coherence have also been confirmed in the polariton lasing regime. We also present in this chapter our study towards realizing a room temperature GaAs-based polariton diode laser by further increasing the Al composition in the active region. However, photoluminescence studies performed on the MBE grown heterostructure shows the dominance of bound excitonic states, which are not conducive to the realization light-matter coupling.

In chapter 5, we present the epitaxial growth, fabrication and characterization of an electrically pumped polariton laser which operates at room temperature. This device has a similar edge emitting geometry as the previously discussed GaAs-based device, however the active region here is bulk GaN. The heterostructure used in this work is grown by plasma assisted molecular beam epitaxy and the material is characterized by

AFM, XRD and photoluminescence measurements. Strong coupling and polariton lasing characteristics of several microcavity diodes are presented in this chapter. The non-linear threshold corresponding to polariton lasing in these devices is within a range of 125- 375 A/cm^2. At more than two orders of magnitude higher injection current densities, conventional photon lasing is also observed. Output polarization characteristics of the bulk GaN microcavity diode polariton laser are also measured and theoretically modeled in this work. A maximum 22% linear degree of polarization is obtained from these bulk GaN-based devices. It is envisaged that an array of these devices presented here will constitute a coherent linearly polarized ultraviolet light source with acceptable power.

In chapter 6, we present the small-signal modulation response of the room temperature polariton diode laser, the steady state characteristics of which were discussed in chapter 5. Based on the high frequency transient response of this electrically pumped device, we derive its modulation bandwidth, resonance frequencies and damping factor. A maximum -3dB modulation bandwidth of 1.18 GHz is measured, whereas the intrinsic bandwidth is estimated to be 1.8 GHz. Gain compression and differential gain are also phenomenologically described and formulated for a polariton device. Based on Boltzmann kinetic equations, we theoretically model the resonance frequency of the device. Interestingly, the role of defects needs to be taken into account in this model to describe the experimental observation. In this chapter, we further discuss the role of defects in the context of dynamic condensation and the effective temperature of the non-equilibrium lower polariton condensate. A simplified theoretical model is presented here as well to further illustrate the observed phenomena.

In chapter 7, we present our experimental study on the prospect of a bulk GaN based optical amplifier operating in the strong coupling regime. The underlying theory of the work is first presented in brief. The heterostructure of the device studied here is identical to those of the polariton laser diodes presented in the previous chapter. However this device does not have a microcavity as the dynamics here are based on bulk polariton modes. Our experimental study does not exhibit any clear indication of optical amplification of the guided polariton mode. Based on the observed results, we discuss the challenges associated with the experimental realization of such a device.

8.2 Suggestions for Future Work

8.2.1 Quantum Well-based Room Temperature Polariton Laser Diode

Though experimental realization of an electrically pumped polariton laser operating at room temperature is a significant milestone, there is ample scope for improvement of both the static and dynamic characteristics of the device. It is expected that better non-linearity, lower lasing threshold, larger modulation bandwidth, and possibly higher output power may be obtained if the active region of the reported microcavity diode is replaced with quantum well(s). Polariton lasing in a GaN-based system containing quantum well(s) active region has only been demonstrated using optical excitation. To this end, we suggest an InGaN/AlGaN quantum well-based electrically pumped polariton laser having the same edge-emitting structure as the bulk GaN polariton laser diode presented in this work. A schematic of the possible heterostructure is shown in Fig. 8.1. The high exciton binding energy of the system should enable room temperature polariton lasing. Also lower In composition in the well

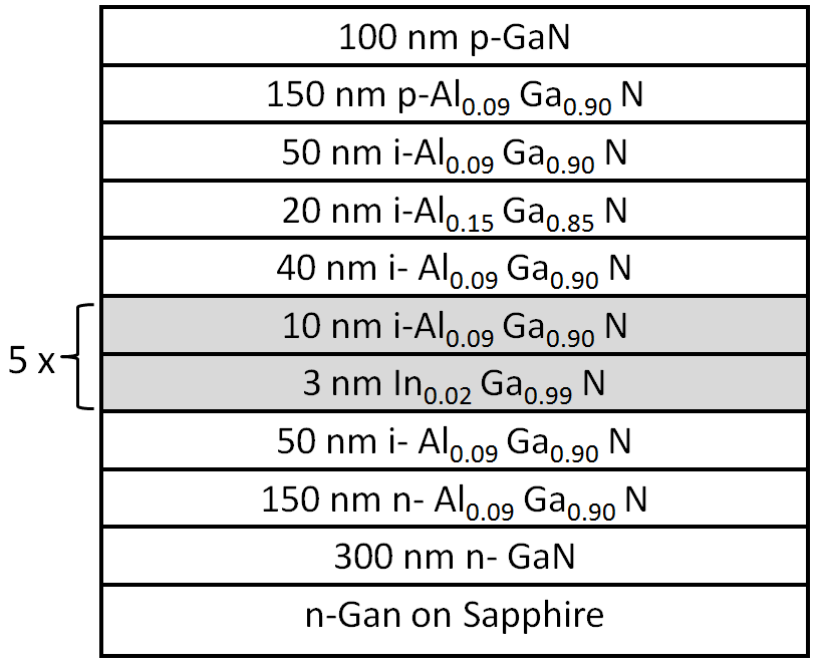

Fig. 8.1 Schematic representation of the proposed GaN/AlGaN quantum well based polariton diode laser

material should minimize alloy broadening and clustering effects [197]. The barrier and cladding layers are designed to provide adequate electrical and optical confinements.

To study the quantum well active region, the heterostructure shown in Fig. 8.1 was grown up to the top $Al_{0.09}Ga_{0.91}N$ barrier layer using PAMBE. Photoluminescence measurements were performed by exciting the sample with a 325 nm He:Cd laser at low and room temperature. Figure 8.2 shows the excitation dependent PL spectra measured at T=20K. The low energy shoulder may be associated with the dopant bound excitonic transition. The higher energy shoulders on the other hand are most likely the X_A and X_B free excitonic transitions, as have been observed in the measured PL spectra of the bulk-GaN active regions shown in chapter 5. The excitonic nature of these shoulders were confirmed by the nearly linear dependence of their integrated intensities on the excitation density and also the peak invariance with the change of excitation density. At room

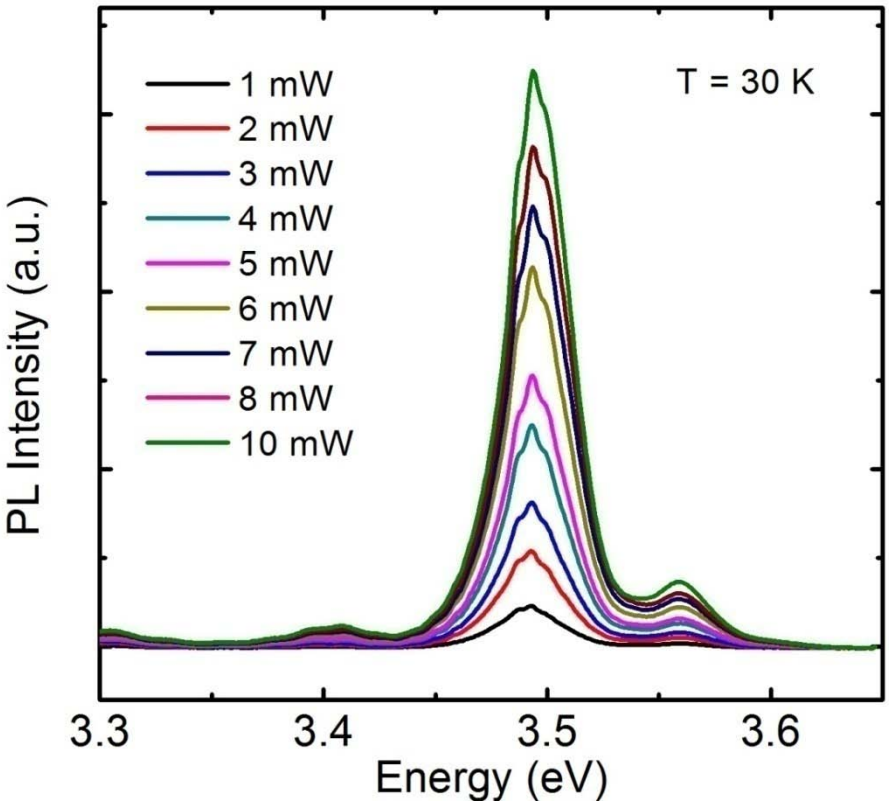

Fig. 8.2 Excitation dependent PL intensities of the InGaN/GaN multiple quantum-well heterostructure at T=30 K

temperature, these distinct transitions merge to show a broad peak at ~3.47 eV. It is expected that further optimization of the material growth will result stronger excitonic transition, thereby facilitating the realization of a quantum well based polariton laser diode which can operate at room temperature.

8.2.2 Electrical Exciton-Polariton Spin Switch

Exciton-polaritons are spin-degenerate quasi-particles which have spin projections of $s_z = +1$ and $s_z = -1$ on the growth axis. Theoretical and experimental studies show that these spin projections can directly couple with circularly polarized light σ^+ and σ^- respectively both in the emission and excitation [94, 95, 199]. Using these

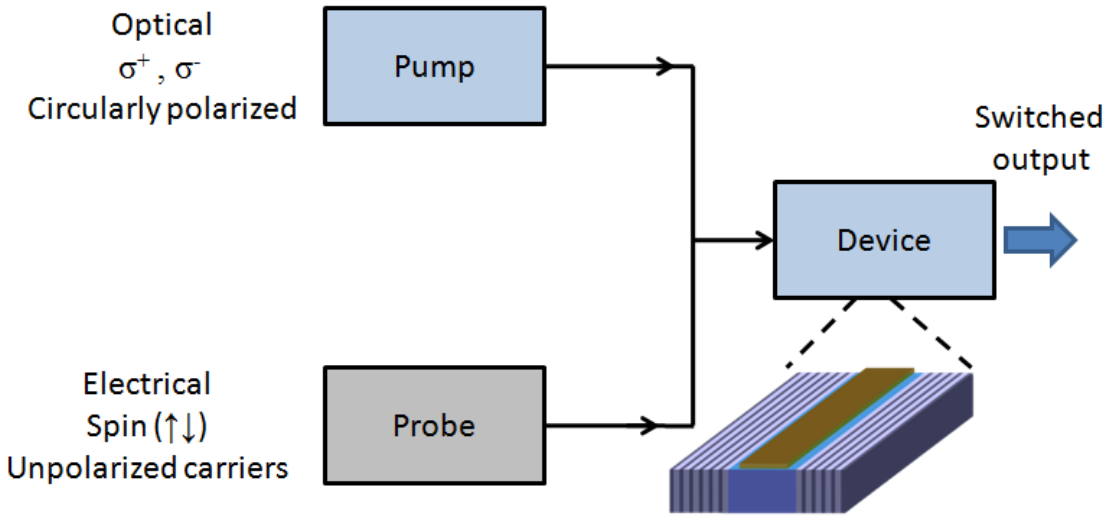

Fig. 8.3 Proposed electrically controllable exciton-polariton spin switching scheme

properties of polaritons, several optically pumped polarization sensitive devices have been theoretically proposed or experimentally demonstrated [198-200]. Here we suggest a bulk GaN-based exciton-polariton spin switch employing the same edge-emitting geometry presented in the current work. In the proposed scheme (Fig. 8.3), the device is expected to operate under simultaneous electrical and optical pumping at room temperature. The device is electrically pumped with spin-unpolarized carriers such that the pre-threshold low intensity output of point I is reached (Fig. 8.4). This is defined as the off-ready state of the device. As shown in our study of the steady state polarization of a polariton laser diode (discussed in section 5.5.5), the output is unpolarized at this injection. By pumping the system further, with additional bias or a probe light, stimulated polariton-polariton scattering is initiated and a linear degree of polarization builds up in the emission output. Because this linearly polarized output contains equal superposition of polaritons having opposite spins, a circularly polarized probing light (σ^+ or σ^-) can

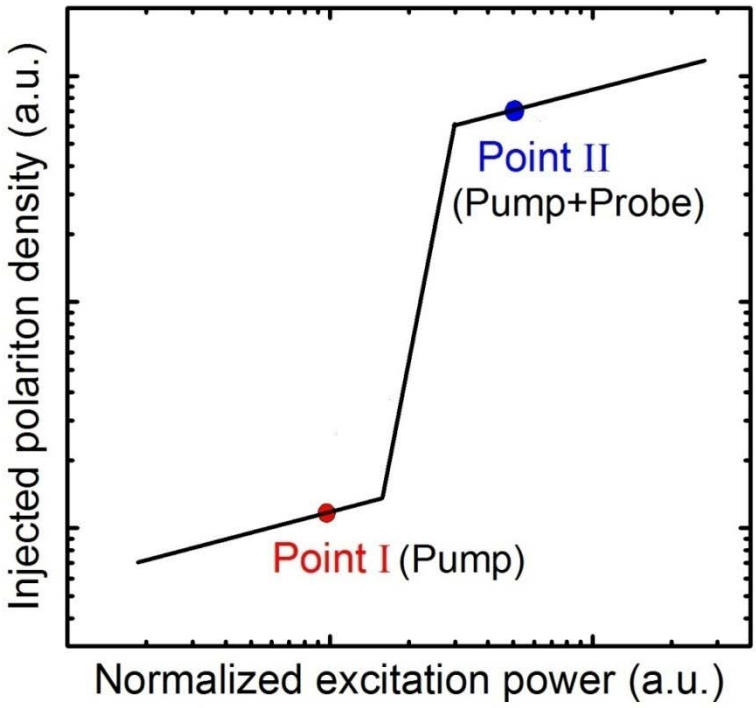

Fig. 8.4 Principle of operation of the exciton polariton spin switch.

be utilized to drive the system to point II for polaritons of one particular spin polarization ($s_z = +1$ and -1 respectively). This phenomenon is related to the stronger interaction between polaritons with parallel spins than between polaritons with anti-parallel spins [200]. Such non-local measurements can play an important role towards the development of spin-based polariton logic devices on a single platform.

8.2.3 Spin-Polarized Exciton-Polariton Spin Switch

It is envisaged that greater control over the operation of an electrical exciton-polariton spin switch can be obtained if spin-polarized carriers are injected into the electrically driven polariton device. To this end, we propose an edge-emitting polariton laser diode in which injected spin polarized carriers will travel by drift and diffusion from a spin injector across the contact and cladding layers and reach the device active region.

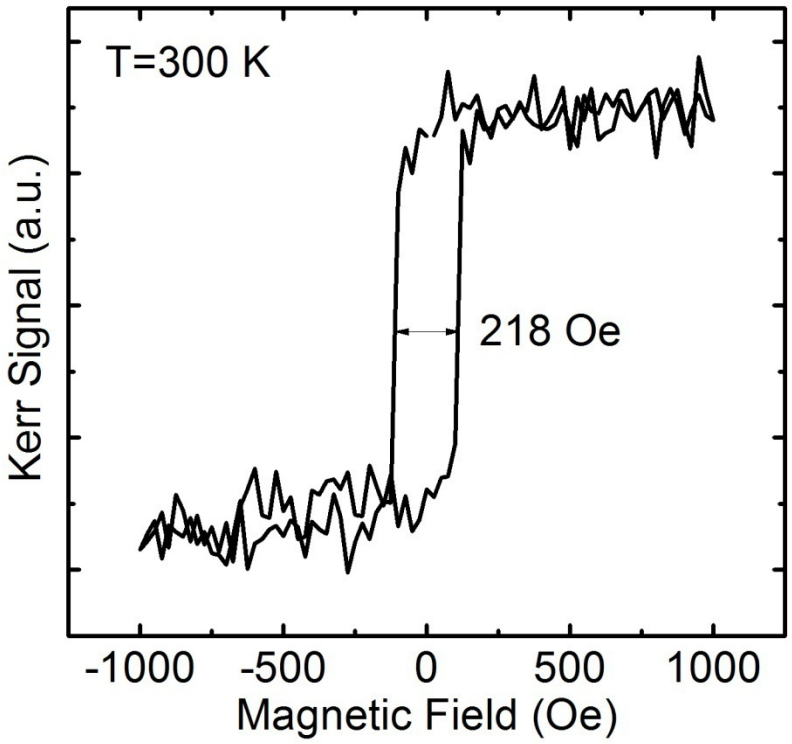

(a)

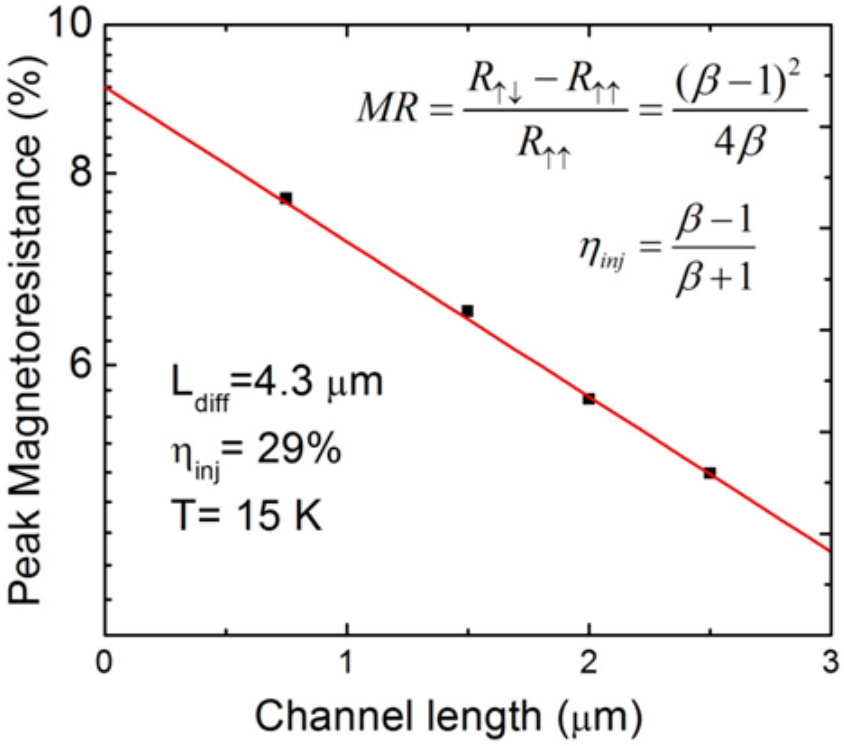

(b)

Fig. 8.5 (a) Magnetization characteristics of the FeCo/MgO tunnel contact obtained by MOKE measurements, (b) peak magnetoresistance measured as function of channel length to obtain the spin injection efficiency and diffusion lengths.

A prospective candidate for the spin injector is FeCo/MgO ferromagnetic tunnel contact which can be deposited using electron beam evaporation technique. The magnetization characteristics of this contact obtained by magneto optic Kerr effect (MOKE) measurements are shown in Fig. 8.5(a). We have already studied the diffusive spin transport properties by four terminal non-local Hanle spin precision measurements in bulk GaAs and GaN, employing the mentioned spin contact [201]. As shown in Fig. 8.5(b), the spin diffusion length and spin injection efficiencies obtained for the GaAs spin valve are 6 μm and 37% respectively, using the approach described in [202]. Based on these values, the GaAs-based spin polarized polariton laser may be designed, grown and fabricated using the conventional non-inverted structure. The device heterostructure may have single or multiple quantum well as the active region and it can be epitaxially grown

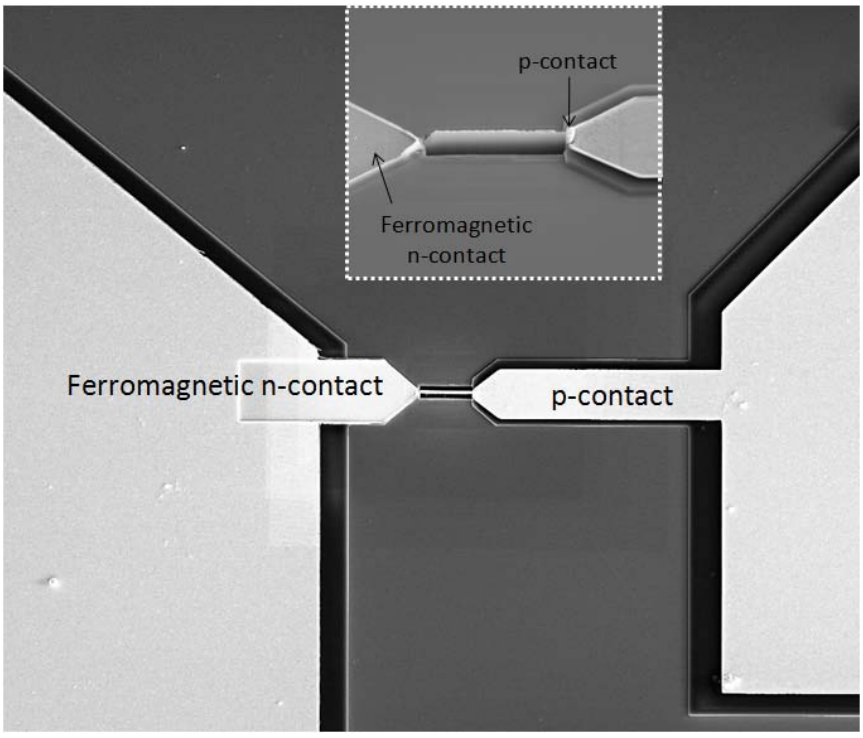

Fig. 8.6 An image of the proposed GaAs-based edge emitting microcavity diode employing spin injectors as the n-type contact; inset shows the magnified cavity region.

on n-doped (001) GaAs substrate. A SEM image of the proposed GaAs-based device is shown in Fig. 8.6. As can be seen, the n- and p-contacts are designed to be within a distance of the spin diffusion length, so that spin-polarized carriers can reach the active region before losing their spin orientations under the influence of different scattering events. This device can be fabricated using standard UV lithography, which has a resolution of 700 nm in our study. However for sub-micron spin diffusion lengths, the fabrication and processing needs to be performed using electron beam lithography, which is a direct-write lithographic technique having sub-10 nm resolution.

An alternate to the proposed device scheme is to employ a inverted heterostructure, which has to be epitaxially grown on a p-doped substrate. This is particularly useful for GaN based systems, in which we have measured a spin diffusion length and spin injection efficiencies of 147 nm and 8% respectively [201]. The proposed

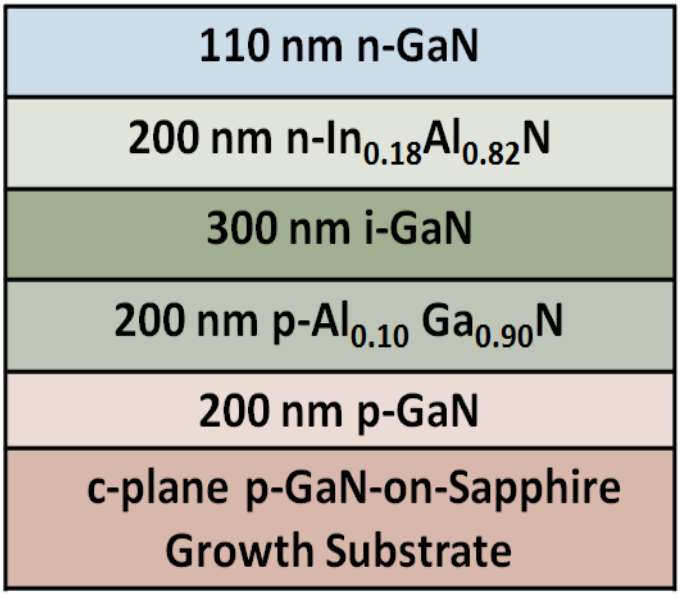

Fig. 8.7 Proposed GaN-based inverted heterostructure for realizing an electrically pumped exciton-polariton spin switch.

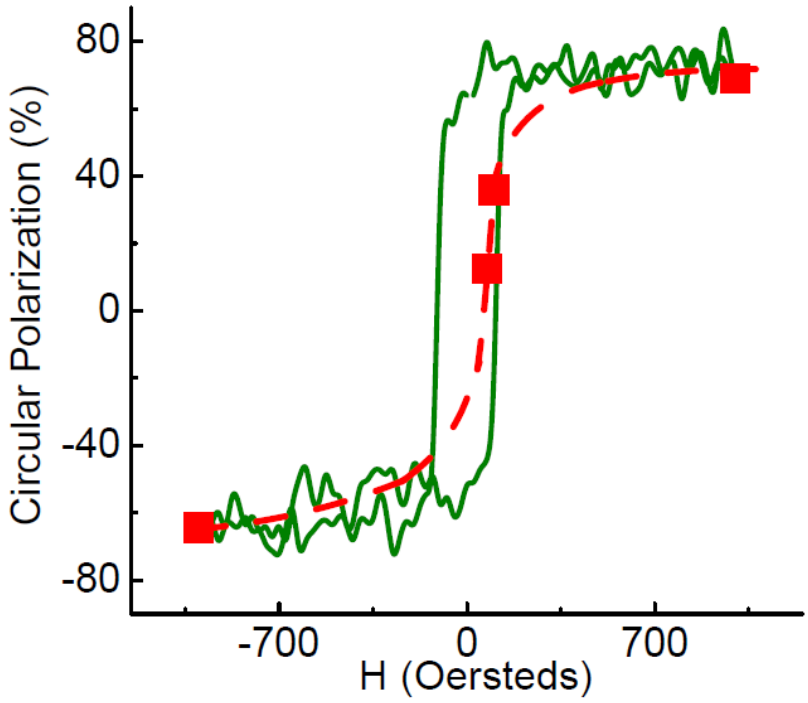

(a)

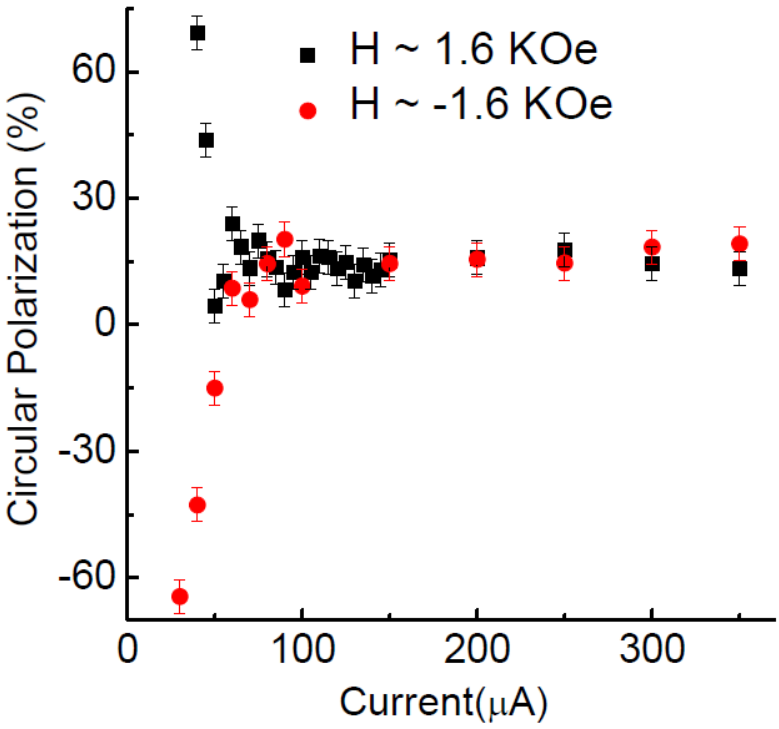

(b)

Fig. 8.8 (a) Output circular polarization alongside the measured magnetization of the tunnel injector contacts (the dashed line is a guide to the eye), (b) output circular polarization as a function of injection.

GaN-based inverted heterostructure is shown in Fig. 8.7. In this scheme, the device can be fabricated using the same design as the bulk GaN-based polariton laser presented in this work. Preliminary results obtained from the measurements performed on such a device are shown in Fig. 8.8. In these measurements, the devices were characterized at various in-plane magnetizing fields of the ferromagnetic spin injector, in the range of to -1.6 kOe to 1.6 kOe. The non-linear threshold is significantly reduced to a very low value of ~ 19μA (48 A/cm^2) at all magnetic fields. The output circular polarization follows the measured magnetization of the spin injection as a function of magnetic field. A peak circular polarization of ~69% is measured, which decreases with increasing injection. The helicity of the output polarization reverses with reversal in the direction of magnetization of the spin injector.

APPENDICES

Appendix A

Exciton-Photon Coupling in Surface- and Edge-Emitting Geometries

The electric dipole of an exciton can strongly interact with the electromagnetic field of light in semiconductor microcavities having both surface- and edge-emitting structures. Here we consider the case of bulk GaN-based surface- and edge-emitting geometries, which are schematically shown in Fig. A.1. As can be seen, in the surface-emitting structure, excitation and light output are in the same direction whereas in the edge-emitting structure, they are in orthogonal directions. The growth axis, which is c-axis for the wurtzite GaN heterostructures used in this study, is parallel to the direction of

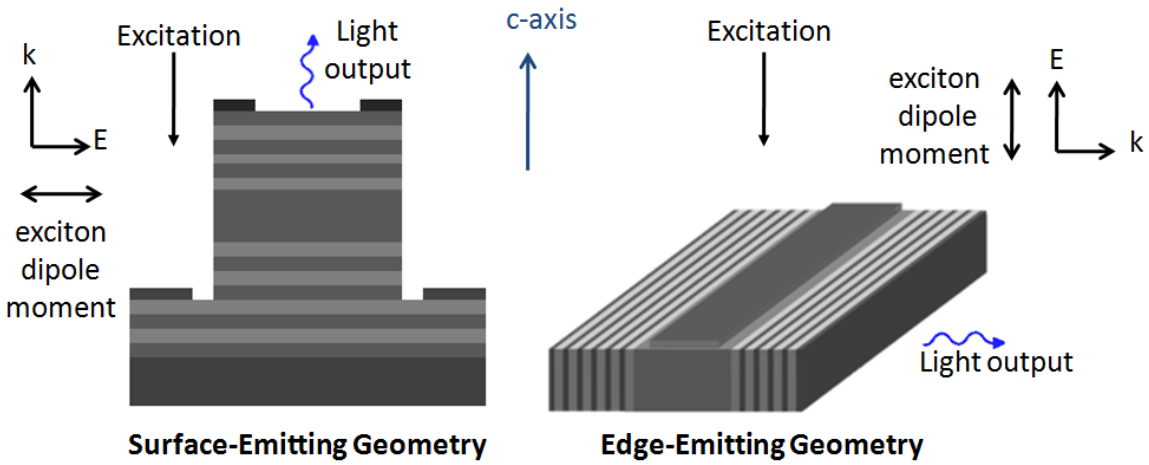

Fig. A.1 Surface- and edge-emitting geometry-based semiconductor microcavities showing the directions of excitation, light output and exciton dipole moment.

optical or electrical excitation. The ground exciton state in wurtzite GaN is 12-fold degenerate, which is split into 12 exciton states in the presence of external excitation. Among these 12 states, five states are optically active, three of which have Γ_5 symmetry and the two others have Γ_1 symmetry [203]. Only these five dipole-allowed excitonic transitions can contribute to the formation of exciton-polaritons in a semiconductor microcavity. Exciton states having Γ_5 symmetry can form exciton-polaritons in the surface-emitting geometry, where the exciton-dipole moment $\vec{E}$ is perpendicular to the c-axis (Fig. A1(a)). On the other hand, the two states having Γ_1 symmetry participate in strong-coupling in the edge-emitting geometry, where $\vec{E}$ is parallel to the c-axis (Fig. A1(b)). Similarly, in GaAs quantum-well based edge-emitting geometry, polarization selection rules indicate that quantum-well excitons couple to TE-polarized cavity photons.

Appendix B

Theoretical Analysis of Steady-State Output Polarization

Experimental results on the output polarization of GaN-based polariton diode lasers can be analyzed by modeling the kinetics of the system with the four coupled stochastic differential equations, as shown by Kavokin et al. [121]

$$\frac{d\psi_\sigma}{dt} = \frac{1}{2}\left[W(t) - \Gamma_c\right]\psi_\sigma + \frac{1}{2}\left(\gamma + i\Omega\right)\psi_{-\sigma} - \frac{i}{\hbar}\left[\alpha_1\left|\psi_\sigma\right|^2 + \alpha_2\left|\psi_{-\sigma}\right|^2\right]\psi_\sigma + \theta_\sigma(t) \quad (1)$$

$$W(t) = a_{ph}N_r(t) + b_{pol}N_r^2(t) \quad (2)$$

$$\frac{dN_r}{dt} = -\Gamma_r N_r - W(t)\left[\left|\psi_-\right|^2 + \left|\psi_+\right|^2 + 1\right] + W_e n_{e-h}(t) \quad (3)$$

$$\frac{dn_{e-h}}{dt} = \frac{J}{q} - \frac{n_{e-h}}{\tau_{e-h}} - W_e n_{e-h} \quad (4)$$

The order parameter $\psi_\pm$ describes the many body wavefunction of polariton condensates with +1 and -1 projections of spin to the structure axis, $N_r$is the exciton reservoir occupation, and $n_{e\text{-}h}$ is the occupation of the free carrier reservoir. $W(t)$ defines the rate of the polariton relaxation towards the ground state. We consider two relaxation mechanisms, namely the polariton-phonon scattering characterized by the scattering rate $a_{ph}$and polariton-polariton scattering with the rate b_{pol}. In all probability, the phonon scattering process (the first term on the right-hand side of equation (2)) does not involve a single scattering event but rather proceeds through a cascade of phonon emissions.

Nevertheless, the phenomenon of final-state stimulation is present and for the rate of polariton-polariton scattering, it is proportional to square of the reservoir occupation as the rate of any two-body collision process. The first term in the right-hand side of equation (2) describes the phonon induced scattering of excitons and is linearly dependent on the exciton reservoir occupation. The two-body collision process is described by the second term in equation (2) which is quadratic in the exciton reservoir occupation. Γ_c is inversely proportional to the polariton lifetime, which is mainly governed by the cavity quality factor. The constants Ω and γ correspond to the effective magnetic field leading to the energy splitting of the polarized condensate states and to the spin relaxation term, respectively. Constants α_1 and α_2 describe the interactions of polaritons with the same and opposite spin projections, respectively. Phenomenological constants Γ_r and W_e describe the decay rate of the excitons in the reservoir and the exciton formation rate, respectively.

The noise term $\theta(t)$ is defined by its correlators:

$$\left\langle \theta_\sigma(t)\theta_{\sigma'}(t')\right\rangle = 0 \qquad (5)$$

$$\left\langle \theta_\sigma(t)\theta^*_{\sigma'}(t')\right\rangle = \frac{1}{2}W(t)\delta_{\sigma\sigma'}\delta(t-t') \qquad (6)$$

The system of equations (1-4) is then numerically solved using the stochastic Runge-Kutta algorithm. For the numerical calculation we use the following parameters corresponding to conventional GaN -based laser diodes [43]: Γ_c = 1.3 ps^{-1}, γ= 0.0035 ps^{-1}, Ω = 0.03 ps^{-1}, α_1=0.0001 ps^{-1}, α_2= -0.1 α_1, a_{ph}= 10^{-11} ps^{-1}, b_{pol}= 10^{-12} ps^{-1}, Γ_r = 0.001 ps^{-1}, W_e= 0.01 ps^{-1}, τ_{e-h}= 2000 ps. The ground state occupation number is given by

$n(t) = |\psi_+|^2 + |\psi_-|^2$ and the components of the condensate pseudospin linked to the output light polarization are:

$$S_x = \mathrm{Re}\left(\psi_+^* \psi_-\right) \tag{7}$$

$$S_y = \mathrm{Im}(\psi_+^* \psi_-) \tag{8}$$

$$S_z = \frac{1}{2}(|\psi_+|^2 - |\psi_-|^2) \tag{9}$$

Time and noise averaged signals have been recorded during the measurements. Namely the degree of linear polarization is given by $s_x = \left\langle \int dt S_x(t) / \int dt n(t) \right\rangle$, where brackets symbolize averaging over the noise. In order to obtain the theoretical values of the degree of linear polarization for Device 2, the following parameters have been varied with respect to the analysis for Device 1: the spin relaxation rate, γ , has been changed from 0.0035 ps^{-1} to 0.005 ps^{-1} , the polariton radiative rate Γ_c has been changed from 1.3 ps^{-1} to 1 ps^{-1} and the internal magnetic field Ω has been changed from 0.03 ps^{-1} to 0.05 ps^{-1}.

Appendix C

Three-level Rate Equation based Modeling of the Polariton Laser

The dynamics of an electrically pumped polariton laser has been theoretically explained by Iorsh. et al. [148], within the framework of Boltzmann kinetics, using a simplified quasianalytical model. In this model, the electron-hole plasma, the exciton reservoir and the ground state polaritons are described by three rate equations, respectively, as follows:

$$\frac{dn_{e-h}}{dt} = \frac{J}{q} - \frac{n_{e-h}}{\tau_{e-h}} - Wn_{e-h} \quad \text{A.1}$$

$$\frac{dn_x}{dt} = -\frac{n_x}{\tau_x} + Wn_{e-h} - an_x\left(n_p+1\right) + ae^{-\beta\Delta_{esc}} n_p n_x - bn_x^2\left(n_p+1\right) - cn_{e-h}n_x\left(n_p+1\right) \quad \text{A.2}$$

$$\frac{dn_p}{dt} = -\frac{n_p}{\tau_{LP}} + an_x\left(n_p+1\right) - ae^{-\beta\Delta_{esc}} n_p n_x + bn_x^2\left(n_p+1\right) + cn_{e-h}n_x\left(n_p+1\right) \quad \text{A.3}$$

Here $n_{e\text{-}h}$ is the electron hole plasma density, n_x is the exciton reservoir density and n_p is the lower polariton occupation. The scattering events are represented by the scattering rates *a, b* and c, where *a* takes into account the acoustic and optical phonon scatterings, *b* accounts for the exciton-polariton scatterings and *c* is the free-carrier mediated relaxation rate. τ_{e-h} , τ_x and τ_{LP} correspond to the free carrier, exciton and ground state polariton lifetimes respectively. *W* is the exciton formation, *J* is the current density, *q* is the

electron charge, S is the contact surface area of the device. $\beta = 1/k_B T$ and Δ_{esc} is the polariton trap depth.

Because exciton-exciton scattering is the dominant relaxation mechanism in the polariton lasing regime, Eqns. A.1-A.3 can be simplified considering $a \gg b, c$. Also above threshold, the $\left(1+n_p\right)$ and $\left(1+n_x\right)$ terms can be approximated as n_p and n_x, respectively. Based on these assumptions, the steady state occupation numbers of the polariton ground state n_{LP}^{∞}, reservoir occupation number n_x^{∞} and the number of free carriers in the system n_{eh}^{∞} can be expressed using the following Boltzmann kinetic equation set:

$$0 = \frac{J \cdot S}{q} - \frac{n_{eh}^{\infty}}{\tau_{eh}} - W n_{eh}^{\infty};$$

$$0 = W n_x^{\infty} - \frac{n_x^{\infty}}{\tau_x} - b n_x^{\infty 2}(1 + n_{LP}^{\infty});$$

$$0 = -\frac{n_{LP}^{\infty}}{\tau_{LP}} + b n_x^{\infty 2}(1 + n_{LP}^{\infty});$$

where W = 0.01 ps^{-1} (ref. 27), and $\tau_{eh} = 1$ ns, $\tau_x = 0.6$ ns, $\tau_{LP} = 0.58$ ps are considered in our analysis. From, a differential analysis of these simplified rate equations, the resonance frequency of the microcavity diode can be expressed as:

$$\omega_R^2(\text{pol}) \cong 2\sqrt{\frac{b}{\tau_{LP}^{\ 3}}} n_p$$

As has been discussed in chapter 6, a term n_T is introduced into this equation to take phenomenologically take into account the role of defects in the active region of the polariton laser.

Appendix D

Change in Refractive Index and Peak Wavelength with Small-Signal Modulation

The dielectric function of a material with a free carrier concentration changes as:

$$\epsilon(\nu, N) = \left(1 - \frac{Ne^2}{\epsilon_0 m_r^* \nu^2}\right)\epsilon_r$$

where N is the free carrier concentration, e is the charge of an electron, ϵ_0 is the permittivity of free space, m_r^* is the carrier mass, and v is the photon frequency, ϵ_r is the relative permittivity [203].Substituting wavelength for frequency

$$\epsilon(\lambda, N) = \left(1 - \frac{Ne^2\lambda^2}{\epsilon_0 m_r^* c^2}\right)\epsilon_r$$

If we ignore the wavelength dependence of the permittivity and only consider the free carrier change, we can simplify this as

$$\epsilon(N) = (1 - NV)\epsilon_r$$

where V is a "volume" intrinsic to the material that we define as:

$$V = \frac{e^2\lambda_0^2}{\epsilon_0 m_r^* c^2}$$

If we modulate the device, we expect a change in permittivity equal to

$$\Delta\epsilon(\Delta N) = \Delta N V \epsilon_r$$

By replacing the constants with known values, we obtain:

$$\Delta\epsilon(\Delta N = 9.65 * 10^{14} cm^{-3}) = 1.9\text{x}10^{-4}$$

With a DC value of n=2.65, we obtain $n_+ = 2.6500376, n_- = 2.649962.$ The cavity length, L, was designed to be $5\lambda_0/n_0$= 688.679 nm.

The peak will shift due to the change in refractive index to:

$$\lambda_+ = \frac{n_+ L}{5} = 365.00557\ nm$$

$$\lambda_- = \frac{n_- L}{5} = 364.99527\ nm$$

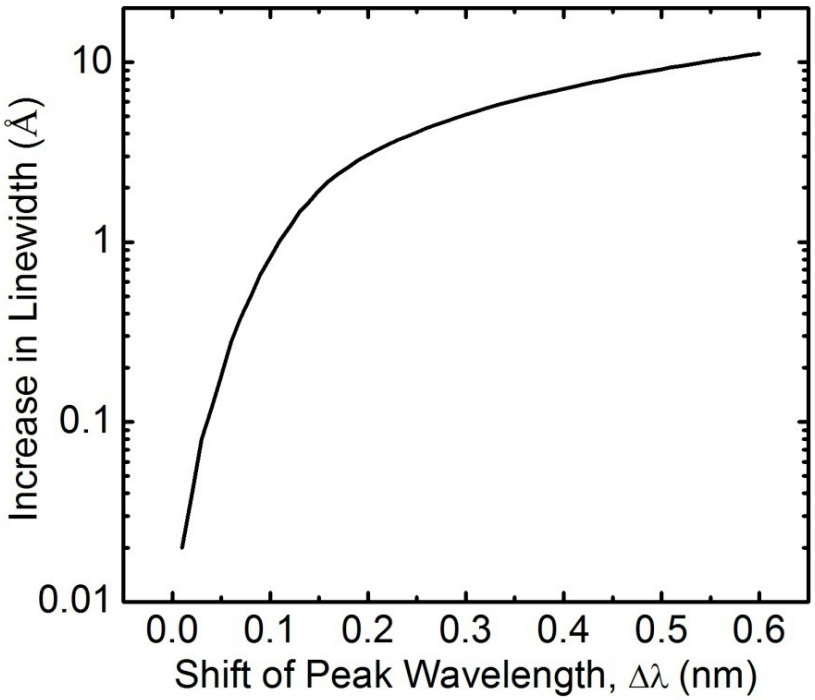

Fig. D.1 Theoretically calculated relation between increase of the emission linewidth and the shift of the peak emission wavelength

So the peak moves from nominal center by $\Delta\lambda$ ~$\pm$0.0557 Å. The correlation between measured broadening of the emission linewidth and frequency chirping is theoretically shown in Fig. D.1 As can observed, for small values of $\Delta\lambda$ (which is the case for polariton lasers), there appears to be no broadening of the peak linewidth. On the other hand, for larger values of $\Delta\lambda$, the linewidth seems to increase approximately linearly, and slightly smaller than $2\Delta\lambda$.

BIBLIOGRAPHY

[1] G. P. Agrawal, N. K. Dutta, "Semiconductor Lasers," 2nd ed. Kluwer Academic Publishers (2001).

[2] X. Liu, W. Zhao, L. Xiong, H. Liu, "Packaging of High Power Semiconductor Lasers," Springer (2015).

[3] T. Numai, "Fundamentals of Semiconductor Lasers," Springer (2004).

[4] W. W. Chow, S. W. Koch, "Semiconductor-laser Fundamentals," Springer (1999)

[5] M. E. Fermann, A. Galvanauskas, G. Sucha, "Ultrafast Lasers: Technology and Applications," Marcel Dekker, Inc. (2013).

[6] A. L. Schawlow and C. H. Townes, Phys. Rev. 112 (6), 1940 (1958).

[7] Hall, R. N., G. E. Fenner, J. D. Kingsley, T. 1. Soltys, and R. O. Carlson. Phys. Rev. Lett.9, 366 (1962).

[8] Nathan, M. 1., W. P. Dumke, G. Burns, F. H. Dill, Jr., and G. Lasher. Appl. Phys. Lett. 1,62 (1962).

[9] Quist, T. M., R. H. Rediker, R. J. Keyes, W. E. Krag, B. Lax, A. L. McWhorter, and H. J. Zeiger, Appl. Phys. Lett. 1, 91 (1962).

[10] Holonyak, N., Jr., and S. F. Bevacqua. Appl. Phys. Leu. 1,82 (1962).

[11] Kroemer, H. Proc. IEEE 51,1782 (1963).

[12] Alferov, Zh. 1., and R. F. Kazarinov. Authors certificate 181737 (U.S.S.R.), 1963.

[13] C. Weisbuch, M. Nishioka, A. Ishikawa, and Y. Arakawa, Phys. Rev. Lett. 69, 3314 (1992).

[14] G. Khitrova, H. M. Gibbs, F. Jahnke, M. Kira, and S.W.Koch,Rev. Mod. Phys. 71, 1591 (1999).

[15] D. Porras, C. Ciuti, J. J. Baumberg, and C. Tejedor, Phys. Rev. B 66, 085304 (2002).

[16] H. M. Gibbs, G. Khitrova, and S. W. Koch, Nature Photonics 5, 273 (2011).

[17] B. Deveaud, "The Physics of Semiconductor Microcavities: From Fundamentals to Nanoscale Devices," Wiley (2007).

[18] H. Deng, D. Press, S. Götzinger, G. S. Solomon, R. Hey, K. H. Ploog, and Y. Yamamoto, Phys. Rev. Lett. 97, 146402 (2006).

[19] J. Kasprzak et al. Nature (London) 443, 409 (2006).

[20] R. Balili, V. Hartwell, D. Snoke, L. Pfeiffer, and K. West, Science 316, 1007–1010 (2007).

[21] A. Das, P. Bhattacharya, J. Heo, A. Banerjee, and W. Guo, Proc. Natl. Acad. Sci. U.S.A. 110, 2735 (2013).

[22] J. J. Baumberg et al. Phys. Rev. Lett. 101, 136409 (2008).

[23] H. Ohadi, E. Kammann, T. C. H. Liew, K. G. Lagoudakis, A. V. Kavokin, and P. G. Lagoudakis, Phys. Rev. Lett. 109, 016404 (2012).

[24] A. Amo et al., Nature Phys. 5, 805-810 (2009).

[25] D. Sanvitto et al., Nature Phys. 6, 527-533 (2010).

[26] A. Amo et al., Science Vol. 332, Issue 6034, pp. 1167-1170 (2011).

[27] J. Keeling, P. R. Eastham, M. H. Szymanska, and P. B. Littlewood Phys. Rev. B 72, (2005).

[28] T. Byrnes, T. Horikiri, N. Ishida, and Y. Yamamoto, Phys. Rev. Lett. 105, 186402 (2010).

[29] G. Malpuech, Y. G. Rubo, F. P. Laussy, P. Bigenwald, and A. V. Kavokin,

Semicond. Sci. Technol. 18, S395 (2003).

[30] Y. G. Rubo, Phys. Rev. Lett. 99, 106401 (2007).

[31] A. Imamoglu, R. J. Ram,S.Pau, and Y. Yamamoto, Phys. Rev. A 53, 4250 (1996).

[32] G. Malpuech, A. Kavokin, A. Di Carlo, and J. J. Baumberg, Phys. Rev. B 65, 153310 (2002).

[33] A. Kavokin and G. Malpuech, "Cavity Polaritons", Thin Films and Nanostructures, Elsevier (2003).

[34] H. Deng, H. Haug, Y. Yamamoto, Rev. Mod. Phys. 82, 1489, 2010.

[35] D. Bajoni, J. Phys. D: Appl. Phys. 45, 313001 (2012).

[36] R. L. Fork, L. A. Burgess, M. L. Davenport, D. M. Ramey, P. J. Reardon, D. B. Pollock, R. G. Lindquist, and D. M. Fork, Proc. SPIE 6952, Laser Source Technology for Defense and Security IV, 69520I (2008).

[37] T. C. H. Liew, A. V. Kavokin, T. Ostatnický, M. Kaliteevski, I. A. Shelykh, and R. A. Abram, Phys. Rev. B 82, 033302 (2010).

[38] A. Amo et al., Nature Photonics 4, 361 - 366 (2010).

[39] T.C.H. Liew, I. A. Shelykh, and G.Malpuech, Physica E 43, 1543–1568 (2011).

[40] A. Kavokin, "Why do we need polariton lasers?," http://spie.org/newsroom/4477-why-do-we-need-polariton-lasers (2012).

[41] D. Ballarini et al., Nature Communications 4, Article number: 1778 (2013).

[42] H. Flayac and I. G. Savenko, Appl. Phys. Lett.103, 201105 (2013).

[43] T. Byrnes, N. Y. Kim and, Y. Yamamoto, Nature Physics 10, 803–813 (2014).

[44] S. I. Pekar, J. Exp. Teor. Fiz. USSR 33: 1022 (1957).

[45] J. J. Hopfield, Phys. Rev., 112:1555 (1958).

[46] D. Fröhlich, E. Mohler, and P. Wiesner, Phys. Rev. Lett. 26, 554 (1971).

[47] C. Weisbuch and R. G. Ulbrich, Phys. Rev. Lett. 39, 654 (1977).

[48] B. Hönerlage, R. Lévy, J.B. Grun, C. Klingshirn, and K. Bohnert, Physics Reports, Volume 124, Issue 3, 161-253 (1985).

[49] R. B. Balili, Thesis, *Bose-Einstein Condensation Of Microcavity Polaritons* (2009).

[50] R. Houdré, C. Weisbuch, R. P. Stanley, U. Oesterle, P. Pellandini, and M. Ilegems, Phys. Rev. Lett. 73, 2043 (1994).

[51] R. Houdre, R. P. Stanley, U. Oesterle, and M. Ilegems, Phys. Rev. B 49, 16761 (1994).

[52] R. P. Stanley, R. Houdré, C. Weisbuch, U. Oesterle, and M. Ilegems, Phys. Rev. B 53, 10995 (1996).

[53] S. Pau, H. Cao, J. Jacobson, G. Björk, Y. Yamamoto, and A. Imamoğlu, Phys. Rev. A 54, R1789(R) (1996).

[54] L. S. Dang, D. Heger, R. André, F. Boeuf, and R. Romestain, Phys. Rev. Lett. 81, p. 3920-3923 (1998).

[55] R. Huang, Y. Yamamoto, R. André, J. Bleuse, M. Muller, and H. Ulmer-Tuffigo, Phys. Rev. B 65, 165314 (2002).

[56] J. J. Baumberg et al., Phys. Rev. B 62, R16247 (2000).

[57] H. Deng, G. Weihs, D. Snoke, J. Bloch, and Y. Yamamoto, Proc. Natl. Acad. Sci.100, 15318 (2003).

[58] P. G. Lagoudakis, M. D. Martin, J. J. Baumberg, G. Malpuech, and A. Kavokin, J. Appl. Phys. 95, 2487 (2004).

[59] M. Richard, J. Kasprzak, R. Romestain, R. André, and L. S. Dang, Phys. Rev. Lett. 94, 187401 (2005).

[60] S. Christopoulos et al., Phys. Rev. Lett. 98, 126405 (2007).

[61] G. Christmann, R. Butté, E. Feltin, J. Carlin and N. Grandjean, Appl. Phys. Lett. 93, 051102 (2008).

[62] A. P. D. Love et al., Phys. Rev. Lett. **101**, 067404 (2008).

[63] D. Bajoni, P. Senellart, E. Wertz, I. Sagnes, A. Miard, A. Lemaître, and J. Bloch, Phys. Rev. Lett. 100, 047401 (2008).

[64] J. D. Plumhof, T. Stöferle, L. Mai, U. Scherf, and R. F. Mahrt, Nature Materials 13, 247–252 (2014).

[65] S. Kéna-Cohen and S. R Forrest, Nat. Photon.4, 371(2010).

[66] S. Azzini, D. Gerace, M. Galli, I. Sagnes, R. Braive, A. Lemaître, J. Bloch, and D. Bajoni, Appl. Phys. Lett. 99, 111106 (2011).

[67] T. Guillet et al., Appl. Phys. Lett. 99, 161104 (2011).

[68] A. Das, J. Heo, M. Jankowski, W. Guo, L. Zhang, H. Deng, and P. Bhattacharya, Phys. Rev. Lett. 107, 066405 (2011).

[69] A. Das, J. Heo, A. Bayraktaroglu, W. Guo, T. Ng, J. Phillips, B. S. Ooi, and P. Bhattacharya, Optics Express 20, 11, 11830-11837 (2012).

[70] J. Heo, S. Jahangir, B. Xiao, and P. Bhattacharya, NanoLett. 13 (6), 2376 (2013).

[71] T. C. Lu et al., Opt Express, 20: 5530–5537 (2012).

[72] F. Li et al., Appl. Phys. Lett. 102, 191118 (2013).

[73] K. S. Daskalakis et al., Appl. Phys. Lett. **102**, 101113 (2013).

[74] D. Xu et al., Appl. Phys. Lett. 104, 082101 (2014).

[75] B. Zhang, Z. Wang, S. Brodbeck, C. Schneider, M. Kamp, S. Höfling, and H. Deng, Light: Sci. Appl. 3, e135 (2014).

[76] M. Nomura, N. Kumagai, S. Iwamoto, Y. Ota, and Y. Arakawa, Nature Phys.6, 279 (2010).

[77] K. Hennessy et al., Nature 445, 896-899 (2007).

[78] D. Bajoni, E. Semenova, A. Lemaître, S. Bouchoule, E. Wertz, P. Senellart, and J. Bloch, Phys. Rev. B 77, 113303 (2008).

[79] S. I. Tsintzos, N. T. Pelekanos, G. Konstantinidis, Z. Hatzopoulos, and P. G. Savvidis, Nature (London) 453, 372, (2008).

[80] C. Schneider et al., Nature (London) 497, 348 (2013).

[81] P. Bhattacharya, B. Xiao, A. Das, S. Bhowmick, and J. Heo, Phys. Rev. Lett. 110, 206403 (2013).

[82] P. Bhattacharya, T. Frost, S. Deshpande, M. Z. Baten, A. Hazari, and A. Das, Phys. Rev. Lett. 112, 236802 (2014).

[83] I. Pelant, and J. Valenta, "Luminescence Spectroscopy of Semiconductors," Oxford Scholarship (2012).

[84] J. Levrat, Thesis, *Physics of Polariton Condensates in GaN-based Planar Microcavities* (2012).

[85] G. Bastard, E. E. Mendez, L. L. Chang, and L. Esaki, Phys. Rev. B 26, 1974 (1982).

[86] S. Koteles, et al., SPIE 792, pp. 302 (1987).

[87] W. Guo, M. Zhang, A. Banerjee, and P. Bhattacharya, Nano Lett. 10, pp 3355-3359 (2010).

[88] S. Bhowmick, M. Z. Baten, T. Frost, B. S. Ooi, and P. Bhattacharya, IEEE J. Quant. Elec. 50, 7 (2014)

[89] A. Imamoglu, D. D. Awschalom, G. Burkard, D. P. DiVincenzo, D. Loss, M. Sherwin, and A. Small, Phys. Rev. Lett. **83**, 4204 (1999).

[90] P. Bhattacharya, "Semiconductor Optoelectronic Devices," 2nd ed. Upper Saddle River, NJ: Prentice Hall (1996).

[91] E. I. Rashba, G. E. Gurgenishvili, Sov. Phys. - Solid State 4: 759–760 (1962).

[92] H. Deng, Thesis, *Dynamic Condensation Of Semiconductor Microcavity Polaritons* (2006).

[93] S. L. Chuang, "Physics of Photonic Devices," Wiley (2012).

[94] K. V. Kavokin, I. A. Shelykh, A. V. Kavokin, G. Malpuech, and P. Bigenwald, Phys. Rev. Lett. 92, 017401 (2004).

[95] I. A. Shelykh, A. V. Kavokin, and G. Malpuech, phys. stat. sol. (b) 242, No. 11, 2271–2289 (2005).

[96] A. Kavokin, J. J. Baumberg, G. Malpuech, and F. P. Laussy, "Microcavities," Oxford University Press (2011).

[97] R. Harel, E. Cohen, E. Linder, Arza Ron, and L. N. Pfeiffer, Phys. Rev. B 53, 7868 (1996).

[98] R. Rapaport, R. Harel, E. Cohen, Arza Ron, and E. Linder, Phys. Rev. Lett. 84, 1607 (2000).

[99] F Tassone, C Piermarocchi, V Savona, A Quattropani, and P Schwendimann, Physical Review B 56 (12), 7554 (1997).

[100] A. J. D. Grundy, Thesis, *Optically Nonlinear Spatial and Spectral Processes in Semiconductor Microcavities* (2009).

[101] J. Kasprzak, Thesis, *Condensation of exciton polaritons* (2006).

[102] D. Sanvitto, V. Timofeev, "Exciton Polaritons in Microcavities: New Frontiers," Springer (2012).

[103] X. Liu et al., Nature Photonics 9, 30–34 (2015).

[104] S. Dufferwiel et al., Nature Communications 6, Article 8579 (2015).

[105] R. Butté, G. Christmann, E. Feltin, A. Castiglia, J. Levrat, G. Cosendey, A. Altoukhov, J. -F. Carlin, and N. Grandjean, Proc. SPIE 7216, 721619 (2009).

[106] M Manasreh, "III-Nitride Semiconductors: Electrical, Structural and Defects Properties," 1st ed., Elsevier Science (2000).

[107] P. G. Savvidis, Nature Photonics 8, 588–589 (2014).

[108] H. Morkoç, J.-I. Chyi, A. Krost, Y. Nanishi, D. J. Silversmith, Proc. IEEE **98**, 1113 (2010)

[109] Y. Lai, Y. Lan, and T. C. Lu, Light: Science and Applications, 2, e76 (2013).

[110] A. A. Tseng, J. Micromech. Microeng. 14, R15 (2004).

[111] Y. Chyr, Thesis, *The Photonic Applications of Focused Ion Beam Micromachining on GaN* (1994).

[112] M. P. Mack, et al. Electron. Lett.,34, 1315(1998).

[113] C. Ambe, et. al. Materials Sci. and Engin. B59, 382 (1999).

[114] Y. Yuan, T. Brock, P. Bhattacharya, C. Caneau, and R. Bhat, IEEE J. Lightwave Tech. **25**, 1826 (1997).

[115] J. Yang and P. Bhattacharya, Opt. Express 16, 5136 (2008).

[116] G. Kamler, J. L. Weyher, I. Grzegory, E. Jezierska, and T. Wosínski, J. Crystal

Growth, 246, no 1–2, pp. 21–24(2002).

[117] D. Zhuang, and J. H. Edgar. Mater. Sci. Eng., R48, pp. 1–46 (2005).

[118] G. Su, T. Frost, P. Bhattacharya, and J. Dallesasse, *Opt. Express.* **23** (10), 12850 (2015).

[119] M. Z. Baten, A. Bhattacharya, T. Frost, I Iorsh, A. Kavokin, P. Bhattacharya, Appl. Phys. Lett. 108 (4), 041102 (2016).

[120] M. Z. Baten et al., Appl. Phys. Lett. 104, 231119 (2014).

[121] A. Bhattacharya, M. Z. Baten, I Iorsh, T. Frost, A. Kavokin, and P. Bhattacharya, Phys. Rev. B, (*in press*), (2016).

[122] M. Z. Baten, T. Frost, I. Iorsh, S. Deshpande, A. Kavokin, and P. Bhattacharya, Scientific Reports 104, 231119 (2015).

[123] L. Sapienza, A. Vasanelli, R. Colombelli, C. Ciuti, Y. Chassagneux, C. Manquest, U. Gennser, and C. Sirtori, Phys. Rev. Lett. 100, 136806 (2008).

[124] A. A. Khalifa, A. P. D. Love, D. N. Krizhanovskii, M. S. Skolnick, and J. S. Roberts, Appl. Phys. Lett. 92, 061107 (2008).

[125] S. Brodbeck et al.,Optics Express 21, 31098 (2013).

[126] P. J. Pearah, W. T. Masselink, J. Klem, T. Henderson, and H. Morkoç, Phys. Rev. B 32, 3857 (1985).

[127] P. K. Bhattacharya, A. Majerfeld, and A. K. Saxena, Inst. Phys. Conf. Ser.45, 199–210 (1979).

[128] R. L. Greene, K. K. Bajaj and D. E. Phelps, Phys. Rev. B 29, 1807 (1984).

[129] G. Roumpos, Thesis, *Phase Fluctuations In Microcavity Exciton Polariton Condensation* (2011).

[130] J. Pipreck, “Semiconductor Optoelectronic Devices,” Academic Press (2003).

[131] J. Singh, K. K. Bajaj, and S. Chaudhuri, Appl. Phys. Lett. 44, 805 (1984).

[132] W.-P. Hong, J. Singh, and P. K. Bhattacharya, IEEE Electron Device Lett. 7, 480 (1986).

[133] T. Bartel, M. Dworzak, M. Strassburg, A. Hoffmann, A. Strittmatter, and D. Bimberg, Appl. Phys. Lett. 85, 1946 (2004).

[134] Z. D. Chen, Q. Wu, M. Yang, J. H. Yao, R. A. Rupp, Y. A. Cao, and J. J. Xu, Opt. Express 21(18), 21329 (2013).

[135] J. Singh, “Electronic and Optoelectronic Properties of Semiconductor Structures,” Cambridge University Press (2003).

[136] L. Pavis, M. Guzzi, J. Appl. Phys. 75, 4779 (1994).

[137] Q. Li, S. J. Xu, M. H. Xie, and S. Y. Tong, J. Phys.: Condens. Matter 17, 4853 (2005).

[138] T. Schmidt, K. Lischka, and W. Zulehner, Phys. Rev. B 45, 8989 (1992).

[139] M. Zamfirescu, A. Kavokin, B. Gil, G. Malpuech, and M. Kaliteevski, Phys. Rev. B 65, 161205(R) (2002).

[140] G. Malpuech, A. D. Carlo, A. Kavokin, J. J. Baumberg, M. Zamfirescu, and P. Lugli, Appl. Phys. Lett. 81, 412 (2002).

[141] Q. Ren, R. P. Gailitis, K. P. Thomson, and J. T. Lin,IEEE J. Quant. Electron. 26 , 2284 (1990).

[142] M. Schadt, K. Schmitt, V. Kozinkov, and V. Chigrinov, Jpn. J. Appl. Phys. 31, 2155 (1992).

[143] M. Hasegawa, and Y. Taira, Journal of Photopolymer Science and Technology 8 , 241 (1995).

[144] N. Kawatsuki, H. Ono, H. Takatsuka, T. Yamamoto, and O. Sangen, Macromolecules 30, 6680 (1997).

[145] B. W. Chwirot et al., Lasers Surg. Med. 21, 149 (1997).

[146] J. M. Phillips et al., Laser & Photon. Rev. 1, 307 (2007).

[147] D. Solnyshkov, E. Petrolati, A. Di Carlo, and G. Malpuech, Appl. Phys. Lett. 94, 011110 (2009).

[148] I. Iorsh, et al., Phys. Rev. B 86, 125308 (2012).

[149] T.-C. Lu, J.-R. Chen, S.-W. Chen, H.-C. Kuo, C.-C. Kuo, C.-C. Lee, and S.-C. Wang, IEEE J. Sel. Top. Quantum Electron. 15, 850 (2009).

[150] T. Frost, Thesis, *Red-Emitting Iii-Nitride Self-Assembled Quantum Dot Lasers* (2016).

[151] R. Butté, G. Christmann, E. Feltin, J. F. Carlin, M. Mosca, M. Ilegems, and N. Grandjean, Phys. Rev. B 73, 033315, (2006).

[152] A. Teke and H. Morkoç, edited by S. Kasap and P. Capper, "Springer Handbook of Electronic and Photonic Materials", Springer, New York (2007).

[153] D. Solnyshkov and G. Malpuech, Superlattices Microstruct. 41, 279 (2007).

[154] I. R. Sellers et al., Phys. Rev. B 74, 193308 (2006).

[155] F. Stokker-Cheregi et al., Appl. Phys. Lett. 92, 042119 (2008).

[156] J. Zuniga-Perez et al., Appl. Phys. Lett. 104, 241113 (2014).

[157] W. Fang and S. L. Chuang, Appl. Phys. Lett. 67, 751 (1995).

[158] N. Peyghambarian, H. M. Gibbs, J. L. Jewell, A. Antonetti, A. Migus, D. Hulin, and A. Mysyrowicz, Phys. Rev. Lett. 53, 2433 (1984).

[159] I. Vurgaftman and J. R. Meyer, J. Appl. Phys. 94, 3675 (2003).

[160] G. Christmann, R. Butté, E. Feltin, A. Mouti, P. A. Stadelmann, A. Castiglia, J-F. Carlin, and N. Grandjean, Phys. Rev. B 77, 085310 (2008).

[161] D. Sarchi and V. Savona, Phys. Rev. B 75, 115326 (2007).

[162] M. D. Martín, D. Ballarini, A. Amo, Ł. Kłopotowsi, L. Viña, A. V. Kavokin, and R. André, Phys. Status Solidi C 2, 3880 (2005).

[163] F. P. Laussy, I. A. Shelykh, G. Malpuech, and A. Kavokin, Phys. Rev. B 73, 035315 (2006).

[164] I. A. Shelykh, Yu. G. Rubo, G. Malpuech, D. Solnyshkov, and A. V. Kavokin, Phys. Rev. Lett. 97, 066402 (2006).

[165] M. Combescot, O. Betbeder-Matibet, and R. Combescot, Phys. Rev. Lett. 99, 176403 (2007).

[166] J. Kasprzak, R. André, Le Si Dang, I. A. Shelykh, A. V. Kavokin, Yuri G. Rubo, K. V. Kavokin, and G. Malpuech, Phys. Rev. B 75, 045326 (2007).

[167] E. del Valle, D. Sanvitto, A. Amo, F. P. Laussy, R. André, C. Tejedor, and L. Viña, Phys. Rev. Lett. 103, 096404 (2009).

[168] D. Read, T. C. H. Liew, Y. G. Rubo, and A. V. Kavokin, Phys. Rev. B 80, 195309 (2009).

[169] J. Levrat, R. Butté, T. Christian, M. Glauser, E. Feltin, J.-F. Carlin, N. Grandjean, D. Read, A. V. Kavokin, and Y. G. Rubo, Phys. Rev. Lett. 104, 166402 (2010).

[170] V. G. Sala, F. Marsault, M. Wouters, E. Galopin, I. Sagnes, A. Lemaître, J. Bloch, and A. Amo, Phys. Rev. B 93, 115313 (2016).

[171] Ł. Kłopotowski, M.D. Martin, A. Amo, L. Viña,I.A. Shelykh, M.M. Glazov, G. Malpuech, A.V. Kavokin, R. Andre, Solid State Commun. 139, 511 (2006).

[172] K. G. Lagoudakis, T. Ostatnický, A. V. Kavokin, Y. G. Rubo, R. André and B. Deveaud-Plédran, Science 326, 974 (2009).

[173] P. Bhattacharya et al., IEEE Trans. Electron Devices 46, 871 (1999).

[174] V. A. Gergel', R. F. Kazarinov, and R. A. Suris, Sov. Phys. JETP 26, 2 (1968).

[175] S. Schmitt-Rink, D. S. Chemla, and D. A. B Miller, Phys. Rev. B **32**, 10 (1985).

[176] T. Frost, A. Banerjee, and P. Bhattacharya, Appl. Phys. Lett. 103, 211111 (2013).

[177] T. Frost et al., Nano Lett. 14, 4535−4541 (2014).

[178] Z. Mi, P. Bhattacharya, and S. Fathpour, Appl. Phys. Lett. 86, 153109 (2005).

[179] J. Kasprzak, D. D. Solnyshkov, R. Andre´, L. S. Dang, and G. Malpuech, Phys. Rev. Lett. 101, 146404 (2008).

[180] W. Guo, M. Zhang, P. Bhattacharya, and J. Heo, Nano Lett. 11(4), 1434–1438 (2011).

[181] G. You, W. Guo, C. Zhang, P. Bhattacharya, R. Henderson, and J. Xu, Appl. Phys. Lett. **102**, 091105 (2013).

[182] B. J. Skromme, J. Jayapalan, R. P. Vaudo, and V. M. Phanse, Appl. Phys. Lett., 74, No. 16, p. 2358 (1999).

[183] M. Leroux, N. Grandjean, B. Beaumont, G. Nataf, F. Semond, J. Massies, and P. Gibart,. J. Appl. Phys. 86, 3721 (1999).

[184] W. Götz, N. M. Johnson, H. Amano, and I. Akasaki, Appl. Phys. Lett. 65, 463 (1994).

[185] H. K. Cho, Kim C S, and Hong C-H, J. Appl. Phys. 94, 1485 (2003).

[186] Private communication with A. Kavokin and I. Iorsh.

[187] K. E. Stubkjaer, IEEE J. Select. Top. Quantum Electron., vol. 6, no. 6, pp. 1428-1435 (2000).

[188] J. Mork, M. L. Nielsen, and T. W. Berg, Optics and Photonics News Vol. 14, Issue 7, pp. 42-48 (2003).

[189] C. Schubert, R. Ludwig, H.-G. Weber, J Optic Comm Rep, Volume 2, Issue 2, pp 171–208 (2005).

[190] M. J. Connelly, "Semiconductor Optical Amplifiers," Kluwer Academic Publishers (2004).

[191] N. K. Dutta, Q. Wang, "Semiconductor Optical Amplifiers," 2nd ed., World Scientific Publishing Company (2013).

[192] D. D. Solnyshkov, H. Terças and G. Malpuech, Appl. Phys. Lett. 105, 231102 (2014).

[193] K. Huang, Proc. Roy. Soc. London, A208:352 (1951).

[194] C. Weisbuch and R.G. Ulbrich, J. Lumin. 18/19, 27 (1979).

[195] S. F. Chichibu et al., Semicond. Sci. Technol. **20**, S67 (2005).

[196] V.A. Kosobukin, R.P. Seisyan, and S.A. Vaganov, Semicond. Sci. Technol. 8, 1235 (1993).

[197] M. Glauser, C. Mounir, G. Rossbach, E. Feltin, J. F. Carlin, R. Butté, and N. Grandjean, J. Appl. Phys. 115, 233511 (2014).

[198] I. Shelykh, K. V. Kavokin, A. V. Kavokin, G. Malpuech, P. Bigenwald, H. Deng, G. Weihs, and Y. Yamamoto, Phys. Rev. B 70, 035320 (2004).

[199] A. Kavokin, G. Malpuech, and M. Glazov, Phys. Rev. Lett. 95, 136601 (2005).

[200] A. Amo, T. C. H. Liew, C. Adrados, R. Houdré, E. Giacobino, A. V. Kavokin, and A. Bramati, Nature Photonics 4, 361 - 366 (2010).

[201] A. Bhattacharya, M. Z. Baten, and P. Bhattacharya, Appl. Phys. Lett. 108, 042406 (2016).

[202] D. Shaha, Thesis, *Ferromagnet/Semiconductor Based Spintronic Devices* (2009).

[203] P. P. Paskov, T. Paskova, P. O. Holtz, and B. Monemar, Phys. Rev. B 70, 035210 (2004).

[204] C. Kittel, "Introduction to Solid State Physics," 8th Edition, Wiley (2004).